



Veröffentlichungen der DGK

Ausschuss Geodäsie der Bayerischen Akademie der Wissenschaften

Reihe C

Dissertationen

Heft Nr. 931

Melanie Elias

**On the Use of Smartphones as Novel Photogrammetric
Water Gauging Instruments
Developing Tools for Crowdsourcing Water Levels**

München 2024

Bayerische Akademie der Wissenschaften

ISSN 0065-5325

ISBN 978-3-7696-5343-4

Diese Arbeit ist gleichzeitig veröffentlicht in:

Qucosa – Dokumenten- und Publikationsserver der Sächsischen Landesbibliothek – Staats- und Universitätsbibliothek (SLUB)
<https://nbn-resolving.org/urn:nbn:de:bsz:14-qucosa2-751602>, Dresden 2021



DGK Veröffentlichungen der DGK

Ausschuss Geodäsie der Bayerischen Akademie der Wissenschaften

Reihe C

Dissertationen

Heft Nr. 931

On the Use of Smartphones as Novel Photogrammetric Water Gauging Instruments

Developing Tools for Crowdsourcing Water Levels

Von der Fakultät Umweltwissenschaften
der Technischen Universität Dresden
zur Erlangung des akademischen Grades
Doktor-Ingenieur (Dr.-Ing.)
genehmigte Dissertation

von

Melanie Elias, M.Sc.

geboren am 12.05.1990 in Freiberg

München 2024

Bayerische Akademie der Wissenschaften

ISSN 0065-5325

ISBN 978-3-7696-5343-4

Diese Arbeit ist gleichzeitig veröffentlicht in:

Qucosa – Dokumenten- und Publikationsserver der Sächsischen Landesbibliothek – Staats- und Universitätsbibliothek (SLUB)
<https://nbn-resolving.org/urn:nbn:de:bsz:14-qucosa2-751602>, Dresden 2021

Adresse der DGK:



Ausschuss Geodäsie der Bayerischen Akademie der Wissenschaften (DGK)

Alfons-Goppel-Straße 11 • D – 80 539 München
Telefon +49 - 331 - 6264 1685 • E-Mail post@dgk.badw.de
<http://www.dgk.badw.de>

Prüfungskommission:

Vorsitzender: Prof. Dipl.-Phys. Dr.-Ing. habil. Dirk Burghardt

Referent: Prof. Dr. habil. Hans-Gerd Maas

Korreferenten: Prof. Dr. Thomas P. Kersten (HCU Hamburg)
Prof. Dr. Roderik C. Lindenbergh (TU Delft, Niederlande)

Tag der mündlichen Prüfung: 03.05.2021

© 2024 Bayerische Akademie der Wissenschaften, München

Alle Rechte vorbehalten. Ohne Genehmigung der Herausgeber ist es auch nicht gestattet,
die Veröffentlichung oder Teile daraus auf photomechanischem Wege (Photokopie, Mikrokopie) zu vervielfältigen

ISSN 0065-5325

ISBN 978-3-7696-5343-4

Preface

This dissertation has been submitted for the degree Doktor-Ingenieur (Dr.-Ing.) at the Faculty of Environmental Sciences, Department of Geosciences, Institute of Photogrammetry and Remote Sensing of the Technische Universität Dresden (TU Dresden). The research has been conducted during the author's occupation at the Institute of Photogrammetry and Remote Sensing, TU Dresden between October 2015 and May 2020 and was funded by the European Social Fund (ESF) and the Freestate of Saxony as part of the PhD scholarship program "Federal innovation doctorates" from October 2015 to September 2018 (grant no. 100235479). Additional funding was granted by the Graduate Academy of TU Dresden between October 2018 and January 2019.

As the thesis title suggests, the work investigates the suitability of smartphones as photogrammetric measurement instruments and deals with the development of a novel photogrammetric water gauging method, running on smartphones. The thesis has been written in a cumulative manner and follows a three-part structure comprising introduction, main section and synthesis. The introductory part starts with an outline of the addressed problem, namely the insufficient water level monitoring in small-scale catchments, which leads to serious impediments in the hydrological modelling of flash floods. This is followed by a discussion of current water gauging techniques, showing their strengths and weaknesses, resulting in four key research questions. Moreover and with regard to the work described in the main part, basic knowledge on smartphone technology, crowdsourcing and mobile software development is provided. The main part essentially consists of four chapters, each chapter being a separate scientific paper that has been published in an international, peer-reviewed journal on photogrammetry or sensor technology. The first two papers are focussed on the smartphone as photogrammetric measurement device, whereas the third and fourth paper concern the development of a smartphone-implemented water gauging tool. A fifth chapter provides three abstracts of associated papers about preliminary work of the published methods and about related work that has been co-authored by the author of this thesis. The synthesis summarises the research results, shows technical limitations of the developed measuring approach and identifies potentials for future developments. The thesis ends with a list of references applicable to the introduction and to the synthesis. The references of each paper in the main section are given at the end of the respective chapters.

The presented thesis uses a uniform layout, which made it necessary to adapt the formatting specifications of the related journals in favour of the reading flow. This leads to adjustments in the formal text design and in the referencing style of figures, tables and equations. The original numbering of figures, tables and equations has been preceded by the respective chapter number to fit into the overall structure of the thesis. The positions and sizes of some figures and tables were slightly adapted to the advantage of the thesis layout. The headings of the scientific articles have been slightly adapted to ensure the coherence of the thesis. Broken links to references have been fixed where possible. Each article is introduced by a cover page providing the original title, the abstract, the recommended citation style and the publication history.

Statement of the authorship

I, Melanie Elias, hereby certify that I have authored this dissertation entitled *On the use of smartphones as novel photogrammetric water gauging instruments - Developing tools for crowdsourcing water levels* independently and without undue assistance from third parties and without additional resources and references than explicitly declared as such in the text by citation or footnote. I have marked both literal and accordingly adopted quotations as such. Unless otherwise stated, all graphics and illustrations were created by myself. The same applies to the software development, where all key library extensions and frameworks are explicitly identified and referenced in this thesis. The individual author contributions to the selected publication used in this cumulative dissertation are declared in the following section. I am aware that violations of this declaration may lead to subsequent withdrawal of the degree.

Dresden, 17th November 2020.

Melanie Elias (nee Kröhnert).

Author's Contribution

This section declares the author's contribution to the individual research articles that establish the main part of the thesis. For the sake of convenience the author of the dissertation Melanie Elias (nee Kröhnert) is just to be referred as "the author".

Paper 1 (Chapter 7) entitled *Assessing the Influence of Temperature Changes on the Geometric Stability of Smartphone- and Raspberry Pi Cameras* has been published in the Special Issue *CMOS Image Sensors and Related Applications of Sensors* by MDPI AG, Basel (CH). The author largely contributed to the design and implementation of the research, to the analysis of the results and to the writing of the manuscript. The software for space resection used in the investigations was developed by Frank Liebold. Additional tools used for data preparation, analysis and visualisation were developed by the author. The applied test field was made by Anette Eltner and calibrated by the author. The manuscript was revised and co-authored by Anette Eltner and Hans-Gerd Maas to a major degree and Frank Liebold to a minor degree.

Paper 2 (Chapter 8) entitled *Investigation on multi-sensor fusion strategies for improved orientation determination in mobile phone imaging applications* has been published in the ISPRS Annals, an open access collection of double-blind peer-reviewed conference papers published by Copernicus Publications, Göttingen (DE), on behalf of the International Society of Photogrammetry, Remote Sensing and Spatial Information Sciences (ISPRS). The work was presented at the ISPRS Virtual Event 2020 of the XXIV ISPRS Congress. The design and implementation of the research, the analysis of the results and the writing of the manuscript were carried out by the author alone. The paper was revised by Hans-Gerd Maas.

Paper 3 (Chapter 9) entitled *Segmentation of environmental time lapse image sequences for the determination of shore lines captured by hand-held smartphone cameras* has been published in the ISPRS Annals and was presented at the ISPRS Geospatial Week 2017 in Wuhan (CN). The work was awarded with the *Zhizhuo best youth oral paper award*. The design and implementation of the research, the analysis of the results and the writing of the manuscript were carried out by the author alone. The manuscript was revised by Robert Meichsner to a minor degree. The paper is an extension of the conference paper *Automatic waterline extraction from smartphone images* that has been published in the ISPRS Archives, a collection of peer-reviewed conference proceedings, and was presented at the ISPRS Congress 2016 in Prague (CZ).

Paper 4 (Chapter 10) entitled *Photogrammetric water level determination using smartphone technology* has been published in *The Photogrammetric Record* by John Wiley and Sons, Hoboken, NJ (US). Conceptualisation, investigation and writing the original draft was largely done by the author. The paper was revised by Christian Kehl and Danilo Schneider. Minor linguistic corrections were made by the editor Stuart I. Granshaw.

Chapter 11 provides cover pages of three related research articles that are either peer-reviewed conference papers containing preliminary work or journal papers being co-authored by the author. Similar to the cover pages of the Chapters 7–10, they comprise the original title, the abstract, the publication history and the recommended citation style as well as information on the author's contribution to the individual papers.

Acknowledgements

First, I would like to acknowledge the European Social Fund (ESF) and the Freestate of Saxony for funding the dissertation project from October 2015 to September 2018 (grant no. 100235479). Furthermore, I would like to thank the Graduate Academy of TU Dresden for their financial support from October 2018 to January 2019.

My personal thanks go to my supervisor Prof. Dr. habil. Hans-Gerd Maas for his guidance through each stage of the process. His door was always open when I was in need of assistance solving methodical and scientific questions and administrative support. I am grateful for his confidence in me and my working methods, his great support during the grant application phases and the academic freedom to solve the tasks.

Furthermore, I would like to express my special thanks to Prof. Dr. Thomas P. Kersten and Prof. Dr. Roderik C. Lindenbergh for reviewing the thesis as independent referees.

In many cases, successful work is not only the merit of one individual. At this point I would like to thank all my colleagues who accompanied, guided and supported me in each phase of the thesis project. In this regard, I wish to express my deepest gratitude to my former office mate Robert Meichsner for his great support in the beginner phase and for training my programming and mathematical skills. Similarly, I am very grateful to Frank Liebold for his guidance solving geodetic adjustment problems. Also, I would like to thank my current office mate Ferdinand Maiwald who always lent an ear during difficult programming and writing sessions that seemed to be insuperable. Furthermore, I would like to acknowledge Richard Boerner for his participation in the development of algorithms to render 3D point clouds during his time as a graduate assistant. Great thanks go to Anette Eltner for the close cooperation resulting in joint publications, comprehensive discussions to solve the one or other problem as well as amazing and exciting field trips. The same gratitude is expressed to Christian Kehl, who is an expert in computer graphics and who gave me valuable suggestions on the transfer of image measurements into the object space. I also want to thank Katja Richter for her numerous suggestions on how to improve the written thesis. Finally, I would like to thank all colleagues who were involved as co-authors in the publications and thus made a substantial contribution to the high quality of the individual articles.

Last but not least, I want to express my gratefulness to my family who gave me helping hands in all regards and who gave me support in situations of desperation. My particular thanks go to my husband Christoph for his unlimited understanding when I worked whole nights and weekends close to submission deadlines and his unbelievable mental support in moments like these.

Abstract

The term global climate change is omnipresent since the beginning of the last decade. Changes in the global climate are associated with an increase in heavy rainfalls that can cause nearly unpredictable flash floods. Consequently, spatio-temporally high-resolution monitoring of rivers becomes increasingly important.

Water gauging stations continuously and precisely measure water levels. However, they are rather expensive in purchase and maintenance and are preferably installed at water bodies relevant for water management. Small-scale catchments remain often ungauged. In order to increase the data density of hydrometric monitoring networks and thus to improve the prediction quality of flood events, new, flexible and cost-effective water level measurement technologies are required. They should be oriented towards the accuracy requirements of conventional measurement systems and facilitate the observation of water levels at virtually any time, even at the smallest rivers.

A possible solution is the development of a photogrammetric smartphone application (app) for crowdsourcing water levels, which merely requires voluntary users to take pictures of a river section to determine the water level. Today's smartphones integrate high-resolution cameras, a variety of sensors, powerful processors, and mass storage. However, they are designed for the mass market and use low-cost hardware that cannot comply with the quality of geodetic measurement technology.

In order to investigate the potential for mobile measurement applications, research was conducted on the smartphone as a photogrammetric measurement instrument as part of the doctoral project. The studies deal with the geometric stability of smartphone cameras regarding device-internal temperature changes and with the accuracy potential of rotation parameters measured with smartphone sensors.

The results show a high, temperature-related variability of the interior orientation parameters, which is why the calibration of the camera should be carried out during the immediate measurement. The results of the sensor investigations show considerable inaccuracies when measuring rotation parameters, especially the compass angle (errors up to 90° were observed). The same applies to position parameters measured by global navigation satellite system (GNSS) receivers built into smartphones. According to the literature, positional accuracies of about 5 m are possible in best conditions. Otherwise, errors of several 10 m are to be expected. As a result, direct georeferencing of image measurements using current smartphone technology should be discouraged.

In consideration of the results, the water gauging app *Open Water Levels (OWL)* was developed, whose methodological development and implementation constituted the core of the thesis project. OWL enables the flexible measurement of water levels via crowdsourcing without requiring additional equipment or being limited to specific river sections. Data acquisition and processing take place directly in the field, so that the water level information is immediately available.

In practice, the user captures a short time-lapse sequence of a river bank with OWL, which is used to calculate a spatio-temporal texture that enables the detection of the water line. In order to translate the image measurement into 3D object space, a synthetic, photo-realistic image of the situation is created from existing 3D data of the river section to be investigated. Necessary approximations of the image orientation parameters are measured by smartphone sensors and GNSS. The assignment of camera image and synthetic image allows for the determination of the interior and exterior orientation parameters by means of space resection and finally the transfer of the image-measured 2D water line into the 3D object space to derive the prevalent water level in the reference system of the 3D data.

In comparison with conventionally measured water levels, OWL reveals an accuracy potential of 2 cm on average, provided that synthetic image and camera image exhibit consistent image contents and that the water line can be reliably detected. In the present dissertation, related geometric and radiometric problems are comprehensively discussed. Furthermore, possible solutions, based on advancing developments in smartphone technology and image processing as well as the increasing availability of 3D reference data, are presented in the synthesis of the work.

The app *Open Water Levels*, which is currently available as a beta version and has been tested on selected devices, provides a basis, which, with continuous further development, aims to achieve a final release for crowdsourcing water levels towards the establishment of new and the expansion of existing monitoring networks.

Zusammenfassung

Der Begriff des globalen Klimawandels ist seit Beginn des letzten Jahrzehnts allgegenwärtig. Die Veränderung des Weltklimas ist mit einer Zunahme von Starkregenereignissen verbunden, die nahezu unvorhersehbare Sturzfluten verursachen können. Folglich gewinnt die raumzeitlich hochaufgelöste Überwachung von Fließgewässern zunehmend an Bedeutung.

Pegelmessstationen erfassen kontinuierlich und präzise Wasserstände, sind jedoch in Anschaffung und Wartung sehr teuer und werden vorzugsweise an wasserwirtschaftlich-relevanten Gewässern installiert. Kleinere Gewässer bleiben häufig unbeobachtet. Um die Datendichte hydrometrischer Messnetze zu erhöhen und somit die Vorhersagequalität von Hochwasserereignissen zu verbessern, sind neue, kostengünstige und flexibel einsetzbare Wasserstandsmesstechnologien erforderlich. Diese sollten sich an den Genauigkeitsanforderungen konventioneller Messsysteme orientieren und die Beobachtung von Wasserständen zu praktisch jedem Zeitpunkt, selbst an den kleinsten Flüssen, ermöglichen.

Ein Lösungsvorschlag ist die Entwicklung einer photogrammetrischen Smartphone-Anwendung (App) zum Crowdsourcing von Wasserständen mit welcher freiwillige Nutzer lediglich Bilder eines Flussabschnitts aufnehmen müssen, um daraus den Wasserstand zu bestimmen. Heutige Smartphones integrieren hochauflösende Kameras, eine Vielzahl von Sensoren, leistungsfähige Prozessoren und Massenspeicher. Sie sind jedoch für den Massenmarkt konzipiert und verwenden kostengünstige Hardware, die nicht der Qualität geodätischer Messtechnik entsprechen kann.

Um das Einsatzpotential in mobilen Messanwendungen zu eruieren, sind Untersuchungen zum Smartphone als photogrammetrisches Messinstrument im Rahmen des Promotionsprojekts durchgeführt worden. Die Studien befassen sich mit der geometrischen Stabilität von Smartphone-Kameras bezüglich geräteinterner Temperaturänderungen und mit dem Genauigkeitspotential von mit Smartphone-Sensoren gemessenen Rotationsparametern.

Die Ergebnisse zeigen eine starke, temperaturbedingte Variabilität der inneren Orientierungsparameter, weshalb die Kalibrierung der Kamera zum unmittelbaren Messzeitpunkt erfolgen sollte. Die Ergebnisse der Sensoruntersuchungen zeigen große Ungenauigkeiten bei der Messung der Rotationsparameter, insbesondere des Kompasswinkels (Fehler von bis zu 90° festgestellt). Selbiges gilt auch für Positionsparameter, gemessen durch in Smartphones eingebaute Empfänger für Signale globaler Navigationssatellitensysteme (GNSS). Wie aus der Literatur zu entnehmen ist, lassen sich unter besten Bedingungen Lagegenauigkeiten von etwa 5 m erreichen. Abseits davon sind Fehler von mehreren 10 m zu erwarten. Infolgedessen ist von einer direkten Georeferenzierung von Bildmessungen mittels aktueller Smartphone-Technologie abzusehen.

Unter Berücksichtigung der gewonnenen Erkenntnisse wurde die Pegel-App *Open Water Levels (OWL)* entwickelt, deren methodische Entwicklung und Implementierung den Kern der Arbeit bildete. OWL ermöglicht die flexible Messung von Wasserständen via Crowdsourcing, ohne dabei zusätzliche Ausrüstung zu verlangen oder auf spezifische Flussabschnitte beschränkt zu

sein. Datenaufnahme und Verarbeitung erfolgen direkt im Feld, so dass die Pegelinformationen sofort verfügbar sind.

Praktisch nimmt der Anwender mit OWL eine kurze Zeitrastersequenz eines Flussufers auf, die zur Berechnung einer Raum-Zeit-Textur dient und die Erkennung der Wasserlinie ermöglicht. Zur Übersetzung der Bildmessung in den 3D-Objektraum wird aus vorhandenen 3D-Daten des zu untersuchenden Flussabschnittes ein synthetisches, photorealistisches Abbild der Aufnahmesituation erstellt. Erforderliche Näherungen der Bildorientierungsparameter werden von Smartphone-Sensoren und GNSS gemessen. Die Zuordnung von Kamerabild und synthetischem Bild erlaubt die Bestimmung der inneren und äußeren Orientierungsparameter mittels räumlichen Rückwärtsschnitt. Nach Rekonstruktion der Aufnahmesituation lässt sich die im Bild gemessene 2D-Wasserlinie in den 3D-Objektraum projizieren und der vorherrschende Wasserstand im Referenzsystem der 3D-Daten ableiten.

Im Soll-Ist-Vergleich mit konventionell gemessenen Pegeldaten zeigt OWL ein erreichbares Genauigkeitspotential von durchschnittlich 2 cm, insofern synthetisches und reales Kamerabild einen möglichst konsistenten Bildinhalt aufweisen und die Wasserlinie zuverlässig detektiert werden kann. In der vorliegenden Dissertation werden damit verbundene geometrische und radiometrische Probleme ausführlich diskutiert sowie Lösungsansätze, auf der Basis fortschreitender Entwicklungen von Smartphone-Technologie und Bildverarbeitung sowie der zunehmenden Verfügbarkeit von 3D-Referenzdaten, in der Synthese der Arbeit vorgestellt.

Mit der gegenwärtig als Betaversion vorliegenden und auf ausgewählten Geräten getesteten App *Open Water Levels* wurde eine Basis geschaffen, die mit kontinuierlicher Weiterentwicklung eine finale Freigabe für das Crowdsourcing von Wasserständen und damit den Aufbau neuer und die Erweiterung bestehender Monitoring-Netzwerke anstrebt.

Contents

I	Introduction	1
1	Motivation	3
2	Hydrometry: Water gauging	5
2.1	Conventional water level monitoring	5
2.1.1	Measuring systems	5
2.1.2	Specifications for water gauging	6
2.2	Alternative water gauging methods	8
2.2.1	Spaceborne water gauging	8
2.2.2	Airborne water gauging	10
2.2.3	In-situ water gauging	10
3	Research objectives	13
4	Smartphone technology	15
4.1	Smartphone camera technology	16
4.1.1	The basic construction of smartphone cameras	17
4.1.2	Smartphone camera control	20
4.1.3	On the use of smartphone cameras in photogrammetric applications	21
4.2	Location awareness of mobile devices	22
4.2.1	Basics on satellite-based positioning	23
4.2.2	Smartphone-implemented GNSS	25
4.2.3	Basics on smartphone sensor technology	27
5	Crowdsourcing	31
5.1	Human sensors	31
5.2	Big data	31
5.2.1	Quality measures	32
5.2.2	On the use of big data in photogrammetry	32
5.3	Activation of citizen scientists	32
6	Developing smartphone applications	35
6.1	Native, hybrid and cross-platform coding	35
6.2	Android versus iOS	36
6.3	The process of software development	37
6.3.1	Requirement analysis for the development of crowdsourcing apps	38
6.3.2	System design - Separation of concerns	39

II	Studies on smartphone technology	43
7	On the geometric stability of low-cost cameras depending on temperature changes	45
7.1	Introduction	46
7.2	Hardware	47
7.2.1	Smartphone camera application	48
7.3	Methods and algorithms	48
7.3.1	Single-image camera calibration	48
7.3.2	Simulating the impact of differently changing IOP at measurements in 3D object space	52
7.4	Results and discussion	53
7.4.1	Self-heating temperature impacts at smartphone cameras	53
7.4.2	Temperature impacts at the stability of RPi cameras	57
7.4.3	Statistical evaluation of temperature dependencies	58
7.4.4	Temperature-related error assessment in object space: Results of Monte-Carlo simulation	60
7.5	Conclusions	63
7.A	Appendix. Monte-Carlo simulation	65
7.A.1	General approach of the Monte-Carlo simulation	65
7.A.2	Implementing the Monte-Carlo simulation	66
8	Investigating sensor fusion strategies for smartphone orientation determination	73
8.1	Introduction	74
8.1.1	Related work	74
8.1.2	Paper structure	75
8.2	Basics	75
8.2.1	Sensors systems for orientation estimation	75
8.2.2	Smartphone coordinate systems	76
8.2.3	Magnetic perturbations	77
8.3	Experiments	78
8.3.1	Hardware	78
8.3.2	Experimental setup	78
8.4	Results	80
8.4.1	Accuracies	81
8.4.2	Stability	82
8.5	Conclusion	83
III	Photogrammetric water level determination	87
9	Identifying 2D water lines in hand-held smartphone camera images	89
9.1	Introduction	90
9.1.1	Related work	91
9.2	Data	92
9.3	Application Development	93
9.3.1	Time lapse image sequence co-registration	94
9.3.2	Investigation of spatio-temporal texture	95

9.3.3	Histogram analysis	95
9.3.4	Image segmentation by region growing	97
9.3.5	Water line detection	98
9.4	Experimental research and results	98
9.5	Evaluation and discussion	99
9.6	Future work	100
10	From image to reality: Transferring 2D water lines into 3D object space to measure water levels	105
10.1	Introduction	106
10.2	Prerequisites	108
10.2.1	3D data	108
10.2.2	Initial values for the 3D position	109
10.2.3	Initial values for the 3D rotation	109
10.3	Algorithmic description	110
10.3.1	Image synthesis	110
10.3.2	Image-to-geometry registration	112
10.3.3	Water level determination	114
10.4	Implementation	114
10.4.1	Client implementation	114
10.4.2	Data exchange and selection	116
10.4.3	Server implementation	116
10.5	Evaluation	116
10.5.1	Reliability and accuracy of smartphone-implemented water-level gauging	118
10.6	Discussion	119
10.6.1	Geometric challenges	119
10.6.2	Radiometric challenges	122
10.6.3	Availability of appropriate 3D Data	124
10.7	Conclusions and future developments	125
11	Related publications	133
11.1	Automatic waterline extraction from smartphone images	133
11.2	Versatile mobile and stationary low-cost approaches for hydrological measurements	134
11.3	Automatic Image-Based Water Stage Measurement for Long-Term Observations in Ungauged Catchments	135
IV	Synthesis	137
12	Smartphones: The new photogrammetric measuring instruments?	139
12.1	Study on the impact of self-heating on the geometric integrity of smartphone cameras	139
12.2	On the use of smartphone MEMS sensors for direct georeferencing in mobile imaging applications	139
12.3	On the use of smartphone-implemented GNSS for direct georeferencing in mobile imaging applications	140
12.4	Summary	140
12.5	Future improvements	141

13 Open Water Levels: A new water gauging tool	143
13.1 Water line detection	143
13.2 From water line to water level: Image-to-geometry registration	145
13.3 Summary	145
13.3.1 Pros and cons of water line detection by spatio-temporal texture analysis	146
13.3.2 Pros and cons of image-to-geometry registration	146
13.4 Future work	147
13.4.1 Water line detection applying machine learning	147
13.4.2 Image matching based on machine learning	148
13.4.3 Increasing the availability of 3D data	150
13.4.4 Technical improvements	151
13.4.5 FlowVelo to go	151
13.5 Outlook: Preparing OWL for crowdsourcing water levels	152
13.5.1 Technical issues	152
13.5.2 Data quality assurance	153
13.5.3 User experience	154
13.5.4 Activation	155
References	157
List of Figures	169
List of Tables	171
List of Abbreviations	173

Part I
Introduction

1 Motivation

The accurate, reliable and continuous observation of hydrometric parameters with high spatio-temporal resolution is mandatory for water management, for understanding water cycles, for the simulation of hydrological processes such as floods and for morphological change detection (Morgenschweis, 2018). In this regard, one of the most important parameters is the water level.

Water levels are usually observed by in-situ measuring (also gauging) stations, which are under the control of official authorities who are also responsible for siting and for specifying requirements, e.g. measurement accuracy and reliability. Basically, gauging stations should be installed at hydrographically representative points like groundwater connections or at sites where the morphological, geological or meteorological conditions change within a catchment (LAWA, 2018). The number of gauging stations in a hydrometric monitoring network depends, for example, on climatic conditions and topography, but mainly on the catchments' relevance for water management (Kirchner, 2006). Due to the fact that monitoring networks are very expensive in construction, operation and maintenance, gauging stations are mainly installed in large-scale and only scarcely in small-scale catchments.

However, since the last decades an increase in extreme precipitation has been observed leading to an increased risk of flash floods (Lehmann et al., 2015). Flash floods occur in the shortest times, in the smallest catchments and are often unpredictable due to the insufficient coverage of these catchments by monitoring networks causing serious data gaps in hydrological modelling (Siedschlag, 2015; Borga et al., 2014). Moreover, the problem becomes much more significant if viewed on a global scale. Comprehensive hydrometric monitoring networks are unaffordable for financially weaker communities, e.g. in developing countries, which means that there is either no or only poorly maintained water gauging infrastructure (Musa et al., 2015). Therefore, these regions are especially vulnerable to get hit by devastating floods as they cannot implement flood prevention measures due to the lack of the necessary information about the local hydrological processes.

For these reasons, new techniques are required that allow for the flexible observation of small-sized catchments to increase the spatio-temporal resolution of hydrometric monitoring networks and thus to improve the prediction and warning quality of extreme events. The techniques, however, should also be low-cost to be implemented in regions that cannot afford conventional water gauging technologies.

This thesis makes a contribution to this and presents a novel approach for measuring water levels based on photogrammetry, smartphones and crowdsourcing. Today's smartphones implement numerous cameras, global navigation satellite system (GNSS) receivers, various sensors, powerful processing units and large storage capacities, to name but a few, and may serve as globally wide-spread water level measurement devices. The idea is to develop an easy-to-use photogrammetric smartphone application (app) that facilitates the acquisition of water levels by crowdsourcing in order to densify the spatio-temporal resolution of hydrometric networks.

In order to permit the integration of smartphone-measured data into existing monitoring networks, the new method has to comply with the requirements of conventional water level measurement, which are briefly discussed in Chapter 2. This is followed by explanations of alternative water gauging approaches, which equally try to bridge the data gap but are associated with problems and limitations either in terms of spatio-temporal resolution, accuracy or flexibility.

From these findings, as well as the fact that low-cost electronics, built in smartphones, should be used in photogrammetric measuring applications, four research objectives have been formulated, which have been addressed in four publications comprising the main part of the thesis. The objectives are given in Chapter 3.

While photogrammetric outlines on the methodical developments have been comprehensively made in the related papers, background information on smartphone technology, crowdsourcing and app programming have not or only slightly been communicated. Thus, the chapters following the research objectives provide basic knowledge on the use of smartphones as measuring devices as well as on issues that need to be taken into account when developing crowdsourcing apps.

First, Chapter 4 gives an overview of state-of-the-art smartphone technology in view of the photogrammetric use focussing on built-in cameras and positioning technologies. This includes short descriptions of the functional principles and an assessment of the applicability in photogrammetric applications with regard to possible difficulties to be considered in the development of the water level app.

The project aims at the development of an app targeting the crowdsourcing of water level data. Thus, Chapter 5 introduces the idea behind crowdsourcing and explains the pros and cons of big data. Furthermore, some aspects are discussed, which are important to consider when activating citizen scientists for data collection.

The development of the water gauging app goes hand in hand with its implementation. This initially requires considerations about the platform and the style of software implementation, which are addressed in Chapter 6. However, the development of software usually undergoes a process in which the implementation is only one phase among others. In order to develop a valuable tool for both the experts and the citizen scientists, the actual implementation should be preceded by a requirements analysis and a system design. Both are described in relation to the intended application.

2 Hydrometry: Water gauging

Targeting the development of a new method to observe water levels requires some basics on hydrometry, which is the science of the measurement, transmission and basic processing of discharge rates of natural and man-made surface waters (Morgenschweis, 2018). Measuring discharge rates requires a continuous observations of the water level. This is the orthogonal distance between the water surface and a reference point, called *gauge datum* or *gauge zero*, which is locally defined slightly below the lowest water level measured over a long time.

The following section deals with conventional water level monitoring and provides the related specifications on accuracy, resolution and reliability. Afterwards, alternative water level measurement techniques, based on photogrammetry and remote sensing, are presented targeting the spatio-temporal densification of hydrometric networks.

2.1 Conventional water level monitoring

The task of water level monitoring is usually assigned to official authorities. In Germany, the planning, construction, operation and maintenance of measuring stations as well as the evaluation, reuse and quality assurance of the measured data is regulated by federal and state water statutes, summarised in a guideline called "Pegelhandbuch" (LAWA, 2018). The measuring stations observe water levels and discharges. Both are regulated in the guide in order to achieve a uniform measuring network throughout Germany. The measurement of discharges is not addressed in this thesis and will not be discussed further. For more information reference is made to LAWA (2018).

2.1.1 Measuring systems

The following explanations are based on the fundamental work "Hydrometry" by Morgenschweis (2018) and describe the classification of commonly applied water gauging systems into non-self-registering and self-registering measuring systems.

Non-self-registering measuring systems

Non-self-registering measuring systems cannot perform automatic data acquisition; instead they require an operator. Each gauging station implements at least one of these systems, usually a staff gauge, which is a geodetically measured vertical staff in the water with 1 or 2 cm graduation and with the base at the gauge zero. Depending on the terrain, the gauge can also be arranged in a sloped (inclined gauges) or staircase-shaped (stair gauges) arrangement on the bank. Staff gauges are manually read by an operator and serve the calibration and control of self-registering measuring systems.

Self-registering measuring systems

Self-registering measuring systems measure and record water levels automatically. Moreover, if a remote data transmission system is installed, the data is transferred directly to the responsive authorities. They comprise length measuring systems, i.e. mechanical systems like float gauge and Time of Flight (ToF)-based systems such as sound navigation and ranging (SONAR) and radio detection and ranging (RADAR), and weight-measuring systems based on pressure measurement such as bubble gauge and pressure probe gauge. All systems measure the water level relatively to gauge zero.

A further distinction can be made into contact and contactless measuring systems. Measuring systems having direct contact with the water body are susceptible to damage by drifting debris and calcification. Furthermore, the measuring accuracy can be influenced by the characteristics of the water, e.g. salinity and turbidity. A remedy is usually the installation of float wells in which the measuring systems are protected, but which make the construction of a single station very expensive. Contactless measuring systems are, for example, ToF-based technologies where the sensor system is installed above the water surface. These systems operate largely independently of the water characteristics but the measurement accuracy can be affected by weather conditions, e.g. air temperature and humidity.

Table 2.1 provides an overview of commonly used measuring systems in gauging stations, based on information by Morgenschweis (2018) and LAWA (2018).

2.1.2 Specifications for water gauging

Conventional water level monitoring is distinguished into the measurement of

- instantaneous values, measured over 1 min, measurement uncertainty 10 cm,
- individual values, measured over 15 min, measurement uncertainty 2.5 cm,
- daily mean values, measured over 24 hours, measurement uncertainty 1 cm.

The measurement uncertainties comprise random errors, e.g. weather-related impairments of the measuring systems, and systematic errors, e.g. calcification of the measuring instruments, morphological changes in the cross section or changes at the reference gauge (LAWA, 2018).

Thus, all measurements are reviewed for plausibility and integrity. If a measuring system fails, the data acquisition still needs to be secured. Therefore, measuring stations use at least two complementary measuring systems whose measuring ranges have to cover all considerable water fluctuations at the site ranging from low to high water. If all implemented systems are in operation, the data of the system operating more reliably at the time of data acquisition should be used further, e.g. float level data are preferable to RADAR data in the case of very rough water surfaces, but RADAR data provide more reliable data than float levels in the case of ice and frost.

Nevertheless, breakdowns of measuring stations and erroneous measurements cannot be completely avoided. Outliers are detected via plausibility control or comparison with data from neighbouring stations. Data gaps caused by outlier elimination or measurement failures need to be filled with reasonable data, either by interpolation of the hydrographs using data from neighbouring gauging stations or by application of statistical methods. Nevertheless, the reasons for the data gaps have to be identified and immediately fixed.

Method	Working principle	Accuracy	Pros	Cons
Non-self-registering measuring systems				
Staff gauge	<ul style="list-style-type: none"> manual water level reading serve as reference to calibrate other measuring systems 	<ul style="list-style-type: none"> 0.5–1.0 cm (vertical staffs) 	<ul style="list-style-type: none"> inexpensive installation & maintenance no energy supply required adjustable measuring range 	<ul style="list-style-type: none"> expensive operation → much manpower required no standardised datasets → error source "human" contact to water body
Self-registering measuring systems				
Float gauge	<ul style="list-style-type: none"> calibrated float immersed in water moves up/down with the water level float is connected with float wheel recording the movement movement indicates water level change 	<ul style="list-style-type: none"> 0.2–0.4 cm 	<ul style="list-style-type: none"> inexpensive installation (only if no float well is used) reliability energy supply optional (only for data transmission) 	<ul style="list-style-type: none"> susceptible to waves & debris → solved by float well (expensive!) limited usability → high accuracies require large-scale floats risk of freezing expensive maintenance
Bubble gauge	<ul style="list-style-type: none"> compressed air is pressed into a pressure transmission line & blown out assuming constant water density, pressure is proportional to water level the used pressure is a measure for the water level & logged via pressure transmitter 	<ul style="list-style-type: none"> 0.5–1.0 cm 	<ul style="list-style-type: none"> quasi contactless (system is used in a tube) high measuring range (0–30 m) reliability inexpensive installation energy supply optional 	<ul style="list-style-type: none"> not for variable waters → water density influenced by e.g. salinity & turbidity measurements influenced by high flow velocities at bubble opening risk of freezing (but less than float gauge) expensive & difficult maintenance
Pressure probe gauge	<ul style="list-style-type: none"> pressure probe inside water measures hydrostatic- & atmospheric pressure hydrostatic pressure is proportional to water level independent measuring of atmospheric pressure permits water level determination 	<ul style="list-style-type: none"> 0.2–1.0 cm 	<ul style="list-style-type: none"> robustness high measuring range (0–40 m) less expensive sensors due to high sensor availability 	<ul style="list-style-type: none"> not for variable waters → water density influenced by e.g. salinity & turbidity susceptible to atmospheric & temperature changes (compensation required) accuracy dependent on water level → low level? high measurement uncertainty! expensive installation (float well required) expensive & frequent maintenance
SONAR	<ul style="list-style-type: none"> use ToF principle to measure distance between sensor & water surface by ultrasonic signals 	<ul style="list-style-type: none"> 0.2–1.0 cm 	<ul style="list-style-type: none"> contactless high measuring range (5–45 m) robustness inexpensive maintenance 	<ul style="list-style-type: none"> susceptible to weather-induced signal interferences & attenuations & waves expensive installation → carrier construction & sound reflector required
Pulse RADAR	<ul style="list-style-type: none"> use ToF principle to measure distance between sensor & water surface by microwaves 	<ul style="list-style-type: none"> K-Band 0.3 mm C-Band 0.1 mm 	<ul style="list-style-type: none"> contactless high measuring range (0–35 m) robustness reliability inexpensive maintenance low-energy consumption 	<ul style="list-style-type: none"> susceptible to waves expensive installation → carrier construction required

Table (2.1): Overview of measuring systems used in conventional water gauging stations.

2.2 Alternative water gauging methods

Even though conventional water level monitoring is highly accurate and reliable, it is expensive and only available at certain sites. For these reasons, there is an increasing research interest into alternative methods to enhance the spatio-temporal data density of hydrometric networks at reasonable costs, meeting the prevailing quality standards and being applicable globally at large scales (Paul et al., 2020). This implies, on the one hand, the need for methods allowing for the areal monitoring of so far ungauged large-scale catchments and, on the other hand, the need for novel in-situ measurement techniques enabling a fast, flexible and low-cost monitoring at small-scale rivers. It has been shown that both photogrammetry and remote sensing can contribute to the development of appropriate methodologies. Some examples, classified into spaceborne, airborne and close-range (in-situ) measuring approaches, are presented below.

2.2.1 Spaceborne water gauging

With the growing understanding of the need to survey the global water resources, the use of satellite data has become increasingly important for hydrological investigations. More and more satellites produce valuable data with ever improving sensors that offer more and more opportunities, e.g. the detection of flooded areas and the areal determination of water levels, either using data from optical sensors or RADAR.

Passive measuring systems

Earth observation satellites using passive optical measuring systems capture the reflected energy from objects on the earth's surface in different spectral ranges, usually from visible light to thermal infrared (TIR). The optical sensors of the first satellites covered only a small part of the visible spectrum and produced images with comparatively poor resolution, e.g. Landsat-1 captured images in four bands with a ground sampling distance (GSD) of 60 m and a revisit time of 18 days. Today's satellites, especially commercial missions, offer data with much higher spatio-temporal resolution, e.g. WorldView-3 that integrates a panchromatic sensor with a GSD of 0.3/1.2 m (nadir/off-nadir) as well as eight multi-spectral, eight short-wave infrared (SWIR) and 12 auxiliary bands for cloud, aerosol, vapor, ice and snow detection. The revisit time for one site is less than one day (off-nadir).

Optical satellite images have been used by hydrologists for some time now, e.g. to monitor water quality or to map water extents during floods. There are several options to detect and segment water surfaces in optical satellite imagery, for example applying texture measurements, e.g. Verma (2011), de Martinio et al. (2003) and He and Wang (1992), classifying the image content using spectral signatures, e.g. Yang et al. (2017), Qiao et al. (2011) and McFeeters (1996), or classifying the image content by means of machine learning, e.g. Miao et al. (2018) and Chen et al. (2018). Using overlapping image data enables to derive digital surface models (DSMs) that can be registered with the classified images to estimate the prevalent water level, whereby the accuracy largely depends on the vertical accuracy of the DSM.

Optical satellite images suffer from cloud coverage, which is likely in case of rainfall-induced floods, dense vegetation, obscuring the water bodies to be monitored, and require good lightning conditions (Huang et al., 2018; Morgenschweis, 2018; Musa et al., 2015).

Active measuring systems

Active measuring systems installed in earth observation satellites use microwave-sensing technologies, such as synthetic aperture radar (SAR), to observe the earth surface almost independently of cloud and vegetation cover as well as lighting conditions. The sensor emits radiation and measures the amount of the reflected energy, which is sensitive to the specific surface characteristics. This permits, for example, to draw conclusions about surface roughness and moisture. Details on SAR technology are given in Meyer (2019).

Water surfaces can be identified by analysing multi-polarised SAR images, analysing the extent of backscatter, using thresholds or applying machine learning for automated classification, e.g. Tanaka et al. (2019), Vickers et al. (2019), Pai et al. (2019) and Musa et al. (2015). The classified data can be registered with surface information, such as DSMs and digital terrain models (DTMs), to derive information about the water level. Vickers et al. (2019) classified SAR images of an arctic lake, captured by three SAR satellite systems over 14 years, and registered the image data with a bathymetric DTM of the sea bed to derive water level hydrographs. The comparison of satellite-based measurements and in-situ measurements shows a mean deviation of 0.4 m. Tanaka et al. (2019) registered SAR images with the global shuttle radar topography mission (SRTM) DTM to measure water levels at rivers and in flood plains after flood events. The satellite-based measurements deviated from in-situ measurements by an average of 2 m at the rivers and 1.3 m in the flood plains, whereby the error was largely due to the coarse resolution of the SRTM model (GSD of 90 m, vertical accuracy of about 2 m).

Beside this, the use of SAR altimetry and interferometric SAR (InSAR) data offers opportunities for the direct measurement of water levels. SAR altimetry allows for the direct measurement of the sea level and ice heights but also for water levels of large-scale rivers and lakes. For example, Dinardo (2020), Shu et al. (2020) and Huang et al. (2019) used Sentinel-3A/3B SAR altimetry data (GSD of 300 m, revisit time of 27 days) to measure water levels in various study areas, including standing and running waters. The measurements were evaluated using in-situ measurements from which they deviated by a few centimetres to decimetres. Unfortunately, SAR altimetry footprints are very large and impede the observation of small-scale rivers. The two-dimensional scanning of the earth's surface using SAR can be extended by the third dimension applying InSAR. Therefore, the measuring system is supplemented by a second system that allows for the generation of 3D surface information. A well-known example of a DTM, generated via InSAR, is the worldwide SRTM DTM. Wdowinski et al. (2008) and Alsdorf et al. (2000) used InSAR for water level monitoring in wetlands and flood plains and detected changes in the water level with accuracies of a few centimetres.

Summary of spaceborne water gauging

Even if the progress in satellite technology is indisputable, the current technical possibilities are not sufficient to meet the hydrometrical requirements. Although the accuracy of water level measurements can already be made to within a few centimetres, a so far major bottleneck is the temporal resolution, which is specified by the revisit times of the satellite systems that are rarely less than a few days. However, especially the freely available data make a major contribution to the monitoring of entirely ungauged catchments facilitating the assessment of hydrological parameters. Satellite images are furthermore helpful when inaccessible large-scale catchments have to be investigated. Moreover, the archives of satellite images contain data of

several decades, which enable the derivation of historical hydrographs that might be interesting for change detection.

2.2.2 Airborne water gauging

In contrast to spaceborne systems, the use of airborne measuring systems, especially the use of unmanned aerial vehicles (UAVs), offers an option for areal monitoring of large catchment areas with higher temporal resolution. Following the statement of Bandini et al. (2017), "Unmanned Aerial Vehicles (UAVs) can fill the gap between spaceborne and ground-based observations, and provide high spatial resolution and dense temporal coverage data, in quick turn-around time, using flexible payload design." In their studies, they used a UAV as versatile sensor platform to measure water levels fusing data from light detection and ranging (LIDAR), RADAR and SONAR sensor systems and achieved accuracies of 5–7 cm provided that the vertical accuracy of the UAV position, determined by on-board GNSS, was better than 3–5 cm.

Similar results could be achieved from Ridolfi and Manciola (2018) who used an UAV, equipped with a camera, to capture images from a dam lake where the dam was marked with ground control points (GCPs). The images were used to identify the water line that has been subsequently transferred into the object space using the GCPs to determine the water level.

Mandlbürger et al. (2015) generated a DTM of a shallow water body together with the shore area and a digital elevation model (DEM) of the water surface applying airborne laser bathymetry (ALB) and UAV-based laser scanning (ULS), which uses UAVs instead of planes as bathymetric sensor platforms. The data was transferred into uniform grids with grid sizes of 0.25 m (ALB) and 0.10 m (ULS). The water surface could be measured with standard deviations of 4 cm (ALB) and 2 cm (ULS). However, a complete mapping of the water surface was not possible due to specular reflections at calm water sections (Mandlbürger et al., 2017).

Put it in a nutshell, the application of airborne measuring systems allows for areal water level measurement with high spatio-temporal resolution at reasonable costs, especially when applying UAVs. The accuracies are within the range of a few centimetres that might be acceptable for hydrological modelling and simulations. In addition, the aerial survey enables the investigation of additional hydro-morphological parameters, e.g. bank erosion. However, the applicability of the methods is strongly restricted either by weather conditions, as rain and heavy wind usually prevent flying UAVs, or by the water surface conditions, as calm water surfaces prevent, for example, the use of ULS for water surface measurement.

2.2.3 In-situ water gauging

Alternative methods for the in-situ observation of water levels can be, similar to the spaceborne and airborne methods, based on active sensing technologies applying LIDAR and passive imaging technologies applying photogrammetry.

In-situ water gauging: active systems

Paul et al. (2020) use low-cost LIDAR sensors, mounted under a bridge perpendicular to the water surface, to measure water levels using near infrared (NIR) laser beams. The system was tested under different conditions with regard to, for example, measuring range, surface

roughness, air temperature and water turbidity. The results show that the water level can be observed with accuracies of about 1 cm when the sensor is placed 10 m above the water surface. However, the result largely depends on the measuring conditions such as surface roughness and air temperature because of increasing bias when the system operates outside the operational temperatures (10–30°C). Considering the monthly average temperatures in Germany, water level measurements with the required accuracies might be only possible from April to October (DWD, 2020). Furthermore, the sensor has to be almost perpendicular to the water surface, which can be realised by mounting the sensors under bridges or using carrier constructions. In the latter case, the approach would be no longer low-cost.

Another interesting approach, applying laser light for measuring water levels, has been proposed by Mulsow et al. (2016). Their method is based on the laser-light-sheet projection technique utilising the specular reflection properties of water surfaces to measure water levels by optical triangulation. In short, a laser line with a wavelength of 660 nm (visible red light) is projected onto a water surface in a 45 degree angle. The light is reflected and projected onto a projection plane arranged perpendicular to the water surface. The image of the laser line varies according to the water level and is observed by a camera arranged parallel to the projection plane. The water level change could be measured with a standard deviation of 0.03 mm using a laser beam profile of 700 mm, which allows for extraordinary high accuracies in water level measurement at comparatively low sensor costs (mainly camera and laser transmitter). However, the method has been developed in the context of experimental hydromechanics and requires a complex setup that is hardly possible in nature. Nevertheless, such an approach might be applicable to man-made water bodies, e.g. drainage channels, which are equally important to observe (Lin et al., 2018).

In-situ water gauging: passive systems

In addition to active measuring methods, image-based, passive systems offer great possibilities to monitor water levels at low costs. A possibly first approach of photogrammetric water level determination was presented by Hodel et al. (1991) using analogue stereo camera systems. Today's known measuring systems consist of a fixed, calibrated camera being installed at a bank. The camera captures images in the direction of the opposite bank where a staff gauge or a calibrated target, e.g. a stage board, is installed. When the water surface is calm, the water line is almost linearly drawn on the reference and can be interpreted as a water level measurement. Some examples are given in Morgenschweis (2018), Lin et al. (2018), Bruinink et al. (2015) and Royem et al. (2012). Such camera-based water level measurement methods can be considered as intelligent staff gauges, which have plenty of advantages over their conventional representatives, e.g. reduction of manpower, the possible use of remote data transmission and less restrictions in terms of permanent gauge accessibility. Moreover, the visual observation of rivers allows for the recognition of changes in the water and shore area, e.g. weed growth, which is important for maintenance. The costs for camera purchase, installation and operation are rather low.

However, most of the above-mentioned measuring methods are locally fixed and require a linear plotting of the water surface on a staff or target and fail as soon as this characteristic is no longer given, e.g. due to waves, debris or dirt on the staffs or boards. Both factors impose significant limitations on the measurement methods. Furthermore, free views to staffs or boards are mandatory. Taken together, these facts represent major limitations for the use of the procedures. Other difficulties might be weather-induced, e.g. fog, heavy rain and snow,

or related to the lighting conditions, e.g. darkness that, however, might be remedied by the use of NIR cameras.

Summary of alternative in-situ water gauging

On the one hand, low-cost LIDAR can be used to measure water levels very accurately. On the other hand, their use is very localised or requires expensive and impractical constructions that in turn contradicts the low-cost idea.

Image-based measuring methods are low-cost, easy to install and allow for, depending on the distance to the shore line, a rather precise determination of the water level. However, the water level is measured in relation to either existing staff gauges, which does not result in an improvement in the spatio-temporal data density of hydrometric networks, or require the installation of stage boards, which are likely to get flooded in case of extreme events and prevent the water level monitoring when most needed. Furthermore, the methods can usually only be used at calm waters, otherwise the water line will not be linearly drawn at the references and thus cannot or only insufficiently be identified.

To sum up, the main issues of conventionally and alternatively applied water level measurement methods are that they are either locally fixed, expensive in installation, maintenance or operation, do not provide the necessary accuracies, suffer from bad temporal resolutions or only apply to waters with specific characteristics. These limitations are particularly challenging in the case of rainfall-induced floods, when a fast "on-the-fly" measurement of water levels is required without the need to take account of the specific characteristics of the prevailing water bodies.

3 Research objectives

This thesis intends to make a contribution to the aforementioned problems and targets the development of a novel approach for image-based water level measurement using ordinary smartphones. The procedure should be implemented in an app aiming at the flexible crowdsourcing of water levels at almost any time and at almost any river. The water level accuracy should be based on the requirements of conventional measuring methods (see Section 2.1.2, permitted measurement uncertainty for instantaneous and individual values is 10 cm and 2.5 cm respectively). This implies investigations on smartphones as next-generation measuring instruments as well as the development of a flexible photogrammetric water gauging method that can be implemented on smartphones. Thus, the work addresses two main issues with regard to the following research questions.

Kersten (2020) emphasises that "the use of smartphones as a professional mapping tool is undoubtedly set to increase" due to more and more built-in cameras, micro-electro-mechanical systems (MEMSs), options for pose estimation, e.g. GNSS, enabling apps the use of location-based services (LBS) as well powerful computing technologies and large storages capacities. However, smartphones still implement low-cost electronics, which are not reaching the same high quality and accuracy as professional equipment. Thus, investigations are required to assess the potential of smartphones as new photogrammetric measuring instruments:

1. It was already explored that the interior geometry of smartphone cameras suffers from instabilities, especially when the respective device is exposed to external forces, e.g. Chikatsu and Takahashi (2009). However, another reason for the instabilities might be that smartphones implement a large number of heat-emitting components causing frequent temperature changes on the camera module that also may impact the sensor-lens integrity. Investigations in this direction have not yet been conducted and are within the scope of the dissertation.
2. The literature contains numerous studies dealing with the accuracy of built-in GNSS as well as the use of smartphone sensors in navigation applications. However, there are still some knowledge gaps regarding the accuracy and stability of smartphone-measured rotation parameters applying MEMS sensor fusion with focus on mobile imaging applications whose investigation form the second objective.

The methodical development of the water gauging tool is centrally based on the technical possibilities of current smartphones. In a first step, 2D water lines need to be extracted from smartphone images, which have to be further transferred into 3D object space. The tool should be suitable for crowdsourcing, i.e. the technical requirements need to be reduced so that it can be used on both flagship and low-cost smartphones. Furthermore, it shall be performant, user-friendly and do not require additional devices or sensors. The accuracy of the underlying measurement procedure should be based on the requirements of conventional measurement systems. In detail, two research questions need to be addressed:

3. An image segmentation method needs to be developed to automatically detect arbitrary water lines in smartphone images. The method should not impose any requirements on the water, i.e. the water lines of artificial clear and calm waters should be recognised just as well the water lines of natural rivers with rough water surfaces and natural shore lines. The smartphone images should be taken from hand without the necessity of additional equipment like tripods, enabling a flexible and simple on-the-fly application of the measurement method.
4. The image-measured water line needs to be transformed into 3D object space to derive information about the prevailing water level. This requires the development of an approach that uses smartphone sensors (MEMSs) and built-in GNSS to estimate the exterior orientation parameters (EOP) of smartphone images to furthermore register the image data with object information, e.g. from a geographic information system (GIS) database. This allows for the scaling of the water line to derive the prevalent water level in the reference system of the object data.

The following three chapters prepare for the work carried out in the main part and provide basic knowledge about currently implemented smartphone technology, crowdsourcing and the development of mobile software with a special focus on the development of crowdsourcing apps.

4 Smartphone technology

Smartphones are very powerful and very flexible. It's an enormous platform that we're only now beginning to think about for science.

(Physicist Daniel Whiteson, University of California, Irvine (CA, US) in 2016)

A life without smartphones and tablets is inconceivable these days. In 2019, the number of global smartphone users broke through the three billion mark with still rising trends and it is estimated that currently 45% of the entire world population are smartphone owners (Newzoo, 2019). Focussing on the German market, almost 58 million Germans owned a smartphone in 2019, which are nearly 70% of the total German population (VuMA, 2019).

Unlike mobile phones, smartphones are not only used for communication. Powerful processors, large storage capacities, built-in modems as well as a wide range of sensors and cameras make them daily helpers, which can be individualised through software called apps. They can be applied in several situations, for example for the organisation of personal schedules, for navigation or for fast image and video acquisition. First smartphone-like devices were already available in the mid-1990s, but the real hype started with Apple's first generation iPhone in 2007, which combined three, so far independent, devices: a music player, a mobile phone and a mobile communication device that could be connected to the internet (Wittlich and Schönball, 2017). The ultimate competitor Google entered the market with the launch of the first Android smartphone HTC Dream in 2008. Since then, the operating systems (OSs) iOS and Android are the leading platforms and it is assumed that others, such as Windows Mobile or Blackberry, have been pushed out of the market these days. Referring to the statistics of Gartner (2020), the worldwide share of Android smartphones amounts to 86.3% and of iOS devices to 13.7% in early 2020.

The competitive market is forcing smartphone manufactures to quick and extensive technical innovations, see Figure 4.1, especially in terms of camera quality and embedded positioning and sensor technology, which makes smartphones increasingly interesting for the photogrammetric use. According to Kersten (2020), smartphones offer several functions to be used as mapping tools, such as high-resolution cameras, as well as GNSS receivers and MEMS sensors, e.g. accelerometers, gyroscopes and compasses, to determine a smartphone's position and rotation in a global context similar to advanced inertial measurement units (IMUs).

In order to fit all these technologies into a single device next to, for example, antennas, modems, processor unit and battery, the components need to be realised by tiniest miniaturised units that most probably cannot compete in quality and functionality with professional measuring hardware. Nevertheless, numerous studies published in the literature demonstrate that smartphones can be used in photogrammetric measuring applications, although their use is not straightforward, e.g. Kehl et al. (2019), Bianchi et al. (2017), Muratov et al. (2016) and Tanskanen et al. (2013).



Figure (4.1): Evolution of smartphones, adapted and updated from Majumder and Deen (2019).

This thesis aims at the development of a photogrammetric measurement tool utilising smartphones to facilitate the crowdsourcing of water levels, which initially requires an analysis of the state-of-the-art smartphone technologies. This helps to find out how established (measuring) instruments, i.e. digital single-lens reflex (DSLR) camera, GNSS receiver and IMU, have been adapted for the use in smartphones and how the adapted technologies substantially differ from the conventionally applied technologies. Thus, the potential, but especially the difficulties associated with the use of the adapted miniaturised electronics in measuring applications, can be assessed and furthermore considered in the development of the water gauging tool.

Therefore, the following Section 4.1 deals with the latest camera technologies used in smartphones to reveal the similarities as well as the differences to DSLR cameras, which are commonly used in photogrammetric applications beside industrial and specialised cameras. This is followed by a basic understanding of smartphone camera control via apps. Finally, a review on the use of smartphone cameras in photogrammetric applications is given with regard to the development of photogrammetric apps.

Subsequently, Section 4.2 provides a short overview of different options for smartphone positioning. Special attention is paid to satellite-based positioning by means of built-in GNSS receivers, as this method enables smartphones the determination of geographical coordinates without the necessity for third-party services targeting the transfer of image measurements into object space by means of 3D data. Thus, the basic principle of satellite-based positioning is briefly described, the working principle of smartphone-implemented GNSS is explained and the accuracy potential is estimated from the literature. With regard to Chapter 8, which deals with the determination of the accuracy potential of rotational parameters measured by smartphone MEMS, basic knowledge on smartphone sensor technology is finally provided.

4.1 Smartphone camera technology

The following explanations about smartphone cameras and their differences to professional cameras are based in large parts on articles by Cervantes (2020), Cardinal (2019), George (2019), Adhikari (2019) and Schiesser (2014). The reader is kindly referred to these articles to obtain a deeper insight into the functional principles of smartphone cameras as well as current trends in smartphone technology.

4.1.1 The basic construction of smartphone cameras

The physical principle of smartphone cameras is similar to any other digital camera. Light enters the camera through the front lens, is bundled in the camera lens and transported to a light-sensitive sensor that converts the light quantities, registered pixel by pixel, into electrical signals to create a digital image. The involved components, basically the lens, which consists of several lens elements of different thickness and curvature, and the sensor, including infrared (IR) filter, colour filter array and image signal processor, are in principle very similar to those built in professional full-frame DSLR cameras but much smaller and low-cost. Thus, both camera types have to differ significantly in their construction.

A fundamental difference is that DSLR cameras are modular, i.e. body and lens are detachable and interchangeable. A smartphone camera fuses all components in a single unit, namely the camera module, whose structure is shown in Figure 4.2. These modules are directly integrated in the smartphone case alongside numerous other components and use very little extra hardware apart from lens and sensor to save costs and space.

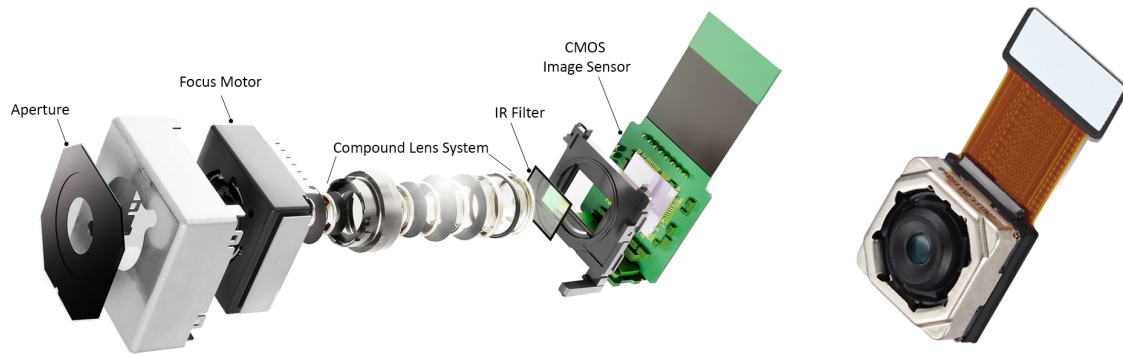


Figure (4.2): Structure of a smartphone camera module. Left: schematic structure. Right: image of a camera module as it can be found in smartphones. Figures adapted from Schiesser (2014).

Lens system

Professional lenses use glass lens elements offering good optical properties and scratch-resistance. They are available as fixed lenses with fixed focal lengths as well as zoom lenses with adjustable lens system to change the focal length by optical zoom. Depending on the camera model, the range of available lenses extends from fisheye to tele lens model and allows for the acquisition of wide panoramic but also close-up images of far distant objects.

In contrast, smartphone lenses consist of tiny plastic lenses or low-cost glass elements. For a long time only fixed lenses were used in smartphones in order to save space and costs required for actuators. The average used focal length was about 4 mm (24–30 mm in 35 mm equivalent, crop factor ~ 7). Zooming was only possible by digital zoom where the image is first cropped and then enlarged to the original image size causing a strong loss of image quality. Thus, today's smartphones are equipped with dual and triple cameras, which are separated camera modules using fixed lenses of different focal lengths, to enable some kind of pseudo-optical zooming. In doing so, the cameras are automatically switched during image acquisition according to the user-defined zoom level where the images of the cameras are interpolated to

generate a hybrid image without big loss of quality. However, this might facilitate changing the field of view between ultra-wide- and wide-angled view but capturing telephoto images, using focal lengths of 10 mm and more (70 mm and more in 35 mm equivalent), is still not possible due to technical reasons, as the required lenses would largely protrude from most smartphones.

Recently, smartphone manufacturers have started to implement so-called periscope-zoom cameras in which camera sensor and lens are rotated by 90 degrees. The larger space is used for the arrangement of the lens elements in order to create true optical zoom lenses that enable focal lengths of effectively 100 mm and more. The light still enters the front lens at the back of the smartphone and is directed towards the sensor by a prism, see Figure 4.3, which is why the principle is also known as folded optics.

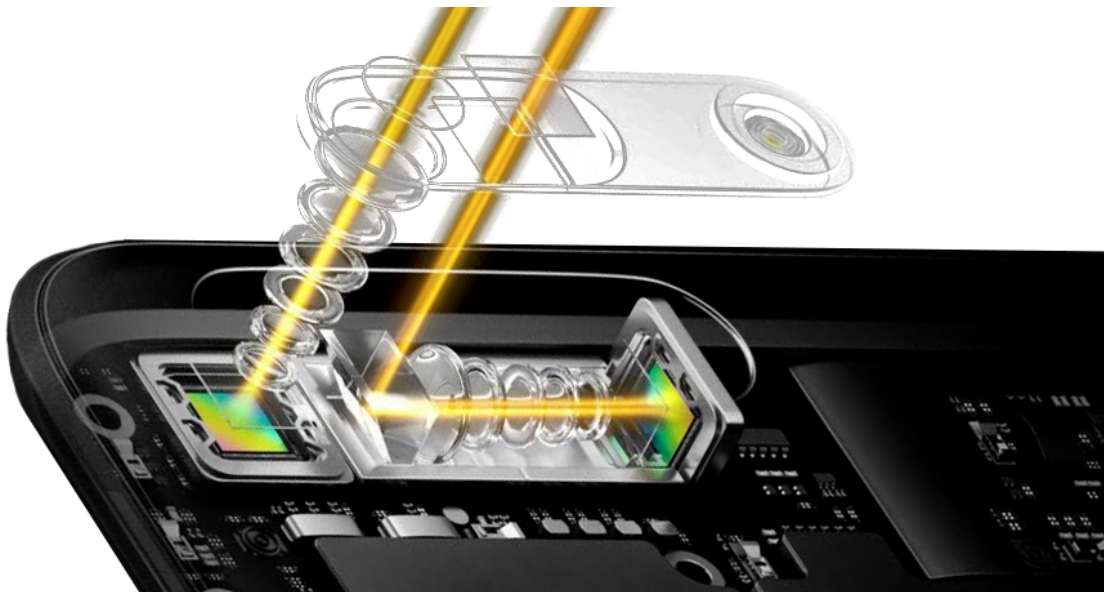


Figure (4.3): Periscope-zoom camera designed for the use in smartphones. Left: theoretically required space when integrating a tele lens in smartphones. Right: space-saving solution applying folded optics. Figure adapted from Rehm (2020).

Focus

The most professional lenses are autofocus (AF) lenses implementing a motor to adjust the lens position in relation to the sensor. Professional cameras widely use phase detection AF that allows for a fast and precise measurement of the focus distance. For this purpose, DSLR cameras usually have a second mirror installed behind the regular mirror, which directs a portion of the incident light to an AF sensor. If the targeted object is not in focus, the light is split into two beams whose distance is measured by the AF sensor. The AF motor then adjusts the lenses so that both beams are in phase, bringing the target object into focus. This AF method is very fast and precise. Nevertheless, each lens can also be manually focused using the front wheel.

Today, almost all smartphones are equipped with cameras allowing for both automatic and manual focussing similar to professional lenses. In both cases, the lenses are adjusted by a tiny voice coil motor that is either automatically controlled when using the AF function or manually controlled when the user defines the focus distance in the camera app (more in

Section 4.1.2). Smartphones usually use contrast AF to measure the focus distance. With contrast AF, the focus is achieved by measuring the contrast in a specified sensor field. The higher the contrast, the more likely the targeted object is in focus. The lens position is changed until the maximum contrast is achieved. Problems need to be expected in darkness and with moving objects. Thus, contrast AF is less precise and rather slow compared to the phase detection AF but also less complex and requires no additional hardware like the AF sensor.

Aperture

All professional cameras enable the amount of light incident on the sensor to be regulated by adjusting the lens aperture either manually or automatically. Smartphone camera modules use fixed apertures because otherwise additional actuators would be required to the detriment of space and costs. To date, smartphone cameras with f-stops of about $f/1.6$ are used, which suggests very large camera openings and narrow depths of field with regard to full frame cameras. However, the depth of field is a function of sensor size, aperture and focal length, with the focal length being squared in the equation. Thanks to tiny sensors enabling lenses with very short focal lengths of a few millimetres, smartphones enable great depths of field despite apparently large aperture numbers that is certainly advantageous in photogrammetric applications.

Sensor

The heart of the imaging system is the camera sensor that converts the received light into image information. Professional full-frame DSLR cameras often use high-quality charge-coupled device (CCD) or complementary metal-oxide-semiconductor (CMOS) sensors with dimensions of about 36×24 mm, resulting in a sensor area of about 864 mm^2 . The sensor is usually preceded by an IR filter, which filters the IR part of the incident light and a colour (usually Bayer) filter array, which breaks down the received light into its red/green/blue (RGB) components.

Smartphone camera sensor units are constructed in a similar manner but differences arise in the sensor quality and size. Smartphone cameras use low-cost CMOS sensors, which are usually more susceptible to noise and less light-sensitive compared to the sensors of professional cameras. Increasingly, smartphone camera sensors of the size $1/1.7''$ are used, which corresponds to a sensor dimension of 7.6×5.7 mm, resulting in a sensor area of about 43 mm^2 . However, considering the total number of pixels on the sensor, it is noticeable that the megapixel (MP) numbers of DSLR and smartphone cameras do not differ greatly from each other. This can only be explained by significant differences in the used pixel sizes.

Pixel size

Taking the sensor resolutions of the current DSLR camera Nikon D850 with 45 MP and the main camera of the current smartphone Huawei P40+ with 50 MP as an example, it becomes clear that the image resolution does not represent a substantial difference between the professional camera and the smartphone camera. The difference only becomes clear when looking at the pixel size. While 1 pixel (Px) on the sensor of the DSLR camera is $4.34 \mu\text{m}$ in size, 1 Px on the sensor of the Huawei P40+ is just $1 \mu\text{m}$ in size. This difference is crucial for light sensitivity and is the main reason why many smartphone cameras struggle with low light situations. Some manufacturers improve low-light imaging by employing monochromatic

cameras in addition to dual or triple RGB cameras while others try to solve low-light imaging problems only by software. The combined use of monochromatic and RGB cameras allows for the acquisition of coloured images with higher levels of detail applying a technique that is comparable to pan-sharpening, e.g. Laben and Brower (2000).

4.1.2 Smartphone camera control

In contrast to professional DSLR cameras, smartphone cameras can only be controlled digitally via apps, which is why at least one camera app is natively installed on any smartphone. Most of today's native camera apps offer a wide range of functions to adjust the camera like changing the focus mode or to define the image format. When implementing own applications, the camera can be integrated in a very simple way by calling the native camera app per intent function for a result (usually the camera image). This option is, for example, used by many map services to annotate points of interest (POIs) with camera images. Decisive disadvantages of this option are that only pre-configured parameters can be adjusted, the adjustments are largely not saved and it is not possible to integrate custom operations in the image processing chains.

Advanced control on built-in cameras can be achieved by accessing the cameras directly through application programming interfaces (APIs), which are provided and regularly updated by the provider of the targeted OS. This enables to build custom vision-based apps as the APIs comprise all necessary functions to configure the cameras, to request images with own configurations and to customise the image signal processing, which is intended in the implementation of the water gauging tool.

However, the direct integration of the camera in apps requires advanced programming skills, as the image processing chains have to be completely defined and implemented by the developer. Moreover, the more advanced the technologies, the more complex the processing chains and the more inconsistencies and errors occur among different smartphone systems. This means that not each parameter that can be controlled via the interface is necessarily exposed by each targeted device, which can cause unpredictable errors. For example, setting the focus distance at infinity works great for a number of smartphones but at some devices the request will cause errors as this focus option is not approved by the smartphone manufacturer for this device type. This should be considered in app programming, e.g. through workarounds.

Summary

Put it in a nutshell, the following key differences between professional DSLR cameras and smartphone cameras could be identified. Smartphone cameras ...

- are not modular. All components are combined in single units, called camera modules, which are firmly integrated in smartphones.
- comprise few, space-saving, miniaturised and low-cost components.
- use sensors with resolutions similar to professional cameras but with much smaller pixels.
- use fixed apertures and focal lengths to save space and costs (except periscope lenses).
- use increasingly two, three or more camera modules with different focal lengths.
- can only be controlled digitally via apps.

Apart from possible problems in low light conditions, today's smartphone cameras capture surprisingly sharp images, so the aforementioned differences cannot have much impact on the

image acquisition itself. The situation might be different, however, if smartphone cameras are to be used for photogrammetric measuring, which is the subject of the following section.

4.1.3 On the use of smartphone cameras in photogrammetric applications

In order to use camera images for the measuring of object surfaces, knowledge of the cameras' imaging parameters is essential. These parameters describe the position of the projection centre in relation to the sensor plane as well as the lens distortion and can be determined by different calibration methods, e.g. test-field or on-the-job calibration. Detailed information on calibration methods and strategies are provided in Luhmann et al. (2013a).

Thus, whenever smartphone cameras should be used for surveying, it is essential to calibrate them. In principle, the imaging geometry of smartphone cameras can be described with the model of the central perspective (describing ultra-wide angle cameras may require additional parameters). In this respect, they hardly differ from most professional cameras. However, with regard to the smartphone camera construction, questions about the calibration stability arise since a calibration is only valid as long as the camera geometry does not change.

A study by Chikatsu and Takahashi (2009) deals with the physical integrity of calibrated smartphone cameras and shows that the calibration becomes easily unstable due to external forces, e.g. shocks. The hypothesis is therefore that the interior orientation of smartphone cameras is generally very susceptible to external influences and to temperature changes. Built-in smartphone cameras are firmly integrated between numerous heat-emitting components. Thus, they are exposed to strong temperature fluctuations, which is why Chapter 7 deals with the assessment of the influence of temperature changes on the geometric stability of these low-cost cameras.

Apart from construction-related difficulties, the geometrical stability of smartphone cameras is questionable for operational reasons. Smartphone cameras are controlled via apps and each time an app is started calling the camera, the camera is reinitialised with respectively provided parameters. One can say, a conducted calibration loses its validity as soon as the therefore used camera app is closed. The same occurs when switching between camera modules.

In summary, before considering smartphone cameras for photogrammetric applications and contactless measurements in crowdsourcing applications their usefulness with respect to stability issues in the camera geometry has to be assessed. This prevents the application of standard calibration procedures as the camera geometry will most likely change between the calibration and the measurement. Consequently, methods are required, which allow for the determination of the interior orientation parameters (IOP) during the actual measurement, similar to on-the-job calibration, but without the necessity of a specific imaging configuration. One option is the registration of the acquired images with 3D object data of the study area that might be stored in a GIS database to determine the image orientation parameters by means of image-to-geometry registration that is further outlined in the main part, see Chapter 10. Approximate values for the IOP, e.g. the focal length as an approximation for the principal distance, can be obtained by functions of the camera APIs.

In order to get corresponding 3D data from a database, information about the image position and rotation in relation to the geographical coordinate system of the 3D data is required. Thus, the following section deals with methods for measuring the position and rotation parameters using built-in GNSS and smartphone sensors intended to serve as EOP of the smartphone images.

4.2 Location awareness of mobile devices

One thing that makes today's smartphones actually "smart" and distinguishable from earlier mobile phones is the use of LBS. LBS allow the user to send and to receive location-dependent information by means of automated location tracking, georeferencing and activity recognition (Google, 2020c). This enables the use and improvement of navigation services, e.g. Gunawan et al. (2020), Qiu et al. (2018) and Wu et al. (2013), but also the collection of geo data to close data gaps in environmental monitoring and disaster management, e.g. Burghardt et al. (2018), Kampf et al. (2018), Zhang et al. (2015) and Muller et al. (2015).

Therefore, smartphones are equipped with a variety of technologies for position determination that might be required in mobile imaging applications to determine the EOP of smartphone camera images. Pei et al. (2013) examined three families of smartphone-based positioning: dead reckoning and visual odometry, positioning through radio frequency (RF) signals and satellite-based positioning by means of built-in GNSS (see Figure 4.4).

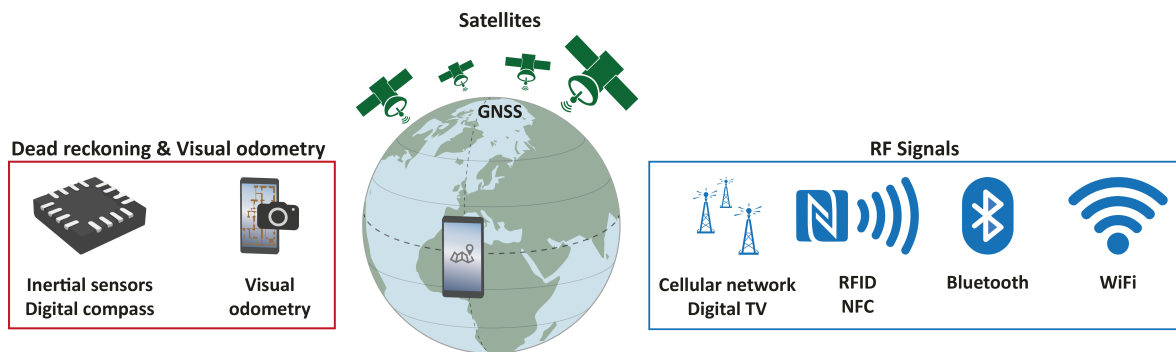


Figure (4.4): Three families of smartphone-based positioning solutions, adapted and updated from Pei et al. (2013).

Dead reckoning and visual odometry

Dead reckoning and visual odometry allow for the determination of the 3D position and rotation parameters of a moving platform in relation to a previous state. In dead reckoning, the motion vector is determined by integrating inertial measurements from accelerometer and gyroscope sensors. In visual odometry, the motion vector is determined by feature tracking between two consecutive images of a moving camera. A hybrid approach is visual-inertial odometry that makes use of the complementary characteristics of the two approaches, e.g. Solin et al. (2018) and Qin et al. (2018). Both methods are very well suited for navigation applications but they are less suitable for measuring the EOP in imaging apps when the smartphone is used in a static mode.

RF signals

The measuring of horizontal position values can be conducted by trilateration using received signal strength indication (RSSI) distance measurements to existing RF infrastructure, i.e. RF identification (RFID) tags, Bluetooth Beacons, WiFi access points or cellular networks. RFID tags allow for a selective location measurement on demand by scanning tags at local reference points. Bluetooth Beacons are small low-cost radio transmitters to be placed in rooms that form a signal network for RSSI-based indoor positioning. Both methods are aimed at indoor navigation.

In contrast, RSSI measurements to georeferenced WiFi access points or cell towers enable smartphone positioning in a global reference frame both indoors and outdoors. However, the position accuracy strongly depends on the availability of WiFi hotspots and cell towers, respectively. According to a study of Zandbergen (2009), the expected accuracies amount to ~ 70 m (best case ~ 20 m) for WiFi-based positioning (applied outdoors) and ~ 600 m for cell-based positioning. The low accuracies and the missing determination of the vertical component make both solutions unattractive for the direct measurement of the EOP of smartphone camera images in mobile imaging applications.

Satellite-based positioning

Satellite-based positioning by means of smartphone-implemented GNSS enables the 3D positioning in a global context without the need for third-party infrastructure. GNSS antennas and receivers are standard in today's smartphones, which is why satellite-based positioning is used in almost any app that uses LBS and is also intended in the photogrammetric water gauging app.

With regard to this, the following section provides some basics on GNSS-based positioning, considering typical error sources as well as difficulties related to smartphone-implemented low-cost technology. Furthermore, the accuracy potential is assessed from the literature in order to take account for possible uncertainties in the development of the water gauging app. Satellite-based positioning is able to determine the 3D position parameters but not the 3D rotation parameters. In order to estimate all six degrees of freedom of a smartphone in a measuring application, the position data need to be fused with inertial and compass measurements from smartphone low-cost sensors based on MEMS technology. Therefore, the chapter concludes with a short review of built-in MEMS, explains in brief their functional principles and reveals construction-related problems to be considered when the derived rotation values have to serve the EOP in mobile imaging apps.

4.2.1 Basics on satellite-based positioning

Pseudorange measurement

Satellite-based positioning uses trilateration based on pseudoranges, which are the distance measurements between navigation satellites and a GNSS receiver. These satellites continuously broadcast information about their position using RF signals. Each signal consists of a carrier wave with a modulated pseudo random noise (PRN) code and navigation data. The PRN code contains information about the signal transmission time, whereas the navigation data comprise almanacs, which are coarse values of the orbital parameters of all satellites belonging to one system, and ephemerides, which are cutting-edge orbital and clock correction data of the broadcasting satellite. Calculating the pseudoranges requires measurements of the signal propagation times that are obtained by measuring the codes.

Code measuring is conducted by shifting the GNSS signal until the PRN code matches a local copy that is generated by the receiver. The required offset refers to the signal propagation time. Due to the relatively low code frequency, defined by the code-chip length, pseudoranges could only be measured with meter precision.

In geodetic surveying, the precision is improved by analysing the high-frequency carrier wave. Assuming a constant observation of the GNSS signal, the cycles of the carrier frequency can be counted. This already would improve the distance measurement to a few centimetres. Solving

the ambiguities of the carrier wave, correcting signal delays and determining the phase offset allow for measurements up to a few millimetres.

However, smartphones aim at a very fast and energy-saving position determination and use by default the *duty-cycle* technique, which periodically shuts down the GNSS receiver for several hundreds of milliseconds to reduce the power consumption. This leads to discontinuities in the carrier phase tracking and impedes carrier phase measurements (GSA, 2017). For this reason, smartphones commonly only use the code measurements to determine pseudoranges that are further used to calculate the position velocity and time (PVT) solution.

Pseudorange impacts

A pseudorange does not represent the true distance between satellite and receiver since the underlying signal propagation time (multiplied by speed of light) is affected by several impacts such as path delays or clock offsets, see Figure 4.5. In order to achieve position accuracies of a few meters by means of code measurements, these impacts, *highlighted in italics* and briefly addressed in the following, should be eliminated as far as possible.

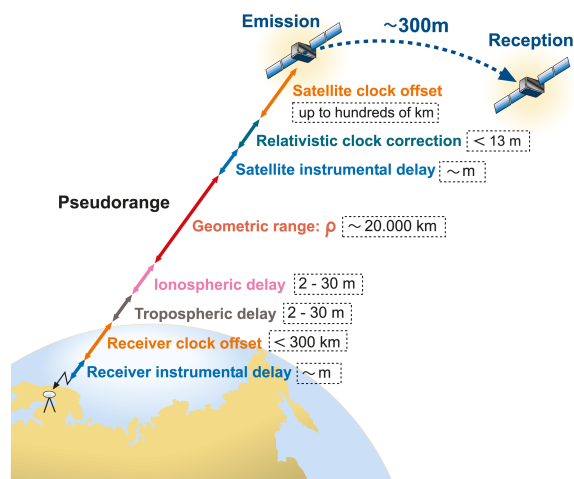


Figure (4.5): Pseudorange measurement impacts, from Subirana et al. (2013).

Any orbital impacts like *satellite* and *relativistic clock offsets* or *satellite instrumental delays* are permanently observed by ground control stations. They can be eliminated by correction data to be included in the PVT calculation. These correction data are either provided by ephemerides or by augmentation data, which are external information from reference station network providers that can be accessed via the internet.

Assuming that the clocks of the receiver and the satellites are perfectly synchronised and other errors are negligible, three pseudoranges would be enough to determine the receiver position. However, this is actually not the case because satellites use very accurate atomic clocks and receivers use ordinary clocks. The resulting *receiver clock offset* leads to ambiguities in position estimation and is eliminated by using at least four pseudorange observations in the PVT calculation.

Tropospheric delays occur due to, for example, temperature variations on the signal path. They can either be predicted through tropospheric models or determined and eliminated in

the adjustment of an overdetermined system of pseudorange observations, which is given when more than four observations are available (van Diggelen et al., 2011).

Ionospheric delays can be eliminated by correction data to be calculated from ionospheric models, which is conducted, for example, by reference station networks. Another option is the use of dual-band receivers as the satellites of the Galileo satellite system and the Global Positioning System (GPS) transfer GNSS signals on two frequencies where the second one is less susceptible to ionospheric delays and can be used to measure and correct the ionospheric impact. For more than a year now, such receivers have also been increasingly built into smartphones.

Receiver instrumental delays are a result of local impacts and noise. Local impacts can be due to multipath, which are multiple signal reflections before the signal reaches the receiver, e.g. at nearby buildings. Multipath can be solved and eliminated by multiple observations, by PVT adjustment assuming a sufficient number of observations, by applying filtering techniques or by eliminating the affected pseudoranges. Other local impacts are due to, for example, bad satellite constellations or too short observation times. Noise-induced errors are mainly related to the employed hardware. Smartphones implement low-cost GNSS receivers and patch antennas that are not well shielded. Therefore, they are highly susceptible to interferences from other electronic components interfering the propagation time measurements (Dabove and Pietra, 2019).

4.2.2 Smartphone-implemented GNSS

The majority of today's smartphones integrate multi-GNSS antennas and receivers that are able to receive and process GNSS signals from GPS, global navigation satellite system (GLONASS), Galileo and BeiDou navigation satellite system (BDS). Basically, the more systems are supported, the faster and the more accurate the positions can be determined due to probably more line of sights to satellites, resulting in more observations to calculate the PVT solution (Szot et al., 2019). Otherwise, the number of required pseudoranges to estimate all unknowns would be hard to achieve, especially in urban areas (GSA, 2017).

Assisted GNSS processing

A major advantage of today's smartphones is that they implement assisted GNSS (A-GNSS) receivers, which can include external information such as augmentation data from the internet or position approximations from RF signals like WiFi in the signal processing in order to get a faster and more precise solution with reduced energy consumption, e.g. Dabove and Pietra (2019), GSA (2017) and Zandbergen and Barbeau (2011). Once a sufficient number of GNSS signals have been received and decoded, the obtained navigation messages, receiver times and biases as well as the derived reception times and code measurements are used to calculate the pseudoranges. These are furthermore used to compute the PVT solution. In this regard, external sensor data, e.g. inertial measurements from accelerometer and gyroscope, can be included to bridge sampling-rate-induced signal gaps applying dead reckoning, e.g. Pei et al. (2013). A simplified scheme of smartphone-implemented GNSS processing is visualised in Figure 4.6. The PVT solution as well as satellite information, e.g. the identities of the involved satellites, can be requested via an API, processing all the data in a black box. The scheme applies to Android devices, but the processing will most likely be similar in Apple devices.

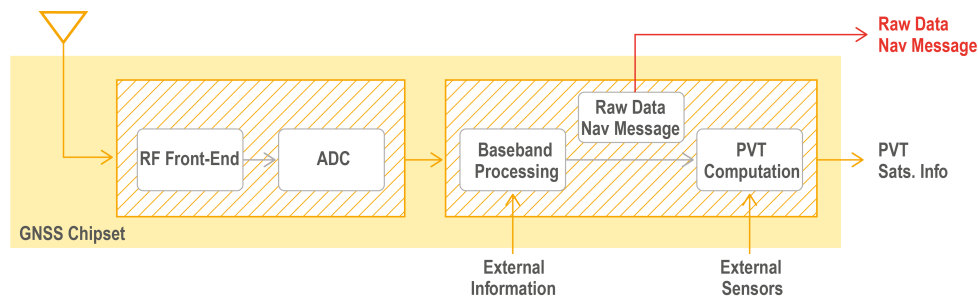


Figure (4.6): Generic block diagram of a smartphone-implemented GNSS receiver, from GSA (2017). ADC means Analogue-to-Digital Converter.

Raw data processing

Beside this, Android released an API in 2016, which allows for direct access to the baseband output of the GNSS module, i.e. the GNSS raw data and the navigation messages, and facilitates the implementation of advanced GNSS processing routines previously reserved for geodetic systems. In this regard, the API enables adjustments on the GNSS receiver, e.g. disabling duty cycle, and thus the use of carrier phase measurements. Working with the raw data enables furthermore the integration of external augmentation data being different from the natively implemented sources as well as the implementation of custom filters to increase the position accuracy and robustness, e.g. Paziewski (2020), Dabove and Pietra (2019) and GSA (2017).

The adaptation of geodetic GNSS processing strategies on smartphones requires advanced knowledge of satellite-based positioning and is still state-of-the-art research. For these reasons, the photogrammetric water gauging tool will use the native PVT solution for determining the smartphone position.

The following section provides a review of the position accuracies to be expected when using the native PVT solution. Reference is also made to recently published papers that deal with the adaptation of geodetic processing techniques on smartphones to show the accuracy potential if using the raw GNSS data.

Smartphone-implemented GNSS: Accuracy potential & technical challenges

Several studies have shown that smartphone positioning using A-GNSS and the natively-implemented PVT processing allows for horizontal positioning accuracies of 5–10 m on average, e.g. Merry and Bettinger (2019), Gikas and Perakis (2016) and Zandbergen and Barbeau (2011). In multipath environments, e.g. in urban areas or close to leafed trees, the accuracies could be worse ($20\text{ m} <$) due to the susceptibility of smartphones to multipath (Merry and Bettinger, 2019). The height component is usually to be expected two to three times worse the horizontal accuracies causing vertical errors of about 15–30 m (no multipath), e.g. Kenyeres (1997).

One of the most challenging aspects when integrating GNSS technology into smartphones is the limited space and the low-cost requirements on hardware, resulting in the use of low-cost GNSS modules and poorly shielded patch antennas. Moreover, the integration of GNSS plays a minor role in hardware design. Consequently, the GNSS hardware is frequently installed where space is left. Thus, it is possible that the GNSS antenna is placed at the bottom of a smartphone where the user usually has his hand. This would lead to heavily attenuated

signals to be amplified, which in turn impairs the signal-to-noise ratio (SNR) (van Diggelen et al., 2011). For these reasons, the aforementioned accuracies may still vary between the devices, which needs to be considered in the development of the photogrammetric water gauging app.

An example of the dependence of hardware and accuracy is provided in the study of Dabove et al. (2020), who processed and compared the GNSS raw measurements from two devices of the same generation (both released in 2017). Although the same processing scheme was applied, one smartphone showed horizontal positional errors of a few decimetres while the other one showed errors of a few metres. The results have been justified with differently installed GNSS chipsets. Nevertheless, it was emphasised that smartphone GNSS is in constant development and better results are expectable from recently built-in GNSS modules.

This is already evident from the following studies where geodetic processing was applied to the GNSS raw data using carrier phase measurements and precise correction data either from reference station networks to get position estimates of about one centimetre via precise point positioning (PPP), e.g. García et al. (2010), or from a base station to get position estimates of a few centimetres via real-time kinematic (RTK), e.g. Rietdorf et al. (2006). The studies give an impression on the accuracy potential of recently implemented GNSS technology.

Dabove and Pietra (2019) have shown that horizontal position accuracies of about 0.5 m can be achieved (vertical accuracies 3 to 4 times worse) processing the raw GNSS data using network RTK. Similar results were achieved by Aggrey et al. (2019) applying PPP. In both studies it was emphasised that a higher precision requires knowledge of the antenna position inside the smartphone that is usually unknown and practically not documented.

However, Wanninger and Heßelbarth (2020) were able to calibrate the antenna being responsible for the reception of the L1 GPS signal, resulting in a fix for ambiguities in the carrier phase measurements. This resulted in 3D positions with standard deviations of less than 4 cm after 5 min of static observation and 2 cm for longer static observation.

4.2.3 Basics on smartphone sensor technology

While the positional accuracies have already been extensively researched, there are still gaps in knowledge regarding the rotational accuracies when using MEMS for rotation determination. In order to accommodate possible uncertainties in the development of the photogrammetric water gauging tool, Chapter 8 presents a comprehensive investigation assessing the rotational accuracy and stability with regard to mobile imaging applications to which the following section is a supplement. First, reference is made to the different types of smartphone-integrated sensors. This is followed by explanations on the functional principles of the sensors used in the study, contributing the understanding of the necessity of sensor fusion.

Classification of smartphone sensors

Basically, smartphones use motion, position and environmental sensors (Google, 2020b).

Motion sensors comprise inertial sensors, i.e. accelerometers and gyroscopes. While the first smartphones merely implemented accelerometers to determine the screen orientation, modern sensor units adapt professional IMUs structures to smartphones using MEMS, i.e. tiniest logical and micro-mechanical elements combined in a chip for signal processing. Motion sensors determine the smartphone rotation in 3D space by integrating the measured accelerations and angular velocities.

Position sensors comprise proximity sensors and digital compasses. Proximity sensors measure the distance between a nearby object, commonly the user, and the smartphone via ToF using eye-safe infrared beams. Digital compasses (also magnetometers or magnetic field sensors) measure the magnetic field strengths acting on a device. They enable the georeferencing of the inertial sensor data in relation to magnetic North by analysing the geomagnetic field components.

Environmental sensors measure ambient parameters such as humidity, air temperature, air pressure, or illumination. Apart from the illumination sensor, controlling the display brightness, they are not standard and often only available in flagship devices.

Working principles of built-in inertial and compass sensors

In the following, the working principles of MEMS accelerometers, gyroscopes and compass sensors are explained. Their basic structures are visualised in Figure 4.7. Note, the sensors are one-dimensional sensors, which is why smartphones implement three sensors per type to get the device orientation in 3D object space.

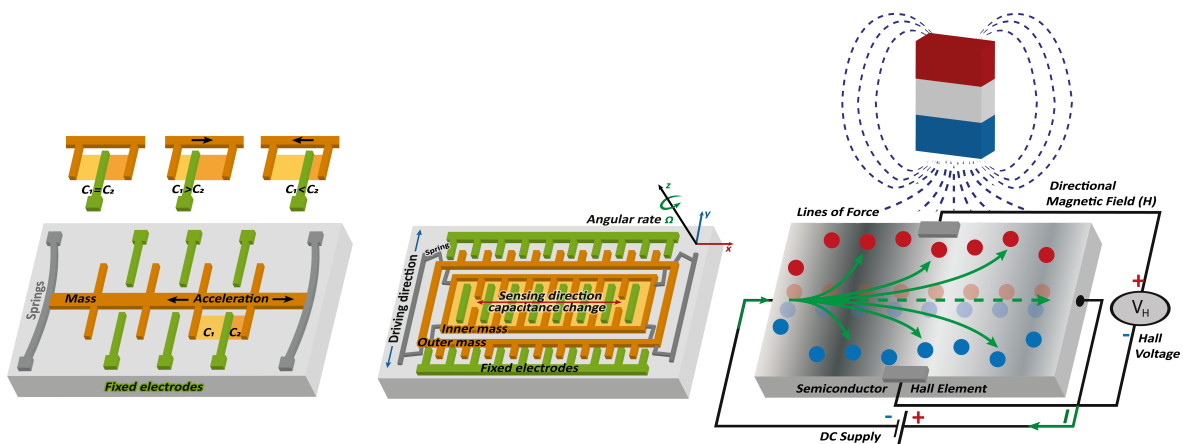


Figure (4.7): Basic structures of MEMSs. From left to right: accelerometer, gyroscope and magnetometer build in smartphones. Figures adapted from Nedelkovski (2015) and Maenaka (2008).

Accelerometers used in smartphones are based on the spring-mass principle. A silicon mass with comb structure is supported by springs on a silicon wafer and moves between fixed electrodes in one direction if a respective acceleration is applied. This leads to capacitance change between the mass and the electrodes that is measured to estimate the strength of the acceleration, see Figure 4.7 on the left.

However, there are a few difficulties. First, orientation changes can only be detected when acceleration is acting on the sensor, i.e. the sensor will not register any movement when the smartphone moves with constant velocity. Secondly, accelerometers measure each force that is applied to the device. Thus, they are very sensitive to any vibration acting on the sensor,

which lead to disturbing linear accelerations. These disturbances can be corrected if the movement is predictable, e.g. by planning the trajectory such as flight path planning when using UAVs. In this way, linear movements exceeding the movement pattern can be detected and eliminated. Another option is the application of thresholds to eliminate particularly strong accelerations that often indicate force rather than true movement, but this interrupts the measuring epoch. Neither trajectory planning nor thresholding is an option for smartphone motion detection. For this reason, the increasing use of smartphones in navigation applications forced manufacturers to install gyroscopes in addition to accelerometers, which have been standard for a few years now.

Gyroscopes are similar in structure to accelerometers. A mass, separated in an inner and outer part, with comb structure is oscillating between fixed electrodes. If an angular rate is applied to the gyroscope, the Coriolis force will act on the mass causing capacitance change, see Figure 4.7 in the center. The angular measurements are very precise, which is why the measurements from gyroscopes are often preferred to measurements from accelerometers in navigation applications, e.g. in dead reckoning. However, there are bias instabilities and a high-frequency noise that result in drift when integrating the angular measurements, called angular random walk (ARW), which can be recognised and eliminated by fusing the gyroscope measurements with measurements from accelerometers.

Compass sensors measure magnetic field strengths acting on the smartphone by means of the Hall effect, see Figure 4.7 on the right. Therefore, a direct current (DC) is applied to a semi-conductive Hall element. When a magnetic field is applied, the uniform flow is disturbed and electrons and protons are each deflected to one side. The strength of the magnetic field is determined by measuring the applied voltage. Thus, measuring the geomagnetic field components enables the determination of the smartphone rotation in relation to magnetic North. Magnetometers are prone to soft and hard iron effects to be remedied to a certain extent by calibration. The assessment of the impact of magnetic perturbations on rotation determination was a main objective of the referred work, which is why more information on soft and hard iron effects are provided in Chapter 8. Fusing the measurements from inertial sensors and compass sensors allows for the translation of the measured heading angle to the azimuth, i.e. the clockwise measured angle between the smartphone direction and true North. Transferring magnetic North to true North is possible by determining the declination angle.

Put it in a nutshell, each sensor has its strengths but also weaknesses to overcome. This can be realised by sensor fusion, which has been comprehensively addressed in the related publication to identify an appropriate method for determining the rotation parameters in the water level measurement app. In this thesis, the term *sensor fusion* is used as an acronym for the integration of different sensors and the fusion of their measurements to determine specific parameters. In order to implement sensor fusion, the sensor data are accessed via corresponding APIs.

5 Crowdsourcing

With the recent developments in technology and society, citizens with great personal interests in science, research and engineering increasingly contribute to scientific investigations by "forming research questions, conducting scientific experiments, collecting and analysing data, interpreting results, making new discoveries, developing technologies and applications, and solving complex problems" (NOAA, 2020) that is commonly referred to as *civil* or *citizen science*. With regard to the spatio-temporal densification of hydrometric monitoring networks, the most interesting aspect is the possibility to collect *big data* in very short times with the assistance of volunteers, which is known as *crowdsourcing*.

Following the explanations of Heipke (2010), the term crowdsourcing is derived from the economics-driven term outsourcing, i.e. the transfer of a production to a remote and cheaper location. He termed crowdsourcing as a "concept where potentially large user groups carry out work, which is expensive and/or difficult to automate" either through *volunteered computing* or *participatory sensing* (Haklay, 2013).

5.1 Human sensors

Volunteered computing makes the least demands on the participants' skills as they will only contribute passively by providing unused computing capacities to the experts so that they can outsource computing-intensive processes, e.g. simulations. In participatory sensing, engaged citizens act as intelligent *human sensors*, collecting data without necessarily having a specific qualification for solving the task. Although the idea of human sensors is not new, it has received considerable attention due to the wide distribution of smartphones. The use of smartphones makes a particularly valuable contribution to volunteered geographic information (VGI) as they enable human sensors the collection of comprehensible amounts of data to, for example, assist the experts in the monitoring of environmental processes while overcoming spatio-temporal issues, e.g. Burghardt et al. (2018) and Goodchild (2007). For this purpose, they are provided by the experts with tools in the form of apps.

The use of human sensors is particularly interesting for water gauging because they are not, like typical sensors, fixed to a single study area, but can act flexible at different sites. This facilitates the measurement of water levels with high spatio-temporal resolution and redundancy according to the experts' requirements. For example, the experts could use the app to communicate the volunteers at which locations data should be collected particularly urgently, e.g. at small rivers with an increased risk of flash flooding.

5.2 Big data

Crowdsourcing indisputably offers new opportunities for the acquisition of big data that might be conventionally inconceivable in terms of spatial range and also in terms of the temporal actuality. However, there are difficulties in the use of user-generated data that should not be

neglected. In this regard, the most serious problems are the "immense degree of heterogeneity, the partially unknown semantics and the varying quality" (Burghardt et al., 2018).

In the context of this thesis work, the water level measurement is considered with a single, dedicated app as data source. While other tools may use common interfaces for data exchange, the constraint necessarily limits data heterogeneity and prevents missing semantics. However, the data quality can still vary due to different skills in data acquisition or differently employed hardware, which is why quality measures are nevertheless essential for data quality assurance.

5.2.1 Quality measures

One option is the use of meta data to detect questionable data, e.g. by means of data acquisition position and date/time. Furthermore, this allows the experts to define constraints on the data acquisition, e.g. the water level measurement could be limited to particular rivers and the position data could be checked for plausibility, i.e. whether there are any water bodies at all at the transmitted coordinates. In doing so, data that do not meet the constraints can be easily identified and excluded, e.g. Cartwright (2016) and Haklay (2013).

Obviously, quality differences in the data can also be caused by quality differences in the employed hardware. This is particularly evident when smartphones are used as measuring devices, as they are known to implement various hardware of different generations and qualities. This problem might be solved by hardware restrictions, e.g. define a minimum platform version and check all necessary functions when starting the app, although the first option would restrict the circle of participants.

5.2.2 On the use of big data in photogrammetry

Since the availability of digital images in the internet literally exploded, voluntary data became also interesting for photogrammetry. A famous example is the 3D reconstruction of historical buildings from tourist images applying structure from motion (SfM) (Snavely et al., 2007). Leberl (2010) highlights the growing role of user-generated street-level imagery to reconstruct 3D city models but also to capture entire interiors, e.g. of malls, and so fundamental data to develop indoor navigation methods. In this regard, he coined the term *neo-photogrammetry* fusing well-established photogrammetric measuring methods with user-generated image content. Thus, the water gauging app can be considered as a neo-photogrammetric measurement tool.

5.3 Activation of citizen scientists

Fundamentally, the water gauging app only allows for the spatio-temporal densification of hydrometric networks when it is used by a sufficient number of human sensors. On the one hand, it is probably easy to convince the general public of the importance of water level monitoring in case of flood events and to motivate their cooperation. On the other hand, the monitoring of water cycles requires continuous water level measurements and thus sustained participation. Therefore, Nielsen (2006) summarised five points to be considered when activating volunteers for crowdsourcing:

- avoid technical, logistic or intellectual barriers
- provide templates for the task to be done
- reward active participants in an appropriate way
- promote high-quality contributors e.g. by reputation ranking
- make participation a side effect

Avoid technical, logistic or intellectual barriers

Preventing technical barriers is particularly important since crowdsourcing is increasingly conducted using apps that have to run on a great number of devices with high performance. Special attention should be paid to this if the apps are aimed at global use in order to overcome the "digital divide" between richer and poorer communities (Goodchild, 2007). For example, smartphones targeting the developing market shall be affordable for the population with usually very low per-capita income requiring low-cost models, e.g. Alliance for Affordable Internet (2020). Low-cost smartphones largely use downsized hardware and thus less performance, which has to be also considered in software design (see Section 6.3.2).

In order to avoid logistic barriers, Haklay (2013) recommend the experts to select study areas close to frequented spots such as residential areas or famous places. Regarding the design of the water gauging app, it is recommended to implement a map on which regions of interests (ROIs) are marked indicating the catchments where data are required. The map could be editable by both sides, so that volunteers can deposit their positions visibly for the experts, who could in turn communicate location-dependent information, e.g. about close ROIs.

Keeping intellectual barriers, which also include language barriers, as low as possible, apps shall be made autoplausible and as simple as possible considering "best practices" when designing interfaces for human-computer interaction, e.g. Moreno et al. (2013). If extensive explanations are required, the use of illustrations and icons is preferable to texts and textual menus to reduce lingual and alphabetical barriers. If background information is required, it should be collected automatically to reduce the user input to a few steps. With regard to the water gauging tool, information about, for example, the camera parameters should be collected automatically by the app at runtime.

Provide templates for the task to be done

Crowdsourcing makes minimal demands on the volunteers' knowledge, skills and efforts to put in, which is why citizen scientists should be assigned with distinct and easy to communicate tasks. Undoubtedly, having a fair degree of skills and knowledge is key to achieve a uniform level in the data and to prevent avoidable false data from the outset. Thus, it is strongly recommended to provide the volunteers appropriate training before starting into a research task and/or guidance through the respective task. With regard to the crowdsourcing of water levels, the app will guide the participant step by step through the assigned task, leaving virtually no room for (avoidable) errors.

Reward active participants/ Promote high-quality contributors

With the development of an evaluation system, particularly active persons or particularly good contributions should be identified and rewarded, either through material rewards or through prestige, e.g. in the social media. Note, the evaluation of particularly good data contributions is closely linked to the existence of quality measures.

Make participation a side effect

One option to make participation a side effect is the gamification of the actual task. One example is provided by von Ahn and Dabbish (2004), who let people play a computer game while labelling images. In the *CrowdWater game* by Strobl et al. (2019), volunteers compete against each other in the playful evaluation of hydrological data that have been acquired

in the crowdsourcing project *CrowdWater* (Etter and Strobl, 2018). In this respect, the main goal, which is the crowdsourcing of hydrological parameters, is split in the two tasks of *data acquisition* and *data evaluation*. This two-way strategy could also be interesting for the crowdsourcing of water level measurements.

In any case, scientists should think about who they actually want to involve in their research because the motivation, beside the qualification, has fundamental impact on data reliability and quality. Following the classification by Heipke (2010), possible drivers are personal interest in the research field, i.e. the hobby scientists, the attainment of prestige or self-promotion by sharing the voluntary activities in the internet, the opportunity to earn awards or payment, e.g. Paolacci and Chandler (2014).

Thanks to the social media, it is relatively easy to find, to contact and to motivate hobby scientists for participation in research (Cartwright, 2016). Due to their personal interests into science, they will most probably work carefully and produce trustworthy data, which is why they might be preferable to participants who act only for payment, pride or self-promotion.

6 Developing smartphone applications

6.1 Native, hybrid and cross-platform coding

Before one starts with smartphone app development, some fundamental programming questions need to be answered. One of the most difficult decisions to make is the choice of the platform as, obviously, most app developers want their software to run on as many devices as possible. Thus, there are basically three app development strategies to consider: native, hybrid and cross-platform coding.

Native apps target one OS. They are developed using the software development kit (SDK) that is provided by the OS vendor. SDKs are comprehensive frameworks providing code libraries, APIs, developing guidelines, code snippets and build tools to compile software for one specific platform. Usually, SDKs support one or two programming languages. For example, Android apps are developed in Java or Kotlin whereas Objective C and Swift are the supported languages for apps running under iOS. Some advantages of natively developed apps are performance and robustness because the source code is compiled before the app is executed and thus has not to be interpreted at runtime. Furthermore, the developers can make use of the smartphone's entire hardware through native APIs, e.g. to access the cameras (Pinto and Coutinho, 2018). However, native coding is very expensive. It requires a lot of developing resources, manpower and time because programming for different platforms requires multi-faceted skills and means programming for each platform from the scratch. Moreover, different platforms have different hardware requirements that may restrict the number of features to be implemented or require appropriate workarounds if the one or the other feature is not available for all targeted platforms.

The increasing demand for multi-platform mobile software forced companies to find more cost-effective solutions and led to the development of web-based/ hybrid coding approaches. Even if smartphones are running different OSs they usually implement at least one natively installed browser app. Web-coding languages like HTML5 or JavaScript are very popular, powerful, standardised and, compared to Java or Objective C, easy to learn and to implement. They can be used to develop lightweight apps while having a similar look-and-feel as native apps (Chebbi, 2019; Pinto and Coutinho, 2018). Such web-based apps could be, on the one hand, accessed through the web browser or, on the other hand, they could be wrapped in a native shell that allows for the app distribution through the respective app store. The advantages of this programming paradigm are platform-independent software development at lower costs with 70–90% reusable and maintainable code (Klubnikin, 2017). Disadvantages are lacking performance as the code is interpreted at runtime and missing APIs that makes the access to hardware components very difficult (Maggini, 2019; Pinto and Coutinho, 2018).

Novel cross-platform frameworks try to fuse the advantages of native and hybrid coding to create high-performance multi-platform apps employing all the natively provided functions and features from the targeted OSs. State-of-the-art cross-platform frameworks enable to create unified APIs on top of those from the native SDKs and to build apps for the global player platforms Android and iOS by shared code bases. Some examples for such frameworks are

Xamarin, React Native or Kotlin Multiplatform Projects (Klubnikin, 2017), which promise to make performance issues in multi-platform coding a thing of the past. However, cross-platform programming requires a deep understanding of all targeted platforms as well as knowledge about the cross-platform bindings. Unfortunately, such experienced developers are hard to find as this coding paradigm is fairly new. This is supported by the fact that some well-known cross-platform frameworks are either far from the first stable release like React Native, or still in experimental mode such as Kotlin Multiplatform Projects, e.g. Maggini (2019). Furthermore, not all features, APIs and libraries from the respective native SDKs are nowadays open to cross-platform development, which still requires time-consuming workarounds when integrating hardware and functions being not yet supported. For example, the famous vacation rental company AirBnB started their mobile business using cross-platform-coded apps but they went back to native coding due to technical challenges, a lack of resources and a lack of experienced developers (Klubnikin, 2017).

Put it in a nutshell, the well-established native programming style is recommended when building complex mobile apps with heavyweight logic and strong hardware dependencies, requiring native APIs and libraries or when creating first-of-a-kind apps such as the photogrammetric water gauging tool. On the contrary, cross-platform development should be considered when a good working solution should be adapted to the mass market by supporting several platforms with focus on code reusability and maintainability. Web-based/ hybrid coding might be an option for apps that do not require access to further hardware, that implement only a few lightweight tasks or that are developed for a unique purpose like surveys for a specific event.

6.2 Android versus iOS

Currently, the mobile market is dominated from two platforms: Android funded by Google and iOS by Apple. Both systems pursue completely different concepts, each with pros and cons, that need to be weighted against each other when developers have to choose one or the other concept.

Android is an open platform that has been designed for the mass market. The Android SDK is freely available for any leading OS, i.e. Windows, Linux and Mac OS, including all APIs, libraries, build tools and several entry-level code samples enabling a comfortable transition into app programming. Third-party libraries can be added as needed. Android makes less stringent demands on smartphone manufacturers, which is why the OS is employed by almost any smartphone (remember, 86.3 % of today's devices use the Android platform). Reviewed apps can be purchased through Google's Play Store but it is also permitted to install unaudited apps from third parties, which is interesting when apps are supposed to be quickly accessible to a certain user group. The reduced hardware requirements are both a blessing and a curse. Although access to specific features is granted by the Android-driven APIs, it does not mean that all the targeted devices will support these features, which has already been discussed in Section 4.1.2. This demands enormous test efforts with numerous devices, proper exception handling and code adaptations actually for each Android version. Purchasing apps from third parties is indeed a fast and easy way to access new apps, e.g. to quickly and easily distribute software for crowdsourcing, but also introduces uncertainties regarding security vulnerabilities due to misuse, e.g. if fake software is distributed in the name of crowdsourcing. Android systems are usually supported for 2–3 years.

In contrast to Android, Apple's iOS is a closed platform that can only be implemented on Apple devices, i.e. iPhone and iPad. App development is only allowed using the development

environment Xcode, which integrates, similar to Android, all core libraries, APIs and build tools. Unfortunately, Xcode is only available for Mac OS and thus inherently impedes app development under other OSs. On the one hand, limiting the OS to Apple devices means a strong limitation of the potential user group. On the other hand, Apple devices use internal hardware standards. If APIs are provided to access hardware components, it is guaranteed that they work on all devices, which is a big advantage over Android. Apps can only be purchased through Apple's App Store after app verification. This might be cumbersome when desiring a fast and easy app distribution to a small user group, e.g. for a test phase, but also prevents security problems. In contrast to Android, Apple guarantees a long-term hardware support for 4–5 years.

Basically, there is no right or wrong in the decision for one platform and against the other. It is rather a question of the app to be developed. When targeting a worldwide user group, one will consider to go for the Android platform due to its global market share. Apple devices are less represented particularly among countries having a lower per-capita income. This is also reflected in app monetisation, where apps for iOS are the clear winners because Apple users are more willing to spend money on apps than Android users who are more likely to use ad-supported services. In terms of complexity and speed of app development, iOS clearly outperforms Android due to its strict hardware rules, which make the test phases and adaptation times of iOS apps much shorter than those of Android apps, e.g. Fitzgerald (2019).

The water gauging tool is aimed for the use on Android devices due to the worldwide much larger group of potential human sensors, although this requires considerable development efforts to support as much hardware as possible.

6.3 The process of software development

The development of software comprises different phases that can be described by procedure models, e.g. the simplified V-model as shown in Figure 6.1.

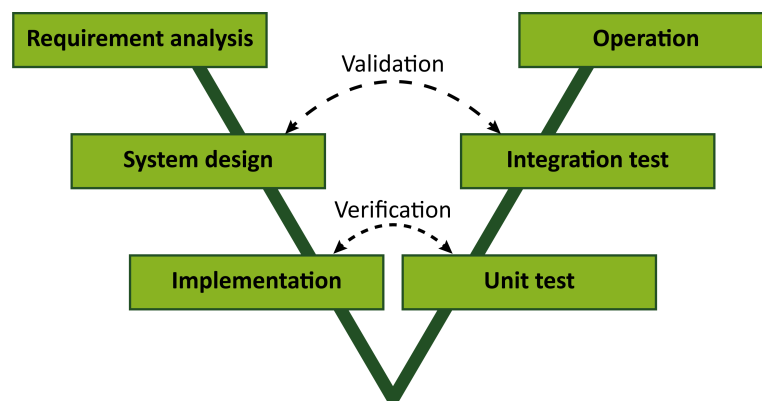


Figure (6.1): Simplified V-model describing six phases in software development, adapted from Hamad (2020).

Software development usually begins with the *analysis of software requirements* and the conceptualisation of the entire system that is commonly referred to as *system design*. The software *implementation* is followed by an extensive test phase to verify the implemented functions by *unit tests* as well as to validate the collaboration of a system's individual components by *integration tests* before the software is put into *operation*.

With regard to the development of an app for crowdsourcing water levels, the following Section 6.3.1 provides an overview of requirements to be considered when developing crowdsourcing apps. In order to keep technical barriers in crowdsourcing and thus the demands on processing hardware as low as possible, a suitable system design is required that enables the separation and outsourcing of individual processes in order to save computing resources. In the upcoming Section 6.3.2, two concepts are introduced allowing for the separation and distribution of logic in view of the water gauging app to make the tool as light on resources as possible. Details on the implementation of the individual components and processes are provided in Chapter 10. Basically, the implemented tool is a prototype that would have to pass a comprehensive testing phase comprising manifold unit and integration tests before it can be released for crowdsourcing. However, this goes beyond the content of the thesis, i.e. the methodological development and implementation, which is why extensive explanations of the test phases up to operation are omitted.

6.3.1 Requirement analysis for the development of crowdsourcing apps

Software requirements are classified into *functional* and *non-functional requirements*. Functional requirements describe *what* the app should do, e.g. which data should be collected by human sensors. Non-functional requirements describe *how to* comply with the functional requirements, e.g. Wiegers and Beatty (2013). For developing crowdsourcing apps, non-functional requirements are of special importance, in particular:

- **data integrity & quality:** The acquired data shall be complete, correct and consistent. The use of quality measures to detect false data is mandatory. Strategies shall be developed to ensure sustained participation.
- **data management & scalability:** Appropriate techniques are required to process, evaluate and store big data.
- **efficiency & resource constraints:** Resources shall be used sparingly, i.e. power, processor, storage and network utilisation shall be reduced to a reasonable extent.
- **extensibility, flexibility, modifiability, maintainability, integrability & up-datability:** The system shall be extensible, modifiable and integrable to react to changes in the functional requirements, e.g. the integration of new functionalities. The individual components of the system shall be independently maintainable and updatable to react to changes of the carrier system.
- **emotional factors:** The app should be appealing.
- **guidance:** Users shall be guided through the application to avoid mistakes and excessive demands.
- **internationalisation:** Lingual and alphabetical barriers shall be avoided when the app is intended for the global use, i.e. language and type system.
- **intuitiveness & user-friendliness:** The app shall be autoplausible and user-friendly.
- **transparency, privacy & security (virtual):** For reasons of confidence, users shall be informed about all data collection, usage and storage. The app shall only collect truly necessary data, delete obsolete data, provide privacy policies and encrypt sensitive data (Balebako and Cranor, 2014).

- **security (physical):** Users shall be informed about physical risks when using the app. This is particularly important when crowdsourcing is applied to investigate environmental parameters, e.g. during extreme events.
- **performance & robustness:** The app shall be performant, robust and crash-safe, independently from low-cost or flagship hardware. Software designers should consider the *separation of concerns* paradigm to separate business logic from the user interface (UI) as well as to outsource heavy processing tasks to remote systems, see Section 6.3.2.
- **compatibility & portability:** The app shall be compatible to the specified platform and version. If more than one platform is targeted, the system shall be fully portable.

It needs to be noted that the mentioned requirements are only an extract, essentially relate to the app for the measurement of water levels and have to be adapted individually for each software project. A full overview of 160 non-functional requirements that can form the basis of software is given by Chung et al. (2000).

6.3.2 System design - Separation of concerns

The requirement analysis is followed by the software design including considerations on system architecture, which is in short the conceptual modelling of a software system in terms of structural, behavioural and collaboration elements (Jaakkola and Thalheim, 2010).

As advised by Google (2020d), smartphone apps should follow the *separation of concerns* paradigm, i.e. divide complex tasks into less complex packages, because small packages are easier to test, to maintain and to adapt. Separation of concerns also means that one instance of an application should be only responsible for one thing implying the outsourcing of processes, for example to remote application servers (Elliott, 2014).

In this regard, two structural design patterns are introduced for graphical user interface (GUI) architecture in order to separate the database and the business logic, i.e. the data processing schemes, from the view logic, i.e. the UI. Furthermore, a design pattern is introduced, which allows for process distribution and thus facilitates the outsourcing of heavyweight tasks to remote application servers. Thus, only lightweight processes have to be performed on smartphones, facilitating the use of an app on less powerful low-cost devices.

Separating business and view logic: GUI architecture

When creating software with a GUI, that applies to almost all smartphone apps, it is good practice to separate the UI from the business logic using different layers for flexible handling and to reduce the risk of overloading the UI with logic. A very well-known design pattern for this purpose is the Model-View-Controller (MVC) pattern where the Model layer holds the business logic and the database, the Controller layer updates the Model and receives user events from the View layer to be processed. The Model transfers the results in the form of state change events to the View that furthermore queries the Model for data to be visualised. Due to the structure of apps, strict adherence to this MVC principle is not straightforward in mobile software development, as Controller and View are usually linked via shared activities. This caused manifold adaptations of the MVC pattern such as the Model-View-Presenter (MVP) pattern, e.g. Muntelescu (2016). MVP aims for a strict distinction of the Model and the View that communicate via a mediating Presenter layer. Both design patterns are visualised in Figure 6.2.

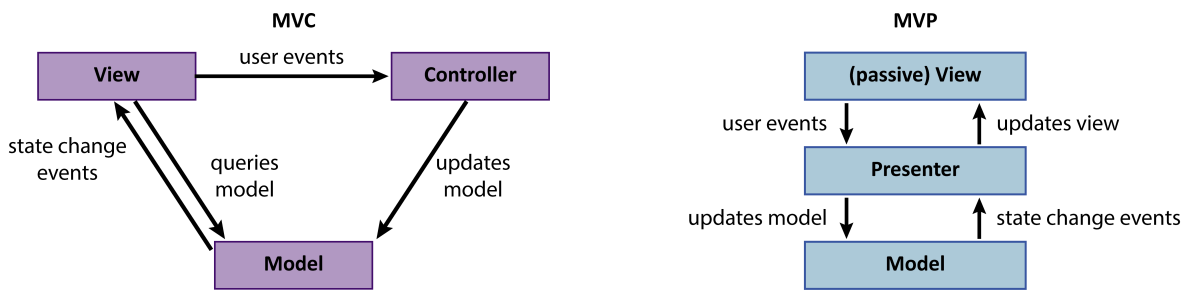


Figure (6.2): MVC and MVP software design patterns, adapted from Chandel (2009).

Applying the MVP pattern is particularly useful when developing smartphone apps integrating the camera. The View can implement the camera preview and the UI, whereas the Model manages all data and logic such as camera settings and image processing lanes. Separating the View from the business logic is essential for a good performance as it enables asynchronous data processing and visualisation by preventing an overload of the UI thread.

A simple example is taking a picture with a camera app. After starting the app, the user triggers the image capturing through the UI of the app, which is managed by the View. The View transfers the user event, i.e. the request for image data, to the Presenter that updates the Model with information about the user request, e.g. capture an image with focus at infinity. The Model holds the logic and the database, e.g. interfaces to access the hardware and camera settings, starts processing the request in a different thread and informs the Presenter about the processing state. The UI remains accessible during the entire processing time and can, for example, receive further user inputs. As soon as the input has been processed and a result (the image) is available, the Presenter is informed about the event, i.e. an image has been captured and stored. The Presenter can then update the View, for example by showing a preview image to the user.

Distribution of processes: Multi-tier client-server architecture

The separation of concerns paradigm is rather important when heavyweight logic is required in smartphone apps that cannot be processed directly on the device due to insufficient computing power, memory or energy supply. Therefore, design patterns are required, which allow for the distribution and outsourcing of processing tasks such as multi-tier client-server architectures, e.g. Shahbudin and Chua (2013) and La and Kim (2010). Multi-tier architecture means the separation and distribution of individual processes to different systems, e.g. data acquisition, processing and visualisation (Eckerson, 1995). This can be applied to the aforementioned MVP design pattern where the Model is outsourced to an application server, the View is managed by the smartphone (the client) and both communicate either directly (two-tier structure) or through a third layer holding the Presenter (three-tier structure).

Thereby, the collaborating elements can be loose coupled or tight coupled. Loosely coupled distributed systems can interact with each other but they are not mutually dependent. The components of tightly coupled systems are mutually dependent, i.e. one component cannot exist without the other. Loose coupling is preferable to tight coupling whenever it is possible in favour of system maintenance, flexibility and reusability. Thus, changing one component will not necessarily lead to changes of the entire system, e.g. updating the smartphone OS will affect the app processes of the client but not the server processes.

The photogrammetric water gauging tool uses a three-tier client-server structure. Lightweight tasks are processed directly on the smartphone having the camera logic separated from the UI according to the MVP pattern. Heavyweight logic and the database are outsourced to an application server. The communication is established by an intermediate layer. All components are loosely coupled. Thus, the app can be used even if no server connection can be established. In such a case, the data is locally stored and processed when the connection becomes available. Also, client and server processes can be individually adapted, e.g. to react to platform changes and updates. More details and a graphical visualisation of the realised system architecture are provided in Section 10.4.1.

Part II

Studies on smartphone technology

7 On the geometric stability of low-cost cameras depending on temperature changes

Chapter 7 published in “Sensors” (eISSN: 1424-8220) as:

Assessing the Influence of Temperature Changes on the Geometric Stability of Smartphone- and Raspberry Pi Cameras

Authors: Melanie Elias^a, Anette Eltner^a, Frank Liebold^a, Hans-Gerd Maas^a
^a Institute of Photogrammetry & Remote Sensing, TU Dresden, 01069 Dresden, Germany

Publication history: submitted 03rd November 2019, accepted 20th January 2020, published 23rd January 2020

Full reference: Elias, M., A. Eltner, F. Liebold and H.-G. Maas (2020). “Assessing the Influence of Temperature Changes on the Geometric Stability of Smartphone- and Raspberry Pi Cameras”. In: *Sensors* 20, 3, p. 643. DOI: 10.3390/s20030643

Abstract: Knowledge about the interior and exterior camera orientation parameters is required to establish the relationship between 2D image content and 3D object data. Camera calibration is used to determine the interior orientation parameters, which are valid as long as the camera remains stable. However, information about the temporal stability of low-cost cameras due to the physical impact of temperature changes, such as those in smartphones, is still missing. This study investigates on the one hand the influence of heat dissipating smartphone components at the geometric integrity of implemented cameras and on the other hand the impact of ambient temperature changes at the geometry of uncoupled low-cost cameras considering a Raspberry Pi camera module that is exposed to controlled thermal radiation changes. If these impacts are neglected, transferring image measurements into object space will lead to wrong measurements due to high correlations between temperature and camera’s geometric stability. Monte-Carlo simulation is used to simulate temperature-related variations of the interior orientation parameters to assess the extent of potential errors in the 3D data ranging from a few millimetres up to five centimetres on a target in X- and Y-direction. The target is positioned at a distance of 10 m to the camera and the Z-axis is aligned with camera’s depth direction.

Keywords: MEMS, Smartphone camera, Raspberry Pi camera, Camera calibration, Photogrammetry, Interior orientation, Low-cost camera

7.1 Introduction

Smartphones have become indispensable in modern human life as they are not just purely communication tools. They are qualified for citizen science applying photogrammetry due to built-in cameras enabling the acquisition and processing of geolocated image data directly on the device. The global increase of climate-related natural hazards (Lehmann et al., 2015) demands new technologies to support their observation, detection and forecasting to improve early-warning systems. The progress in smartphone technology creates new possibilities in this regard. Current devices comprise high storage capacity, large processing power, a wide range of built-in sensors and high-resolution cameras. Therefore, they are already a centrepiece in several early warning systems that are supported by volunteered geographic information with user-generated content (Burghardt et al., 2018; Price and Shachaf, 2017). Recently published water-level monitoring and flood-forecasting tools adapt well-established photogrammetric methods to smartphone- and Raspberry Pi (RPi) cameras to use them as versatile measurement instruments, e.g., Elias et al. (2019), Eltner et al. (2018), Davids et al. (2019), Peña-Haro et al. (2018) and Kröhnert and Meichsner (2017). To restore the collinearity between the 2D image and the related 3D object scene, i.e., to determine the linear relationships of 2D image points and 3D object points that lie on image rays with a shared origin called projection centre, knowledge about the interior orientation parameters (IOP) is required, which can be determined via photogrammetric camera calibration, e.g., Luhmann et al. (2016), Clarke and Fryer (1998) and Fraser (1997).

A calibration is valid as long as the camera geometry does not change. Alternating IOP can be caused by aperture- or focus adjustment on the one hand or due to physical impacts such as strong motion on the other hand, e.g., Chikatsu and Takahashi (2009) and Läbe and Förstner (2004). In addition, Yu et al. (2014), Podbreznik and Potočnik (2012), Smith and Cope (2010) and Mitishita et al. (2009) have shown that ambient temperature changes greatly influence the IOP of webcams, digital single-lens reflex (DSLR) cameras and bridge cameras resulting in image shifts and zooming effects. However, there is still a knowledge gap regarding the relationship between changing temperatures and the interior geometry of low-cost cameras based on the micro-electro-mechanical system (MEMS) technology built in smartphones or used as RPi cameras. Information is missing about error quantities that must be expected when these cameras are considered for measuring purposes. The cameras use smallest sensors (diagonals much smaller than 1 cm) resulting in small pixels with a size of about 1 μm . They are equipped with simple, focusable lenses with fixed focal lengths of a few millimetres. The sensors are glued to the sensor plate to achieve small device sizes. As stated by Wang et al. (2014), "the performance of a MEMS device can be strongly affected by thermal stresses resulting from constraining interactions among device's multiple layers and between the package and the device". Referring to the camera design, changes of the camera temperature may have strong impact on the camera geometry stability and thus on the measurement accuracies compared to e.g., DSLR cameras. With regard to water-level monitoring applications described by Elias et al. (2019) and Eltner et al. (2018), deviations in the IOP will cause errors in the translation of 2D water lines measured in images to 3D object space. These errors range from a few millimetres to several centimetres depending on the camera-to-object distance. Apart from measurement applications provided for environmental monitoring, temperature-induced variations of the camera geometry are considerable issues in, e.g., machine vision (Yu et al., 2014; Podbreznik and Potočnik, 2012), automotive (Marita et al., 2006) or medicine (Handel, 2008a).

This study provides a comprehensive investigation to examine the impact of self-heating and ambient temperature changes with regards to the interior camera geometry to further assess possible measurement errors. Self-heating impacts are expected for smartphones where the camera is firmly integrated close to components emitting heat such as the battery, the display or the Central Processing Unit (CPU). Uncoupled low-cost cameras, e.g., RPi cameras, are assumed to be less affected by self-heating effects. Due to their potential for outdoor monitoring applications (Kröhnert and Eltner, 2018), they might be exposed to ambient temperature changes that can range from strong heat due to direct solar radiation to strong cold due to icing or snow.

In previous work, Handel (2007) and Handel (2008a) made extensive investigations on camera warming effects on image acquisition. The authors provide different approaches to correct image drifts resulting from self-heating and ambient temperature changes. In this respect, they consider two types of cameras. Firstly, cameras with interchangeable lenses, where the projection center is independent from the sensor and thermal expansion affects only the sensor plane. Secondly, cameras with directly mounted lens and sensor board, e.g., mobile phone cameras, where thermal expansion affects both, the image plane and the projection center. In the latter case, Handel (2008a) and Handel (2008b) suggest that image drifts are only related to changes of the camera position and orientation, i.e., the exterior orientation parameters (EOP). However, in this study it is assumed that especially the IOP of low-cost cameras are prone to temperature variation due to the camera design. Thus, this study explains on the example of two smartphone cameras and one RPi camera, how to use single-image camera calibration based on spatial resection to observe the IOP while the investigated camera is exposed to temperature changes. Furthermore, Monte-Carlo simulations are used, considering the changed IOP due to temperature variations, to estimate the effect of errors on image measurements transferred into object space.

7.2 Hardware

The primary built-in cameras of the smartphones LG Google Nexus 5 and Samsung Galaxy S8 were used to investigate temperature changes on the IOP stability due to self-heating, and the original RPi camera module v2.1 with a fixed focal length of 3 mm was used to evaluate the impact of ambient temperature fluctuations (detailed device specifications are given in Table 7.1).

The reason why the cameras of two smartphones were investigated are their device characteristics affecting the temperature inside the smartphone housing and thus the camera temperature. First, Nexus devices use plain Android operation systems in contrast to other manufactures who implement own user interfaces or background services resulting in higher processor load and higher heat emission. Secondly, Samsung's Galaxy S8 is used representative for smartphones with built-in cooling systems. It is highly likely that the heatpipe-cooling system has significant influence on the camera temperature. In short, thermal energy is absorbed from sources emitting heat, e.g., the CPU, and transferred to lower temperature ends. In this case, these temperature ends are close to the camera sensor. Furthermore, the cases of both devices are completely different, which influences heat dissipation (Nexus 5: plastic back and frame (GSMArena, 2020); Galaxy S8: glass back, aluminium frame (Corning Inc., 2020)). In summary, it is assumed that the cameras of both devices will react differently to self-heating-induced temperature changes.

Table (7.1): Device information and camera specifications (DeviceSpecifications, 2020; Raspberry Pi, 2020). Picture of Sony IMX333 Exmor RS by iFixit (2020). Abbreviations: Complementary metal-oxide-semiconductor (CMOS), Megapixel (MP).

	LG Google Nexus 5	Samsung Galaxy S8	RPi Camera v2.1
Release	October 2013	March 2017	2016
Operation system	Android 6.0.1	Android 8.0	(-)
Camera specifications			
			
CMOS Sensor	Sony IMX179 Exmor R	Sony IMX333 Exmor RS	Sony IMX219PQ
Sensor size	4.6 mm × 3.5 mm	5.6 mm × 4.2 mm	3.7 mm × 2.8 mm
Total pixels	3288 × 2512 (8.26 MP)	-	3296 × 2512 (8.28 MP)
Active pixels	3264 × 2448 (7.99 MP)	4032 × 3024 (12.2 MP)	3280 × 2464 (8.08 MP)
Pixel size	1.40 μm × 1.40 μm	1.40 μm × 1.40 μm	1.12 μm × 1.12 μm
Focal length	3.97 mm	4.25 mm	3.0 mm

7.2.1 Smartphone camera application

In the following experiments, an in-house smartphone camera application was used, which is based on the framework Open Camera 1.3.8 (Harman, 2020), providing full control over the camera. Options were implemented to disable autofocus and to fix the focus at a defined distance using the Android camera API 2 (Google, 2020a). The application further enables the activation of several sensors to increase the workload, which results in self-heating of the smartphone. During image acquisition the battery and the CPU temperature are recorded. Background tasks that are unrelated to the measurements are cancelled.

7.3 Methods and algorithms

7.3.1 Single-image camera calibration

A method was developed to monitor the IOP continuously while the investigated device is exposed to temperature changes to study camera stabilities during heating and cooling. Photogrammetric camera calibration allows to determine the camera parameters using a single image of a 3D test field with a large number of targets with known reference coordinates. Taking serial images of the 3D test field permits nearly continuous determination of the camera parameters during ambient temperature changes.

IOP Estimation

The photogrammetric calibration strategies imply the determination of the IOP, thereby solving a non-linear equation system of collinearity equations, which describe the transformation of a 3D object point into a 2D image point (see Figure 7.1).

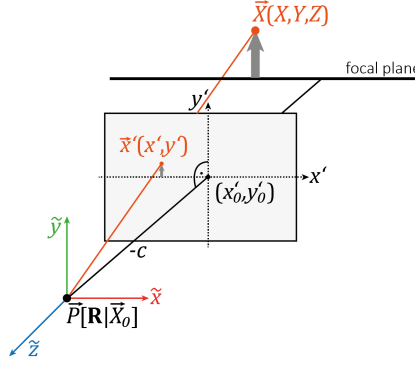


Figure (7.1): Transformation of a 3D object point \vec{X} into a 2D image point \vec{x}' where $\vec{P}[\mathbf{R}|\vec{X}_0]$ is the camera projection center in a world coordinate system.

This transformation is described with:

$$\begin{pmatrix} \tilde{x} \\ \tilde{y} \\ \tilde{z} \end{pmatrix} = \mathbf{R}^T (\vec{X} - \vec{X}_0) \quad (7.1)$$

where $\vec{X} = (X, Y, Z)^T$ is a 3D object point in the world reference system that is transformed into the camera coordinate system $(\tilde{x}, \tilde{y}, \tilde{z})$ utilizing the EOP given by a 3×3 rotation matrix $\mathbf{R}^T (r_{i,j} \in \mathbf{R}^T)$ and a 3D translation vector $\vec{X}_0 = (X_0, Y_0, Z_0)^T$ to the camera projection centre in object space. The 2D image coordinates can be derived in the camera coordinate system with:

$$x'' = \frac{\tilde{x}}{\tilde{z}}; y'' = \frac{\tilde{y}}{\tilde{z}} \quad (7.2)$$

$$x' = x_0' - c \cdot x'' \quad (7.3)$$

$$y' = y_0' - c \cdot y'' \quad (7.4)$$

where $\vec{x}' = (x', y')^T$ are coordinates of the 2D image point and c, x_0', y_0' are IOP with the principal distance c , where $-c = z'$, and the principal point x_0', y_0' . Usually, camera lenses are influenced by lens distortion that has to be considered in the point-to-point transformation. Lens correction terms $\Delta x'_{rad}, \Delta y'_{rad}$ (radial lens distortion) and $\Delta x'_{dec}, \Delta y'_{dec}$ (decentering lens distortion) are added to the 2D image coordinates, which are adapted from Browns standard camera model (Brown, 1971):

$$x' = x_0' - c \cdot (x'' + \Delta x') \quad (7.5)$$

$$y' = y_0' - c \cdot (y'' + \Delta y') \quad (7.6)$$

with:

$$\Delta x' = \Delta x'_{rad} + \Delta x'_{dec} \quad (7.7)$$

$$\Delta y' = \Delta y'_{rad} + \Delta y'_{dec} \quad (7.8)$$

and:

$$r^2 = x''^2 + y''^2 \quad (7.9)$$

$$\Delta x'_{rad} = x'' \cdot (a_1 \cdot r^2 + a_2 \cdot r^4 + a_3 \cdot r^6) \quad (7.10)$$

$$\Delta y'_{rad} = y'' \cdot (a_1 \cdot r^2 + a_2 \cdot r^4 + a_3 \cdot r^6) \quad (7.11)$$

$$\Delta x'_{dec} = b_1 \cdot (r^2 + 2 \cdot x''^2) + 2 \cdot b_2 \cdot x'' \cdot y'' \quad (7.12)$$

$$\Delta y'_{dec} = b_2 \cdot (r^2 + 2 \cdot y''^2) + 2 \cdot b_1 \cdot x'' \cdot y'' \quad (7.13)$$

The resulting equations are commonly known as collinearity equations (Kraus, 1993) extended by lens correction terms (Luhmann et al., 2013b):

$$x' = x'_0 - c \cdot \left(\frac{r_{11} \cdot (X - X_0) + r_{21} \cdot (Y - Y_0) + r_{31} \cdot (Z - Z_0)}{r_{13} \cdot (X - X_0) + r_{23} \cdot (Y - Y_0) + r_{33} \cdot (Z - Z_0)} + \Delta x' \right) \quad (7.14)$$

$$y' = y'_0 - c \cdot \left(\frac{r_{12} \cdot (X - X_0) + r_{22} \cdot (Y - Y_0) + r_{32} \cdot (Z - Z_0)}{r_{13} \cdot (X - X_0) + r_{23} \cdot (Y - Y_0) + r_{33} \cdot (Z - Z_0)} + \Delta y' \right) \quad (7.15)$$

The unknown camera parameters are derived solving a overdetermined non-linear collinearity equation system considering least-squares adjustment based on spatial resection. The solution of this equation system requires initial estimates of the camera parameters as well as of image observations of known 3D object points (also known as reference points). The determination of six EOP parameters ($X_0, Y_0, Z_0, \omega, \phi, \kappa$), where ω, ϕ, κ are 3-axis Euler rotation angles that can be expressed by rotation matrix \mathbf{R}^T , and eight IOP ($c, x'_0, y'_0, a_1, a_2, a_3, b_1, b_2$) requires at least seven 3D reference points that provide 14 observations, i.e., the measured image coordinates (x', y'). To avoid singularities, the reference points have to be spatially distributed, i.e., they cannot lie in one plane. Furthermore, the reference points and the projection centre must not be located on a danger surface, e.g., a cylinder (Luhmann et al., 2013b). Spatial point distribution is also necessary if the lens distortion has to be described because this requires format-filling image observations. The quality of spatial resection is assessed calculating the standard deviation of the unit weight \hat{s}_0 , which represents the accuracy of the image measurements. Moreover, the individual standard deviation of each investigated parameter \hat{s}_k as well as information about the correlation between the parameters are derived from the corresponding variance-covariance matrix (e.g., Förstner and Wrobel (2016)).

Single-image camera calibration permits the continuous investigation of camera parameters but impedes the direct differentiation into camera-internal and camera-external variations due to correlations between the IOP and EOP. Thus, changes in the exterior geometry (related to housing deformations) will be reflected in the IOP as well as changes in the interior geometry (related to sensor-to-lens deformations) will be reflected in the EOP. As can be taken from the literature, correlations are mainly found between the depth direction and the principal distance $t_z \Leftrightarrow c$ as well as the principal point and the EOP $x'_0, y'_0 \Leftrightarrow t_x, t_y, t_z, \omega, \phi, \kappa$ (Luhmann et al., 2013b; Godding, 1999). Exemplary for this, Yu et al. (2014) point out in their study on temperature-related image shifts that the principle point and the translation parameters t_x, t_y show similar motion patterns, which is mainly related to correlations between the involved parameters. For that reasons, one should be cautious with conclusions about the origin of camera effects in interpreting changes of the camera model. In the following experiments, the EOP were fixed to avoid superimposing relative changes of the continuously estimated IOP, e.g., due to residual errors of the EOP or correlations between IOP and EOP.

Designing the 3D Test Field

The 3D test field consists of 60 spatially distributed, partially coded markers, including four "out-of-the-plane" reference points in different depths (see Figure 7.2¹). The test field itself was calibrated via camera self-calibration prior to the experiments following the calibration scheme given by Godding (1999). The image data required for this was captured with the DSLR camera Nikon D700 (28 mm fixed focal length) and processed with the photogrammetry software AICON 3D Studio v12.0 resulting in 3D reference point coordinates, which were determined with mean standard deviations of 7.8, 7.9 and 15.2 μm in x-,y- and z-direction, respectively. The image measurement accuracy, given by \hat{s}_0 , amounts to 7.6 μm .

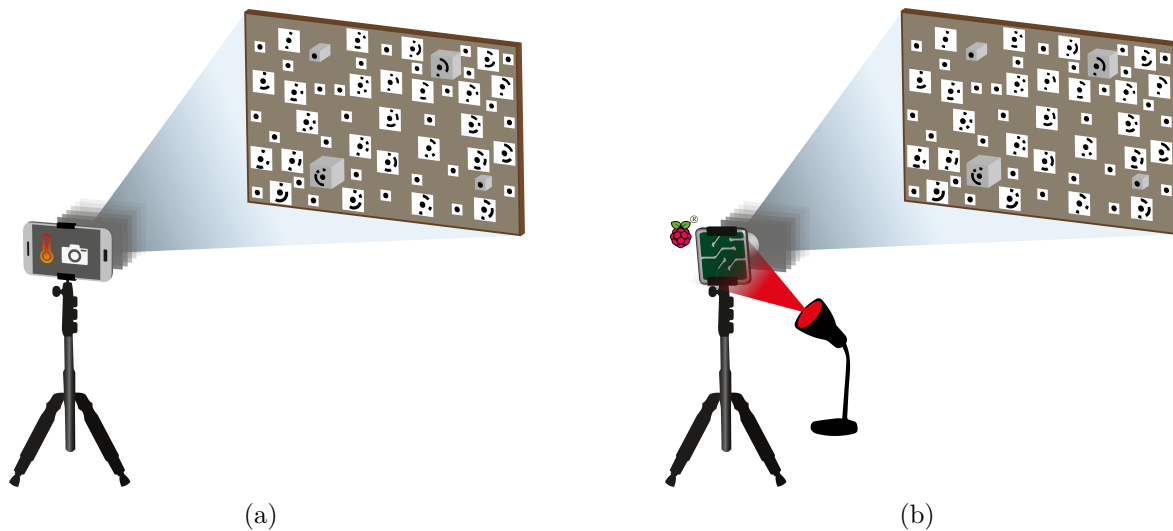


Figure (7.2): Measurement setup to investigate the relation between the IOP and temperature variations occurring from (a) self-heating and (b) ambient temperature variations using smartphone cameras and low-cost RPi cameras, respectively. Camera-to-object distance: about 90 cm. Test field dimensions: 70 \times 50 cm, Marker diameter: 10 mm.

Data Acquisition and Processing

At the beginning of each experiment, the investigated camera was fixed in a stable position with a temperature invariant mount. For that purpose, a carbon tripod was combined with a smartphone camera mount that fixed the device from all sides according to the device frame. A gauge stand with insulated holders and clamps was used to fix the RPi camera in front of the test field. Once the camera was mounted, it was manually focussed looking straight at the test field with a format-filling image configuration. The focus was not changed by the operator during one measurement series. Spatial resection was used to determine both, the IOP and the EOP using approximations for the IOP whose determination is trivial (principal distance $c \approx$ nominal focal length, principal point $x_0', y_0' \approx 0$, radial distortion $a_1, a_2, a_3 \approx 0$, decentring distortion $b_1, b_2 \approx 0$ (Luhmann et al., 2013b)). Parameters for the EOP were determined within the calibration of the test field. The behaviour of the camera parameters was now observed using images of the 3D test field for spatial resection, which were taken in a sequence with an interval of ten seconds while the observed camera was exposed to temperature changes. In this way, the IOP as well as the stochastic models were determined according to the number of images while the EOP were fixed after the first measurement.

¹Correction of the image reference in the original paper

The required reference points were measured within the calibration images using a subpixel accuracy image point measurement tool implemented in AICON 3D Studio v12.0.

Smartphone self-heating was caused by the implemented camera application as described in Section 7.2.1 whereas ambient temperature changes were provoked externally by alternating the radiation intensity of a thermal infrared lamp (which was turned on and off for approximately ten minutes) pointed at the RPi camera. To quantify changing temperatures, the smartphone CPU temperature was logged each time an image was captured, and a temperature sensor DHT 11 was installed at the back of the RPi camera, which was connected to a RPi computer that triggered the camera and requested the temperature each time an image was shot. The experimental setup is visualised in Figure 7.2 for both heating sources.

The relation between the IOP of each camera and the temperature change was investigated with at least two consecutive measurement series M1 and M2 in different scenarios for each device keeping the same camera geometry. For the smartphone cameras eight measurements were made in total, two series each for cold- and warm start-ups of the two devices. During the cold start-up image acquisition starts immediately after switching on the device, and during the warm start-up data capture starts shortly after a warm-up period. These two different approaches have a strong impact on the initial device temperature and thus the temperature amplitude during device heating. Each smartphone camera took 150 images during self-heating of the device. The RPi camera took 250 images, while it was alternately heated and cooled using the infrared lamp. Thereby, the lamp was left turned on until temperature was not changing anymore (at a temperature of about 60 °C). Afterwards, the lamp was turned off until temperature did not change again (25–30 °C). The IOP were determined for each image of the entire sequence via spatial resection.

7.3.2 Simulating the impact of differently changing IOP at measurements in 3D object space

If changes of the camera geometry occur due to temperature changes, it is important to estimate the impact at measurements in 3D object space (Al-Durgham et al., 2018; Lichti et al., 2009; Habib and Morgan, 2005). The Monte-Carlo simulation was used to evaluate how different changes of the camera geometry affect errors in object space. Especially, Monte-Carlo simulation allows to consider the complex interaction between the individual IOP and temperature in relation to the accuracy of image-based measurements transferred into 3D object space. Therefore, sets of k ($k \in \mathbb{N}$) parameters, reflecting the IOP, are randomly generated n -times ($n \in \mathbb{N}$) considering residuals and mathematical correlations, to project n regular grids of image points onto a virtual object plane in 3D object space. As indicated by Al-Durgham et al. (2018) and Habib and Morgan (2005), IOP-related variations in object space are highly correlated with the reference object that is used for intersection and "should be as close as possible to the expected object products of the photogrammetric application of interest" (Al-Durgham et al., 2018). If this is not considered, more degrees of freedom related to the object scene are introduced that might mitigate or intensify IOP-related variations due to depth variations of the reference object. In this study, the focus is not at one specific application. Therefore, the usage of a plane is the most general way to provide information about the point scattering even if the depth component cannot be considered. Details about the implementation are provided in Appendix 7.A allowing for an application-specific adaptation of the simulation.

In this case, 50.000 multivariate random vectors $\vec{X}_k(c, x_0', y_0', a_1, a_2, a_3, b_1, b_2)$ are considered when a raster of nine image points is projected onto a virtual object plane at a depth, i.e., camera-to-object distance, of $Z=10$ m. The image rays intersect the object plane in a defined distance. Thereby, iteratively changing camera geometries cause shifts in the virtual object plane leading to scattered intersection points. The error magnitudes of the projected points in object space are defined by the principal standard deviations in X - and Y -direction as well as the maximum and mean distances of the scattered object points to the projected object points of a camera with error-free IOP (see Appendix 7.A).

7.4 Results and discussion

The subsequent section investigates how changing temperature affects the IOP separated in self-heating and ambient temperature impacts. The obtained knowledge is used to simulate temperature-related changes of the camera parameters in order to assess the error metric in object space.

7.4.1 Self-heating temperature impacts at smartphone cameras

Cold-started and warm-started cameras are considered as two individual cameras to be investigated. Table 7.2 shows the deviations between the last and the first estimated variables after 150 measurements (25 min of heating), respectively for each investigated camera and two measurement periods M1, M2. In Figure 7.3, the difference of the estimated IOP to the expected parameters, corresponding to the initial values when the cameras were not affected by temperature variations, are visualised. In addition to this, the differences of the standard deviation of the unit weight $\Delta\hat{s}_0$ are visualised that indicate possible changes of the measurement accuracy.

All smartphone experiments reveal that the higher the rise in temperature, the more the principal point (x_0', y_0') is shifting and the more the principal distance c is increasing. These effects are also visible in Table 7.3, where the image content seems to move although the camera device, i.e., the smartphone, was fixed. Figure 7.4 confirms the changes in the principal distance and the principal point resulting in directional zooming effects. Similar observations were made by Yu et al. (2014). Focussing on the different camera types, the principle point of the LG Google Nexus 5 camera moves to the lower right, whereas the principle point of the Samsung Galaxy S8 camera moves to the upper left. This may be related to the mounting direction of the built-in camera sensors that may be rotated by 180° . Having cold started cameras with a strong increase of the device temperature, the changes in the IOP are significantly higher compared to warm started cameras. The principle point of the Samsung Galaxy S8 camera is changing nearly twice as much as the principle point of the LG Google Nexus 5 camera (about 40 vs. 16 pixels in terms of cold started cameras and 11 vs. 8 pixels in terms of warm started cameras). It is highly likely that this is related to the greater temperature increases of the Samsung device compared to the Google Nexus smartphone that was already expected from the different hardware designs. This finding would support the assumption of housing deformations affecting the exterior orientation of the camera module and/or internal camera deformations due to different kinds of heat dissipation.

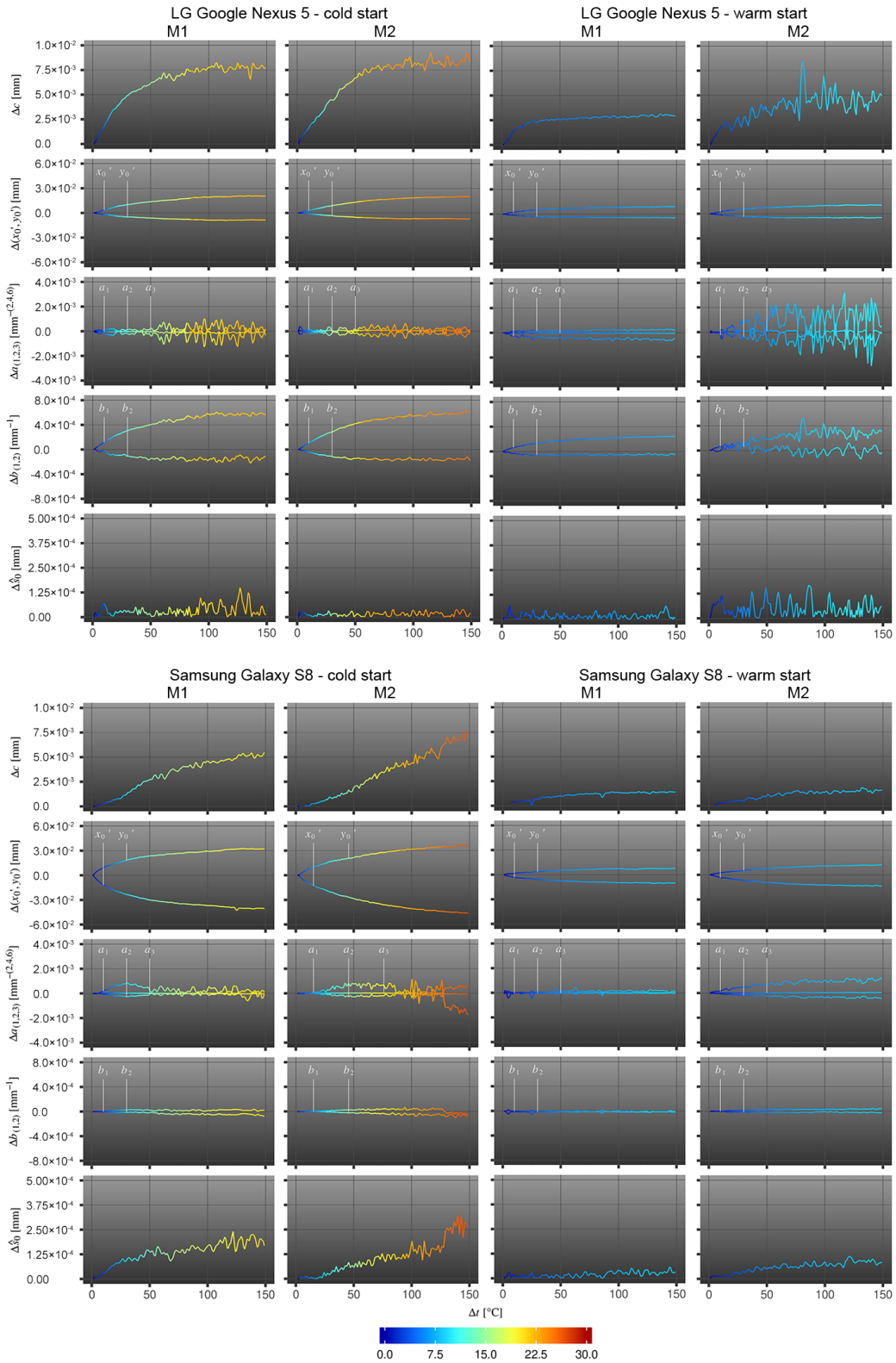
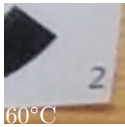
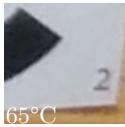
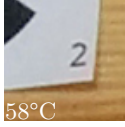
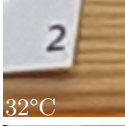
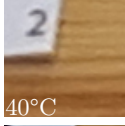


Figure (7.3): IOP-to-temperature assessment; x-axis: number of measurements per measurement series M1/M2; y-axis: estimated deviation per parameter Δk compared to the respective initial value; color-code: temperature difference Δt (measured at the battery) to the initial temperature value when the phone was started.

Table (7.2): Changes in the IOP of the built-in smartphone cameras from LG Google Nexus 5 and Samsung Galaxy S8 between the last and first estimated variables. Δt_{cpu} and Δt_{batt} are the deviations between the temperatures of the device measured at the CPU and the battery, respectively. Δk are the deviations of the estimated IOP.

	LG Google Nexus 5, Cold Started		LG Google Nexus 5, Warm Started		Samsung Galaxy S8, Cold Started		Samsung Galaxy S8, Warm Started	
	M1	M2	M1	M2	M1	M2	M1	M2
$\Delta t_{cpu}/\Delta t_{batt} [^{\circ}\text{C}]$	23.1/22.9	23.6/25.0	9.9/7.9	13.4/9.9	21.9/21.3	25.9/26.9	8.1/8.6	8.1/8.6
$\Delta c [mm]$	0.0078	0.0082	0.0028	0.0045	0.0055	0.0075	0.0014	0.0018
[Px]	5.60	5.85	2.03	3.19	3.95	5.37	1.00	1.27
$\Delta x'_0 [mm]$	0.0205	0.0200	0.0092	0.0102	-0.0408	-0.0460	-0.0105	-0.0138
[Px]	14.62	14.32	6.56	7.28	-29.17	-32.87	-7.48	-9.87
$\Delta y'_0 [mm]$	-0.0085	-0.0071	-0.0041	-0.0045	0.0328	0.0367	0.0077	0.0118
[Px]	-6.11	-5.11	-2.96	-3.19	23.46	26.22	5.53	8.41
$\Delta a_1 [mm^{-2}]$	-5.7×10^{-4}	-5.3×10^{-4}	-5.0×10^{-4}	-3.8×10^{-4}	-1.6×10^{-4}	-9.8×10^{-4}	-4.2×10^{-4}	-8.4×10^{-4}
$\Delta a_2 [mm^{-4}]$	-3.6×10^{-4}	-4.1×10^{-4}	-2.4×10^{-4}	-1.2×10^{-4}	-1.4×10^{-4}	-2.8×10^{-4}	-1.1×10^{-4}	-2.5×10^{-4}
$\Delta a_3 [mm^{-6}]$	-7.2×10^{-5}	-7.3×10^{-5}	-3.6×10^{-5}	-4.9×10^{-5}	-2.0×10^{-5}	-2.0×10^{-5}	-9.1×10^{-6}	-2.2×10^{-5}
$\Delta b_1 [mm^{-1}]$	-5.9×10^{-4}	-5.8×10^{-4}	-2.5×10^{-4}	-2.7×10^{-4}	-6.9×10^{-6}	-6.7×10^{-5}	-2.6×10^{-5}	-4.8×10^{-5}
$\Delta b_2 [mm^{-1}]$	-1.1×10^{-4}	-1.6×10^{-4}	-2.9×10^{-5}	-6.4×10^{-5}	-6.0×10^{-5}	-5.0×10^{-5}	-2.1×10^{-5}	-3.3×10^{-5}
$\Delta \hat{s}_0 [mm]$	-2.7×10^{-5}	-1.8×10^{-5}	-3.6×10^{-5}	-2.7×10^{-5}	-1.7×10^{-4}	-3.0×10^{-4}	-8.0×10^{-5}	-1.2×10^{-6}
[Px]	0.02	0.01	-0.03	0.02	0.12	0.21	0.06	0.00

Table (7.3): Extracts from a subset of images of measurement series M1 with temperature overlay (measured at the battery). All extracts were sampled at the same image position. They reveal temperature-induced camera sensor movements and out of focus appearances due to changing temperatures.

Measurement m	1	25	50	75	100	125	150
LG Google Nexus 5, cold start							
LG Google Nexus 5, warm start							
Samsung Galaxy S8, cold start							
Samsung Galaxy S8, warm start							

The extent to which the principal distance c is changing is influenced by the magnitude of temperature change and shows similar results for both tested cameras (average deviation is about 0.007 mm at cold start and 0.003 mm at warm start). This would mean a depth of field variation of 5 mm and 3 mm (Nexus/ S8) for cold started- and 3 mm and 2 mm (Nexus/S8) for warm started devices assuming a camera whose focus distance was set to 1 m. These changes in the captured images lead to decreasing image point measurement quality,

which becomes obvious by the increasing noise reflected in the standard deviations $\hat{\sigma}_0$ and in the measurements of especially the principal distance and the radial lens distortion in the later measurements. It can be observed that the IOP changes towards an equilibrium, which was also observed by e.g., Robson et al. (2016), Yu et al. (2014) and Handel (2008a), when smartphones are protected against overheating by reducing the CPU load. Moreover, the camera parameters and the temperature reveal a linear relationship that is further investigated in Section 7.4.3.

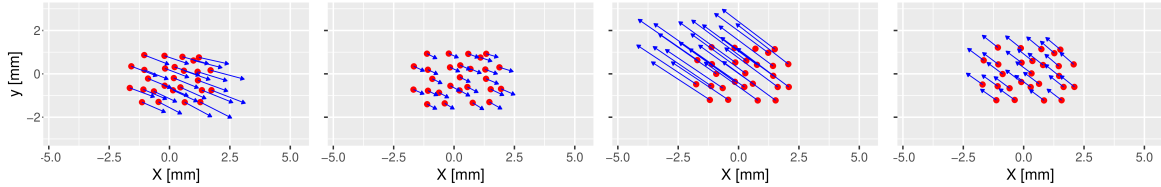


Figure (7.4): Visualisation of image point shifts and zooming effects between the first (red dots) and the last (heads of the blue arrows) measurement within measurement series M1 respectively for (from left to right) the LG Google Nexus 5 camera (cold-started, warm-started) and for the Samsung Galaxy S8 camera (cold-started, warm started). The arrow length is superimposed by a factor of 50.

Considering the increase of measurement uncertainties, it is important to evaluate if the estimated IOP-variations are significant. For that purpose, temperature-related two-sided moving variances s_k^2 are calculated over n_1 consecutive measurements for each investigated camera parameter k . They are compared to the two-sided moving averages of n_2 squared standard deviations \hat{s}_k^2 of each investigated camera parameter k (see Section 7.3.1) via f-test to examine if s_k^2 is significantly greater than \hat{s}_k^2 . Usually, f-test requires measurements with a normal distribution, but a large sample size ($n > 30$) can excuse violations of the normality assumption according to Ghasemi and Zahediasl (2012). The size of the moving window was set to $n_{1,2} = 51$. The test parameters are given in Table 7.4 assuming a significance level of $\alpha = 0.05$.

Table (7.4): F-test parameters.

Null Hypothesis	Alternative Hypothesis	Test Statistic	Critic f-Value	Rejection Criteria
$H_0 : \sigma_1^2 \leq \sigma_2^2$	$H_1 : \sigma_1^2 > \sigma_2^2$	$Q = \frac{s_x^2}{s_y^2} (s_x^2 > s_y^2)$	$f_{n_x-1, n_y-1, 1-\alpha}$	$Q > f$

The f-test was performed for each time stamp of one measurement series (provided that the moving variance could be calculated over $n_1 = n_2$ measurements) summarising the number of success. Success means that the null hypothesis could be rejected, i.e., the temperature-related variances are significantly greater than the measurement uncertainties and thus significant. The success ratios $\zeta(k)$ (number of success divided by the total number of tests) are given in Table 7.5 summarising the test results from measurement series M1 and M2, respectively.

The results indicate that variations due to temperature changes are significant with regards to individual measurement series. In a few individual measurements, where H_0 could not be rejected, measurement uncertainties are greater than temperature-related deviations. This is usually the case when the test field drifted out of the focus resulting in an insufficient estimation of the image coordinates and thus leading to higher measurement uncertainties.

Table (7.5): F-test success ratios $\zeta(k)$ to assess whether the temperature-related variance s_k^2 of parameter k is significant compared to the measurement precision \hat{s}_k^2 .

	$\zeta(c)$	$\zeta(x_0')$	$\zeta(y_0')$	$\zeta(a_1)$	$\zeta(a_2)$	$\zeta(a_3)$	$\zeta(b_1)$	$\zeta(b_2)$
LG Google Nexus 5, cold started	0.94	0.90	0.88	1.00	1.00	1.00	0.86	1.00
LG Google Nexus 5, warm started	1.00	0.71	0.85	1.00	1.00	1.00	1.00	1.00
Samsung Galaxy S8, cold started	0.87	1.00	1.00	0.81	0.71	0.72	0.50	1.00
Samsung Galaxy S8, warm started	0.96	0.89	0.86	1.00	1.00	1.00	1.00	1.00
total	0.94	0.87	0.90	0.95	0.93	0.93	0.84	1.00

7.4.2 Temperature impacts at the stability of RPi cameras

Influences of changing temperatures at the camera stability of RPi cameras are shown in Figure 7.5.

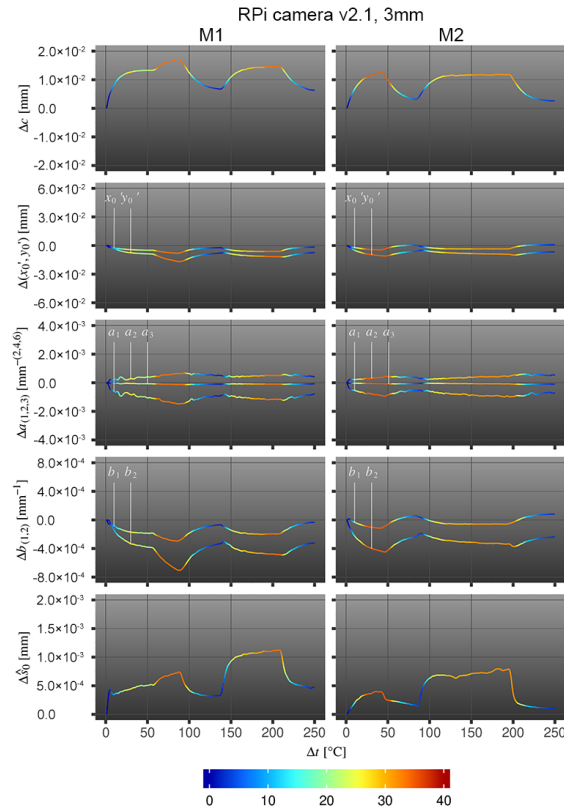


Figure (7.5): IOP-to-temperature assessment with RPi camera v2.1, which was exposed to alternating temperature, evaluating two measurement series (M1, M2); x-axis: number of measurements per measurement series; y-axis: estimated deviation per investigated parameter compared to the initial value; color-code: temperature difference Δt to the initial temperature value before the red-light radiation lamp was switched on for the first time.

The relation between the individual IOP changes due to camera exposure to heating and cooling are compared to the initial values using the same approach as for the smartphone camera Section 7.4.1. The estimated changes in the IOP of RPi camera v2.1 with 3 mm lens are highly correlated with temperature changes in both measurements, which is further examined in Section 7.4.3.

For the RPi camera module, back and forth focus shifts due to expansion and contraction of the principal distances c because of alternating temperatures are revealed. The principal point (x_0', y_0') is changing as well. When the temperature rises, the point moves into one direction (lower left) and when the temperature decreases, the point moves almost completely back along the same direction. Both can be seen in Table 7.6 and Figure 7.6; the image content moves wave-like and is out of focus when temperature rises and again in focus when temperature decreases. It is of special interest that the image points do not return to their starting position when the temperature changes to its initial state. For that purpose, some permanent changes of the camera geometry due to temperature changes must be assumed either due to changes of the relationship between sensor board and projection center or due to camera movements. Similar to the smartphone cameras, the changing interior geometry causes strong fluctuations in the image point measurement accuracies, which results in lower reliabilities of the estimated parameters when the camera is exposed to direct radiation. The influence of the temperature changes at the measurement accuracy can be seen towards the standard deviation of the unit weight \hat{s}_0 which is up to 3.5 times higher at the maximum temperature compared to the initial measurement accuracy. These conclusions are also confirmed by f-test, which was performed in the same way as for the smartphone measurements (see Section 7.4.1). The success rates $\zeta(k)$ amount to $\zeta(c) = 0.96$, $\zeta(x_0') = 0.96$, $\zeta(y_0') = 0.89$, $\zeta(a_1) = 1.00$, $\zeta(a_2) = 1.00$, $\zeta(a_3) = 1.00$, $\zeta(b_1) = 0.75$ and $\zeta(b_2) = 0.80$.

Table (7.6): Extracts from a subset of images of both measurement series M1 and M2 using the RPi camera v2.1 with a fixed focal length of 3 mm. All extracts were sampled at the same image position and superimposed with information about the prevalent temperature measured by DHT 11 sensor.

Measurement m	1	25	50	75	100	125	150	175	200	225	250
RPi camera v2.1, M1											
RPi camera v2.1, M2											

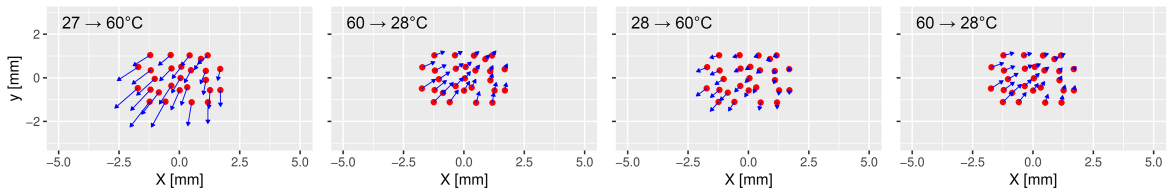


Figure (7.6): Visualisation of image point shifts and zooming effects considering the turning points between the heating and cooling phases of the RPi camera investigation M1. The arrow length is superimposed by a factor of 50.

7.4.3 Statistical evaluation of temperature dependencies

The experiments reveal a linear relationship between temperature changes and the determined IOP (see Figure 7.7). To assess the statistical relevance of the relation between temperature change and IOP stability, the Pearson correlation coefficients ρ are calculated for the estimations of the² interior orientation parameter k and the simultaneously measured temperature t .

²Correction of a word repetition in the original paper.

To estimate the significance of the correlation coefficient between independently estimated variables, t-test is applied to determine the significance levels given by the p -values (must be less than $\alpha = 0.05$).

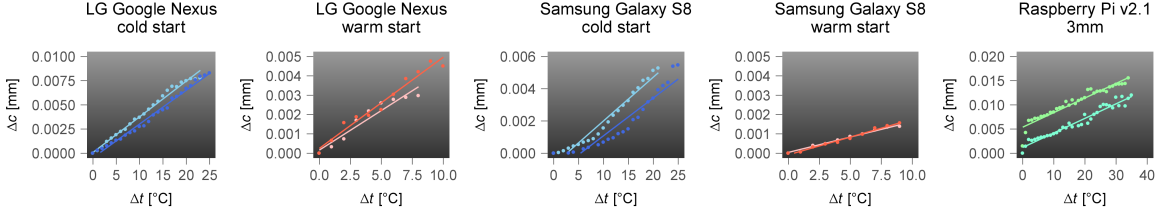


Figure (7.7): Visualisation of the linear dependencies between changing IOP and temperature on the example of principal distance c . Considering the RPi observations, the aggregated data is sorted by temperature change. Light colors refer to the respective measurement series M1 and darker colors refer to the respective measurement series M2.

A high correlation of nearly 100% between temperature and principal distance c as well as principal point (x_0', y_0') is revealed in this study (see correlation matrix in Figure 7.8). Thereby, reversed correlations of the principal point coordinates x_0' and y_0' (except for the RPi camera) close to $\rho \pm 1.0$ are noticeable. Moderate correlations between temperature and radial lens distortion parameters a_1, a_2, a_3 are observable. Furthermore, strong correlations between temperature and decentering lens distortion, described by b_1, b_2 , are noticeable for the RPi camera and the smartphone camera integrated in the LG Google Nexus 5. It is worth mentioning that the measurement accuracies \hat{s}_0 of the Samsung Galaxy S8- and the RPi measurements are highly correlated with the temperature but not the measurements made with the LG Google Nexus 5 camera. The reason can be found considering the image clips given in Table 7.3 and the parameter deviations shown in Figure 7.3. The images of LG Google Nexus 5 appear to be less effected by focus changes than the images of Samsung Galaxy S8. One reason might be that the direction of movement of the principal point of the camera of the LG Google Nexus 5 counteracts the extension of the principal distance whereas the moving direction of Samsung Galaxy S8's principal point amplifies the impact of the change of the focus (see Figure 7.4). Together with the correlation coefficients, p -values were determined which were less than the significance level $\alpha = 0.05$ in all calculations. Thus, the determined correlations are considered to be significant for all assessed parameters.

	c	x_0'	y_0'	a_1	a_2	a_3	b_1	b_2	\hat{s}_0
LG Google Nexus 5, cold start	0.98	0.99	-0.99	-0.07	0.11	-0.19	0.99	-0.88	0.08
LG Google Nexus 5, warm start	0.84	0.97	-0.93	-0.34	0.47	-0.54	0.88	-0.37	0.09
Samsung Galaxy S8, cold start	0.97	-0.99	1.00	-0.37	0.48	-0.52	0.24	-0.88	0.90
Samsung Galaxy S8, warm start	0.97	-0.99	0.99	0.75	-0.72	0.68	0.15	-0.14	0.83
RPi camera v2.1, 3mm	0.96	-0.93	-0.69	-0.66	0.03	0.03	-0.93	-0.72	0.69

Figure (7.8): Correlation between changing IOP and changing temperature given by Pearson's correlation coefficient ρ , calculated from the measurement series M1 and M2 for each camera.

Using Monte-Carlo simulations to assess temperature-related measurement errors in object space requires knowledge about the correlations between the IOP, although they are reduced as far as possible by using an adapted 3D test-field- and camera configuration. The correlations were obtained from the variance-covariance matrices, which were also calculated during camera parameter determination. The correlations between the parameters should be consistent within

the measurements of one measurement series because of a constant camera configuration. However, temperature-related measurement uncertainties resulted in noise of the correlation coefficients. The noise amounts to $\rho \pm 0.01$ using warm started smartphone cameras and the RPi camera. With regards to cold started smartphone cameras, the noise is getting bigger at the end of the measurement series when the temperature increase is at its highest. To further obtain one significant value to use in the subsequent Monte-Carlo simulations, the median values were determined considering all observations in both given series M1 and M2 (see Figure 7.9).

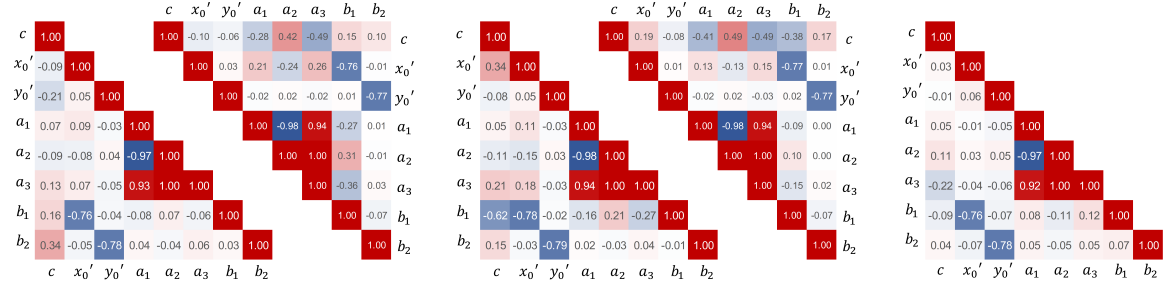


Figure (7.9): Median correlations $\bar{\rho}$ between the individual IOP determined for each camera using the observations of measurement series M1 and M2. From left to right, LG Google Nexus 5 cold-started, warm-started; Samsung Galaxy S8 cold-started, warm-started, Raspberry Pi camera v2.1.

Most parameters of the IOP are less- or completely uncorrelated. Significant correlations are reported between the parameters of the radial lens distortion ($a_1 \Leftrightarrow a_2 \Leftrightarrow a_3$) and between the principal point and the parameters of the decentering lens distortion ($x'_0, y'_0 \Leftrightarrow b_1, b_2$). As described by Luhmann et al. (2013b), these mathematical correlations are related to the principle of camera calibration and cannot be avoided. However, all estimated correlations are considered in the Monte-Carlo simulations to ensure plausible sets of IOP in agreement with temperature-induced changes.

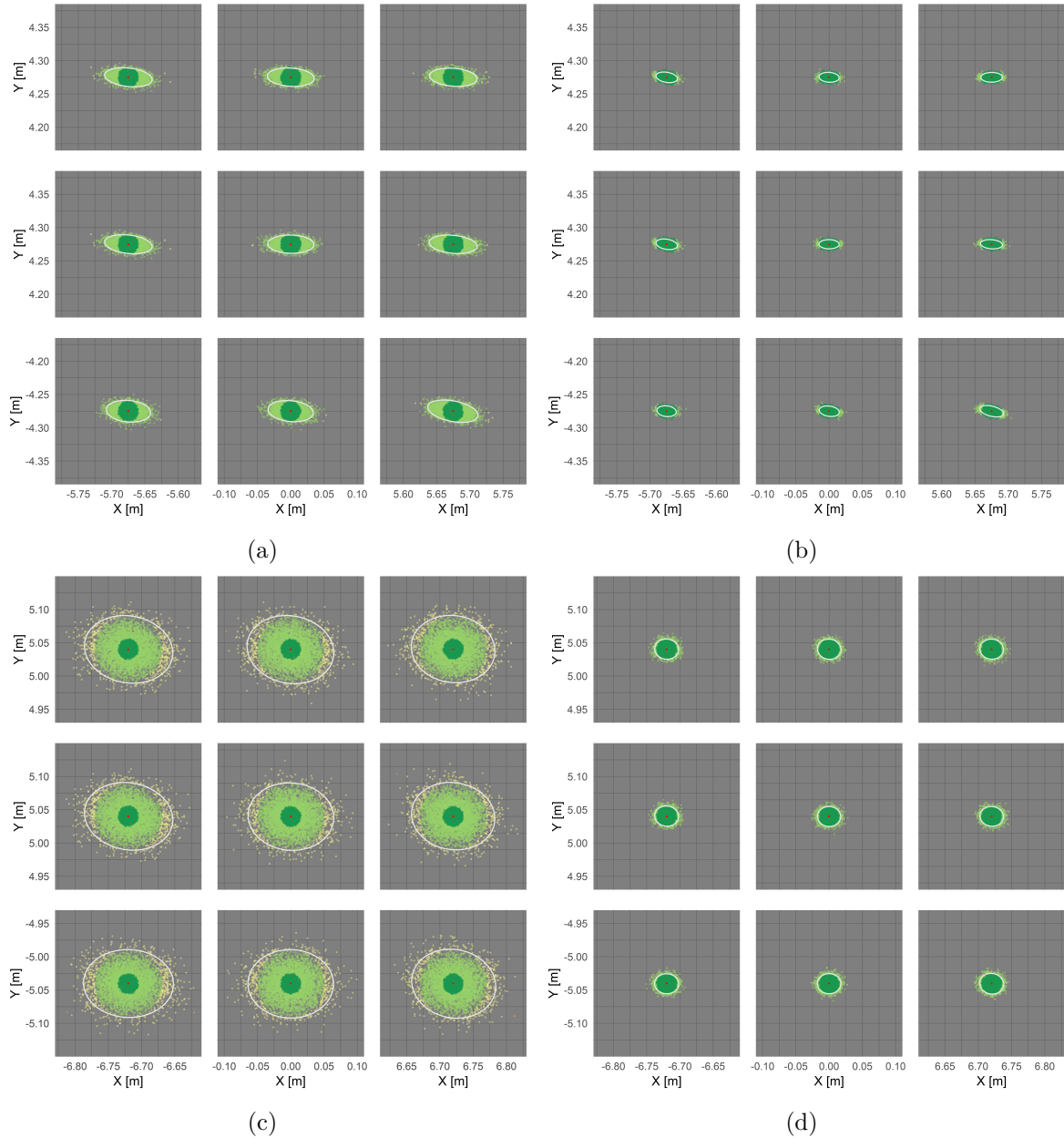
7.4.4 Temperature-related error assessment in object space: Results of Monte-Carlo simulation

Monte-Carlo simulation was applied for each investigated camera as described in Section 7.3.2, i.e., 50.000 sets of modified IOP are simulated that can result from temperature change. The simulated parameters were used to project a 3×3 raster of image points onto a virtual object plane parallel to the camera sensor in a distance of 10 m. The results are visualised in Figure 7.10 where the point color refers to the Euclidean distance $d(P_i, P_\mu)$ between the projected object point and the expected, red-coloured object point. The Euclidean distances, which are used to determine the magnitude of errors due to temperature change, were clustered in distances <1.5 cm (dark green), 1.5–5.0 cm (light green) and 5–10 cm (yellow). Errors >10 cm (pink) appeared hardly ever.

As might be expected, the individual plots of Figure 7.10 reveal that cold started smartphone cameras show significantly higher errors in the point projection than warmed up cameras. Table 7.7 gives the percentage of point projections in relation to the visualised error clusters.

Considering all 50.000 iterations, the probability of temperature-related errors less than 1.5 cm amounts to 98% and 93% using the warmed up smartphone cameras of the LG Google Nexus 5 and the Samsung Galaxy S8 smartphone. Deviations of more than 5 cm are unlikely for both

cameras. Similar results could be achieved for the RPi camera whose initial device temperature was similar to the device temperatures of the warm started smartphone cameras. Considering the cold-started smartphone cameras of LG Google Nexus 5 and Samsung Galaxy S8, only 67% and 20% of all projected points show deviations less than 1.5 cm. It has also been shown for the S8 camera that errors up to 10 cm are likely. Focussing on the extension and orientation of the deviations between the expected and the projected object point coordinates, which are visualised in Figure 7.11 by light orange s_1^* and dark orange s_2^* points, the errors show directionality for all investigated cameras. For the most cameras, the deviations are larger in X - than in Y -direction due to the greater scattering of the principal point in \tilde{x} -direction. Moreover, projected object points that originate from image points lying at the image edges and corners show higher deviations that points inside the image, which is also due to the principal distance. The changing principal distance has less impact on point projections from the image center but great impact on point projections from the image edges and corners.



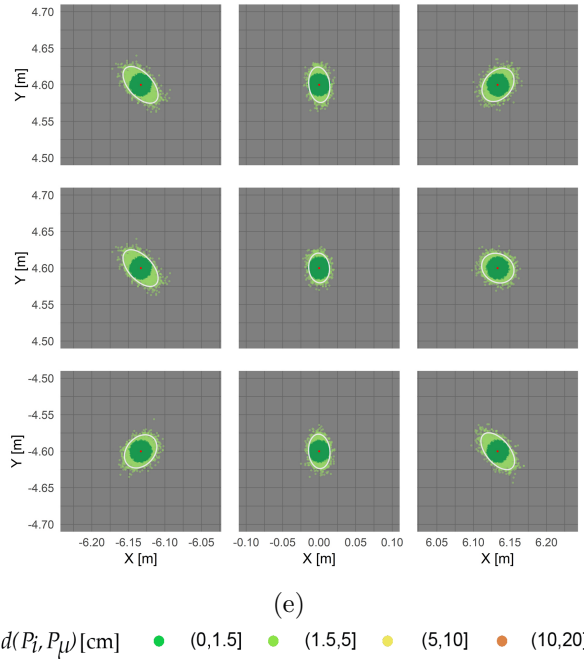


Figure (7.10): Projection of image points $p'_i(x', y')$ onto a virtual object plane in a distance of $Z = 10$ m with fixed EOP- and simulated IOP (visualisation of every 10th point $P_i(X, Y)$). LG Google Nexus 5, cold started (a) and warm started (b); Samsung Galaxy S8, cold started (c) and warm started (d) and Raspberry Pi v2.1 (e). The generated object points were coloured by means of their Euclidean distance $d(P_i, P_\mu)$ to the expected object point coordinates. The white ellipses are the confidence ellipses with 95% probability.

Table (7.7): Percentages of projected object points classified by their Euclidean distances to the expected object point coordinates. Clusters equal the classes used in Figure 7.10.

Clusters of Euclidean Distances $d(P_i, P_\mu)$ [cm]	(0,1.5]	(1.5,5]	(5,10]	(10,20]
LG Google Nexus 5, cold started	66.6	33.3	0.10	0.0
LG Google Nexus 5, warm started	98.0	2.0	0.0	0.0
Samsung Galaxy S8, cold started	19.5	69.7	10.8	0.0
Samsung Galaxy S8, warm started	92.6	7.40	0.0	0.0
RPi camera, 3 mm	79.4	20.6	0.0	0.0

This becomes visible when comparing the largest deviations given by the maximum Euclidean distances $d_{max}(P_i, P_\mu)$ (light green squares) in Figure 7.11. In relation to this, the highest deviations are shown by the cold-started smartphone cameras. Calculating the mean of the maximum deviations considering all nine projected image points (visualised in Figure 7.11 by a red dashed line) results in deviations of 6.2 cm and 12.9 cm for LG Google Nexus 5 and Samsung Galaxy S8, respectively.

In contrast, warm started smartphone cameras show deviations up to 2.9 cm and 3.5 cm and thus a reduced temperature-related error by half. Considering the RPi camera, the maximum deviations depend more on the image point position (lowest - image center, highest - upper right corner) with a mean of 4.5 cm. The mean of the Euclidean distances $\bar{d}(P_i, P_\mu)$ between the coordinates of the projected image points in object space and the expected coordinates of the respective object points are visualised Figure 7.11 with dark green triangles.

To give a final magnitude of errors to be expected when the camera is exposed to changing temperature, the mean of all Euclidean distances of each projected point per investigated camera was determined (independently from the original image point position on the camera sensor). An error magnitude of 1.3 cm (cold start) and 0.6 cm (warm start) was determined for the investigated LG Google Nexus 5 camera. Furthermore, an error magnitude of about 3.0 cm (cold start) and 0.8 cm (warm start) was investigated for the applied Samsung Galaxy S8 camera. Finally, an average error of 1.1 cm was established for the used RPi camera v2.1 with a fixed focal length of 3 mm that was exposed to ambient temperature changes. Overall, the temperature-related error clearly depends on the used camera model and its construction and can be significantly reduced using warmed up devices (considering smartphone cameras). The average temperature-related measurement error that should be expected using (warmed up) cameras as measurement devices is between 1 cm and 2 cm in a camera-to-object distance of 10 m.

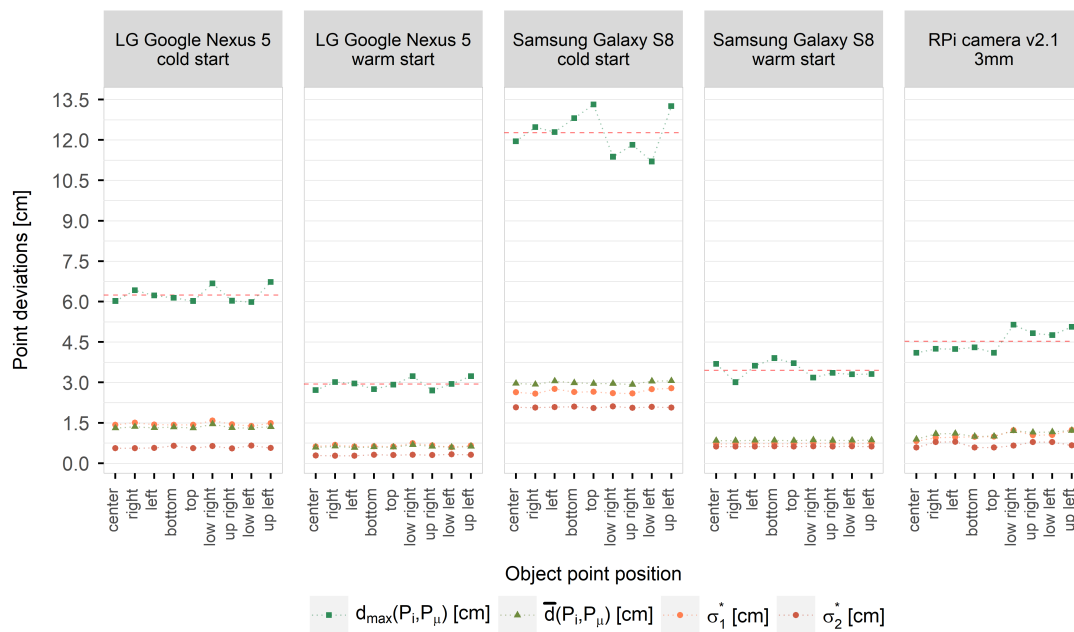


Figure (7.11): Principal standard deviations s_1^* and s_2^* giving the directional error in object space for each projected object point and for each investigated camera.

7.5 Conclusions

In this study, three cameras (two built in smartphones and one external RPi module) were investigated to evaluate dependencies between temperature changes resulting from self-heating or changes in the ambient temperature and the IOP. Each observed camera was installed in front of a 3D calibration test field taking serial images while the camera was exposed to temperature change. Each image was processed via spatial resection to estimate the IOP focal length, principal point, radial lens distortion and decentering lens distortion. For the smartphone cameras, which were affected by smartphone self-heating, a strong dependency between the magnitude of temperature change and the magnitude of variations of the IOP was detected. This finding was supported by visual assessment of the calibration images, which became unfocused due to changes in the principal distances and the principal points. This effect complicated the image measurements because blurry images lead to less accurate point

measurements, which was reflected in higher standard deviations of the IOP. Although the parameters reveal a linear correlation with the temperature, the rate of parameter changes is slightly different in each measurement series and for each camera, which complicates the modelling of temperature-related changes. Unfortunately, the construction of smartphone camera modules as well as their integration into smartphone bodies impedes definite statements about the physical integrity of the camera geometry. Changes in the IOP are likely due to changes of the camera module itself, such as temperature-induced tilting of the sensor plane and the projection center, or due to changes in camera's exterior orientation due to housing deformations. Also for the RPi camera module a dependency between temperature and IOP became obvious with a strong increase of the standard deviation $\hat{\sigma}_0$ when temperatures reached extreme values, e.g., high temperature decrease or high temperature increase. This results in both, alternating image shifts and zooming effects due to changes of the depth of the focus.

Cameras of different types show gradual warming effects that stagnate over a certain time (e.g., Yu et al. (2014) and Handel (2008a)), which is however not feasible in citizen science because the citizen scientists will not wait 0.5–1 h until the camera stabilises. Furthermore, smartphone temperature can change very rapidly due to varying background tasks, sensors, etc., which impedes a direct modelling of the effects of image drift. A Monte-Carlo simulation revealed that temperature-related errors between 1 cm and 2 cm at a distance of 10 m are to be expected provided that the camera is warmed up. Errors larger than 10 cm are less frequent, but should still be considered because the results of this study are rather optimistic due to the chosen reference object in form of a plane being parallel to the camera at a close distance of 10 m. Thus, it is recommended to estimate the error always in context of a specific photogrammetric application adapting the described simulation method.

In view of the above-mentioned low-cost early warning flood systems using mobile and stationary cameras, these errors should be detected and compensated in applications of long-term observations using fixed object points in river's environment to determine the prevalent camera geometry at the time of data acquisition, e.g., using image-to-geometry registration (Elias et al., 2019; Schwalbe and Maas, 2017; Kehl et al., 2017). Otherwise, image drifts can lead to false measurements of the water level, for instance considering the case that the water level increases but an image shift towards the riverbed would compensate the trend. In case of flood observation, the errors resulting from temperature-related changes in the IOP can be neglected because the reliability of water level estimation, e.g., with methods introduced by e.g., Elias et al. (2019), Lin et al. (2018) and Bruinink et al. (2015), decreases strongly due to large waves at the water surface that impede a unique detection of the shore line.

Further investigations will show whether, and if so, how to model temperature-related changes at the camera geometry, e.g., to enhance the reliability of low-cost water monitoring systems. Therefore, more iterations and more cameras of the same type would be advisable to detect trends in the parameters that can be assigned to the respective camera type. Furthermore, the calibration procedure can be improved using multi-image bundle adjustment using, for example, a robot controlled 3D test field that can be moved and rotated with known EOP. Thus, correlations between the IOP and EOP could be solved promising new insights at which effects are related to variations of the camera module and which effects are related to the camera module geometry. Moreover, experiments on ambient temperature changes should be repeated in a climate chamber providing full control on the temperature.

Author contributions

Conceptualization, M.E. and A.E.; data curation, M.E. and A.E.; formal analysis, M.E.; funding acquisition, M.E. and H.-G.M.; investigation, M.E.; methodology, M.E., A.E. and F.L.; project administration, M.E. and H.-G.M.; software, M.E. and F.L.; supervision, H.-G.M.; validation, A.E., F.L. and H.-G.M.; visualization, M.E.; writing–original draft preparation, M.E.; writing–review and editing, M.E., A.E., F.L. and H.-G.M. All authors have read and agreed to the published version of the manuscript.

Funding

This research was funded by European Social Fund (ESF) and the Free State of Saxony during the funding period 2014-2020 (grant number 100235479 and 100270097).

Acknowledgements

The authors gratefully acknowledge the Open Access Funding by the Publication Fund of TU Dresden.

Conflicts of interest

The authors declare no conflict of interest. The funders had no role in the design of the study; in the collection, analyses, or interpretation of data; in the writing of the manuscript, and in the decision to publish the results.

Abbreviations

The following abbreviations are used in this manuscript

CMOS	complementary metal-oxide-semiconductor
CPU	central processing unit
DSLR	digital single-lens reflex
EOP	exterior orientation parameters
IOP	interior orientation parameters
MEMS	micro-electro-mechanical systems
MP	megapixel
RPi	Raspberry Pi

7.A Appendix. Monte-Carlo simulation

7.A.1 General approach of the Monte-Carlo simulation

A vector of multivariate random numbers is used to simulate the IOP:

$$\vec{X}_k = \vec{\mu}_k + \mathbf{V}_k \cdot \mathbf{\Lambda}_k^{\frac{1}{2}} \cdot \vec{Z}_k \quad (7.A1)$$

where \vec{X}_k is the multivariate random vector of length k (according to the number of IOP), $\vec{\mu}_k$ is the vector of expected values and \mathbf{V}_k and $\mathbf{\Lambda}_k$ are the eigenvector- and diagonal matrix that

can be obtained from the variance-covariance matrix $\Sigma_{\mathbf{k}}$ via eigen decomposition taking into account parameter correlations:

$$\Sigma_{\mathbf{k}} = \mathbf{V}_{\mathbf{k}} \cdot \Lambda_{\mathbf{k}} \cdot \mathbf{V}_{\mathbf{k}}^T \quad (7.A2)$$

with:

$$\Sigma_{\mathbf{k}} = \begin{bmatrix} \sigma_1^2 & \sigma_1 \sigma_2 \rho_{1,2} & \cdots & \sigma_1 \sigma_k \rho_{1,k} \\ \sigma_1 \sigma_2 \rho_{1,2} & \sigma_2^2 & \cdots & \sigma_2 \sigma_k \rho_{2,k} \\ \vdots & \vdots & \ddots & \vdots \\ \sigma_1 \sigma_k \rho_{1,k} & \sigma_2 \sigma_k \rho_{2,k} & \cdots & \sigma_k^2 \end{bmatrix} \quad (7.A3)$$

where $\rho_{i,j}$ ($i, j \in k, \rho_{i,j} \in \mathbb{R}$) are the estimated correlations between parameters k and $\sigma_1, \dots, \sigma_k$ are the corresponding standard deviations. \vec{Z}_k is the vector of k independent, standard normally-distributed random numbers with:

$$\vec{Z}_k \sim N(0, \mathbf{I}_k) \quad (7.A4)$$

where \mathbf{I}_k is the identity matrix.

7.A.2 Implementing the Monte-Carlo simulation

Within the Monte-Carlo simulation $n \cdot \vec{X}_k$ multivariate random vectors with $n = 50.000$ iterations were calculated with random IOP using Equation (7.A1). Assuming a distortion-free ideal camera, the vector of expectation values $\vec{\mu}_k$ is defined by the principal distance c_m given by the manufacturer specification, the image-centred principal point with $x_0' = y_0' = 0$ and zero lens distortion:

$$\vec{\mu}_k = (c_m, 0, 0, 0, 0, 0, 0)^T \quad (7.A5)$$

The variance-covariance matrix $\Sigma_{\mathbf{k}}$ is based on the standard deviations σ_k , which are calculated from repeatedly estimated IOP of each series. Furthermore, each estimation of the IOP provides stochastic information about the correlation between the investigated IOP. $\Sigma_{\mathbf{k}}$ uses the mean correlation coefficients $\rho_{i,j}$ that are calculated from all estimations that belong to each camera. In the case of repeated measurement periods that are made successively under similar conditions, i.e., camera, setup and the parameters to be estimated remain unchanged, the standard deviations σ_k and median correlations $\rho_{i,j}$ can be combined taking their arithmetic mean (here the measurement series M1, M2 per camera).

$$\Sigma_{\mathbf{k}} = \begin{bmatrix} \sigma_c^2 & \sigma_c \sigma_{x_0'} \rho_{(c,x_0')} & \cdots & \sigma_c \sigma_{b_2} \rho_{(c,b_2)} \\ \sigma_c \sigma_{x_0'} \rho_{(c,x_0')} & \sigma_{x_0'}^2 & \cdots & \sigma_{x_0'} \sigma_{b_2} \rho_{(x_0',b_2)} \\ \vdots & \vdots & \ddots & \vdots \\ \sigma_c \sigma_{b_2} \rho_{(c,b_2)} & \sigma_{x_0'} \sigma_{b_2} \rho_{(x_0',b_2)} & \cdots & \sigma_{b_2}^2 \end{bmatrix} \quad (7.A6)$$

with:

$$\sigma_k^2 = \sum_{i=1}^n (x_{ki} - \bar{x}_k)^2 \quad \text{with } k = c, x_0', y_0', a_1, a_2, a_3, b_1, b_2 \quad (7.A7)$$

$$\rho_{k_i,j} = \frac{\sum_{l=1}^n (k_{il} - \bar{k}_i)(k_{jl} - \bar{k}_j)}{\sqrt{\sum_{l=1}^n (k_{il} - \bar{k}_i)^2 \cdot \sum_{l=1}^n (k_{jl} - \bar{k}_j)^2}} \quad (7.A8)$$

Having $n \cdot \vec{X}_k$ multivariate vectors of IOP, a regular grid of image points (x', y') is projected into object space n -times (see Section 7.3.1). The image points are located in the image centre, the image corners, and in the middle of the image plane edges. Considering the intersected virtual 3D object plane parallel to the sensor plane with a known depth, the EOP parameters can be simplified to:

$$\mathbf{R}^T = \mathbf{I}; \quad \vec{X}_0 = 0 \quad (7.A9)$$

which results in the simplified collinearity descriptions to generate ideal image coordinates (x', y') in camera's coordinate system:

$$x' = -c \cdot \frac{X}{Z}; \quad y' = -c \cdot \frac{Y}{Z} \quad (7.A10)$$

However, before the image rays are generated, the image points must be distorted considering the simulated principal point, the radial lens distortion and the decentering lens distortion (see Equations (7.5)–(7.13)). Using Equations (7.1)–(7.4), the object point coordinates (X, Y, Z) can be determined from the distorted image coordinates (x_{dist}', y_{dist}') via projective transformation for each:

$$X = \frac{Z \cdot (x_{dist}' - x_0')}{c} \quad (7.A11)$$

$$Y = \frac{Z \cdot (y_{dist}' - y_0')}{c} \quad (7.A12)$$

Then, the error metric can be determined by means of the empirical variance-covariance matrices \mathbf{s}^* that are determined for each point of the image grid transferred into object space:

$$\mathbf{\Sigma}^* = \begin{bmatrix} s_X^{*2} & s_{XY}^* \\ s_{XY}^* & s_Y^{*2} \end{bmatrix} \quad (7.A13)$$

with:

$$s_X^{*2} = \frac{1}{n} \cdot \sum_{i=1}^n (X_i - \mu_X)^2 \quad (7.A14)$$

$$s_Y^{*2} = \frac{1}{n} \cdot \sum_{i=1}^n (Y_i - \mu_Y)^2 \quad (7.A15)$$

$$s_{XY}^* = \frac{1}{n} \cdot \sum_{i=1}^n (X_i - \mu_X) \cdot (Y_i - \mu_Y) \quad (7.A16)$$

where s_X^{*2}, s_Y^{*2} are the variances of the distorted object point coordinates $P_i(X_i, Y_i)$ to the ideal, error-free object point coordinates $P_\mu(\mu_X, \mu_Y)$ and s_{XY}^* are the corresponding covariances. Performing eigenvalue decomposition of $\mathbf{\Sigma}^*$ enables the determination of the principal standard deviations s_1^*, s_2^* , which are used as quality measures:

$$\mathbf{\Sigma}^* = \mathbf{V}^* \cdot \mathbf{\Lambda}^* \cdot \mathbf{V}^{*T} = \mathbf{V}^* \cdot \begin{bmatrix} s_1^{*2} & 0 \\ 0 & s_2^{*2} \end{bmatrix} \cdot \mathbf{V}^{*T} \quad (7.A17)$$

where $\mathbf{\Lambda}^*$ represents the diagonal eigenvalue matrix and \mathbf{V}^* represents the eigenvector matrix. Also, the Euclidean distances $d(P_i, P_\mu)$ are calculated between the distorted- and the error-free object coordinates with

$$d(P_i, P_\mu) = \|P_i - P_\mu\| \quad (7.A18)$$

to quantify the accuracy using the mean and maximum distances $\bar{d}(P_i, P_\mu)$ and $d_{max}(P_i, P_\mu)$, respectively.

References

- Brown, D. C. (1971). “Close-range camera calibration”. In: *Photogrammetric Engineering* 37, 8, pp. 855–866. URL: https://www.asprs.org/wp-content/uploads/pers/1971journal/aug/1971_aug_855-866.pdf.
- Bruinink, M., A. Chandarr, M. Rudinac, P. J. van Overloop and P. Jonker (2015). “Portable, automatic water level estimation using mobile phone cameras”. In: *Proceedings of 2015 14th IAPR International Conference on Machine Vision Applications (MVA). Tokyo, JP (18–22 May 2015)*. IEEE, pp. 426–429. DOI: 10.1109/MVA.2015.7153102.
- Burghardt, D., W. Nejd, J. Schiewe and M. Sester (2018). “Volunteered Geographic Information: Interpretation, Visualisation and Social Computing (VGIScience)”. In: *Proceedings of the ICA 1*, pp. 1–5. DOI: 10.5194/ica-proc-1-15-2018.
- Chikatsu, H. and Y. Takahashi (2009). “Comparative evaluation of consumer grade cameras and mobile phone cameras for close range photogrammetry”. In: *Proceedings of SPIE 7447 Videometrics, Range Imaging, and Applications X. San Diego, CA, US (2–6 Aug 2009)*. Vol. 7447. International Society for Optics and Photonics. SPIE, pp. 130–141. DOI: 10.1117/12.825746.
- Clarke, T. A. and J. G. Fryer (1998). “The Development of Camera Calibration Methods and Models”. In: *The Photogrammetric Record* 16, 91, pp. 51–66. DOI: 10.1111/0031-868x.00113.
- Corning Inc. (2020). *Samsung Galaxy S8*. online. Accessed: 20th January 2020. URL: <https://www.corning.com/gorillaglass/worldwide/en/products-with-gorilla-glass/smartphones/samsung/samsung-galaxy-s8.html>.
- Davids, J. C., M. M. Rutten, A. Pandey, N. Devkota, W. D. van Oyen, R. Prajapati and N. van de Giesen (2019). “Citizen science flow – an assessment of simple streamflow measurement methods”. In: *Hydrology and Earth System Sciences* 23, 2, pp. 1045–1065. DOI: 10.5194/hess-23-1045-2019.
- DeviceSpecifications (2020). *Comparison between LG Google Nexus 5 and Samsung Galaxy S8 Exynos*. online. Accessed: 20th January 2020. URL: <https://www.devicespecifications.com/en/comparison/54eec4126>.
- Al-Durgham, K., D. D. Lichti, I. Datchev, G. Kuntze and J. L. Ronsky (2018). “Bundle Adjustment-based Stability Analysis Method with a Case Study of a Dual Fluoroscopy Imaging System”. In: *ISPRS Annals of Photogrammetry, Remote Sensing and Spatial Information Sciences IV-2*, pp. 9–16. DOI: 10.5194/isprs-annals-iv-2-9-2018.

- Förstner, W. and B. P. Wrobel (2016). *Photogrammetric Computer Vision*. Geometry and Computing. Springer: Berlin/Heidelberg, DE. ISBN: 9783319115504. DOI: 10.1007/978-3-319-11550-4.
- Fraser, C. S. (1997). “Digital camera self-calibration”. In: *ISPRS Journal of Photogrammetry and Remote Sensing* 52, 4, pp. 149–159. DOI: 10.1016/s0924-2716(97)00005-1.
- Ghasemi, A. and S. Zahediasl (2012). “Normality Tests for Statistical Analysis: A Guide for Non-Statisticians”. In: *International Journal of Endocrinology and Metabolism* 10, 2, pp. 486–489. DOI: 10.5812/ijem.3505.
- Godding, R. (1999). In: *Handbook of Computer Vision and Applications – Sensors and Imaging*. Academic Press: San Diego, CA, US. Chap. Geometric Calibration and Orientation of Digital Imaging Systems, pp. 442–462.
- Google (2020a). *Android Developers. Android API Guide. Package Index*. online. Accessed: 20th January 2020. URL: <https://developer.android.com/reference/android/hardware/package-summary>.
- GSMArena (2020). *LG Nexus 5*. online. Accessed: 20th January 2020. URL: https://www.gsmarena.com/lg_nexus_5-5705.php.
- Habib, A. and M. Morgan (2005). “Stability Analysis and Geometric Calibration of Off-the-Shelf Digital Cameras”. In: *Photogrammetric Engineering & Remote Sensing* 71, 6, pp. 733–741. DOI: 10.14358/pers.71.6.733.
- Handel, H. (2007). “Analyzing the Influences of Camera Warm-Up Effects on Image Acquisition”. In: *Proceedings of 8th Asian Conference on Computer Vision (ACCV 2007). Tokyo, JP (18–22 Nov 2007)*. Vol. 4844. Springer, pp. 258–268. DOI: 10.1007/978-3-540-76390-1_26.
- Handel, H. (2008a). “Analyzing the influence of camera temperature on the image acquisition process”. In: *Proceedings of SPIE 6805 Three-Dimensional Image Capture and Applications 2008. San Jose, CA, US (28 Feb 2008)*. Vol. 6805. SPIE, pp. 264–271. DOI: 10.1117/12.766442.
- Handel, H. (2008b). “Compensation of thermal errors in vision based measurement systems using a system identification approach”. In: *Proceedings of 2008 9th International Conference on Signal Processing Beijing, CN (26–29 Oct 2008)*. IEEE, pp. 1329–1333. DOI: 10.1109/icosp.2008.4697377.
- Harman, M. (2020). *Open Camera - Camera app for Android, Version 1.38*. online. Accessed: 20th January 2020. URL: <https://sourceforge.net/projects/opencamera/>.
- iFixit (2020). *Samsung Galaxy S8+ Teardown*. online. Accessed: 20th January 2020. URL: <https://de.ifixit.com/Teardown/Samsung+Galaxy+S8++Teardown/87086>.
- Kehl, C., S. J. Buckley, S. Viseur, R. L. Gawthorpe and J. A. Howell (2017). “Automatic Illumination-Invariant Image-to-Geometry Registration in Outdoor Environments”. In: *The Photogrammetric Record* 32, 158, pp. 93–118. DOI: 10.1111/phor.12188.
- Kraus, K. (1993). *Photogrammetry, Vol.1, Fundamentals and Standard Processes*. Dümmler: Bonn, DE. ISBN: 9783427786849.
- Läbe, T. and W. Förstner (2004). “Geometric stability of low-cost digital consumer cameras”. In: *International Archives of Photogrammetry, Remote Sensing and Spatial Information Sciences XXXV-B1*, pp. 528–535.

- Lehmann, J., D. Coumou and K. Frieler (2015). “Increased record-breaking precipitation events under global warming”. In: *Climatic Change* 132, 4, pp. 501–515. DOI: 10.1007/s10584-015-1434-y.
- Lichti, D. D., A. Habib and I. Datchev (2009). “An Object-space Simulation Method for Low-cost Digital Camera Stability Testing”. In: *Photogrammetric Engineering & Remote Sensing* 75, 12, pp. 1407–1414. DOI: 10.14358/pers.75.12.1407.
- Lin, Y.-T., Y.-C. Lin and J.-Y. Han (2018). “Automatic water-level detection using single-camera images with varied poses”. In: *Measurement* 127, pp. 167–174. DOI: 10.1016/j.measurement.2018.05.100.
- Luhmann, T., S. Robson, S. Kyle and J. Boehm (2013b). In: *Close Range Photogrammetry and 3D Imaging*. 2nd ed. De Gruyter, Berlin, DE. Chap. 4.2.3 Analytical methods: Space resection, 684: 263–271. ISBN: 9783110302783.
- Luhmann, T., C. Fraser and H.-G. Maas (2016). “Sensor modelling and camera calibration for close-range photogrammetry”. In: *ISPRS Journal of Photogrammetry and Remote Sensing* 115, pp. 37–46. DOI: 10.1016/j.isprsjprs.2015.10.006.
- Marita, T., F. Oniga, S. Nedevschi, T. Graf and R. Schmidt (2006). “Camera Calibration Method for Far Range Stereovision Sensors Used in Vehicles”. In: *Proceedings of 2006 IEEE Intelligent Vehicles Symposium. Tokyo, JP (13–15 Jun 2006)*. IEEE, pp. 356–363. DOI: 10.1109/ivs.2006.1689654.
- Mitshita, E., J. Cortês, J. Centeno and A. Machado (2009). “Small-format digital camera: A study into stability analysis of the interior orientation parameters through temperature variation”. In: *Proceedings of 6th International Symposium on Mobile Mapping Technology. Presidente Prudente, BR (21–24 Jul 2009)*. Vol. XXXVIII-I/3, pp. 1–7. URL: https://www.isprs.org/proceedings/XXXVIII/part1/03/03_03_Paper_62.pdf.
- Peña-Haro, S., B. Lüthi, M. Carrel and T. Philippe (2018). “DischargeApp: A smart-phone App for measuring river discharge”. In: *Geophysical Research Abstracts of EGU General Assembly 2018. Vienna, AT (4–13 Apr 2018)*. Vol. 20. Copernicus Publications, p. 1757. URL: <https://meetingorganizer.copernicus.org/EGU2018/EGU2018-1757.pdf>.
- Podbreznik, P. and B. Potočnik (2012). “Assessing the influence of temperature variations on the geometrical properties of a low-cost calibrated camera system by using computer vision procedures”. In: *Machine Vision and Applications* 23, 5, pp. 953–966. DOI: 10.1007/s00138-011-0330-3.
- Price, C. and H. Shachaf (2017). “Using smartphone data for studying natural hazards”. In: *Geophysical Research Abstracts of EGU General Assembly 2017. Vienna, AT (23–28 Apr 2017)*. Vol. 19. Copernicus Publications, p. 2659. URL: <https://meetingorganizer.copernicus.org/EGU2017/EGU2017-2659.pdf>.
- Raspberry Pi (2020). *Hardware Documentation - Camera Module*. online. Accessed: 20th January 2020. URL: <https://www.raspberrypi.org/documentation/hardware/camera/>.
- Robson, S., L. MacDonald, S. Kyle and M. R. Shortis (2016). “Close range calibration of long focal length lenses in a changing environment”. In: *International Archives of the Photogrammetry, Remote Sensing and Spatial Information Sciences XLI-B5*, pp. 115–122. DOI: 10.5194/isprs-archives-xli-b5-115-2016.

-
- Schwalbe, E. and H.-G. Maas (2017). “The determination of high-resolution spatio-temporal glacier motion fields from time-lapse sequences”. In: *Earth Surface Dynamics* 5, 4, pp. 861–879. DOI: 10.5194/esurf-5-861-2017.
- Smith, M. J. and E. Cope (2010). “The effects of temperature variation on single-lens-reflex digital camera calibration parameters”. In: *International Archives of Photogrammetry, Remote Sensing and Spatial Information Sciences XXXVIII-V/5*. URL: <https://www.isprs.org/proceedings/XXXVIII/part5/papers/158.pdf>.
- Wang, Y., M. Kong and Y.-C. Lee (2014). “Thermal Stress in MEMS”. In: *Encyclopedia of Thermal Stresses*. Springer: Dordrecht, NL, pp. 5237–5248. ISBN: 9789400727397. DOI: 10.1007/978-94-007-2739-7_275.
- Yu, Q., Z. Chao, G. Jiang, Y. Shang, S. Fu, X. Liu, X. Zhu and H. Liu (2014). “The effects of temperature variation on videometric measurement and a compensation method”. In: *Image and Vision Computing* 32, 12, pp. 1021–1029. DOI: 10.1016/j.imavis.2014.08.011.

8 Investigating sensor fusion strategies for smartphone orientation determination

Chapter 8 published in “ISPRS Annals of the Photogrammetry, Remote Sensing and Spatial Information Sciences” (eISSN: 2194-9050) as:

Investigation on multi-sensor fusion strategies for improved orientation determination in mobile phone imaging applications

Authors: Melanie Elias¹, Hans-Gerd Maas¹
¹ Institute of Photogrammetry and Remote Sensing, Technische Universität Dresden, Germany

Publication history: submitted February 2020, accepted March 2020, published June 2020

Full reference: Elias, M. and H.-G. Maas (2020). “Investigation on multi-sensor fusion strategies for improved orientation determination in mobile phone imaging applications”. In: *ISPRS Annals of Photogrammetry, Remote Sensing and Spatial Information Sciences V-1-2020*, pp. 181–187. DOI: [10.5194/isprs-annals-v-1-2020-181-2020](https://doi.org/10.5194/isprs-annals-v-1-2020-181-2020)

Abstract: Thanks to the rapid technological progress in the field of mobile devices, smartphones are increasingly becoming valuable for science. They can serve as photogrammetric measurement devices with built-in cameras, micro-electro-mechanical systems for orientation- and position assessment, as well as powerful processing units allowing field-based data acquisition and processing. This paper outlines a comprehensive investigation focusing on the accuracy and stability of smartphone camera rotation parameters determined by built-in smartphone sensors. For that purpose, the rotation parameters were measured under a range of different conditions. Four test scenarios were defined considering indoor- and outdoor measurements using three different devices being in static and dynamic modes. Furthermore, the influence of magnetic perturbations was investigated. The rotation parameters were determined from the measurements applying different sensor fusion approaches. Reference values for accuracy assessment were provided by a superior precision inertial measurement unit that measured the rotation parameters simultaneously to the smartphone in each experiment. The analysis of the smartphone-based rotation parameters, separated in the Euler angles azimuth, pitch and roll, shows average accuracies below 2° for pitch and roll. In comparison, azimuth shows significantly lower accuracies of more than 30° especially when the smartphone is in motion and when it is exposed to magnetic perturbations. In this regard, advanced multi-sensor fusion approaches were examined that handle such interferences to considerably improve the accuracy of azimuth measurements. In conclusion, a summary of accuracies and stabilities to be expected from smartphone sensors is given referring to ambient conditions and investigated sensor fusion strategies.

Keywords: Smartphone, Sensor fusion, MEMS, Exterior orientation

8.1 Introduction

Smartphones are ubiquitously available in modern society. They are not only pure communication tools, but also equipped with cameras and a variety of sensors to measure the device position and orientation. Thus, smartphones are increasingly used as versatile measurement devices, which has been demonstrated in different studies. For instance, Bruinink et al. (2015) and Elias et al. (2019) developed photogrammetric smartphone applications for water level observation and flash flood prediction. Novakova and Pavlis (2017), Kröhnert et al. (2017) and Kehl et al. (2019) use smartphones for field-based interpretations of geological features. Bianchi et al. (2017) have shown that smartphones are suitable for the determination of forest inventory parameters. Muratov et al. (2016) introduced a method to perform 3D reconstruction based on structure from motion (SfM) on smartphones. Each of these applications requires precise information about smartphone camera's position- and rotation parameters, i.e. the exterior orientation. Referring to this, state-of-the-art global navigation satellite system (GNSS) receivers, implemented in smartphones, promise accuracies of less than 1 m for the position parameters using real-time precise point positioning (PPP) strategies (Chen et al., 2019a). Despite numerous technical innovations, the smartphone-based determination of absolute rotation parameters using built-in micro-electro-mechanical system (MEMS) inertial measurement units (IMUs) is still challenging due to sensor instabilities and external magnetic field interferences, e.g. Poulou et al. (2019a), and requires a comprehensive investigation.

For that purpose, typical problems in rotation parameter determination must be simulated in relation to the above-mentioned applications, e.g. when the device is exposed to magnetic perturbations during field-based measurements.

8.1.1 Related work

Elias et al. (2019) address the challenge of smartphone-based rotation parameters in their description of a smartphone application enabling the determination of water levels in flood events. The presented approach is based on image-to-geometry registration and needs good approximations for smartphone camera's exterior orientation. They point out that the success of water level determination highly depends on the rotation parameters and may be impeded when the determined azimuth (also known as heading or compass angle) deviates by more than 40° from the actual value, which is quite possible according to the work of Blum et al. (2013). They determined deviations of about 30° regarding azimuth with significant drifts after a few minutes in an augmented reality (AR) application where the smartphone is used in a static mode. Similar observations were made by Kok et al. (2017). Novakova and Pavlis (2017) even determined azimuth-related errors up to 90° using the smartphone as a compass in geological applications.

It is obvious that the precise determination of rotation parameters using built-in smartphone sensors is not trivial and a subject in manifold research. However, most studies are focussed on the measurement of relative rotation parameters, necessary for e.g. indoor navigation, using the output directly from physical sensors or from virtual sensors that implement standard sensor fusion approaches, e.g. Ma et al. (2013), Aicardi et al. (2014), Gikas and Perakis (2016) and Kuznetsov et al. (2018). This paper affiliates these investigations with a particular focus on the above-mentioned issues regarding photogrammetric applications. For that purpose, the rotation parameters were determined in relation to a world reference frame under a range of different conditions utilising three Android devices, equipped with low-cost IMUs based on MEMS technology, and implementing three inertial multi-sensor fusion approaches. Of course,

inertial sensors can also be coupled with GNSS, e.g. Hide et al. (2009) and Sheta et al. (2018), cellular signals or visual sensors, e.g. Angelino et al. (2012), Solin et al. (2018) and Qin et al. (2018), to improve the rotation measurements, but only provided that the device is in motion. In view of the mentioned applications predominantly requiring the smartphone in static mode, however, this paper is focused on the accuracy and stability assessment of rotation parameters (f)using only inertial sensors. The accuracy was determined comparing the rotation parameters from smartphones to those from a superior precision IMU and the stability was determined observing the variability of the rotation parameters when the investigated smartphone was used in a static mode.

Smartphone camera, MEMSs and GNSS module are closely mounted on a single circuit board. With respect to the expected reduced accuracies in comparison to high-end sensor systems used in, for example, airborne laser scanning applications, the determination of the boresight alignment was neglected in the following investigations.

8.1.2 Paper structure

Before starting with the measurements, Section 8.2 provides basic knowledge about physical and virtual sensors that are commonly used to determine rotation parameters. Furthermore, the relation between the smartphone sensor coordinate system and a world coordinate system is described. As the paper investigates the impact of magnetic perturbations on the measurement of rotation parameters, a short outline is provided dealing with magnetic effects and how to calibrate them. Section 8.3 provides information about the conducted experiments including a description of the test scenarios, of the applied hardware and sensor fusion techniques and of the experimental setup. Furthermore, the synchronisation of smartphone and IMU is described. The measurement results are given in Section 8.4 separated in investigations on accuracy and on stability. Finally, a short summary is provided in Section 8.5.

8.2 Basics

8.2.1 Sensors systems for orientation estimation

As the term *sensor fusion* indicates, the measured values from multiple physical sensors are combined to generate advanced virtual sensors. Such sensor fusion concepts are commonly implemented by state-of-the-art IMUs and increasingly by smartphones with the purpose of rotation parameter determination.

Physical sensors are MEMSs built in smartphones that can be classified into three groups (Google, 2020b):

- Environmental sensors, e.g. barometer
- Position sensors, e.g. magnetometer (+ GNSS)
- Motion sensors, e.g. gyroscope and accelerometer

By default, the sensor data of magnetometer, gyroscope and accelerometer is used to determine the rotation parameters. In this regard, the accelerometer measures linear accelerations and gravities along three axes, the magnetometer measures the ambient magnetic field and the gyroscope measures angular velocities and accelerations in 3D space.

Virtual sensors are a result of fusing the data from physical sensors. They show significant advantages over the exclusive usage of single physical sensors. On the one hand, integrating position sensors in addition to motion sensors allows to determine the absolute device orientation in Earth-North-Up reference frame. On the other hand, sensors with complementary strengths and weaknesses can be combined to overcome sensor-specific issues. As an example, accelerometers measure inertial forces at the device, but they are susceptible to smallest vibrations and non-gravity accelerations that result in noisy angular measurements. Gyroscopes accurately measure the angular acceleration of a device, but they are prone to drift effects due to bias instability and high-frequency noise called angular random walk (ARW). Fusing the measurements from both sensors helps to reduce noise occurring from non-gravity forces and drift effects. More details are given in Beavers (2017). Sensor fusion is mostly implemented by means of a Complementary Filter (CF), a Linear Kalman Filter (LKF) or an Extended Kalman Filter (EKF) including the data from the physical sensors, e.g. Natarajasivan and Govindarajan (2016), Islam et al. (2017), Cloud et al. (2019) and Poulouse et al. (2019b).

8.2.2 Smartphone coordinate systems

The orthogonal smartphone sensor coordinate system is defined in relation to the natural orientation of the device¹ where

- \mathbf{x} points to the right edge of the device
- \mathbf{y} points to the top edge of the device
- \mathbf{z} points out of the display

The world coordinate system is expressed as orthogonal coordinate system where

- \mathbf{X} ($\mathbf{Y} \times \mathbf{Z}$) is tangential to the ground pointing to East
- \mathbf{Y} is tangential to the ground pointing to magnetic North
- \mathbf{Z} is perpendicular to the ground pointing in direction of the sky

Smartphone-based rotation parameters will be zero when the smartphone is flat on the ground with the screen facing the sky and with the top edge pointing to magnetic North (see Figure 8.1). The respective Euler angles are derived in azimuth-pitch-roll order, where

- **Azimuth** rotates about $-\mathbf{Z}$ -axis in North East South West (NESW) compass direction $[0, \frac{\pi}{2}, \pi, -\frac{\pi}{2}]$
- **Pitch** rotates about $-\mathbf{X}$ -axis $[-\pi, \pi]$
- **Roll** rotates about \mathbf{Y} -axis $[-\frac{\pi}{2}, \frac{\pi}{2}]$

More details about the different coordinate systems are given by Google (2020b).

¹natural device orientation of smartphones and phablets: portrait mode; tablets: landscape mode (valid for most devices)

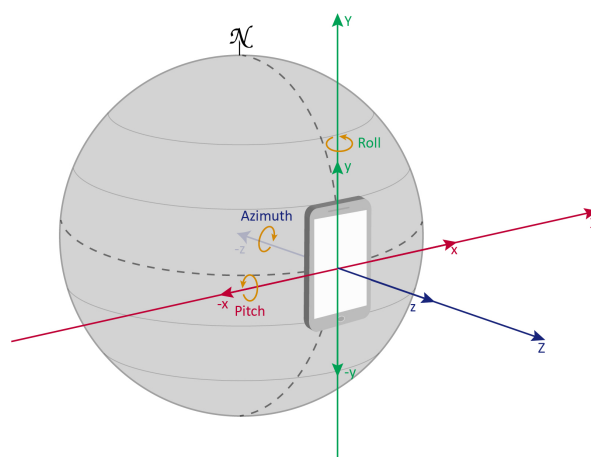


Figure (8.1): Smartphone sensor coordinate system in relation to a world coordinate system.

Note: Using the device upright, e.g. in AR- and photogrammetric applications, requires remapping of the sensor coordinate system in order to align camera's principal axis with the Y-axis.

8.2.3 Magnetic perturbations

Measuring the azimuth in relation to the world reference system requires measurements of Earth's magnetic field that can be described by three components. **Declination** and **inclination** describe Earth's magnetic field orientation where the declination provides information about the deviation from magnetic North to true North. 3D magnetometers are able to measure the third component, the magnetic field **intensity**, which is used to determine the device direction in relation to magnetic North. Unfortunately, magnetometers are prone to errors occurring from inferences with the geomagnetic field, called magnetic perturbations. These can be classified in soft- and hard iron effects. Details are given in Caruso (2000), Seco and Jiménez (2018) and Muraccini et al. (2019).

Hard iron effects arise from fixed-installed magnetised objects close to the sensor system, which applies to almost all components built in smartphones. These error sources will cause a constant bias to the sensor measurements resulting in a 3D offset of the measured magnetic field intensities that need to be calibrated.

Soft iron effects occur from flexible magnetised objects close to the sensor system that can distort and deflect Earth's magnetic field measurements. This results in bias towards the sources of interference. Soft iron effects can occur indoor and outdoor, for example when the device is exposed to changes of the physical environment.

Magnetometer calibration implies the correction of hard- and soft iron effects including, on the one hand, the determination of the offset referring to hard iron effects and, on the other hand, the establishment of the complex relationship between the magnetic field and soft-iron-induced distortions (Vishwatheja et al., 2016). Magnetometer calibration is mandatory and must be performed immediately before the actual measurement. However, soft iron effects are highly variable and will thus influence the measurements even if the sensor has been calibrated in advance. For that reason, they were considered in the experiments to quantify

their impact on the determined rotation parameters with a special focus on the measurements of the compass angle azimuth.

8.3 Experiments

Three sensor systems, built in three different Android devices, were used to investigate the accuracy and the stability of smartphone rotation parameters determined from three virtual sensors. For that purpose, four indoor and outdoor test scenarios were defined, where the device was in:

1. static mode
2. static mode being exposed to soft iron effects
3. dynamic mode
4. dynamic mode being exposed to soft iron effects

8.3.1 Hardware

Details on the investigated devices are given in Table 8.1. Each investigated smartphone has a 6-axis MEMS gyroscope and accelerometer (see Table 8.1, Inertial sensor system) and a 3-axis electronic compass (see Table 8.1, Magnetometer). The reference values, given in Euler angles, were determined using the IMU *Spatial v6.1* by Advanced Navigation. It comes with a virtual sensor that fuses the measurements from built-in 3D accelerometer, gyroscope and magnetometer. Table 8.2 shows IMU's specifications, provided by Advanced Navigation (2020).

Table (8.1): Smartphone specifications. Abbreviations: Central Processing Unit (CPU), Graphics Processing Unit (GPU), System on Chip (SoC).

	LG Google Nexus 5	Samsung Galaxy S8	Samsung Galaxy S10+
Operation System	Android 6.0	Android 8.0	Android 9.0
SoC	Snapdragon 800	Exynos 8895	Exynos 9820
CPU	4 x 2.26 GHz	8 x 2.3 GHz	8 x 1.9-2.7 GHz
GPU	450 MHz Adreno 330	900 MHz Mali-G71 MP20	900 MHz Mali-G76 MP12
Inertial sensor system	InvenSense MPU-6515	STMicroelectronics LSM6DSL	STMicroelectronics LSM6DSO
Magnetometer	Asahi Kasei AK8963	Asahi Kasei AK09916C	Asahi Kasei AK09918C

Table (8.2): Manufacturer's information to IMU *Spatial*.

Static		Dynamic	
Azimuth	Pitch, Roll	Azimuth	Pitch, Roll
0.5°	0.1°	0.8°	0.2°

8.3.2 Experimental setup

The experiments were carried out with a smartphone and the IMU being fixed on a stable bar at a distance of 1 m to ensure that both sensor systems do not disturb each other (see Figure 8.2). Smartphone and IMU were aligned in such a way that the sensor coordinate systems of both devices were parallel. Note, *Spatial* measures the pitch as rotation around the y-axis whereas the smartphone measures the pitch as rotation around the -x-axis, which resulted in opposite directions of rotations that must be considered in the data analysis.

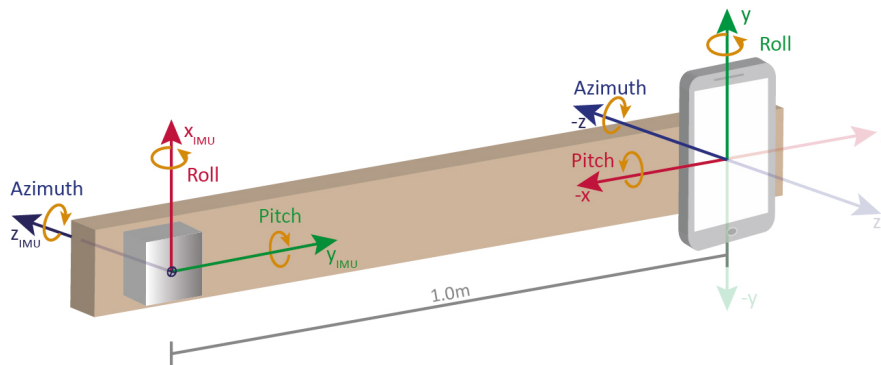


Figure (8.2): Experimental setup.

Three repeated measurements were performed with measuring times of about 90 seconds. At the beginning of each experiment, both sensor systems were calibrated with regard to the magnetic field following the explanations given in Google (2020b) and Advanced Navigation (2020) while information about the calibration validity was given by the operating system. After that, the bar, being parallel to the ground, was roughly aligned to true North. Regarding experiments where the device was used in a dynamic mode, the bar was moved in a slight rowing motion. Soft-iron effects were induced by means of magnetised objects that were placed close to the smartphone with varying positions.

Smartphone implementation

The experiments were conducted using a self-developed smartphone application that implements the virtual sensors:

- Android Rotation Vector (ARV)
- Improved Rotation Sensor 1 (IRS1)
- Improved Rotation Sensor 2 (IRS2)

to determine the rotation parameters to be compared with those from the reference IMU. The default-implemented ARV measures the rotation parameters in relation to a world coordinate system (see Figure 8.1) fusing the measurements from accelerometer, gyroscope and magnetometer by means of an EKF. In this regard, the gyroscope gives the orientation, the accelerometer provides the correction measuring the gravity forces at the device and the magnetometer provides the correction to magnetic North (Pacha, 2015). Unfortunately, ARV shows residual drift effects that seem to be related with the gyroscope, as ARV uses the raw gyroscope measurements directly from the physical sensor. The multi-sensor fusion approaches IRS1 and IRS2, developed by Pacha (2015), promise solutions for this issue fusing ARV with the Android-implemented virtual sensor *Calibrated Gyroscope*. According to the developer, IRS1 combines the angular acceleration measurements of both sensors and is recommended for most AR applications when the device is used in a static mode. In contrast to this, ARV fuses the angular accelerations as well as the angular velocities measured by the *Calibrated Gyroscope* and is recommended for applications where the device is used in a dynamic mode. The implementation of both virtual sensors, IRS1 and IRS2, used here, is based on the source code provided by Pacha (2015).

In the experiments, the virtual smartphone sensors ran with a frequency of 25 Hz that allowed for motion tracking when the device was moved with moderate speed and provided reasonable numbers of about 2250 measurements in a 90-second measurement period.

Observing magnetic perturbations

Magnetic perturbations can be detected comparing the measured magnetic field intensities with expectation values given by the World Magnetic Model 2015 (WMM-2015) that provides superior information about the Earth's magnetic field depending on the device location and current time. Further details can be found in Chulliat et al. (2015). In this study, the measured intensity must equal the expected intensity with a tolerance of $\pm 5 \mu\text{T}$, otherwise it was assumed to be affected by uncalibrated soft iron effects. As the smartphone application informs the user about the ambient magnetic field intensity, deviations could be provoked to simulate soft iron effects that ranged between $10 \mu\text{T}$ and $15 \mu\text{T}$ in the respective experiments. Stronger magnetic perturbations were avoided as they are likely to heavily impair the magnetometer so that this could not work properly.

Data logging and synchronisation

Regarding data logging, the smartphone application recorded the measurements including the time stamp in milliseconds given by Unix time, the rotation parameters azimuth (to true North), pitch and roll measured by three virtual sensors and the deviation of the measured magnetic field intensity referring to magnetic perturbations. Similar to this, the IMU recorded azimuth (to true North), pitch and roll together with a Unix time stamp at a frequency of 40 Hz.

Even if both datasets can be synchronised by Unix time, the sensor systems showed different latencies that must be corrected to make them comparable. Considering the experiments, the lag was determined and fixed for each investigated device by means of sample cross correlation on the trajectories of azimuth, pitch and roll considering the dynamic-mode measurements. Then, it was applied to the corresponding measurements when the device was used in a static mode.

8.4 Results

In summary, 216 measurement series were conducted whereby one data set contains the rotation parameters from three virtual sensors (including four test scenarios performed indoor and outdoor applying three devices and three repeated measurements per setting). The accuracies were determined for each setting and for each device calculating the root mean square errors (RMSEs) between the synchronised smartphone- and IMU measurements for azimuth, pitch and roll, respectively. In relation to this, the RMSEs were individually determined for the measurements of ARV, IRS1 and IRS2. The sensor stability was assessed by means of the standard deviations that were calculated for the smartphone-based rotation parameters involving each measurement series where the device was used in a static mode.

The results are visualised in Figure 8.3–8.5 with regard to accuracy and stability, respectively, taking account of the measurement settings, the used devices and the individual virtual sensors.

8.4.1 Accuracies

As illustrated in Figure 8.3, devices used in dynamic mode show higher deviations to the ground truth in all rotation parameters compared to the measurements performed with devices used in static mode. Calculating the median values of the RMSE values of a measurement series for azimuth, pitch and roll results in 24.0° , 0.9° and 0.6° when the device was used in a static mode. In contrast, median deviations of 41.9° , 2.1° and 2.8° occurred when the device was used in a dynamic mode.

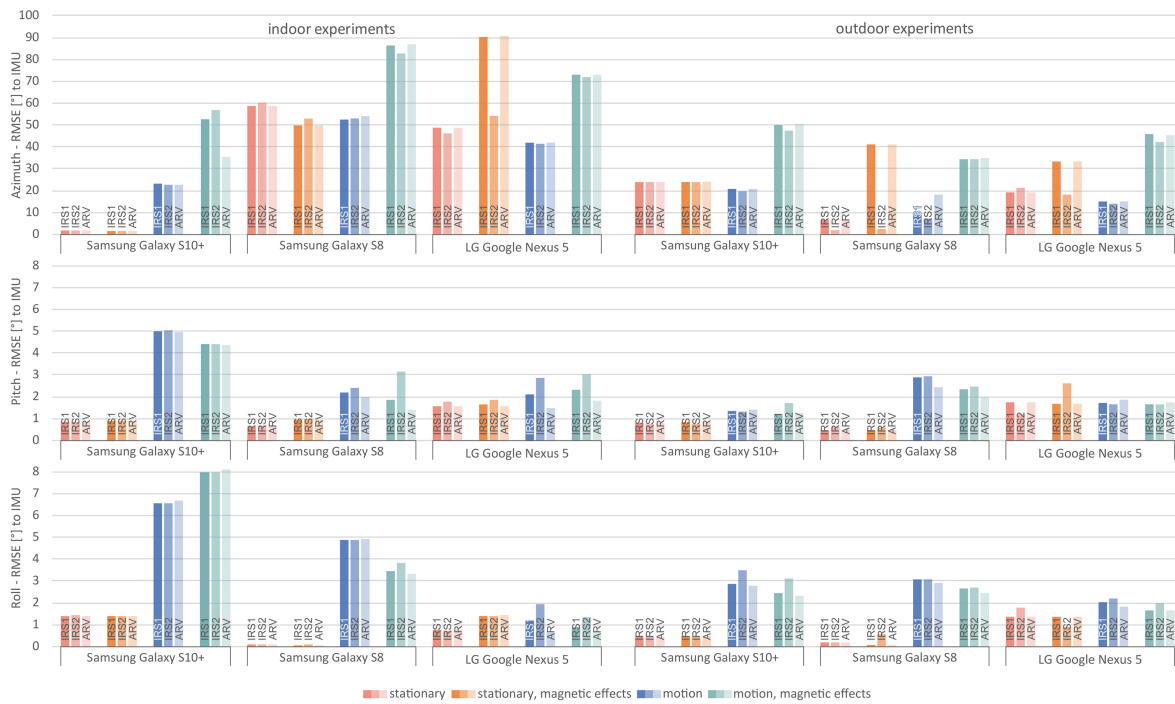


Figure (8.3): Accuracy investigation of smartphone-based rotation parameters. Accuracy is defined by the RMSE calculated from the deviations between the rotation parameters from the smartphone and the reference values from IMU *Spatial*.

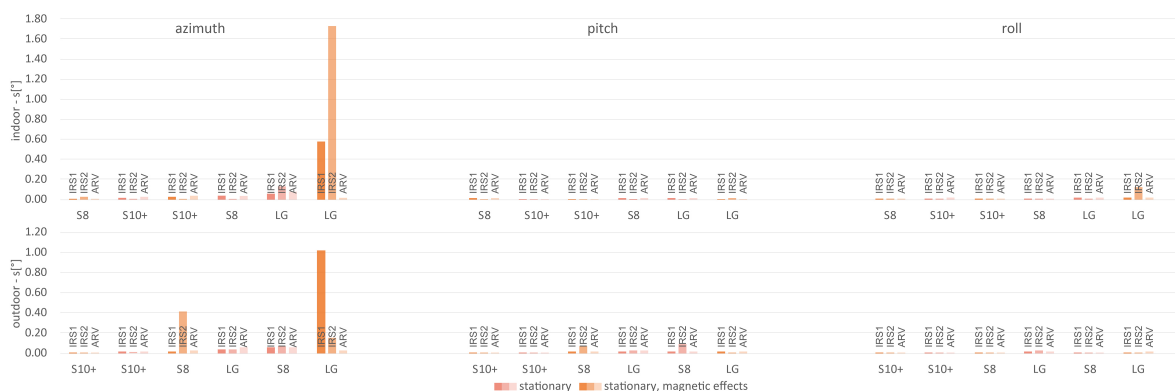


Figure (8.4): Stability investigation of smartphone-based rotation parameters. Stability is defined by the standard deviation s of one measurement series when the smartphone was used in static mode.

This is particularly evident for azimuth when the device is exposed to magnetic perturbations. In this regard, the medians show deviations of 45.6° , 1.6° and 1.4° for azimuth, pitch and

roll irrespective of whether they were captured in dynamic- or in static mode or whether the experiment was performed indoors or outdoors. On the contrary, devices that were not affected by magnetic perturbations show deviations of only 22.0° , 1.7° and 1.4° . Focussing on pitch and roll, the impact of magnetism is negligible as it results in a loss of accuracy of less than 1.0° . Comparing the results from indoor- and outdoor measurements, the azimuth angles measured outdoor are significantly more accurate as when they were measured indoor.

One reason for this may be stronger interferences occurring inside a building due lamps, radiators, pipes etc. Calculating the median deviations results in 51.2° , 1.7° and 1.4° as well as 23.7° , 1.6° and 1.7° for azimuth, pitch and roll with respect to indoor and outdoor measurements. Despite the rather small deviations for pitch and roll that were measured in both environments, azimuth shows maximum deviations up to 50.8° when it was measured outdoors and even up to 90.9° when it was measured indoors.

Comparing the results of IRS1, IRS2 and ARV, no significant differences became apparent between the respective measurements of pitch and roll. However, significantly better results could be achieved for azimuth using IRS2, especially in case of magnetic perturbations.

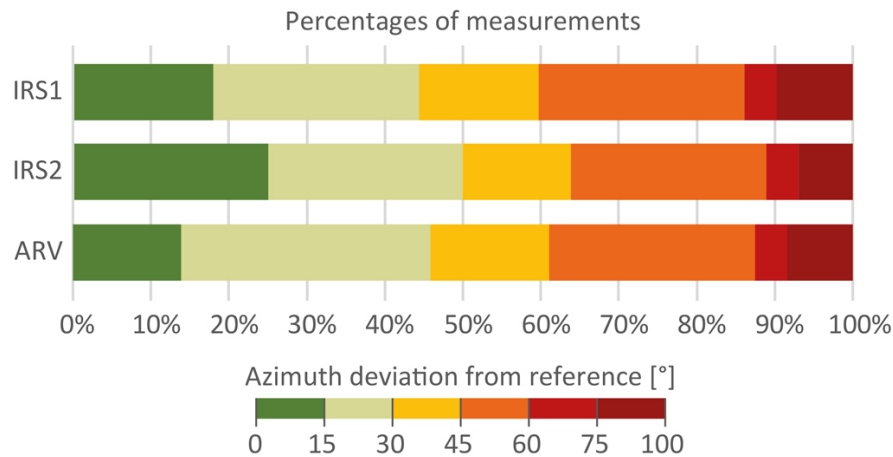


Figure (8.5): Histograms of the total deviations regarding azimuth in relation to the measurements from IRS1, IRS2 and ARV.

Focussing on Figure 8.5, 25% of all IRS2 measurements show deviations of less than 15° from the ground truth. In contrast, the percentage of measurements differing less than 15° amounts to only 18% for IRS1- and 13% for ARV measurements. Beside this, 50% of all IRS2 measurements show deviations of less than 30° .

8.4.2 Stability

The sensor stability was investigated when the devices were used in static mode. As visualised in Figure 8.4, ARV shows slight, negligible variations in all measurements. In contrast, IRS1 and IRS2 show variations of 0.6° and 1.8° for azimuth measured by LG Google Nexus 5 when the device was exposed to magnetic perturbations. These effects may be related with device's sensor type that might be more susceptible to interferences than the other sensor types. However, stabilities similar to the results of pitch and roll could also be observed for azimuth considering the measurements from Samsung Galaxy S8 and Samsung Galaxy S10+.

8.5 Conclusion

This paper addresses the complex issue of the determination of absolute rotation parameters using built-in smartphone sensors. For that purpose, their accuracy potential and stability were investigated from different perspectives considering indoor- and outdoor measurements, magnetic perturbations, smartphones running in static and dynamic modes, as well as different (multi-) sensor fusion concepts. In each experiment, the rotation parameters were simultaneously measured from a superior precision IMU whose measured rotation parameters served as ground truth.

The experiments have shown that the rotation angles pitch and roll can be measured with accuracies of a few degrees under different conditions using built-in smartphone sensors. In contrast, the accuracy of the azimuth varies between 1° and 90° whereby the highest errors occurred when the smartphones were used in dynamic mode or when they were exposed to magnetic perturbations. However, it was detected that the measurements of the azimuth angle could be significantly improved applying multi-sensor fusion approaches like IRS2 that provide errors of less than 30° in 50% of all measurements.

It is obvious that these accuracies, especially the accuracies determined for azimuth, impede the direct georeferencing of smartphone images in photogrammetric applications. Poulose et al. (2019b) have shown that implementing sensor fusion by means of an Unscented Kalman Filter (UKF) could further improve the direct measurement of the azimuth, which, however, must be evaluated in future investigations. Nevertheless, using these values as rough estimates enables the application of image-to-geometry registration to precisely determine the azimuth with the aid of landmarks within spatial resection, e.g. Schwalbe and Maas (2017), Eltner et al. (2018), Kehl et al. (2019) and Elias et al. (2019).

New advanced approaches integrate deep learning in sensor fusion and promise significantly more accurate measurements of the rotation parameters combining also (low-cost) inertial sensors, provided that the smartphone is used in dynamic mode, e.g. Silva do Monte Lima et al. (2019). In this regard, Chen et al. (2019b) have shown how to use deep learning to improve the robustness of visual-inertial odometry to deal with imperfect sensor data, i.e. feature tracking errors and noisy IMU data. Shamwell et al. (2019) even trained a neuronal network with RGB-depth imagery and IMU data to enable the determination of absolute camera trajectories merely using consecutively captured camera images. Such approaches could be very helpful to improve photogrammetric applications like *3DCapture* (Muratov et al., 2016), where precise information about the camera trajectory is mandatory to perform 3D reconstruction directly on the smartphone.

Acknowledgements

This research is supported by the European Social Fund (ESF) and the Free State of Saxony (funding no. 100235479).

References

Advanced Navigation (2020). *Spatial reference manual, v4.4*. online. Accessed: 21th January 2020. URL: <https://advancednavigation.com/de/product/3>.

- Aicardi, I., P. Dabove, A. Lingua and M. Piras (2014). “Sensors integration for smartphone navigation: Performances and future challenges”. In: *International Archives of Photogrammetry, Remote Sensing and Spatial Information Sciences* XL-3, pp. 9–16. DOI: 10.5194/isprsarchives-XL-3-9-2014.
- Angelino, C. V., V. R. Baraniello and L. Cicala (2012). “UAV position and attitude estimation using IMU, GNSS and camera”. In: *Proceedings of 15th International Conference on Information Fusion. Singapore, SG (9–12 Jul 2012)*. IEEE, pp. 735–742. URL: <https://ieeexplore.ieee.org/document/6289875>.
- Beavers, I. (2017). “Rarely Asked Questions-139. The Case of the Misguided Gyro”. In: *Analog Dialogue* 51, 3, pp. 1–2. URL: <https://www.analog.com/media/en/analog-dialogue/raqs/raq-issue-139.pdf>.
- Bianchi, S., C. Cahalan, S. Hale and J. M. Gibbons (2017). “Rapid assessment of forest canopy and light regime using smartphone hemispherical photography”. In: *Ecology and Evolution* 7, 24, pp. 10556–10566. DOI: 10.1002/ece3.3567.
- Blum, J. R., D. G. Greencorn and J. R. Cooperstock (2013). In: *Mobile and Ubiquitous Systems: Computing, Networking, and Services. MobiQuitous 2012. Lecture Notes of the Institute for Computer Sciences, Social Informatics and Telecommunications Engineering*. Vol. 120. Springer: Berlin/Heidelberg, DE. Chap. Smartphone sensor reliability for augmented reality applications, 288: 127–138. DOI: 10.1007/978-3-642-40238-8_11.
- Bruinink, M., A. Chandarr, M. Rudinac, P. J. van Overloop and P. Jonker (2015). “Portable, automatic water level estimation using mobile phone cameras”. In: *Proceedings of 2015 14th IAPR International Conference on Machine Vision Applications (MVA). Tokyo, JP (18–22 May 2015)*. IEEE, pp. 426–429. DOI: 10.1109/MVA.2015.7153102.
- Caruso, M. J. (2000). “Applications of magnetic sensors for low cost compass systems”. In: *Proceedings of IEEE 2000 Position Location and Navigation Symposium. San Diego, CA, US (13–16 Mar 2000)*. IEEE, pp. 177–184. DOI: 10.1109/plans.2000.838300.
- Chen, B., C. Gao, Y. Liu and P. Sun (2019a). “Real-time Precise Point Positioning with a Xiaomi MI 8 Android Smartphone”. In: *Sensors* 19, 12, p. 2835. DOI: 10.3390/s19122835.
- Chen, C., S. Rosa, Y. Miao, C. X. Lu, W. Wu, A. Markham and N. Trigoni (2019b). “Selective Sensor Fusion for Neural Visual-Inertial Odometry”. In: *Proceedings of 2019 IEEE/CVF Conference on Computer Vision and Pattern Recognition (CVPR). Long Beach, CA, US (15–20 Jun 2019)*. IEEE, pp. 10542–10551. DOI: 10.1109/cvpr.2019.01079.
- Chulliat, A., S. Macmillan, P. Alken, C. Beggan, M. Nair, B. Hamilton, A. Woods, V. Ridley, S. Maus and A. Thomson (2015). *The US/UK World Magnetic Model for 2015-2020*. Tech. rep. Boulder, CO, US: National Geophysical Data Center, NOAA. DOI: 10.7289/V5TH8JNW.
- Cloud, B., B. Tarien, A. Liu, T. Shedd, X. Lin, M. Hubbard, R. P. Crawford and J. K. Moore (2019). “Adaptive smartphone-based sensor fusion for estimating competitive rowing kinematic metrics”. In: *PLOS ONE* 14, 12, e0225690. DOI: 10.1371/journal.pone.0225690.
- Gikas, V. and H. Perakis (2016). “Rigorous Performance Evaluation of Smartphone GNSS/IMU Sensors for ITS Applications”. In: *Sensors* 16, 8, p. 1240. DOI: 10.3390/s16081240.
- Google (2020b). *Android Developers. Android API Guide. Sensors Overview*. online. Accessed: 21th January 2020. URL: <https://developer.android.com/guide/topics/sensors>.

- Hide, C., T. Botterill and M. Andreotti (2009). “An Integrated IMU, GNSS and Image Recognition Sensor for Pedestrian Navigation”. In: *Proceedings of 22nd International Technical Meeting of the Satellite Division of The Institute of Navigation (ION GNSS 2009). Savannah, GA, US (22–25 Sep 2009)*, pp. 527–537.
- Islam, T., M. S. Islam, M. Shajid-Ul-Mahmud and M. Hossam-E-Haider (2017). “Comparison of complementary and Kalman filter based data fusion for attitude heading reference system”. In: *AIP Conference Proceedings* 1919, 1, p. 020002. DOI: 10.1063/1.5018520.
- Kehl, C., J. R. Mullins, S. J. Buckley, J. A. Howell and R. L. Gawthorpe (2019). “Interpretation and mapping of geological features using mobile devices in outcrop geology – a case study of the Saltwick Formation, North Yorkshire, UK”. In: *AGU Books – Special Issue*. Wiley.
- Kok, M., J. D. Hol and T. B. Schön (2017). “Using Inertial Sensors for Position and Orientation Estimation”. In: *Foundations and Trends in Signal Processing* 11, 1–2, pp. 1–89. DOI: 10.1561/20000000094.
- Kröhnert, M., C. Kehl, H. Litschke and S. J. Buckley (2017). “Image-to-Geometry Registration on Mobile Devices – Concepts, Challenges and Applications”. In: *Proceedings of 20th Workshop of 3D-NordOst, Berlin, DE (7–8 Dec 2017)*, pp. 99–108.
- Kuznetsov, N. A., R. K. Robins, B. Long, J. T. Jakiela, F. J. Haran, S. E. Ross, W. G. Wright and C. K. Rhea (2018). “Validity and reliability of smartphone orientation measurement to quantify dynamic balance function”. In: *Physiological Measurement* 39, 2, 02NT01. DOI: 10.1088/1361-6579/aaa3c2.
- Ma, Z., Y. Qiao, B. Lee and E. Fallon (2013). “Experimental evaluation of mobile phone sensors”. In: *Proceedings of 24th IET Irish Signals and Systems Conference (ISSC 2013). Letterkenny, IE (20–21 Jun 2013)*. DOI: 10.1049/ic.2013.0047.
- Muraccini, M., A. Mangia, M. Lannocca and A. Cappello (2019). “Magnetometer Calibration and Field Mapping through Thin Plate Splines”. In: *Sensors* 19, 2, p. 280. DOI: 10.3390/s19020280.
- Muratov, O., Y. Slynko, V. Chernov, M. Lyubimtseva, A. Shamsuarov and V. Bucha (2016). “3DCapture: 3D Reconstruction for a Smartphone”. In: *Proceedings of 2016 IEEE Conference on Computer Vision and Pattern Recognition Workshops (CVPRW). Las Vegas, NV, US (26. Jun–01. Jul 2016)*. IEEE, pp. 893–900. DOI: 10.1109/CVPRW.2016.116.
- Natarajasivan, D. and M. Govindarajan (2016). “Filter Based Sensor Fusion for Activity Recognition using Smartphone”. In: *International Journal of Computer Science and Telecommunications* 7, 5, pp. 26–31.
- Novakova, L. and T. L. Pavlis (2017). “Assessment of the precision of smart phones and tablets for measurement of planar orientations: A case study”. In: *Journal of Structural Geology* 97, pp. 93–103. DOI: 10.1016/j.jsg.2017.02.015.
- Pacha, A. (2015). *Sensor Fusion for Robust Outdoor Augmented Reality Tracking on Mobile Devices. Master’s Thesis, Augsburg University, DE*. GRIN Verlag: Munich, DE. ISBN: 9783656964025.
- Poulose, A., O. S. Eyobu and D. S. Han (2019a). “An Indoor Position-Estimation Algorithm Using Smartphone IMU Sensor Data”. In: *IEEE Access* 7, pp. 11165–11177. DOI: 10.1109/access.2019.2891942.

- Poulose, A., B. Senouci and D. S. Han (2019b). “Performance Analysis of Sensor Fusion Techniques for Heading Estimation Using Smartphone Sensors”. In: *IEEE Sensors Journal* 19, 24, pp. 12369–12380. DOI: 10.1109/jsen.2019.2940071.
- Qin, T., P. Li and S. Shen (2018). “VINS-Mono: A Robust and Versatile Monocular Visual-Inertial State Estimator”. In: *IEEE Transactions on Robotics* 34, 4, pp. 1004–1020. DOI: 10.1109/tro.2018.2853729.
- Schwalbe, E. and H.-G. Maas (2017). “The determination of high-resolution spatio-temporal glacier motion fields from time-lapse sequences”. In: *Earth Surface Dynamics* 5, 4, pp. 861–879. DOI: 10.5194/esurf-5-861-2017.
- Seco, F. and A. R. Jiménez (2018). “Smartphone-Based Cooperative Indoor Localization with RFID Technology”. In: *Sensors* 18, 1, p. 266. DOI: 10.3390/s18010266.
- Shamwell, E. J., K. Lindgren, S. Leung and W. D. Nothwang (2019). “Unsupervised Deep Visual-Inertial Odometry with Online Error Correction for RGB-D Imagery”. In: *IEEE Transactions on Pattern Analysis and Machine Intelligence* 42, 10. [Preprint updated to Journal ver.], pp. 2478–2493. DOI: 10.1109/tpami.2019.2909895.
- Sheta, A., A. Mohsen, B. Sheta and M. Hassan (2018). “Improved Localization for Android Smartphones Based on Integration of Raw GNSS Measurements and IMU Sensors”. In: *Proceedings of 2018 International Conference on Computer and Applications (ICCA). Beirut, LB (25–26 Aug 2018)*. IEEE, pp. 297–302. DOI: 10.1109/comapp.2018.8460352.
- Silva do Monte Lima, J. P., H. Uchiyama and R.-i. Taniguchi (2019). “End-to-End Learning Framework for IMU-Based 6-DOF Odometry”. In: *Sensors* 19, 17, p. 3777. DOI: 10.3390/s19173777.
- Solin, A., S. Cortes, E. Rahtu and J. Kannala (2018). “PIVO: Probabilistic Inertial-Visual Odometry for Occlusion-Robust Navigation”. In: *Proceedings of the 2018 IEEE Winter Conference on Applications of Computer Vision (WACV). Lake Tahoe, NV, US (12–15 Mar 2018)*. IEEE, pp. 616–625. DOI: 10.1109/WACV.2018.00073.
- Vishwatheja, S., P. P. Venkataratnam and Y. Siva (2016). “Algorithm development for soft and hard iron calibration of magnetic compass”. In: *International Research Journal of Engineering and Technology (IRJET)* 3, 8, pp. 179–182.

Part III

Photogrammetric water level determination

9 Identifying 2D water lines in hand-held smartphone camera images

Chapter 9 published in “ISPRS Annals of the Photogrammetry, Remote Sensing and Spatial Information Sciences” (eISSN: 2194-9050) as:

Segmentation of environmental time lapse image sequences for the determination of shore lines captured by hand-held smartphone cameras

Authors: Melanie Kröhnert^a, Robert Meichsner^a
^a Institute for Photogrammetry & Remote Sensing, TU Dresden, Germany

Publication history: submitted May 2017, accepted July 2017, published September 2017

Full reference: Kröhnert, M. and R. Meichsner (2017). “Segmentation of environmental time lapse image sequences for the determination of shore lines captured by hand-held smartphone cameras”. In: *ISPRS Annals of Photogrammetry, Remote Sensing and Spatial Information Sciences IV-2/W4*, pp. 1–8. DOI: 10.5194/isprs-annals-IV-2-W4-1-2017

Abstract: The relevance of globally environmental issues gains importance since the last years with still rising trends. Especially disastrous floods may cause in serious damage within very short times. Although conventional gauging stations provide reliable information about prevailing water levels, they are highly cost-intensive and thus just sparsely installed. Smartphones with inbuilt cameras, powerful processing units and low-cost positioning systems seem to be very suitable wide-spread measurement devices that could be used for geo-crowdsourcing purposes. Thus, we aim for the development of a versatile mobile water level measurement system to establish a densified hydrological network of water levels with high spatial and temporal resolution. This paper addresses a key issue of the entire system: the detection of running water shore lines in smartphone images. Flowing water never appears equally in close-range images even if the extrinsics remain unchanged. Its non-rigid behavior impedes the use of good practices for image segmentation as a prerequisite for water line detection. Consequently, we use a hand-held time lapse image sequence instead of a single image that provides the time component to determine a spatio-temporal texture image. Using a region growing concept, the texture is analyzed for immutable shore and dynamic water areas. Finally, the prevalent shore line is examined by the resultant shapes. For method validation, various study areas are observed from several distances covering urban and rural flowing waters with different characteristics. Future work provides a transformation of the water line into object space by image-to-geometry intersection.

Keywords: Flood monitoring, Geo-crowdsourcing, Spatio-temporal texture, Time lapse image analysis, Smartphone application

9.1 Introduction

Because of huge costs, the overall observation of flood-prone areas by permanently installed measurement stations is often just scantily available. Unfortunately, several hydrological networks have an insufficient coverage for the effected regions of interest (ROI) in case of need. Minor rivers are often neglected but ensure serious damages in case of flash floods. A small municipality called Braunsbach in Baden-Wuerttemberg, Germany received worldwide recognition in summer of 2016. After heavy rainfalls, a small river passing Braunsbach became a devastating stream with high increased flow rates by more than 500 times compared to flood situations known there. Exact values are not available due to only one measurement station, located approximately 10 km away from the hot spots. High waters and several landslides led to high structural damages and complicated rescue operations (Agarwal et al., 2016). For the development of a versatile mobile water level measurement system, the necessary input data is provided by geo-crowdsourcing using smartphones to capture and process hand-held time lapse image sequences to extract the prevalent water line as a basic requirement for the observation of water level changes (see Figure 9.1). Subsequently, the detected water line has to be transferred into object space to determine the final water level (not addressed in this paper). However, the segmentation of running water and nearshore environment is a non-trivial task and has been treated frequently in image processing fields (see Section 9.1.1). An individual image is only a snapshot which barely covers the characteristics of non-rigid objects like water. In addition to the image space, the use of the time axis provides an efficient complement for image segmentation by means of spatio-temporal variability.



Figure (9.1): Schematic use case of water level determination using hand-held smartphone.

Due to the investigation of the mobile water level monitoring system, the water line detection of diverse running waters represents a core function of the entire system. Thus, the approach is applied to several study regions of different characteristics and weather conditions concerning shooting distances and time lapse frequencies (see Section 9.2). In Section 9.3 we present the methodology starting with the geometric co-registration of a monoscopic time lapse image sequence (see Section 9.3.1), immediately followed by spatio-temporal texture and pixel by pixel mean value calculation using the registered dataset (see Section 9.3.2). Using the application interface, user interaction takes place in the form of a coarse selection of the shore line to be extracted. The resultant image areas mark respectively the predominant dynamic or static part of the ROI and must be analyzed for their spatio-temporal distribution to assess the texture significance (see Section 9.3.3). Depending on the results, an automatic steered

region growing is applied for image segmentation (see Section 9.3.4). Using the specified regions, the prevalent shore line is investigated and described in Section 9.3.5. Whereas Section 9.4 illustrates the resulting water lines of the introduced study areas, Section 9.5 gives an evaluation respectively. The paper ends with a critical examination of the proceeding and give a short outlook for future work (see Section 9.6).

9.1.1 Related work

In geosciences, especially in remote sensing, multispectral imagers provide spectral signatures from natural objects depending on their physical conditions, like the approved NDWI for water recognition (Feyisa et al., 2014; Gao, 1996; Li et al., 2014; Sarp and Ozcelik, 2017). Currently, it seems to be obvious that the application of mobile multispectral imaging using smartphones is not possible due to technical reasons.

An alternative approach is provided by the analysis of image texture. A fundamental work written by Haralick et al. (1973), defines texture as "one of the important characteristics used in identifying objects of regions of interests in an image, whether the image be a photomicrograph, an aerial photograph, or a satellite image." Thus, the combined application of single textural features and spectral information has been proven for image classification and was frequently applied and enhanced for precise image segmentation in geosciences (Kim et al., 2009; Ferro and Warner, 2002; de Martino et al., 2003¹; Verma, 2011; Zhang, 1999). But, the calculation of various texture features requires high performance which may impede the use of smartphones beside flagship systems. Referring to Varma and Zisserman (2005), "a texture image is primarily a function of the following variables: the texture surface, its albedo, the illumination, the camera and its viewing position. Even if we were to keep the first two parameters fixed, i.e. photograph exactly the same patch of texture every time, minor changes in the other parameters can lead to dramatic changes in the resultant image. This causes a large variability in the imaged appearance of a texture and dealing with it successfully is one of the main tasks of any classification algorithm." In contrast to remote sensing, texture surfaces of close-range camera observations are highly affected by the mentioned influence factors regarding varying camera constellations. Tuceryan and Jain (1999)¹ termed texture as a "prevalent property of most physical surfaces in the natural world" which is why motion has to be treated as textural criterion as well. Figure 9.2 demonstrates the strongly different appearances of running waters due to varying camera constellations and mutable image content. The complementary use of time and space enables the investigation of spatio-temporal texture and thus a situation-based image segmentation in respect of time-dependent image content (Szummer and Picard, 1996; Peh and Cheong, 2002; Hu et al., 2006; Nelson and Polana, 1992; Xu et al., 2011). On this basis, we add the temporal variability by means of time lapse image sequences. Subsequently, the proper segmentation starts in accordance to the defined feature space. Several approaches prefer a supervised classification that may be enhanced by deep neural networks for training robust classifiers (Maggiori et al., 2017; He et al., 2016; Ciregan et al., 2012; Krizhevsky et al., 2012; Reyes-Aldasoro and Aldeco, 2000). Moreover, the investigation of a sufficient training dataset for image classification regarding running waters, appears rather difficult. In conclusion, the presented approach for water line detection is primarily based on image segmentation and classification which must fulfil two basic criteria: firstly, the algorithm deals with running waters high variability and secondly, it should be appropriate to run on common smartphone devices. Thus, high intensive processing should be avoided as much as possible.

¹Correction of a quotation mistake in the original paper.



Figure (9.2): Appearances of different running waters, captured with varying camera constellations.

A similar approach provided by Kröhnert (2016), successfully demonstrates the segmentation of running water and shore land using spatio-temporal texture. However, the approach has issues regarding rotation invariance of the water line location within the image and processing time. Besides this, the implemented segmentation uses hard-defined parameters which may fail in cases of running waters with highly different characteristics than the presented one. Our approach enhances the calculation of spatio-temporal texture regarding processing time and demonstrates an orientation-invariant segmentation procedure due to multiple seeded region growing (see Section 9.3.4) with automatic set up avoiding empirical determined parameters (see Section 9.3.2).

9.2 Data

Considering variable image content of close-range images, the texture of an individual image will not have a generally valid significance for proper image segmentation which is why our approach regards the time component. By means of time lapse image sequences, the mutable textures provide significant advantages for image classification (e.g. reflections on running water surfaces). Moreover, it allows for image segmentation and thus for boundary extraction like shore lines by means of the mapped dynamics only.

In environmental sciences, monoscopic time lapse image sequences are good practice for change detection and long-term monitoring, e.g. for glaciological investigations using permanently installed camera setups (Maas et al., 2010; Koschitzki et al., 2014). In case of on-the-fly captured time lapse images or video sequences with hand-held smartphone cameras, the acquired images will be co-registered against a defined master scene to solve the issue of hand instability. In consideration of the prospective water line transformation into object space and regarding the determination of its corresponding level, the use of undistorted images is advantageous. Thus, we recommend the optional use of our implemented camera calibration tool to acquire an undistorted time lapse image sequence. As indicated above, the temporal component and the viewing position mainly influences texture and consequently the spatio-temporal texture as well. Thus, we have applied the approach to seven study regions that cover four urban and three rural rivers to extract the prevalent water lines.

The urban scenes correspond to one river with different forms of appearance and characteristics due to varying points of view and camera distances. For the investigation of rural waters, we have observed two small creeks and one large river in forest areas using a HTC One M7 smartphone, released in 2013, as measurement device with operating system Android 5.1.

Thereby, the dimension of the time lapse image sequences amounts to 1920 x 1080 pixels in all test cases. Furthermore, the temporal variability is easily assessable through² the number of images within the time lapse image sequence. Thus, two combinations of frame rate and sequence length are investigated in order to test the dependency of flow velocity and time lapse. Table 9.1 gives a detailed overview over the investigated areas and environmental conditions for image capturing.

Table (9.1): Study areas covering urban and rural running waters regarding situative specifications of environment and camera configurations.

Study region	Urban areas				Rural areas		
	(I)	(II)	(III)	(IV)	(V)	(VI)	(VII)
							
River width	8 m	8 m	21 m	16 m	15 m	≈ 2 m	≈ 1 m
ØFlow Rate Q	$3.5 \frac{m^3}{s}$		≈ $3.4 \frac{m^3}{s}$	$3.3 \frac{m^3}{s}$	$6.9 \frac{m^3}{s}$	$0.034 \frac{m^3}{s}$	$0.0086 \frac{m^3}{s}$
Weather	cloudy, no rain		heavy rain	sun		cloudy, no rain	
Shore line specs	natural gravel, bricks		quay wall	nat. gravel	reed	gravel, bricks	cliffs, grass
FPS	3 fps / 5 fps						
Sequence Length	5 s						
Object distance	30 m	15 m	35 m	20 m		15 m	5 m

9.3 Application Development

The process pipeline, illustrated in Figure 9.3, starts with the preliminary work of time lapse image sequence co-registration in direct succession to the initially data acquisition. By means of the gray level magnitudes concerning the co-registered image sequence (see Section 9.3.1), the corresponding spatio-temporal texture as well as the mean value (hereinafter referred to as “average image”) will be calculated pixel by pixel (see Section 9.3.2). Afterwards, human interaction takes place in the form of a coarse selection of the shore line to be extracted. For this, a graphical user interface (GUI) is used displaying the calculated average image to the user, which depicts a virtually homogenized surface of the dynamic image part (see Figure 9.3, top right).

The resultant image areas mark either the predominant dynamic or static part of the ROI. Both regions are analyzed for their spatio-temporal distribution to assess the prevalent texture significance (see Section 9.3.3). Possibly for slow-running rivers or large object distances, the spatio-temporal texture may not have sufficient resolution to serve as appropriate input for image segmentation purposes. In this case, the average image of the time lapse sequence provides a basis for the further processing.

The segmentation process itself (see Section 9.3.4) is automatic steered and demands an automatic definition of input data and variables. The data required for this purpose bases on the results of the previously texture significance analyses. For both options, Section "Segmentation by spatio-temporal texture analysis" and Section "Segmentation using the average image" describe the automatic definition of variables, necessary for the following segmentation with the application of region growing (see Section 9.3.4). Finally, the resultant image segments are analyzed for the prevalent shore line (see Section 9.3.5).

²Correction of a typo in the original paper.

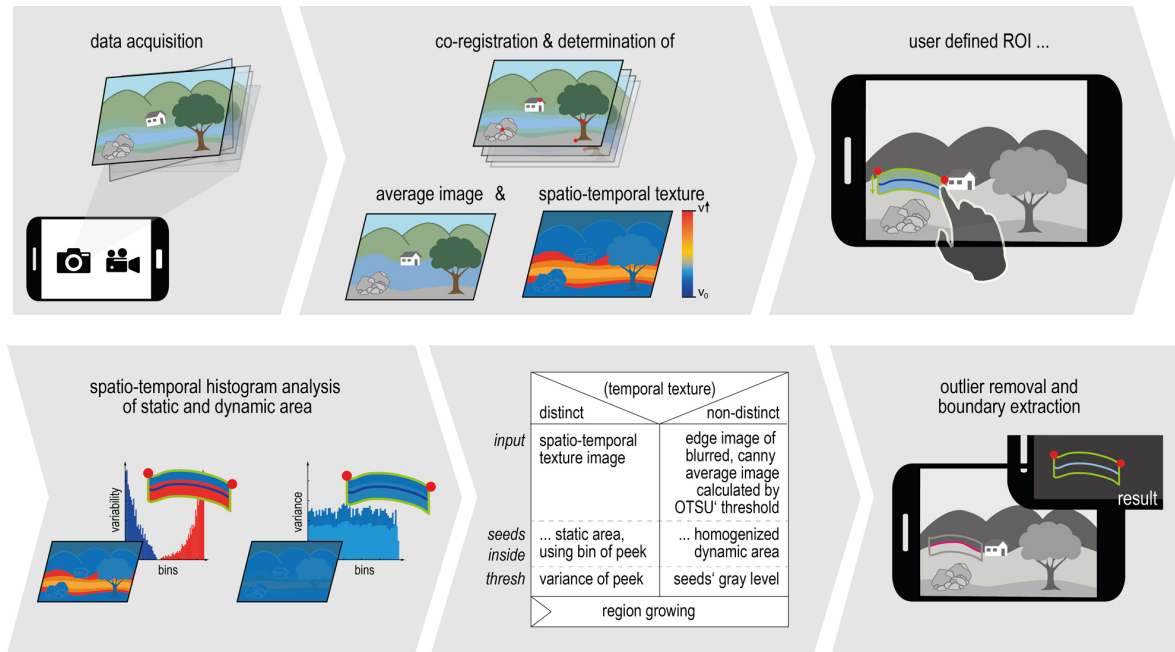


Figure (9.3): Process pipeline from data acquisition to result display.

9.3.1 Time lapse image sequence co-registration

After image acquisition, an attempt is being made to co-register all individual images of a time lapse image sequence. In doing so, the first scene acts as so-called master image whereas all remaining images will be treated as slaves. In principle, we calculate the image homographies respectively for all slave images in dependence on the master scene. Consequently, all co-registered images belong to the geometry of the master image. The procedure comprises in general the repeated detection and description of potential key points, their matching and finally the homography calculation using suitable matches to carry out the perspective transformation. For the App implementation, we make use of OpenCV's framework, version 3.1.0 for Android development (Bradski, 2000).

Using the Harris-Operator presented by Harris and Stephens (1988) for the fast detection of potential feature points in each image, only image points that refer to discrete corners are considered like stones, railings or walls. For feature description, we use the scale-invariant feature transform (SIFT) algorithm followed by fast feature point matching, described in Lowe (2004) and Muja and Lowe (2009). At least we need a minimum of four good matches to calculate the homography of each master-slave image pair. Otherwise, the slave has to be rejected (which may result due to blurred images). In doing so, RANSAC is applied with a threshold of three pixels to detect and eliminate outliers affecting the transformation. With the aid of the estimated slave image points that refer to individual positions as a function of the master point coordinates, the slave images could be co-registered in consideration of the master geometry using a perspective transformation with cubic interpolation. Obviously, the approach does not need further input data for image registration, but account must be taken during data acquisition. The homographies may not handle major changes in scale well which means that the camera must be held steadily until the acquisition has finished. However, this should not cause problems in case of short time lapse image sequences.

9.3.2 Investigation of spatio-temporal texture

The investigation of spatio-temporal texture as well as the average image are treated relating to previously introduced image co-registration. Moreover, the transformed images are checked in a consecutive manner for absolute pixel differences. Difference images thus generated are summed up and map the magnitude of spatio-temporal variability known as spatio-temporal texture (see Figure 9.3, bottom). Additionally, the average image of the processed image sequence is calculated pixel by pixel per mean value. Referring to this, the appearance of the original dynamic image content belongs to a homogenized surface, depending on image frequency and observation time. In case of time lapse sequences, the representation of running rivers looks almost homogeneous or smoothed. Figure 9.4 shows a single image of a shallow urban river (study area (I)) in comparison to its average image and the appropriate spatio-temporal texture, calculated with 15 co-registered images (3 fps, 5 s).

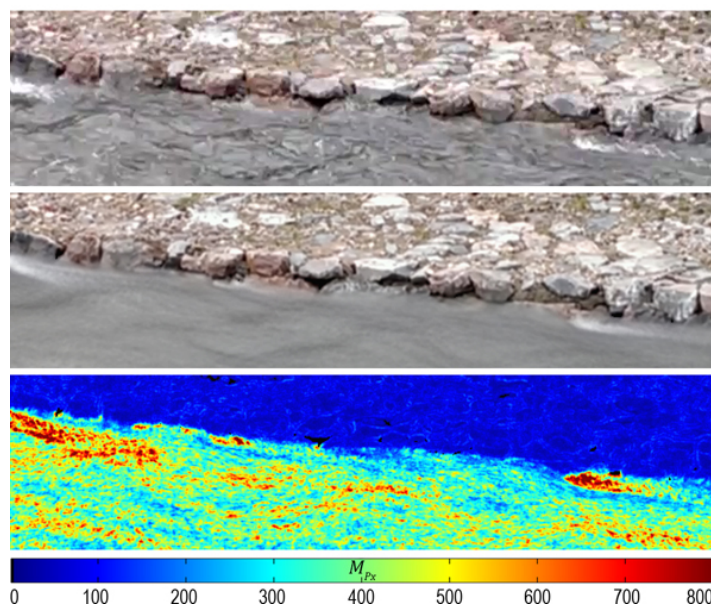


Figure (9.4): Detail view of a co-registered time lapse image sequence taken with 3 fps over 5 s in study area (I). Top down: master image, associated average image & spatio-temporal texture visualized by observed pixel magnitudes M_{Px} .

9.3.3 Histogram analysis

After texture calculation, the user is requested to trace the water line within the displayed average image (see Figure 9.3, top right). In doing so, every selected image point that refers to the initial water line is captured. To specify the ROI for further processing, the line has to be expanded by a defined value orthogonally using the respective points. The extension value initially amounts to 50 pixels but can be adapted using the GUI to fit the prevalent camera resolution and object distance. Using the water line selection and the buffered region, one of the halves represents the major part of static and the other one the part of dynamic features. Closing up, the algorithm is trained by a single finger tap inside the most static image region which refers to the land area.

Immediately afterwards, the temporal variability of both regions is investigated respectively through spatio-temporal histograms (see Figure 9.3, bottom left). The number of bins amounts to the spatio-temporal magnitudes within the defined ROI. We assume that both histograms

are highly different because of immutable and non-rigid image contents. Afterwards, both histograms are correlated to qualify their similarity. In case of a correlation coefficient less than 90%, both regions can be clearly separated by pixels spatio-temporal variability. Consequently, the spatio-temporal texture provides a sufficient basis for the segmentation via the characteristics of imaged dynamics. Otherwise, both regions appear too similar in their spatio-temporal texture which may be caused by the image acquisition system or environmental issues like deep shadows or reflections. However, less spatio-temporal texture is associated with less variabilities inside of the imaged running water. Thus, average image serves as a complementary alternative for the following segmentation of water and environment due to its homogeneous appearance. Both types are visualized in Figure 9.5 and Figure 9.6.

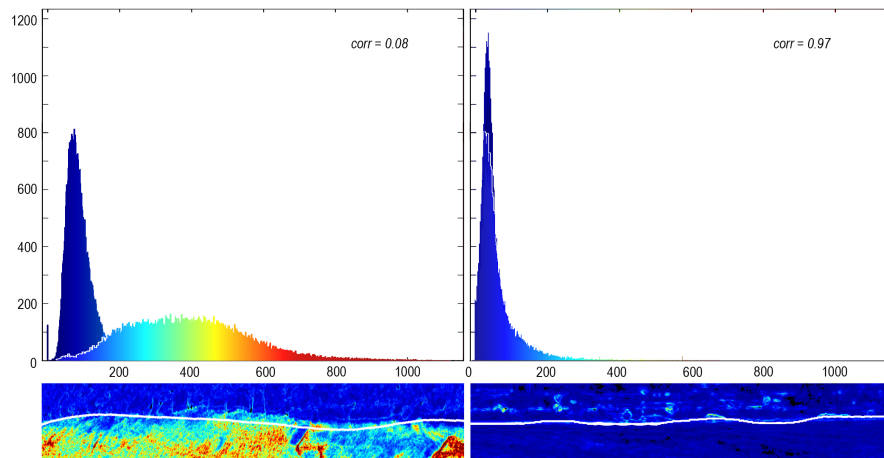


Figure (9.5): Histogram analyses of spatio-temporal textures in relation to respective ROIs. Left: Study area (II), dissimilarities enable spatio-temporal texture, correlation factor $corr = 0.08$. Right: less spatio-temporal variability ($corr = 0.97$).

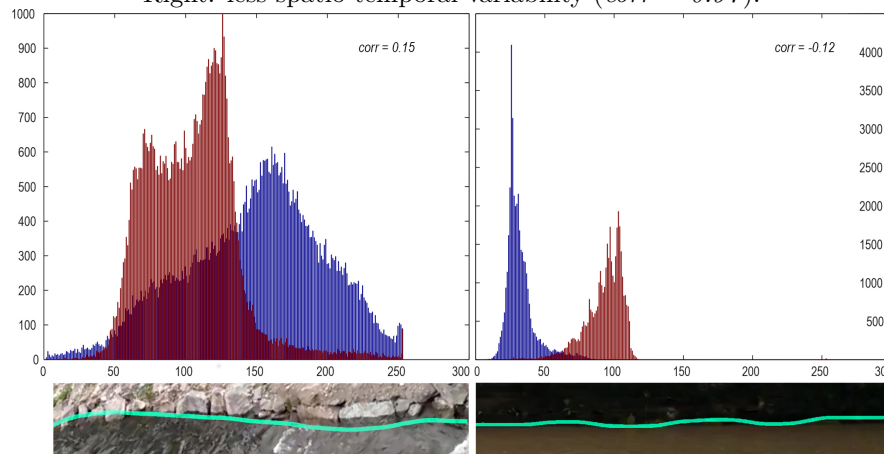


Figure (9.6): Histogram analysis of average image in respect of respective ROIs. Left: gray level distribution of mean values provides no useful information for image segmentation. Right: Study area (III), classifiable due to homogenized image content by averaged gray values.

For shallow water in study area (I) it could be noticed that the spatio-temporal texture provides a good basis for image segmentation with respect to the static area. In contrast to this, the average image holds good for a region growing-based image separation in consideration of the homogenized water surface, approved in study area (III).

9.3.4 Image segmentation by region growing

Depending on the results of the histogram analysis, either the spatio-temporal texture or the average image serves as input for image segmentation. We decided to use region growing because of its simplicity due to multiple seed point definition with a clear representation of image properties as well as its robustness against image noise (Kamdi and Krishna, 2012). Moreover, region growing is able to detect connected regions in dependency of variable pixel neighborhoods. A well-known shortcoming of region growing is the high computation time. Hence, we use the defined ROI to restrict the search area which enhances the processing time significantly.

The approach compares the prevalent attributes of a seed point with the characteristics of its close proximity. In doing so, a defined threshold value (or vector for multiple attributes) serves as a criterion for similarity between the starting point and the investigated neighborhood. If similarity is given, the considered points belong to one image segment whose boundary provides the points now to check for neighbor affiliations. In case of non-fitting points or when the boundary of the defined ROI is reached, the procedure terminates.

According to the input data the parameters for both, seed point and threshold should be defined automatically. Section "Segmentation by spatio-temporal texture analysis" describes the steering based on the spatio-temporal texture whereas Section "Segmentation using the average image" regards the approach using the average image.

Segmentation by spatio-temporal texture analysis

In case of significant spatio-temporal texture, the definition of seed points depends on the initial masked area that relates primarily to immutable image content. Probably, changes which may occur from weather influences like rainfall or changing light conditions in case of moving clouds would lead to spatio-temporal noise. Another reason for noise may cause by small residual errors in the image sequence co-registration. Thus, we look for a threshold that corresponds to the main area of static image content while neglecting outliers. A solution for the issue is provided by the associated histogram whereas the threshold belongs to the most prevalent magnitude. Image points whose attributes equals the threshold value are carried out as potential seed points. One of the seeds is randomly selected as starting point for a first iteration. All values that show less or equal temporal stability $I(x, y) \leq thresh$ are assigned to the region of immutable image content. The remaining seeds are checked for their region assignment and if necessary, the process repeats until all predefined seeds are in connection by means of the developed region. This conversely means that the left pixels within the ROI point to dynamic image content and thus to running water (see Figure 9.7).

Segmentation using the average image

If the spatio-temporal texture may not be sufficient to qualify distinct areas of motion and rigidity, the average image offers a great alternative for region growing. Leading edges within the ROI mainly represent contours between immutable and variable objects due to homogenized image content. For this, an edge map is generated by means of the Gaussian blurred mean value using the Canny (1986) edge detector with an automatic defined threshold by application of Otsu's approach (Fang et al., 2009; Otsu, 1975). Because of its simplicity only one seed point within the homogenized surface is needed for region growing based image segmentation. For this, we determine the closest bounding box around the masked water

area with regards to the ROI using its center as seed point. When executed, the approach terminates in case of striking an edge value (see Figure 9.8).

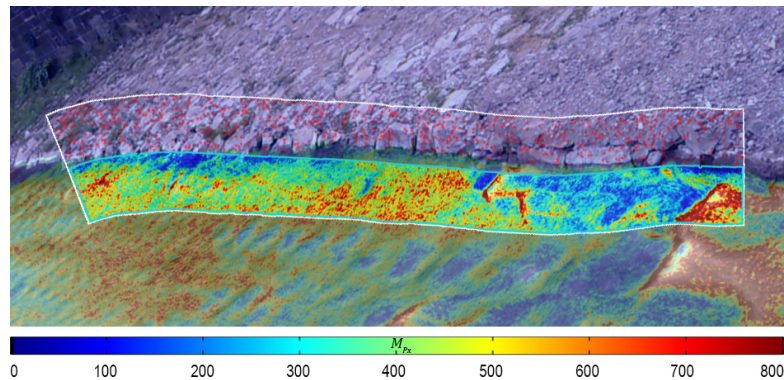


Figure (9.7): Spatio-temporal texture overlay referring to study region (II).

White polygon: ROI from coarse water line preselection,
 Blue polygon: Initial water body pointing to dynamic image content; Red dots: Potential seed points.



Figure (9.8): Average image with canny edge map overlay of study region (III).

White polygon: ROI from coarse water line preselection; Blue polygon: Initial water body pointing to homogenized dynamic image content; Red: Seed point.

9.3.5 Water line detection

Closing the processing, the water line is derived using the observed image segments. Whether for the region of immutable image content, examined by spatio-temporal texture or for the dynamic image part, described by means of the alternatively engaged average image of the time lapse image sequence, the resultant shape covers the shore line being observed. But apart from the water line, the contour also comprises points near or upon the ROI boundary and have to be eliminated. Region Growing can detect undercuts which may occur e.g. due to rising stones in the near shore area. For our water level monitoring system, we only need one shoreline which is why we eliminate such occurrences by means of Cleveland's Locally Weighted Regression (Cleveland, 1979).

9.4 Experimental research and results

As already was mentioned, we apply the algorithm in different study areas using several camera constellations and two time lapse configurations respectively (see Table 9.1 above). Regarding each processing step, the processing times are listed in Table 9.2. The size of bounding boxes (labeled 'BBox' in Table 9.2) helps to qualify the processing time regarding

the initial ROI. It should be mentioned that the first step refers to the whole image to ensure a sufficient number of suitable features for image co-registration regarding the running water environment. Both, the average and the spatio-temporal texture are generated parallel to the images co-registration but without a significant influence to processing time. The investigation results for the urban study areas (I)–(IV) and the rural areas (V)–(VII) are visualized in detail in Table 9.3 (description in caption).

Table (9.2): Summary of processing times regarding two frame rates of 3 & 5 fps with a time lapse interval of 5 seconds to observe the study areas (I)–(VII). Bounding box (BBox) for ROI description in pixels. Processing times in seconds with respect to single processing steps: (1) Co-registration, average image & spatio-temporal texture calculation, (2) Histogram analysis & initialization of step (3) image segmentation, (4) water line extraction.

	Urban areas						Rural areas							
Study region	(I)		(II)		(III)		(IV)		(V)		(VI)		(VII)	
BBox	(765x140)		(1395x135)		(1755x185)		(550x1650)		(984x216)		(692x253)		(643x213)	
Processing times														
Frame rate	3	5	3	5	3	5	3	5	3	5	3	5	3	5
Step 1	45.4	83.3	43.9	86.0	47.1	78.5	44.5	80.3	47.8	86.2	44.3	85.1	43.1	83.2
Step 2	1.4		1.9		0.8		0.6		1.0		1.4		1.2	
Step 3	9.1		12.1		6.4		6.7		5.6		4.7		3.8	
Step 4	0.3		0.4		0.4		0.1		0.2		0.2		0.1	

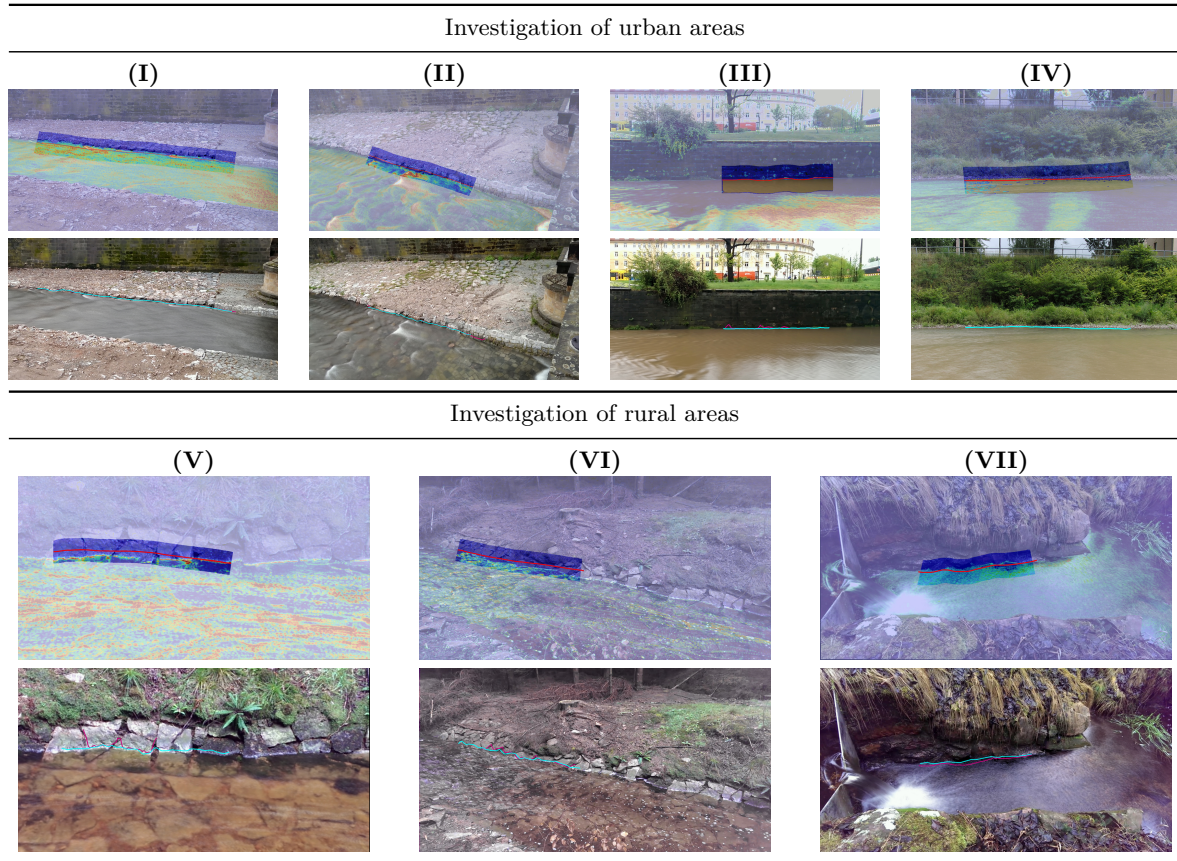
9.5 Evaluation and discussion

Our paper presents a reliable approach for mobile image segmentation on the basis of mapped image dynamics with the objective of a versatile water level measurement system. We show an enhancement of the approach from Kröhnert (2016) with respect to processing time and image adjustment, proven in several urban and rural regions with differing running rivers and environmental situations. Furthermore, we integrate an alternative processing for images with less spatio-temporal information. Our approach is (semi-) automatically steered with a unique user interaction to define the region of interest.

As being expected, the bottleneck regarding processing times occurs due to images co-registration. The longest times are taken by feature detection and description using SIFT that affects the first processing step only in respect of varying frame rates. The times for the remaining processing steps stay -compared to the different frame rates- mostly the same or very close together which is why we have not provided an individual statement for each (see Table 9.2). Compared to other feature detectors like ORB (see Kröhnert, 2016), SIFT's accuracy and robustness were given priority over processing time. Naturally, the hard tasks are processed in background to avoid an overloaded UI thread.

In conclusion, the water line could be successfully derived in all experiments. Thereby, a time lapse initialization with a frame rate of 3 fps and a sequence length of 5 s seems to be the best combination that covers the most urban and land river characteristics due to flow velocity and does take account of processing time. Higher frame rates result in more images being processed and thus to avoidable long processing times. Furthermore, Table 9.2 shows that the processing time increases nearly exponential with respect of the image number. In this connection, an important point that should be kept in mind is the spatio-temporal noise which may occur due to scaling issues during homography calculations. The stronger users

Table (9.3): Experimental investigations of water lines using the spatio-temporal texture (urban study areas (I) & (II)) and rural areas (V)-(VII) or the average image (urban study areas (III) & (IV)) for image segmentation. Top rows: Overlay of average & spatio-temporal texture image containing masked ROI & initial shore line (red). Lower lines: determined water line using 3 fps (blue) & 5 fps (pink) for investigation.



motion and the higher the number of images, the more noise may occur and distort the result (see Table 9.3, study area (V)). The same applies for high changing backgrounds of shore environments which may lead to a high amount of falsely taken key points that could not be detected by RANSAC (e.g. vegetation moving in the wind).

Finally, it should be noticed that the investigated boundary reflects the mapped situation and is valid for the corresponding observation time only. For the derivation of instantaneous water levels, this may not be relevant but should be considered in relation to other possible applications.

9.6 Future work

To improve the approach, future enhancements could deal with the bottleneck of processing time by outsourcing calculations to the graphic chip (GPU processing). Furthermore, the region growing needs more investigation in case of occurring leaks that are a frequently treated problem in image processing concerning region growing approaches. In our investigations, we have not detected large leaks but we cannot exclude that they will not have influences on water line derivation in general.

The main aspect being developed comprises the intersection of the derived water line and digital terrain data to transfer the image to the object space which allows for the on-the-fly water level determination. Moreover, we will be able to verify the derived water levels with conventionally acquired data and estimate the accuracy.

Acknowledgements

Gratefully, we acknowledge the European Social Fund (ESF) and the Free State of Saxony for their financial support on a grant.

References

- Agarwal, A., B. Boessenkool, M. Fischer, I. Hahn, L. Kohn, J. Laudan, T. Moran, U. Ozturk, A. Riemer, V. Rozer, T. Sieg, K. Vogel and D. Wendi (2016). *Die Sturzflut in Braunsbach, Mai 2016 - Eine Bestandsaufnahme und Ereignisbeschreibung. Final Report Taskforce DFG graduate college Natural Hazards and Risks in a Changing World: 'Flash Flood in Braunsbach (Germany) in May 2016'*. Research rep. Universität Potsdam. URL: https://gfzpublic.gfz-potsdam.de/pubman/item/item_1659896.
- Bradski, G. (2000). "The OpenCV Library". In: *Dr. Dobb's Journal of Software Tools* 25, 11, pp. 120–125.
- Canny, J. (1986). "A Computational Approach to Edge Detection". In: *IEEE Transactions on Pattern Analysis and Machine Intelligence* PAMI-8, 6, pp. 679–698. DOI: 10.1109/tpami.1986.4767851.
- Ciregan, D., U. Meier and J. Schmidhuber (2012). "Multi-column deep neural networks for image classification". In: *Proceedings of 2012 IEEE Conference on Computer Vision and Pattern Recognition. Providence, RI, US (16–21 Jun 2012)*. IEEE, pp. 3642–3649. DOI: 10.1109/CVPR.2012.6248110.
- Cleveland, W. S. (1979). "Robust Locally Weighted Regression and Smoothing Scatterplots". In: *Journal of the American Statistical Association* 74, 368, pp. 829–836. DOI: 10.1080/01621459.1979.10481038.
- de Martino, M., F. Causa and S. B. Serpico (2003). "Classification of optical high resolution images in urban environment using spectral and textural information". In: *Proceedings of IGARSS 2003. 2003 IEEE International Geoscience and Remote Sensing Symposium. Proceedings (IEEE Cat. No.03CH37477). Toulouse, FR (21–25 Jul 2003)*. Vol. 1, pp. 467–469. DOI: 10.1109/IGARSS.2003.1293811.
- Fang, M., G. Yue and Q. Yu (2009). "The Study on An Application of Otsu Method in Canny Operator". In: *Proceedings of 2009 International Symposium on Information Processing (ISIP'09). Huangshan, CN (21–23 Aug 2009)*. Academy, pp. 109–112.
- Ferro, C. J. and T. A. Warner (2002). "Scale and texture in digital image classification". In: *Photogrammetric Engineering and Remote Sensing* 68, 1, pp. 51–63.
- Feyisa, G. L., H. Meilby, R. Fensholt and S. R. Proud (2014). "Automated Water Extraction Index: A new technique for surface water mapping using Landsat imagery". In: *Remote Sensing of Environment* 140, pp. 23–35. DOI: 10.1016/j.rse.2013.08.029.

- Gao, B.-C. (1996). “NDWI – A normalized difference water index for remote sensing of vegetation liquid water from space”. In: *Remote Sensing of Environment* 58, 3, pp. 257–266. DOI: 10.1016/s0034-4257(96)00067-3.
- Haralick, R. M., K. Shanmugam and I. Dinstein (1973). “Textural Features for Image Classification”. In: *IEEE Transactions on Systems, Man, and Cybernetics* SMC-3, 6, pp. 610–621. DOI: 10.1109/TSMC.1973.4309314.
- Harris, C. G. and M. Stephens (1988). “A Combined Corner and Edge Detector”. In: *Proceedings of 4th Alvey Vision Conference. Manchester, UK (31. Aug–02. Sep 1988)*. AVC, pp. 147–152. DOI: 10.5244/C.2.23.
- He, K., X. Zhang, S. Ren and J. Sun (2016). “Deep Residual Learning for Image Recognition”. In: *Proceedings of 2016 IEEE Conference on Computer Vision and Pattern Recognition (CVPR). Las Vegas, NV, US (27–30 Jun 2016)*. IEEE, pp. 770–778. DOI: 10.1109/cvpr.2016.90.
- Hu, Y., J. Carmona and R. F. Murphy (2006). “Application of temporal texture features to automated analysis of protein subcellular locations in time series fluorescence microscope images”. In: *Proceedings of 3rd IEEE International Symposium on Biomedical Imaging: Nano to Macro, 2006. Arlington, VA, US (6–9 Apr 2006)*, pp. 1028–1031. DOI: 10.1109/ISBI.2006.1625096.
- Kamdi, S. and R. Krishna (2012). “Image segmentation and region growing algorithm”. In: *International Journal of Computer Technology and Electronics Engineering (IJCTEE)* 2, 1, pp. 103–107.
- Kim, M., M. Madden and T. A. Warner (2009). “Forest Type Mapping using Object-specific Texture Measures from Multispectral Ikonos Imagery”. In: *Photogrammetric Engineering & Remote Sensing* 75, 7, pp. 819–829. DOI: 10.14358/pers.75.7.819.
- Koschitzki, R., E. Schwalbe and H.-G. Maas (2014). “An autonomous image based approach for detecting glacial lake outburst floods”. In: *International Archives of the Photogrammetry, Remote Sensing and Spatial Information Sciences* XL-5, pp. 337–342. DOI: 10.5194/isprsarchives-XL-5-337-2014.
- Krizhevsky, A., I. Sutskever and G. E. Hinton (2012). “ImageNet Classification with Deep Convolutional Neural Networks”. In: *Proceedings of 25th International Conference on Neural Information Processing Systems - Volume 1 (NIPS’12). Lake Tahoe, NV, US (Dec 2012)*. Curran Associates Inc, pp. 1097–1105. DOI: 10.5555/2999134.2999257.
- Li, B., H. Zhang and F. Xu (2014). “Water Extraction in High Resolution Remote Sensing Image Based on Hierarchical Spectrum and Shape Features”. In: *Proceedings of 35th International Symposium on Remote Sensing of Environment (ISRSE35). Beijing, CN (22–26 Apr 2013)*. Vol. 17. IOP Conference Series: Earth and Environmental Science. IOP Publishing Ltd, p. 012123. DOI: 10.1088/1755-1315/17/1/012123.
- Lowe, D. G. (2004). “Distinctive Image Features from Scale-Invariant Keypoints”. In: *International Journal of Computer Vision* 60, 2, pp. 91–110. DOI: 10.1023/B:VISI.0000029664.99615.94.
- Maas, H.-G., G. Casassa, D. Schneider, E. Schwalbe and A. Wendt (2010). “Photogrammetric determination of spatio-temporal velocity fields at Glaciar San Rafael in the Northern

- Patagonian Icefield”. In: *The Cryosphere Discussions* 4, 4, pp. 2415–2432. DOI: 10.5194/tcd-4-2415-2010.
- Maggiori, E., Y. Tarabalka, G. Charpiat and P. Alliez (2017). “Convolutional Neural Networks for Large-Scale Remote-Sensing Image Classification”. In: *IEEE Transactions on Geoscience and Remote Sensing* 55, 2, pp. 645–657. DOI: 10.1109/tgrs.2016.2612821.
- Muja, M. and D. G. Lowe (2009). “Fast approximate nearest neighbors with automatic algorithm configuration”. In: *Proceedings of 4th International Conference on Computer Vision Theory and Applications - Volume 1: VISAPP (VISIGRAPP 2009). Lisboa, PT (5–8 Feb 2009)*. INSTICC Press, pp. 331–340. DOI: 10.5220/0001787803310340.
- Nelson, R. C. and R. Polana (1992). “Qualitative recognition of motion using temporal texture”. In: *CVGIP: Image Understanding* 56, 1, pp. 78–89. DOI: 10.1016/1049-9660(92)90087-j.
- Otsu, N. (1975). “A Threshold Selection Method from Gray-Level Histograms”. In: *Automatica* 11, 285–296, pp. 23–27.
- Peh, C.-H. and L.-F. Cheong (2002). “Synergizing spatial and temporal texture”. In: *IEEE Transactions on Image Processing* 11, 10, pp. 1179–1191. DOI: 10.1109/TIP.2002.804265.
- Reyes-Aldasoro, C. C. and A. L. Aldeco (2000). “Image segmentation and compression using neural networks”. In: *Advances in Artificial Perception and Robotics CIMAT. Guanajuato, MX (23–25 Oct 2000)*, pp. 23–25.
- Sarp, G. and M. Ozcelik (2017). “Water body extraction and change detection using time series: A case study of Lake Burdur, Turkey”. In: *Journal of Taibah University for Science* 11, 3. [Preprint updated to Journal ver.], pp. 381–391. DOI: 10.1016/j.jtusci.2016.04.005.
- Szumner, M. and R. W. Picard (1996). “Temporal texture modeling”. In: *Proceedings of 3rd IEEE International Conference on Image Processing. Lausanne, CH (19 Sep 1996)*. Vol. 3. IEEE, pp. 823–826. DOI: 10.1109/ICIP.1996.560871.
- Tuceryan, M. and A. K. Jain (1999). In: *Handbook of Pattern Recognition; Computer Vision*. 2nd ed. World Scientific Publishing Co., Inc: River Edge, NJ, US. Chap. Texture Analysis, pp. 207–248. DOI: 10.1142/9789812384737_0007.
- Varma, M. and A. Zisserman (2005). “A Statistical Approach to Texture Classification from Single Images”. In: *International Journal of Computer Vision* 62, 1–2, pp. 61–81. DOI: 10.1023/B:VISI.0000046589.39864.ee.
- Verma, A. (2011). “Identification of land and water regions in a satellite image: a texture based approach”. In: *International Journal of Computer Science Engineering and Technology* 1, pp. 361–365.
- Xu, Y., Y. Quan, H. Ling and H. Ji (2011). “Dynamic texture classification using dynamic fractal analysis”. In: *Proceedings of 2011 International Conference on Computer Vision. Barcelona, ES (6–13 Nov 2011)*. IEEE, pp. 1219–1226. DOI: 10.1109/ICCV.2011.6126372.
- Zhang, Y. (1999). “Optimisation of building detection in satellite images by combining multispectral classification and texture filtering”. In: *ISPRS Journal of Photogrammetry and Remote Sensing* 54, 1, pp. 50–60. DOI: 10.1016/s0924-2716(98)00027-6.

10 From image to reality: Transferring 2D water lines into 3D object space to measure water levels

Chapter 10 published in "The Photogrammetric Record" (eISSN: 1477-9730) as:

Photogrammetric water level determination using smartphone technology

Authors: Melanie Elias^a, Christian Kehl^b, Danilo Schneider^a
^a Institute for Photogrammetry & Remote Sensing, TU Dresden, Germany
^b DTU Compute, Danmarks Tekniske Universitet, Kongens Lyngby, Denmark

Publication history: submitted 20th November 2018, accepted 08th April 2019, published 19th June 2019

Full reference: Elias, M., C. Kehl and D. Schneider (2019). "Photogrammetric water level determination using smartphone technology". In: *The Photogrammetric Record* 34, 166, pp. 198–223. DOI: 10.1111/phor.12280

Abstract: Rapid technological progress has made mobile devices increasingly valuable for scientific research. This paper outlines a versatile camera-based water gauging method, implemented on smartphones, which is usable almost anywhere if 3D data is available at the targeted river section. After analysing smartphone images to detect the present water line, the image data is transferred into object space. Using the exterior orientation acquired by smartphone sensor fusion, a synthetic image originating from the 3D data is rendered that represents the local situation. Performing image-to-geometry registration using the true smartphone camera image and the rendered synthetic image, image parameters are refined by space resection. Moreover, the water line is transferred into object space by means of the underlying 3D information. The algorithm is implemented in the smartphone application "Open Water Levels", which can be used on both high-end and low-cost devices. In a comprehensive investigation, the methodology is evaluated, demonstrating both its potential and remaining issues.

Keywords: Exterior orientation, Hydrology, Image-to-geometry registration, Outdoor application, Sensor fusion, Smartphone

10.1 Introduction

The past decade has been characterised by a continual increase, across the globe, of devastating flash floods after heavy rainfall. Conventional gauging stations provide precise information about water levels measured over short time periods. Because of the high purchase and maintenance costs associated with their complex sensing devices, gauging stations are located sparsely. Thus, many creeks and rivers are not monitored during flood events when the greatest protection is required.

As a result of these deficiencies, approaches for camera-based water-level gauging are envisaged to increase measurement coverage. Lin et al. (2018) used a digital single-lens reflex (DSLR) camera located on one side of a man-made river facility (channel or reservoir). The camera looked down on the opposite side of the channel, observing the water level in a marked calibration area to determine, on the one hand, the exterior camera parameters and, on the other hand, the reference water lines (indicated by straight lines within the camera image). This method allows for water-level detection with accuracies of about 1 cm. A similar technique was described by Hies et al. (2012). However, both approaches are limited to man-made facilities or artificial embankments adjacent to very calm waters, as well as to fixed, pre-calibrated cameras for observation. A more flexible method was published by Eltner et al. (2018) who installed low-cost cameras in small- and medium-scale catchment areas for long-term river observation. The camera images were used to detect the prevalent water line, which were further registered with metrically scaled 3D data to derive the water level.

Introduced by Kröhnert and Eltner (2018), smartphones with inbuilt low-cost cameras can serve as versatile measurement devices for camera-based water gauging, aiming at spatio-temporal densification of monitoring hydrological networks. Bruinink et al. (2015) proposed an accurate measurement technology utilising smartphones without requiring additional equipment, such as tripods, in the field. Water levels were detected by analysing smartphone images of pre-installed staff gauges. Depending on the staff gauge visibility, the automatically detected water levels matched the indicated values in 97% of observed cases. Unfortunately, this approach is limited to open and visible pre-installed staff gauges. The first (commercial) smartphone-implemented gauging tools that enable data crowdsourcing by the public have been published, for example, by Kisters (2014) and Etter and Strobl (2018). Nevertheless, in both applications the water level is observed by citizens who again photograph tide gauges close to rivers that may present a potential danger to themselves.

Considering the remaining issues in the established literature, this paper outlines an algorithmic approach for flexible camera-based water gauging, implemented in a smartphone application. Thus, tools are provided for citizen scientists enabling the acquisition of volunteered geographic information (VGI) that contributes to a hydrometric data inventory. The developed technology, visualised in Figure 10.1, can be divided into four steps:

1. Image acquisition with a hand-held smartphone camera and image-based 2D water-line detection.
2. Projection of previously recorded 3D data into a synthetic image (rendering) representing the same local situation as the real camera image.
3. Feature-based image matching between the real and synthetic images in order to establish the 2D–3D correspondence necessary for a subsequent space resection.
4. Transferring the image measurements (the detected 2D water line) into object space, and thus into metrically scaled 3D water-level values, using the 3D scene data and the exterior orientation determined by the space resection.

With regards to step 1 (image acquisition and 2D water-line detection), the reader is referred to Kröhnert and Meichsner (2017), which should be considered as an integral part of the proposed workflow. In a nutshell, short time-lapse image sequences of a target river section are used to distinguish a static shore area from a dynamic river area, which provides information about the water line. This is necessary to separate water from non-water areas in cases where the river is not distinguishable from its adjacent shore in a single image, for example, due to dynamic image content.

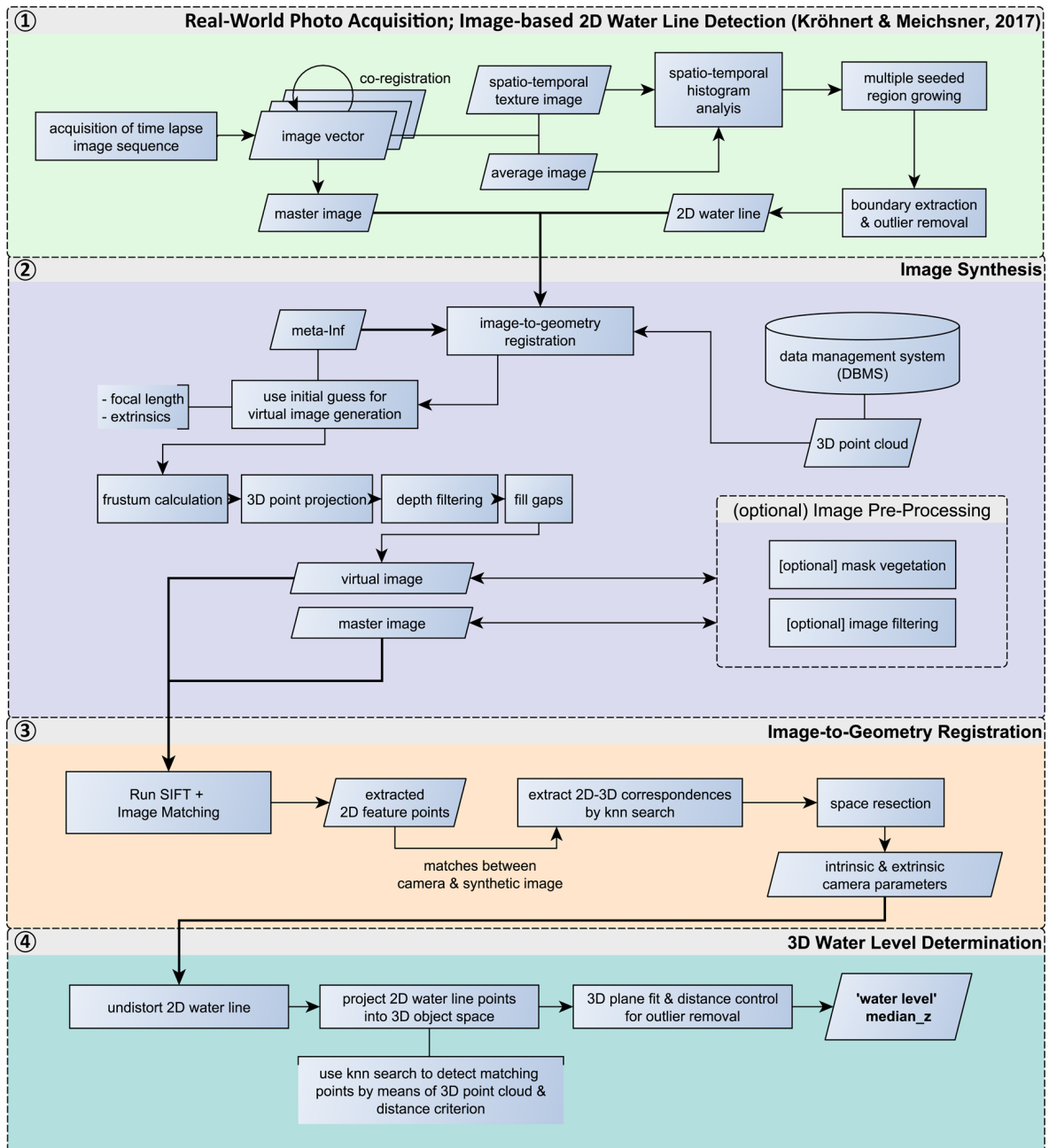


Figure (10.1): Four-step algorithmic concept for camera-based water gauging, implementing image-to-geometry registration.

The sections within this article describe steps 2 to 4, comprising the stages to establish the context of 2D image data and 3D object data, used to derive 3D water-level measurements from the image-based 2D water line. In the following sections the requirements, for instance the necessity for 3D data and initial values for the camera exterior orientation, are explained. The proposed algorithmic structure is then detailed, explaining the image synthesis (step 2), its usage for the subsequent image-to-geometry registration (step 3) and the transformation of image measurements into object space (step 4).

Practical implementation takes place by means of the Android application "Open Water Levels", for which the implementation constraints and the application scope are explained in detail in a dedicated section. Subsequently, a brief introduction about the software architecture assists in understanding the working principles concerning challenges in mobile software engineering. A comprehensive evaluation of the technology is conducted by means of a case study of an urban river to evaluate the technology's accuracy potential. This research also improves the general understanding of challenges regarding mobile sensor location and rotation, and their impact on the registration of true images with 3D object data. Besides these geometrical issues, radiometric variances are outlined, assessing their significance for water-level estimation with regard to future developments.

10.2 Prerequisites

10.2.1 3D data

Metrically scaled, georeferenced and coloured 3D data, covering the nearshore environment of a targeted river section, is fundamentally necessary for the presented approach. The 3D data is used to determine the exterior orientation of the smartphone image via image-to-geometry registration and to scale the image-based 2D water line. Thinking of 3D representations in their simplest form, dense 3D point clouds can be acquired quickly by applying, for example, compact laser scanning systems (Blaskow et al., 2018) or image-based methods for 3D reconstruction, such as structure from motion (SfM). When trying to match 2D camera images and 3D object data in terms of a synthesised image, it is advisable to have an option of 3D datasets, captured at different times but covering the same location, that can be used for synthetic image rendering. In this way, the most appropriate 3D dataset matching the camera image can be chosen with consideration to spatio-temporal changes in terms of radiometry (such as vegetation or snow coverage, or illumination differences (Figure 10.2)), or geometry (for example, terrain alteration).

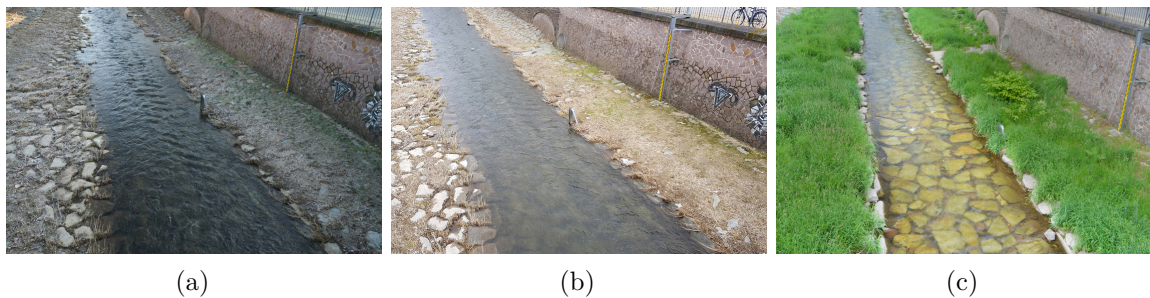


Figure (10.2): Radiometric variances regarding the case study of River Weißeritz in Dresden-Altplauen, Germany. Images captured on: (a) 14th February 2018 at 08:30; (b) 30th March 2018 at 16:00; and (c) 23rd May 2018 at 18:00.

Both the accuracy of the determined exterior orientation and, conversely, the accuracy of the scaled 2D water line, directly depend on the 3D data. Thus, the 3D data needs to be precisely measured, scaled and georeferenced in order to establish a joint coordinate system between the initial exterior orientation of the real camera image, which is described below, and the 3D data. Furthermore, the 3D data should include red/green/blue (RGB) or intensity values that are necessary for image-to-geometry registration.

However, challenges arise from the rareness of readily available 3D datasets of (critical) shore environments which have complied with all the above conditions; they are primarily acquired on a case-by-case basis. Thus, several current research projects aim at acquiring hydrological parameters as well as land (shore and river bank) information in terms of high-resolution 3D point clouds in short time spans on large scales utilising a boat which is equipped with different sensors, such as laser scanners and cameras (Scherer et al., 2012; Nuske et al., 2015; Sardemann et al., 2018). Outside the academic research environment there is also a significant economic interest in river mapping, such as Google River View, providing an option for expansion to many rivers on a global scale.

10.2.2 Initial values for the 3D position

Besides the 3D data, knowledge about the camera exterior orientation is necessary to initially restore the collinearity condition between the image and the object data. Using smartphones as measurement devices carries a decisive advantage: most are equipped with global navigation satellite system (GNSS) receivers, determining the georeferenced device position. Furthermore, low-cost sensor systems for rotation assessment are widely integrated into smartphones, mostly used for display rotation control. Recently, many research groups discussed the accuracy potential of smartphone outdoor localisation strategies, as summarised in Table 10.1. Regarding height estimation, error margins should be expected to be 2.5 times higher compared with the horizontal components (for example, Liu et al., 2014).

Table (10.1): Investigation of smartphone potentials regarding absolute positing via inbuilt sensors.

Research group	Device	Lateral accuracies	Immediate surroundings
Blum et al. (2013)	iPhone 4	10-15 m	Buildings <3 floors
Fritsch et al. (2011)		30-60 m	Skyscrapers >3 floors
Zhu et al. (2013)	HTC Hero	15-25 m	-
Zandbergen and Barbeau (2011)	Nexus S	6-8 m (mean)	-
Meek et al. (2013)			

10.2.3 Initial values for the 3D rotation

As the initial values are one of the most critical factors for a successful outcome, this paper describes their influence on the success of the suggested approach in the Section 10.6.1 "Geometric challenges". From evaluation of the experiments, it is argued that smartphone rotation values, captured by their inbuilt sensors, are unstable and drastically less reliable compared to the values produced by professional inertial measurement units (IMUs). With regard to the globally aligned azimuth angle, errors of more than 30° need to be expected. If affected by electromagnetic disturbances (such as having metallic handrails close to the device) these errors will increase significantly, resulting in completely wrong directions due to

a worse signal-to-noise ratio (SNR) of the magnetometer (Blum et al., 2013; Kok et al., 2017). As well as the azimuth, the pitch and roll angles are determined using an accelerometer and a gyroscope. Both sensors measure angular acceleration but, respectively, suffer from a poor SNR and drift effects. Thus, sophisticated approaches apply sensor fusion, which combines sensor data with complementary properties to improve the stability and accuracy of rotation values (Pacha, 2015).

10.3 Algorithmic description

After detailing the prerequisites of the outlined topic, the focus is on the three main steps after water-line detection, as shown in Figure 10.1. First, the technique necessary for image synthesis using a 3D point cloud is introduced (step 2). The next subsection deals with the image-to-geometry registration itself, based on true-to-synthetic image matching (step 3). The last subsection looks at subsequent back-mapping of the 2D water line into 3D object space (step 4).

10.3.1 Image synthesis

Projection principle

In comparison to familiar mesh-based rendering approaches, as used for example by Kehl et al. (2016a) for mobile applications, point projection seems to be a good alternative for point-based rendering that saves computational resources. Here, object points are simply projected onto an image plane using perspective projection, applying the collinearity equation (for example, Luhmann et al., 2013c) assuming a distortion-free ideal camera with a central principal point (Meierhold et al., 2010) and the initial exterior orientation parameters given by the smartphone's sensors.

Frustum limitations

Performing the perspective projection for all object points is time-consuming, especially in the mobile rendering scenario. Due to object occlusion, observation distance and finite image resolution, it is also unnecessary to project all points to the image plane. Therefore, a region of interest for point projection is defined to cull the render content of the virtual camera to the user's field of view (see Figure 10.3c). The horizontal view frustum's bounding box is calculated using the position and azimuth angle from smartphone sensor fusion. Because of possible uncertainties regarding exterior information, the bounding box should be enlarged to guarantee that all visible points are included in the view frustum. Thus, the concept of "halo expansion" is applied from computer graphics to enlarge the frustum (see Figure 10.3a and 10.3b). An uncertainty correction in depth (distance from the camera) is performed by frustum expansion. Thus, the box is widened by the smartphone camera's horizontal H and vertical V view angles with a fixed depth d . The degree of parameter inaccuracy is derived from the sensor accuracy estimate as well as the provided camera characteristics.

Using the defined pyramidal view frustum as the region of interest with a local reference system, the image plane for 3D point rendering is defined by perspective projection of the remote XZ plane (Figure 10.3c) with equation (10.1) for the bounding-box background plane, described by its upper left $\mathbf{p}_{B_{ul}}$ and lower right corner $\mathbf{p}_{B_{lr}}$. Then, points outside the near and far clipping planes are eliminated using the pyramid frustum.

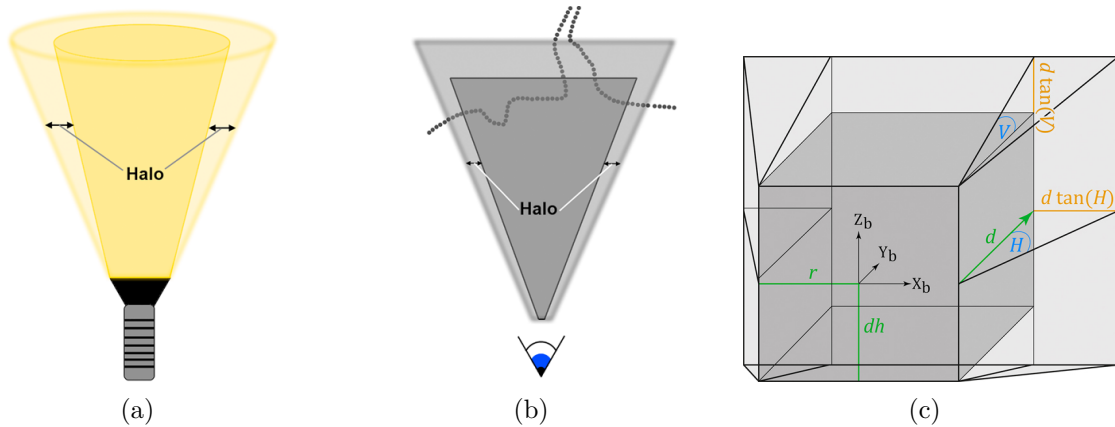


Figure (10.3): View frustum and halo expansion. (a) Visual analogue between partial illumination halo of a light bulb. (b) Partial visibility halo of perspective view and projection. (c) The defined bounding box.

$$\mathbf{P}_{B_{ul}} = \begin{pmatrix} -r - d \tan(H) \\ d \\ dh + d \tan(V) \end{pmatrix}, \dots \mathbf{P}_{B_{lr}} = \begin{pmatrix} r + d \tan(H) \\ d \\ -dh - d \tan(V) \end{pmatrix} \quad (10.1)$$

Overlapping projections

The finite image-plane resolution and limited point size during rasterisation result in multiple 3D object points corresponding to the same image pixel. Generally, image coordinates have no depth information and they prohibit resolving point visibility and occlusions a posteriori. In contrast, synthetic images originating from 3D data still retain a link to the underlying 3D coordinates. Thus, scale-space image pyramids of multiple synthetic images with halved image resolutions per layer are used to overcome occlusion ambiguities. Four pixels are combined, assigning the distance value of that pixel which is the closest to the virtual projection centre. By comparison of the determined depth values in the respective scales, hidden points can be isolated as they are not present in lower resolutions. In this context, a point is retained in the case where the calculated distances are similar at each scale; otherwise the point will be rejected due to high contrast in the depth image. Figure 10.4 visualises the issue of occlusion using the example of a building before and after correction.

Gap filling

In contrast to overlapping point projections, the finite image resolution results in gaps between the projected points, impeding, for example, feature-based image-to-geometry registration. A gap-filling algorithm provides a smoothly interpolated depth map using a binary search in the depth domain with respect to the nearest-neighbour points (Bentley, 1975), which preserves the underlying point cloud accuracy. Therefore, an empirically determined distance criterion of 2.5 cm was applied, meaning the closest point must be within the range of 2.5 cm of an object point. This is to avoid interpolating at object boundaries and extremal edges. If an object point is assigned, its colour information is used to fill the empty pixel. A before-and-after comparison applying this method is shown in Figure 10.5.

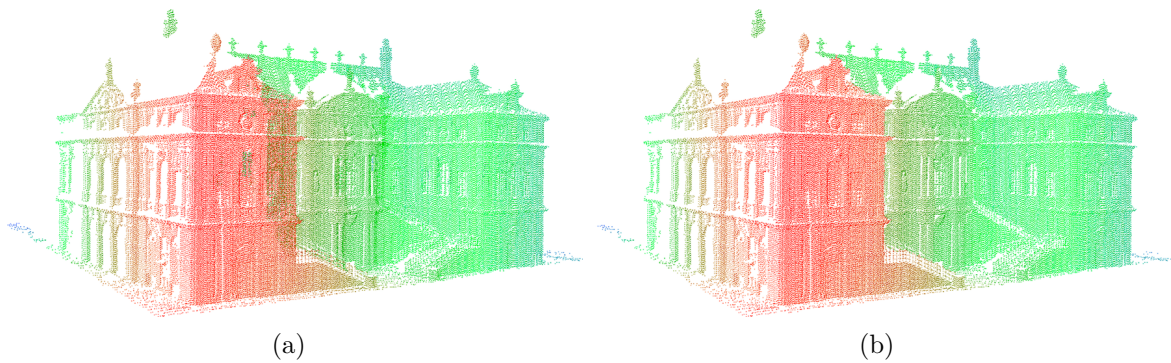


Figure (10.4): Occlusion ambiguities. (a) Translucent, falsely mapped 3D points. (b) Result after filtering. Colouration is a function of the distance from the virtual projection centre to the 3D object points (red – near; blue – far).

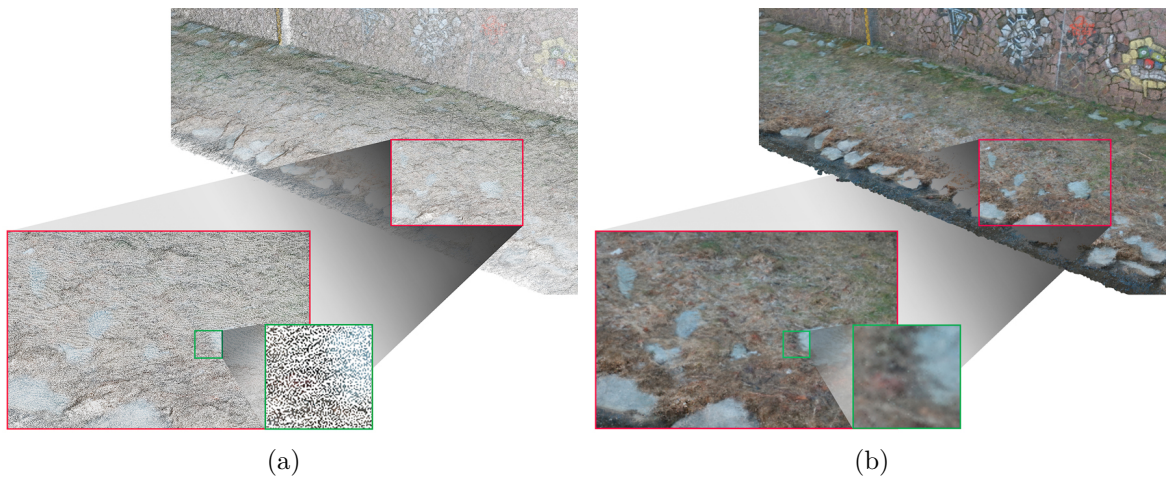


Figure (10.5): Visualisation of the gap-filling algorithm using the example of a 3D point cloud showing a shore area with stones and dried vegetation. (a) Projected points with gaps due to the discrete point cloud density. (b) Gaps between the projected points are filled by the gap-filling algorithm to provide continuous image information. Both images show the projected points of this 3D point cloud at the same scale.

10.3.2 Image-to-geometry registration

Image-to-geometry algorithms aim at the registration of 2D images to the given 3D data (Figure 10.6a), providing a transformation from 3D object points to 2D image coordinates. In this context, 3D coordinates are assigned to the synthetic image. Using this coordinate system transformation in combination with a known camera interior orientation it is, conversely, possible to project each image onto an appropriate 3D point cloud.

In the published literature, feature-based registration algorithms are the most common due to their implementation simplicity, rapid execution speed, application-specific constraints and the wealth of available code that can be used. Besides the applications already presented, these registration algorithms are frequently discussed in computer vision applications and literature, such as in augmented reality (Gauglitz et al., 2014; Sweeney et al., 2015). Salient points (for example, Mikolajczyk and Schmid, 2004) within the photograph and the rendered image of the target 3D model are used to establish a true-to-synthetic image correlation. Thus, the common matching approach combining the scale-invariant feature transform (SIFT) of

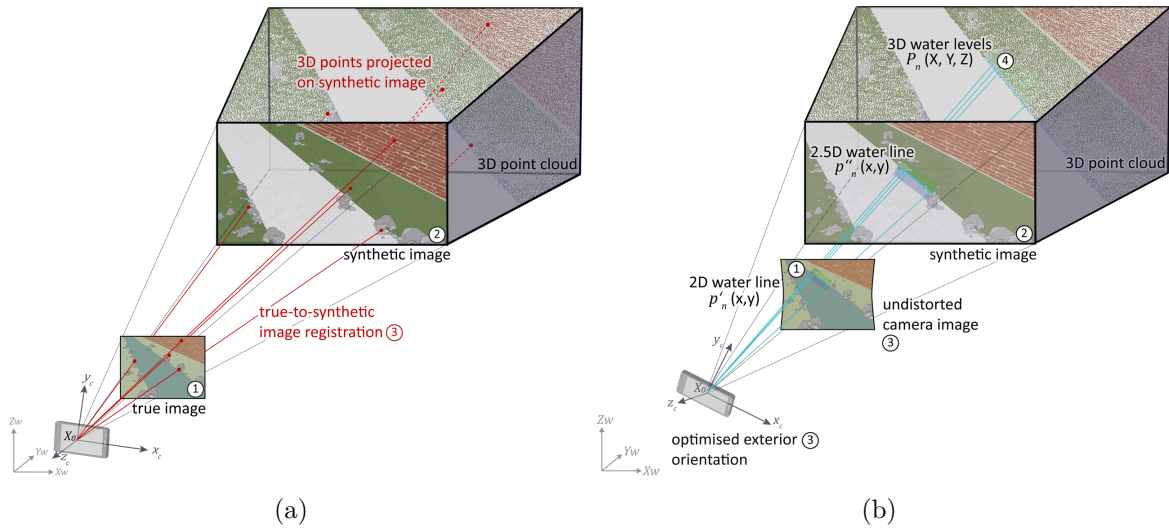


Figure (10.6): Visual workflow summary. Numbering corresponds to the steps given in Figure 10.1.

(a) Image-to-geometry registration using a synthetic image.

(b) Projection of the detected 2D water line into 3D object space.

Lowe (2004) with nearest-neighbour matching (Muja and Lowe, 2009) is advisable. Sattler et al. (2011) and Sibbing et al. (2013) have provided examples for this approach, which has also been implemented in this paper. In the case of slight illumination variations, local contrast adjustments can be applied before performing feature detection and description, for example, by applying Wallis or Gaussian filtering as described in Kröhnert et al. (2017) or Kehl et al. (2017). It has been previously demonstrated that image registration can work just by using terrestrial laser scanning (TLS) and its return signal intensity together with an RGB camera image (Wang et al., 2012; Guislain et al., 2016). However, this requires very stable radiometric (illumination) conditions and a prohibitively complex mutual information (MI) framework to retrieve reliable 2D–3D point correspondences to further determine the exterior orientation. Registering outdoor photographs with significant radiometric variance requires colour information for the photograph as well as the 3D point cloud of which the synthetic image is rendered (Kehl et al., 2017).

Once the true camera image and the synthetic image are registered, this image-to-image registration expands to the three-dimensional object space by assigning 3D coordinates to the matched image points of the true image. When these 2D–3D point pairs are used to calculate a space resection with the exterior orientation as unknown parameters, the sensor information serves as the initial parameters. If enough well-distributed 2D–3D point pairs are provided, together with a suitable initial estimate of the focal length (say, from manufacturer information), the camera interior orientation and lens distortion can be integrated as well (Wester-Ebbinghaus, 1985; Luhmann et al., 2013a) in order to support the description of the geometric relationship between image space and object space. "Well-distributed" means that the matched 2D image points should be distributed over the whole camera image with related 3D object points located at different depths. Non-linear optimisation systems, such as Levenberg–Marquardt, are applied to estimate the set of desired parameters (Torr and Zisserman, 2000). Alternatively, a direct linear transformation (DLT) can be applied which provides a solution in case the non-linear optimisation fails due to inadequate initial values for the interior or exterior orientation.

10.3.3 Water level determination

To transfer the 2D water line into object space (see Figure 10.6b), the determined interior and exterior orientation is used to assign the polyline of 2D points, representing the 2D water line, with 3D object points; the closest 3D point to the image ray is chosen with a distance criterion of 0.25 cm. Finally, the median value of the assigned 3D points is extracted to obtain one robust value pointing to the present water level.

10.4 Implementation

Mobile devices are ubiquitously available in modern society, so applications for a diverse range of purposes have emerged over the past decade. Such smartphones, used as digital field instruments with inbuilt cameras, sensors for rotation and position assessment, as well as powerful processing units, are also increasingly applied for scientific purposes. Within the geosciences, smartphones are gaining increasing popularity to solve computational tasks in outdoor and field-study environments, such as in mobile mapping (Westhead et al., 2013; Masiero et al., 2016; Ishihara et al., 2017) or 3D reconstruction and visualisation (Rodriguez et al., 2012; Muratov et al., 2016; Kehl et al., 2019). Geoscience apps for assessing 2D and 3D data have been available for several years now: examples include geological field interpretations as demonstrated by Kehl et al. (2016b), Viseur et al. (2014) and Hama et al. (2013). Such application domains benefit from developments in acquisition technology allowing the analysis of the data on small-scale devices directly in the field.

What makes mobile software distinct is the modality of the supported device. On the one hand, the mobility, array of sensors, inbuilt cameras and opportunity to connect to mobile networks are great advantages compared with conventional workstations. On the other hand, a number of non-functional requirements need consideration regarding mobile software design (Wasserman, 2010). A well-known issue is the way user interaction has to take place on small touch screens. More serious problems are the diversity of hardware suppliers and varying quality between flagship smartphones and low-cost devices. Great disparities in the camera or sensor qualities, in particular, lead to major issues developing tools, for example, for geodetic purposes. Furthermore, severe restrictions on data memory and power consumption are non-trivial issues for field tasks.

The outlined concept for flexible and camera-based water-level gauging is implemented in an open source application named "Open Water Levels", which is based on a client-server architecture (Weiss and Lockhart, 2012; Shahbudin and Chua, 2013) as visualised in Figure 10.7. Lightweight tasks can be processed directly on the device, whereas very time- and memory-intensive computations are outsourced to remote workstations. In this way, the efficiency of the app can be guaranteed, even for low-cost devices.

10.4.1 Client implementation

Generally, the client application of Open Water Levels can be implemented on smartphones and tablets running Android 4.3 (released in July 2013). However, it is recommended to use newer versions (Android 5.0 or higher) due to the optimised camera management. At its core, the app is based on the comprehensive open source Android camera framework "Open Camera" (Harman, 2017). The client-implemented lightweight tasks include, in particular:

1. Time-lapse image acquisition, processing and 2D water-line detection (see Kröhnert and Meichsner, 2017, for more details about the implementation.)
2. Determination of the initial camera exterior orientation using smartphone sensors.
3. Collecting metadata information about the smartphone camera, that is approximate values of the camera interior orientation and the acquisition time to support the selection of convenient 3D data, referring to season and time of day.

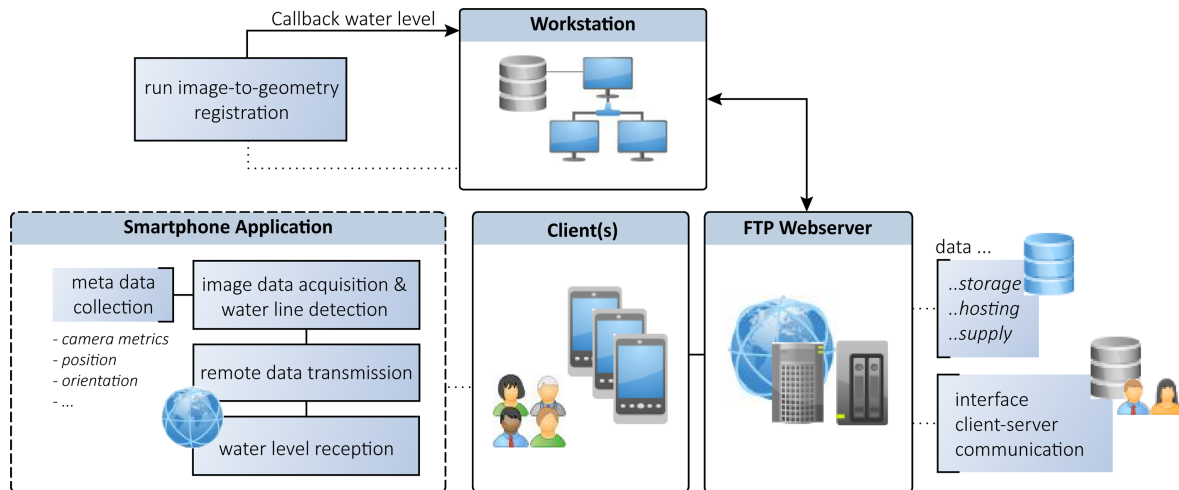


Figure (10.7): Client-server architecture applied to "Open Water Levels" (adapted from Kröhnert and Eltner, 2018).

Referring to task (1), Open Water Levels implements the image processing library OpenCV 2.4.11 (Bradski, 2000)¹. To determine the initial exterior orientation (task 2), the Cordova plugin "Sensor-Fusion" is integrated into the app, providing a sensor-fusion approach developed by Pacha (2015). This virtual sensor implements weighted data from the physical sensor's accelerometer, gyroscope and magnetometer to obtain rotation values; these are more precise but less stable. Collecting the metadata is triggered by the first shot of the time-lapse image sequence used for 2D water-line detection. Thus, the rotation values do not necessarily have to be stable in the long term. Otherwise visual odometry can be applied to reset the IMU using the time-lapse images. Regarding the initial estimate of the camera interior orientation, the principal distance specified by the manufacturer is used (task 3).

In order to locate the smartphone within the 3D data, a joint coordinate system is a prerequisite. Open Water Levels use the inbuilt GNSS sensor to receive initial position values in the Universal Transverse Mercator (UTM) common global reference frame, with elevation data above the World Geodetic System 1984 (WGS 84) reference ellipsoid. Beside the position information, Android returns the horizontal accuracy. Thus, viewpoints being critical due to shadings of the signals can be identified prior to the measurements. As described in the Section 10.2 "Prerequisites", the errors in elevation determination are 2.5 times higher than the horizontal component. Considering this uncertainty range, Open Water Levels is able to call the Google elevation service (Google Maps Platform, 2019) for improvements, which stores elevation data from diverse private and public suppliers.

¹Correction of a quotation mistake in the original paper.

10.4.2 Data exchange and selection

Besides the client application, a web interface is provided for client–server communication that watches for incoming data from connected clients which are transferred via the file transfer protocol (FTP). All the data (the 2D water line; the image to which the sequential time-lapse images are registered (Figure 10.1, step 1); and the collected metadata) is stored locally until the transfer to the exchange server. This intermediate layer manages both the received client data and the attributed 3D data. After successful transmission, an attempt is being made to find an entry in the database suitable for image-to-geometry registration. Therefore, storing the tiled 3D data with meta-information (such as location, time and date of data acquisition) helps the connection with incoming 2D data via a rapid geometry-in-frustum containment check. If there are multiple point clouds which are close to the initially given user position (for example, captured at different times and seasons), the dataset with the most similar temporal resolution, compared to the input data timestamp, is chosen for further processing. With regard to the data streams, the workstation has a continuous connection to this exchange layer. In this context, the user decides whether the client application opens the server communication only for file transmission, or closes the connection once the data is processed to get information about the results. Thanks to smartphones' inbuilt mass storage, the input data can also be saved temporarily and transferred (after Internet connection delays) for post-processing in cases of missing connectivity to a mobile network.

10.4.3 Server implementation

The Section 10.4.1 "Client implementation" above has already outlined lightweight tasks (1) to (3). Once the appropriate 3D data has been selected, the following four heavyweight tasks are performed on the workstation:

4. Image synthesis.
5. Point-based true-to-synthetic image matching.
6. Space resection to determine the camera exterior and interior parameters.
7. Transferring the 2D water line into 3D object space.

Tasks (4), (6) and (7) are implemented in C++, including the latest version of the image processing library OpenCV 3.0. More details about the OpenCV framework are given in the original paper of Bradski (2000). Task (5), comprising feature-based image matching to assign the true camera image and the synthetic image, is outsourced to SiftGPU (Wu, 2007) that returns the inlier matches for image-to-geometry registration.

10.5 Evaluation

Currently, the remote database of Open Water Levels contains 3D data of three urban river sections in Dresden, Germany, two captured during winter and one in summer. For evaluation purposes, attention was focused on the case study of the River Weißeritz in the district of Dresden-Altplauen (shown in Figure 10.2). This area was affected by flash flood events two times in the last decade, with devastating damage to buildings and infrastructure. Usually, the medium-scale river width here is about 9 m, having an average water discharge rate of about $3 \text{ m}^3/\text{s}$.

In the target section an administrative gauging station, which was installed after the large flood in 2002, operates day and night to provide water levels every 15 minutes on average (Extruso, 2019). Besides its gauging staff, a self-registering pressure sensor has been installed to gauge

water stages with accuracies of a few millimetres for idealised river profiles. (In hydrology, *stage* refers to the water level in a river relative to a chosen reference height.) Due to the uneven riverbed and the irregular embankment at the Weißeritz, water-level accuracies of 1 to 2 cm can be expected. However, the base measurements comply with state requirements and serve as ground truth to evaluate the smartphone-implemented camera-based water gauging approach. A schematic representation of the gauging systems is given in Figure 10.8.

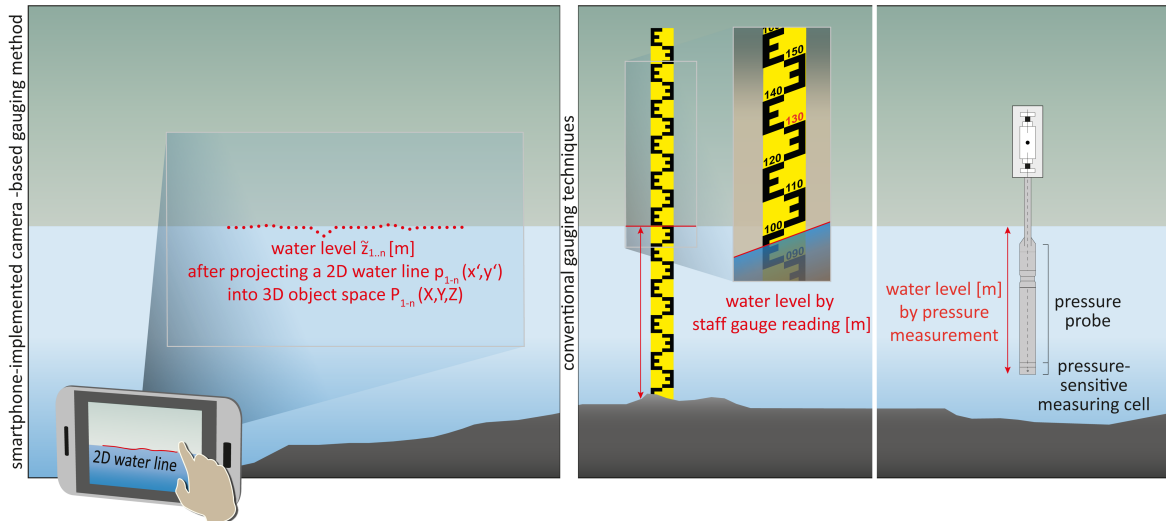


Figure (10.8): Set-ups of the smartphone-implemented camera-based gauging method (left) and two conventional gauging systems (middle and right) installed at the River Weißeritz, Dresden. Pressure gauge visualisation adapted from Morgenschweis (2010).

For evaluation purposes, the coordinate systems of the local water stages and the georeferenced camera-based water stages need to be aligned. Therefore, corresponding reference points of both coordinate systems allow for a consistent evaluation. Marked staff gauges, only used for accuracy evaluation in this study, provide points of reference for the estimated water line.

Regarding the evaluation area, 3D data was generated via SfM (see the "Prerequisites" Section 10.2) on two occasions. In the first, 130 images were captured with the full-frame Sony Alpha 7II digital system camera, with a 24 mm lens. This took place in February 2018 when the shore area was almost free from vegetation and the river had a low water level. On the second occasion, 126 images were captured when the river environment was highly vegetated but had almost no water due to a long dry season. Basically, it is recommended to capture the 3D data during periods when the river level is low so that the entire shore area is free of water. However, more realistic conditions mean that 3D datasets will be mainly acquired when rivers have normal waters and thus partially water-covered shore areas. This requires water refraction effects to be considered in 3D data processing to compensate for refraction causing the overestimation of depths (Dietrich, 2017; Mulsow et al., 2018). In this example, the water depth was less than 5 cm and the shore area was almost free of water during both acquisition periods.

For metric scaling and georeferencing, 22 artificial target points were installed in the nearshore environment and their locations determined by total station from two positions. Both positions were measured using real-time kinematic (RTK) GNSS involving the Geodetic Postprocessing Positioning Service (GPPS) from the Satellite Positioning Service (SAPOS) of the Official German Surveying and Mapping Agency for Geoinformation and State Survey of Lower

Saxony (LGLN) for signal correction. The total station positions could be measured with standard deviations of 0.75 cm, in the global reference frame UTM zone 33, WGS 84. Using five well-distributed target points as check points, the degrees of accuracy for the remaining 17 points are in ranges of ± 1.5 , ± 1.1 and ± 0.7 cm in eastings, northings and height, respectively. Finally, Agisoft PhotoScan v1.2.6 was used for data processing, resulting in two true-coloured 3D point clouds covering areas of about 700 m².

10.5.1 Reliability and accuracy of smartphone-implemented water-level gauging

Following the algorithmic description, the accuracy potential was assessed by means of the case study of the Weißeritz. This river was observed twice daily for one period of 4 days in mid-March 2018 and another of 6 days during late-March 2018, using Open Water Levels. A bridge across the river served as an ideal viewpoint, where the average distance between the smartphone position and the shore close to the reference gauge amounted to 18 m.

Comparing the camera-based water levels obtained by Open Water Levels with the reference values from the administrative gauging station, the anticipated accuracy potential can be estimated, as visualised in Figure 10.9. Table 10.2 shows the number of measured water levels, the absolute maximum deviation and the standard deviation $\sigma_{\Delta z}$ in relation to each measurement series. Considering all the measurements, the water level was detected in 17 of 20 cases, with a $\sigma_{\Delta z}$ of about 2 cm. No water level could be detected in three cases.

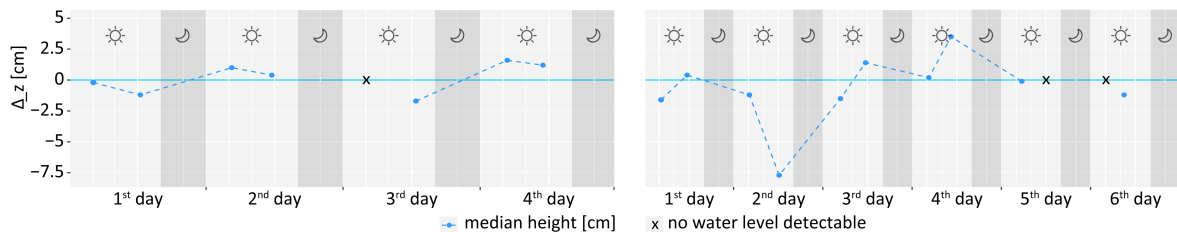


Figure (10.9): Weißeritz observation for 4 days (12th–16th March 2018 – left) and 6 days (26th–31st March 2018 – right). Visualisation of the water-level deviation between the camera-based water levels and the reference values.

Table (10.2): Accuracy investigation comparing water levels measured by the smartphone-implemented water gauging method with values from a stationary installed gauging station.

Measurement series	No. of measured water levels (no. of outliers in brackets)	Maximum deviation (cm)	Standard deviation, $\sigma_{\Delta z}$ (cm)
1 (4 days)	7 (1)	1.7	1.1
2 (6 days)	10 (2)	7.7	2.7
Mean of the two series	-	4.7	1.9

Generally, the spatial resolution and single-point accuracy of the 3D data has a major influence on the camera-based outcome. Conversely, small deviations can also result from the respective gauging modalities, for example, different temporal resolutions. Camera-based water stages are a snapshot at a given moment whereas the reference values are averaged over 15 minutes. Thus, minimal fluctuations are only present in camera-based water stages. Beside this, the proposed method determines the median height of the re-projected water levels whereas the

reference values are measured at one fixed point causing slightly different measuring points. Unlike the camera-based method, the pressure gauge is not susceptible to waves.

Figure 10.10 visualises one failed sample. The water line itself was detected very well but the image registration failed due to geometric and feature sampling problems. These are comprehensively discussed in the following section.

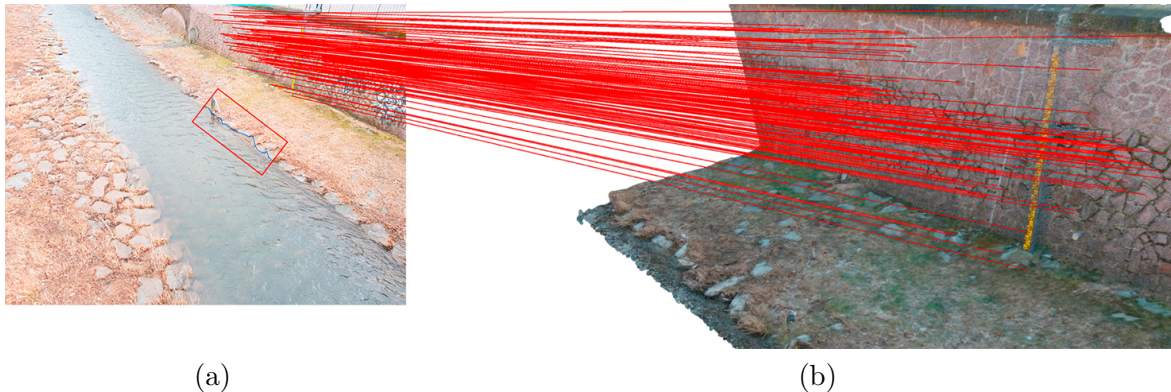


Figure (10.10): True-to-synthetic image registration with failed 3D water-level detection.
 (a) Camera image showing the detected 2D water line (red edge).
 (b) Synthetic image generated with smartphone sensor information.

10.6 Discussion

Similar to the division made by Kehl et al. (2017), who provided extensive research into major error sources affecting image-to-image and image-to-geometry registration under realistic field conditions, the error sources affecting the proposed workflow are separated into geometric and radiometric problems, as discussed below. Furthermore, restrictions due to the availability of appropriate 3D data are also to be discussed.

10.6.1 Geometric challenges

Geometric relation between 2D image data and 3D object data

One challenge is the description of the geometric relationship between the image space and the object space. Therefore, a set of parameters comprising the camera's interior and exterior orientation is required. The relationship can be established by applying a space resection using appropriate spatially distributed object points. Regarding the addressed application, namely citizen scientists (members of the general public) using their smartphones to generate data in instances of extreme events, camera pre-calibration is usually not practicable. Thus, the parameters for interior orientation should either be considered as known (from manufacturer process of the space resection).

In practical terms, actual available 3D object points may not be appropriately distributed in object space. For example, most of the points correspond to a wall, represent a plane in the shore area, or are far from the present water line. During floods, it is also very likely that most of the camera image is covered by the river itself, resulting in an adverse feature-point distribution. In these cases, it is advisable to fix the camera's interior orientation parameters and to determine only the six parameters of the exterior orientation.

Similarity of the real camera and the synthetic image

An adverse spatial distribution of matched 2D–3D points, such as region clutter (excessive number points in certain parts of the image) or recurring image patterns, will have a negative impact on the set of parameters to be determined. These issues are the expected consequences of errors in image synthesis, which is essential for the entire approach. In the procedure, the initially determined exterior orientation parameters, originating from the smartphone’s sensors, provide the basis of the method. Due to smartphone sensor characteristics, errors in the initial exterior orientation are very likely; these errors will have a major influence on the synthetic image and, thus, on the image-to-geometry registration. For this reason, these errors in the orientation parameters used for image synthesis are considered as the most serious issues requiring special consideration. The authors distinguish three problematic cases, (a), (b) and (c), concerning image rendering, which are highlighted by the colours pink, orange and purple, respectively, in Figure 10.11 and 10.12:

- (a) The synthetic image is completely out of the field of view compared to the camera image, meaning no image-to-geometry possible.
- (b) The synthetic image has only a partial overlap with the camera image, resulting in an adverse distribution of matched features for space resection and false values for the interior and exterior orientation. The water line cannot be registered due to missing 3D data.
- (c) Like case (b), the synthetic image has only a partial overlap, resulting in false orientation values. The water line is assigned with wrong object coordinates.

Dependence of the determined water level on the initial exterior orientation

A test dataset was generated to quantify the impact of variances in image synthesis on the resultant water level. This dataset consisted of a smartphone camera image covering the case study area, as well as position and rotation data appropriate to the real conditions. To provide unbiased data and to avoid correlations with radiometric variances, the image was captured at the same date and time as the 3D data. A known, distinctive natural feature point, namely a conspicuous spot on a cobble stone, within the direct shore area, served as an imaginary water-level point. Altering the values for position and rotation within the synthetic input dataset allowed conclusions to be drawn about their respective impact on the feature-based registration result by comparing it with the spot’s true height.

First, the easting, northing and height components were each varied from 0 to ± 25 m in steps of 1 m. Second, the azimuth, pitch and roll angles were modified in increments of 5° from 0° to $\pm 90^\circ$, thus turning clockwise and counter-clockwise, respectively. The results of the image syntheses are visualised in the extracts in Figure 10.11, with consideration to the three problematic cases (a), (b) and (c).

Figure 10.12 shows the height deviations between the projected feature point and its known height in 3D space when altering the position or rotation. As might be expected, the more the camera image conforms with the synthetic image, the higher the quantity of (well-distributed) matched feature points (visualised by the green-to-red colour gradient).

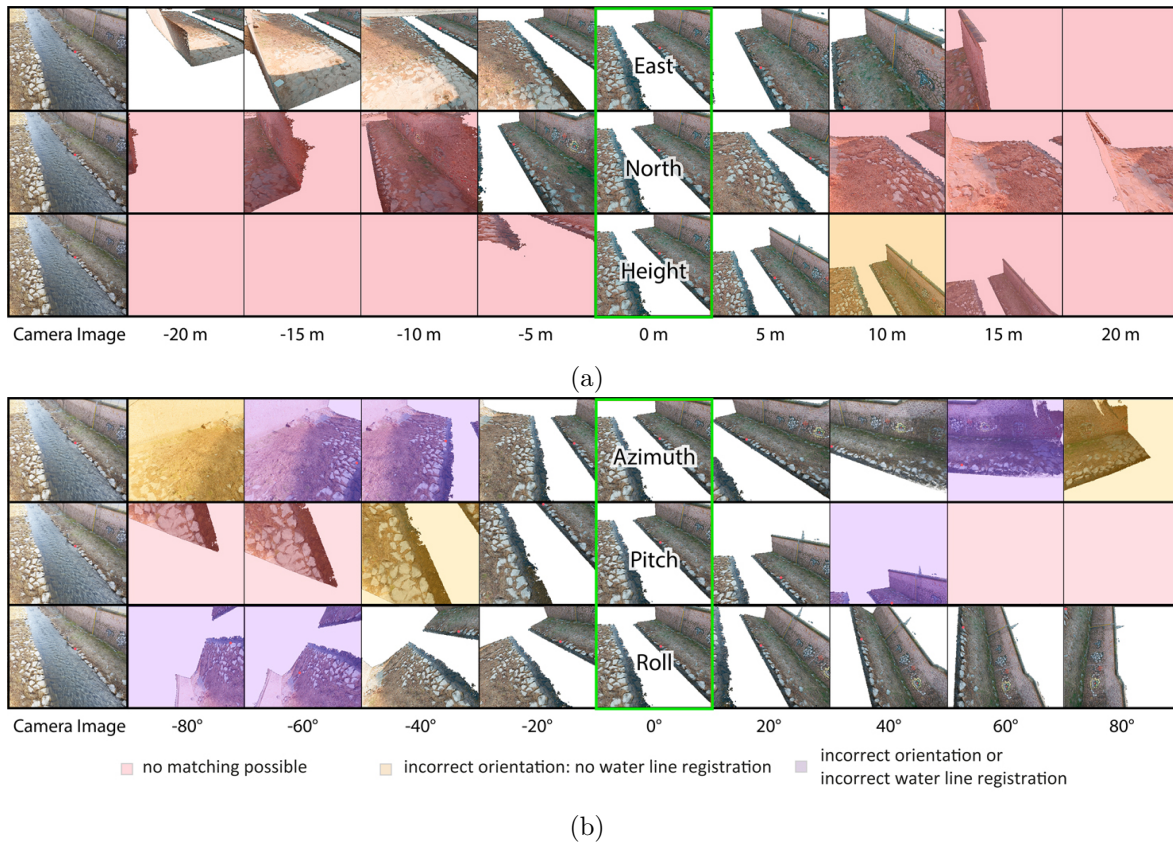


Figure (10.11): Image synthesis influencing water level determination: (a) with erroneous position values; (b) with erroneous rotation values. No matching in pink; no water line in orange; incorrect water line in purple.

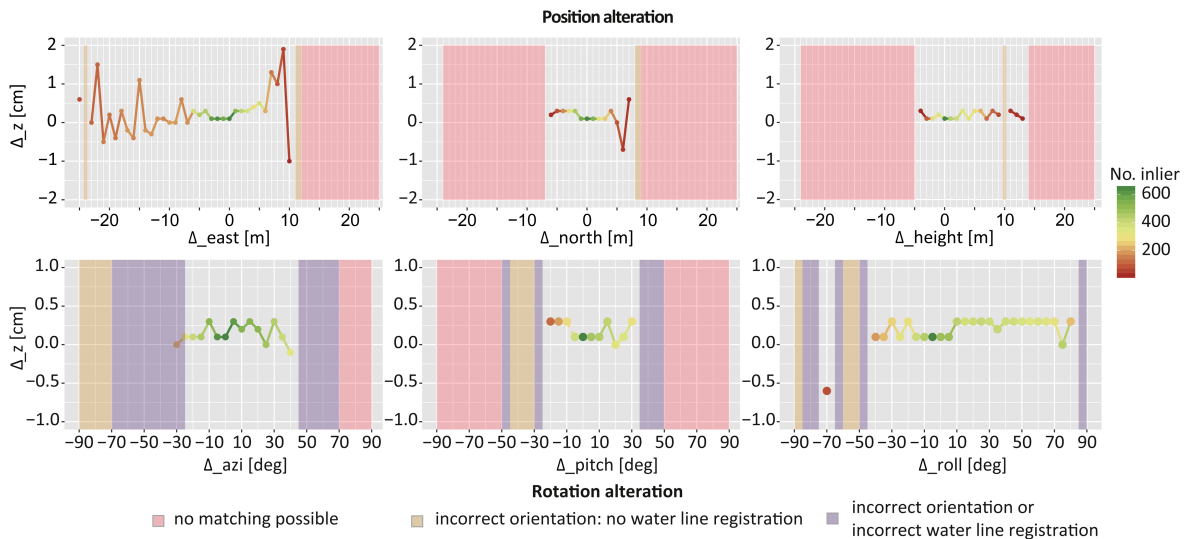


Figure (10.12): Deviation of synthetic water stage (cm) regarding position errors (top) and rotation errors (bottom). No matching in pink; no water line in orange; incorrect water line in purple.

Position errors

Regarding image translation, image-to-geometry registration fails completely (case a) or the matching outcome leads to errors in space resection resulting in a water line that cannot be registered due to missing 3D data (case b). It can be observed that the 3D water level can be detected as long as the 2D water line is within the synthetic image. In this context, the calculated water stage values either deviate from the true values to a small extent (up to ca. 1 cm) or they are not measurable at all. In this matter, moderate deviations in position assessment are acceptable due to halo expansion in image synthesis. Furthermore, recent developments in the field of sensor technology promise improvements in the domain of global smartphone positioning (Moore, 2017).

Rotation errors

Examining the rotation variances, the initial value of the most sensitive angle, the azimuth, can vary in the range of $[-30^\circ, 40^\circ]$ still providing reliable water stage values. Beyond these initial azimuth values, the water line is not or incorrectly transferred into object space (cases b and c). A similar situation emerges for pitch variation for which the reliability range is about $[-20^\circ, 30^\circ]$. Beyond these limits, the camera points in a completely wrong (compass) direction or only sees the sky or the ground. On the contrary, roll shows a slightly different behaviour. Thinking on the methods implemented for image matching, the rotation-invariant SIFT algorithm explains why changing the roll angle does not have a major influence on the outcome as long as the water line is visible inside the synthetic image. This is similar to the results of position errors. It should be noted, however, that all parameters of the exterior orientation are correlated. Otherwise, the water-level detection may fail due to case (b) or case (c).

Compared to the given sensor accuracy measurements in the "Prerequisites" Section 10.2, the results are generally satisfactory when using smartphone sensor fusion for the determination of the initial exterior orientation parameters. Only the azimuth could be problematic in the case of magnetic perturbations, which may lead to seriously disturbed values.

10.6.2 Radiometric challenges

Beside geometric issues, radiometric variances caused by changed ambient illumination or vegetation within the shore area may affect the detection and description of salient points and thus the registration of image and geometry data. Kehl et al. (2017) pointed out that radiometric variances, such as irregular illumination caused by casting shadows or overexposure, as well as environmental conditions like vegetation cover, are the principal reasons for SIFT-based matching failures. Regarding the case study given in Figure 10.10, feature points were mainly detected on the wall but not in the partially vegetated shore area. Thus, further consideration is given to radiometric changes resulting in different visual appearances at the same location.

To investigate the influence of radiometric differences, eight realistic samples were captured on different days, times, weather conditions and seasons, but with comparable exterior orientations (Figure 10.13). Unlike the study of geometric variances, the initial exterior orientation was fixed while different approaches of image preprocessing were performed to examine whether these radiometric adjustments have positive effects on the registration result. In relation to this, the same natural feature point served as an imaginary water-level point, as in the previous geometric experiments.

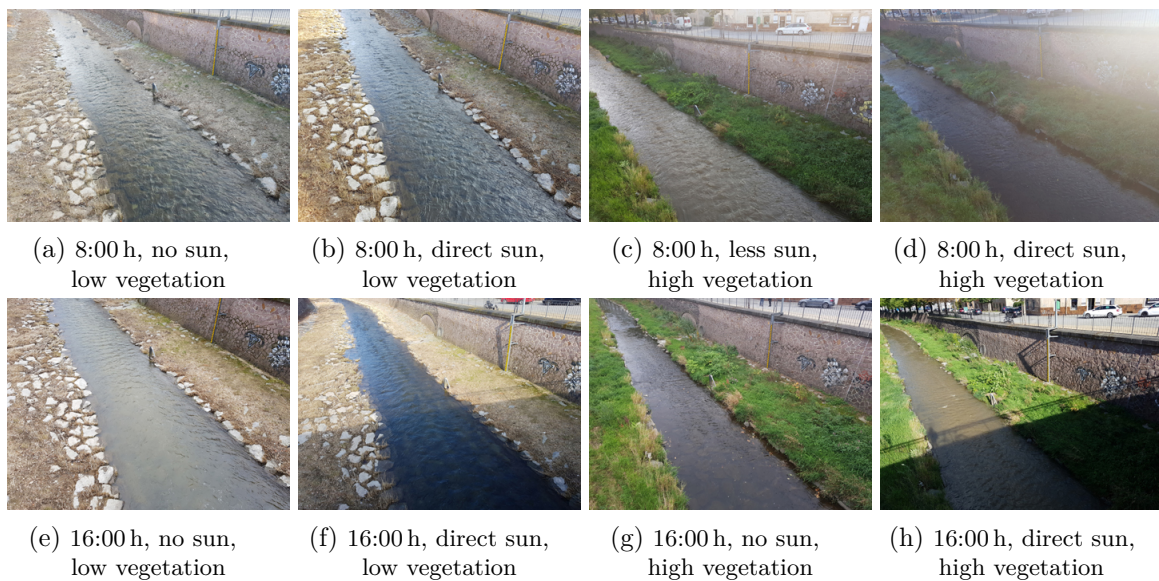


Figure (10.13): Cases used to quantify the influence of radiometric variances on image-to-geometry registration for smartphone-implemented water-level gauging: no filter techniques applied.

Vegetation masking

The triangular greenness index (TGI) promises to detect healthy vegetation using wavelengths of the visible spectrum (Hunt et al., 2013). Thus, TGI is used to mask out image areas likely to be error-prone for feature matching, that is, with high vegetation cover (Figure 10.14), which, however, greatly decreases the overall quantity of features.

Image contrast adjustment

In contrast to TGI, Wallis filtering is recommended to brighten and darken under- and overexposed image areas (Figure 10.15). This means the original mean intensity and contrast are maintained, resulting in a locally uniform value distribution in each colour channel within the overlapping, kernel-sized filter region. As expected, the locally adaptive 3×3 Wallis filter (default 8-bit target mean value of 127 and target standard deviation of 11 per image channel, without altered gain or weights) compensates for over- and underexposed image content, for example, due to direct or low sunlight. Conversely, it flattens the necessary contrast for feature delimitation and description.

As visualised in Figure 10.16, applying filtering techniques has no significant effect on depth estimation. In the cases where both shore areas are completely covered with significant vegetation (situations c, d, g and h in Figure 10.13–10.15), the approach fails in almost all situations. Generally, it is advisable to have rigid objects with long-term stability within the camera image area, providing fixed points for feature-based image registration, for example, retaining walls in urban areas or larger stones in rural areas.

Due to the application scope of the algorithm, these situations will be given very often in case of high river levels when the shore area is completely flooded, including its vegetation. Focusing on illumination variances (situations a, b, e and f in Figure 10.13–10.15), the technique works without image preprocessing, even if the sun is low resulting in over- and underexposure. In such situations, the deviation in the elevation of the fictitious water level, compared to the known reference, is negligible.

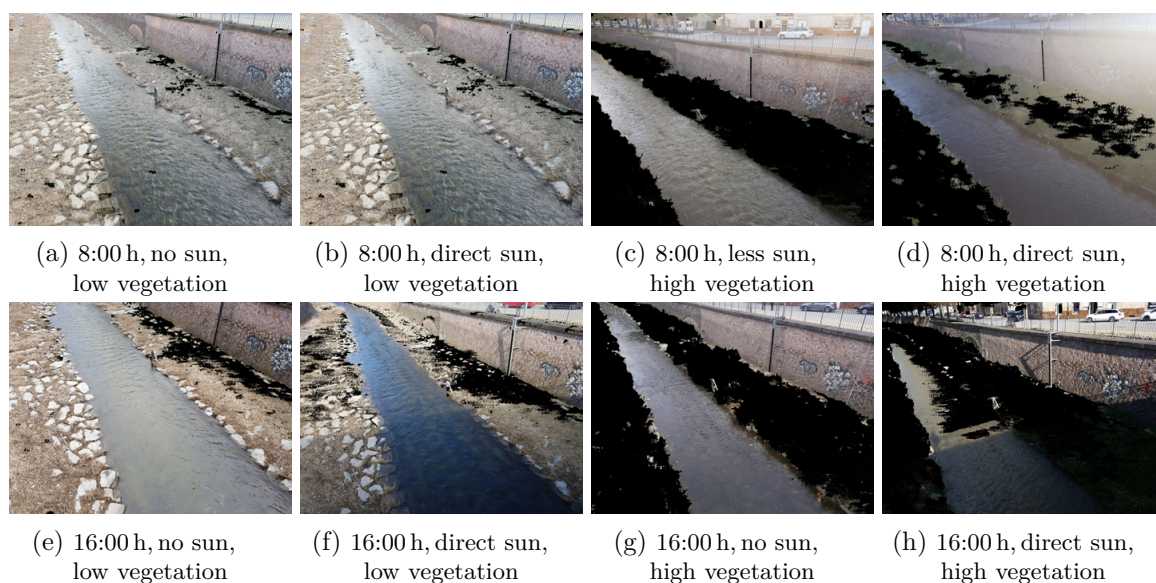


Figure (10.14): Same cases as Figure 10.13 but with TGI vegetation masking applied.

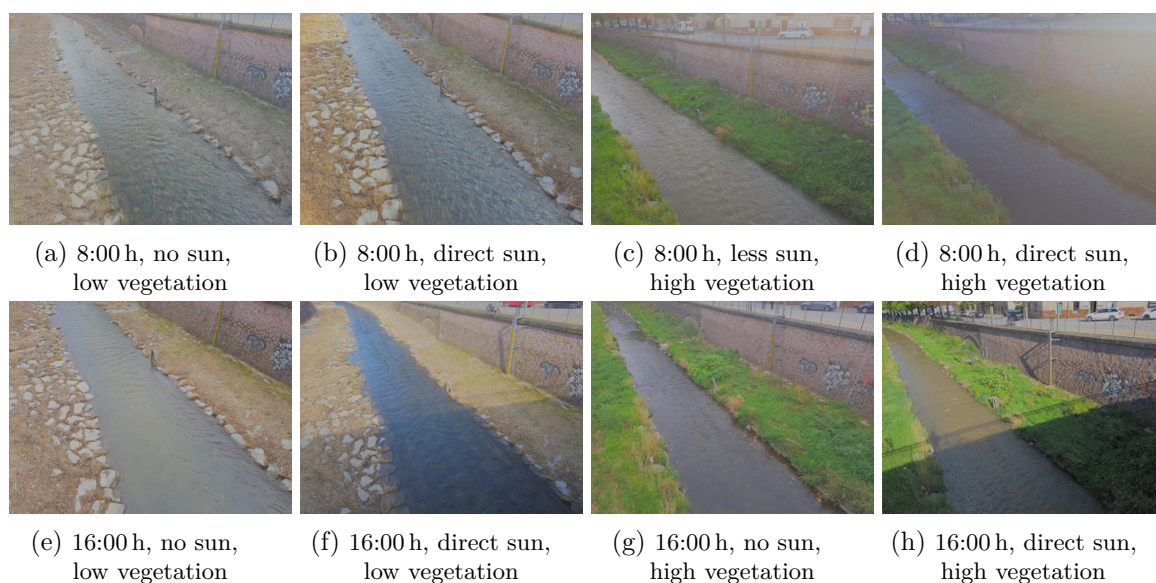


Figure (10.15): Same cases as Figure 10.13 but with a Wallis filter applied.

10.6.3 Availability of appropriate 3D Data

Beside geometric and radiometric issues, the restricted availability of coloured and georeferenced high-resolution 3D dataset limits the presented approach. However, the results of the given case studies confirm its versatility in densifying existing hydrological networks in cases of flooding. Thus, the technique may be attractive for national surveillance authorities who may consider the above-mentioned requirements in the generation of appropriate 3D city models. There are several options to address the issue of comprehensive 3D reference data.

More restrictions are imposed by both the accuracy and density of the 3D data to which the image data becomes registered. A sparse 3D point cloud results in fewer points which can be used to extract the water level. This means that the approach is more susceptible to outliers

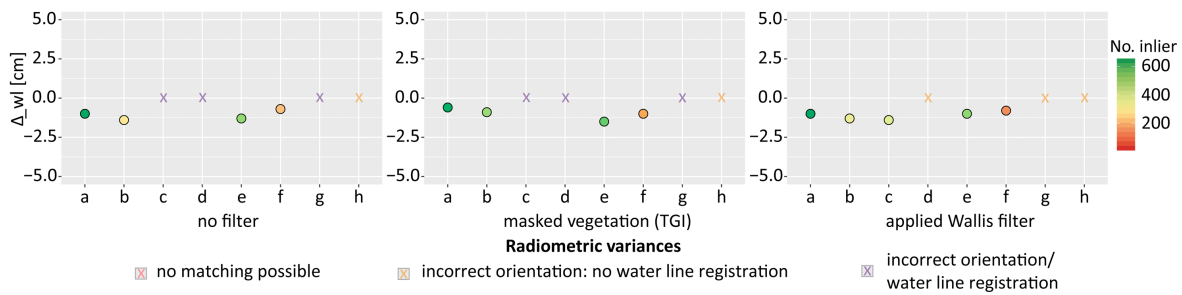


Figure (10.16): Deviation of synthetic water stage (cm) with radiometric variances applying different types of image preprocessing (no filter; TGI; Wallis). Abscissa labels a to h correspond to the cases shown in Figure 10.13–10.15.

due to a lower redundancy of assigned 2D–3D point pairs representing the water line in the image and object spaces. Using 3D surface data (meshed 3D point clouds) may produce relief but means greater efforts in 3D data processing. Furthermore, it should always be considered that errors in the scale of the 3D data will be transferred to the determined water levels.

Challenges such as image registration under changing illumination conditions and with reduced image resolution can be considered as "sufficiently solved" to apply the technology in real-world outdoor settings, while still leaving room for improvement in quality and performance. However, the treatment of vegetation within scanned and photographed data during water level determination remains a challenge. Three-dimensional data is obtained less frequently than it is used in a given outdoor setting. Vegetation itself is visually dynamic content that complicates image registration to existing 3D data. However, highly accurate 3D datasets collected on multiple occasions to solve for season- or illumination-dependent appearances for a given region of interest produce favourable results.

10.7 Conclusions and future developments

This paper addresses the development of a flexible algorithm for camera-based water-level gauging, designed for smartphone operation. Due to research efforts in recent years, for example, in the efficient treatment of 3D data as well as the development of algorithmic concepts for image-to-geometry registration on mobile devices, smartphones are increasingly attractive for professional use. The technique exemplifies how to bridge the gap between laboratory assessment and outdoor field work for gathering data as a prerequisite for interpretation. Consequently, the algorithm has to be operable on various low-cost devices, utilising the Internet to outsource heavyweight processes (3D processing and image-to-geometry registration). Such techniques open the door to a large audience for information gathering.

Compared to other camera-based gauging technologies, this method allows for flexible water gauging without the use of other referencing tools, such as staff gauges, and can be applied in regions where the permanent installation of gauging tools may be problematic. The workflow is similar to the technique presented in Eltner et al. (2018) who provided precise low-cost expert tools to monitor river sections without gauging stations using a fixed calibrated-camera installation. The exterior orientation was established using photogrammetric targets installed in the area surrounding the nearshore. The approach shown here emphasises spatio-temporal flexibility and facilitates on-the-fly water-level gauging. Common smartphones should be used to generate data in cases of extreme events without the need for professional expertise. Thanks to image-to-geometry registration, the installation and measurement of targets is

unnecessary to determine the camera's exterior orientation. Other than water-line detection, which itself requires minimal user interaction, the process is fully automatic and is able to process the data directly in the field. Merely the input of a 3D dataset is required. Due to its software architecture, the approach can be used by interested members of the public (citizen scientists) without assuming heavy hardware requirements. In this way, water stages can be acquired with accuracies of around 2.0 cm from viewing (smartphone-to-object) distances of about 20 m. In the case of larger distances, consideration must be given to the smartphone's image resolution and pixel size, which are key to detecting and registering the water line properly. If the number of potential volunteers is considered, data could be acquired with considerable redundancy, allowing the water level to be determined from the average of several contributors, rather than from single measurements.

Regarding technical issues affecting the water-level investigation, a comprehensive study of smartphone sensors for orientation assessment, as well as the interior stability of smartphone cameras, is under consideration. Future developments in hardware and software design mean it is likely that currently outsourced heavyweight processing tasks can be processed directly on the smartphone. These tasks include point-based true-to-synthetic image matching, space resection and the transfer of the 2D water line into 3D object space (see tasks e to g in the "Implementation" Section 10.4). Only the synthetic image needs to be rendered on a workstation and transferred to the smartphone, which would reduce data exchange and traffic using the mobile network. Considering the discussed radiometric challenges in point-based image matching under realistic field conditions, Kehl et al. (2017) have shown that improvements could be achieved using other feature detectors, such as colour point detectors like maximally stable colour regions (MSCR), that should be considered in future versions of Open Water Levels. Furthermore, frameworks have been published supporting the development of smart augmented reality applications, such as ARKit (Apple, 2019) and ARCore (Google, 2019). Both frameworks implement tools for feature detection and matching, as well as rendering algorithms. These smartphone-optimised solutions may be adapted for image-to-geometry registration and should be considered in future software development too.

Acknowledgements

The authors would like to thank Richard Boerner from TU Munich, Germany for his assistance with developing the approach of image synthesis. This research is supported by the European Social Fund (ESF) and the Free State of Saxony (Funding No. 100235479).

References

- Apple (2019). *Apple Documentation. ARKIT2: Developer Guide*. online. Accessed: 5th April 2019. URL: <https://developer.apple.com/arkit/>.
- Bentley, J. L. (1975). "Multidimensional binary search trees used for associative searching". In: *Communications of the ACM* 18, 9, pp. 509–517. DOI: 10.1145/361002.361007.
- Blaskow, R., M. Lindstaedt, D. Schneider and T. Kersten (2018). "Untersuchungen zum Genauigkeitspotential des terrestrischen Laserscanners Leica BLK360". In: *Photogrammetrie, Laserscanning, Optische 3D-Messtechnik - Beiträge der Oldenburger 3D-Tage 2018. Oldenburg, DE (31. Jan–01.Feb 2018)*. [Reference fixed.] Wichmann, VDE Verlag GmbH, pp. 284–295.

- Blum, J. R., D. G. Greencorn and J. R. Cooperstock (2013). In: *Mobile and Ubiquitous Systems: Computing, Networking, and Services. MobiQuitous 2012. Lecture Notes of the Institute for Computer Sciences, Social Informatics and Telecommunications Engineering*. Vol. 120. Springer: Berlin/Heidelberg, DE. Chap. Smartphone sensor reliability for augmented reality applications, 288: 127–138. DOI: 10.1007/978-3-642-40238-8_11.
- Bradski, G. (2000). “The OpenCV Library”. In: *Dr. Dobb’s Journal of Software Tools* 25, 11, pp. 120–125.
- Bruinink, M., A. Chandarr, M. Rudinac, P. J. van Overloop and P. Jonker (2015). “Portable, automatic water level estimation using mobile phone cameras”. In: *Proceedings of 2015 14th IAPR International Conference on Machine Vision Applications (MVA). Tokyo, JP (18–22 May 2015)*. IEEE, pp. 426–429. DOI: 10.1109/MVA.2015.7153102.
- Dietrich, J. T. (2017). “Bathymetric Structure-from-Motion: extracting shallow stream bathymetry from multi-view stereo photogrammetry”. In: *Earth Surface Processes and Landforms* 42, 2, pp. 355–364. DOI: 10.1002/esp.4060.
- Etter, S. and B. Strobl (2018). *CrowdWater*. online. Accessed: 5th April 2019. URL: <http://www.crowdwater.ch/de/home/>.
- Extruso (2019). *Water Stage Measurements of Gauging Station 551206 Plauen/Joined Weißeritz*. online. Accessed: 5th April 2019. URL: <https://extruso.bu.tu-dresden.de/map/?lang=eng>.
- Fritsch, D., A. M. Khosravani, A. Cefalu and K. Wenzel (2011). “Multi-sensors and multiray reconstruction for digital preservation”. In: *Proceedings of 53th Photogrammetric Week 2011. Stuttgart, DE (5–9 Sep 2011)*. Wichmann, pp. 305–323. URL: <https://phowo.ifp.uni-stuttgart.de/publications/phowo11/300fritsch.pdf>.
- Gauglitz, S., C. Sweeney, J. Ventura, M. Turk and T. Hollerer (2014). “Model Estimation and Selection towards unconstrained real-time tracking and mapping”. In: *IEEE Transactions on Visualization and Computer Graphics* 20, 6, pp. 825–838. DOI: 10.1109/tvcg.2013.243.
- Google (2019). *Android Developers. ARCore: Developer Guide*. online. Accessed: 5th April 2019. URL: <https://developers.google.com/ar/>.
- Google Maps Platform (2019). *Google Developers. Web Services: Elevation API*. online. Accessed: 5th April 2019. URL: <https://developers.google.com/maps/documentation/elevation/intro>.
- Guislain, M., J. Digne, R. Chaine and G. Monnier (2016). “Fine scale image registration in large-scale urban LIDAR point sets”. In: *Computer Vision and Image Understanding* 157, pp. 90–102. DOI: 10.1016/j.cviu.2016.12.004.
- Hama, L., R. A. Ruddle and D. Paton (2013). “3D mobile visualization techniques in field geology interpretation: evaluation of modern tablet applications”. In: *AAPG Hedberg Research Conference: 3D Structural Geologic Interpretation: Earth, Mind and Machine. Reno, NV, US (23–27 Jun 2013)*. AAPG, pp. 1–4.
- Harman, M. (2017). *Open Camera - Camera app for Android, Version 1.38*. online. Accessed: 5th April 2019. URL: <https://sourceforge.net/projects/opencamera/>.

- Hies, T., S. B. Parasuraman, Y. Wang, R. Duester, H. S. Eikaas and K. M. Tan (2012). “Enhanced water-level detection by image processing”. In: *Proceedings of 10th International Conference on Hydroinformatics (HIC 2012), Hamburg, DE (14–18 Jun 2012)*, pp. 1–8.
- Hunt, E. R., P. C. Doraiswamy, J. E. McMurtrey, C. S. Daughtry, E. M. Perry and B. Akhmedov (2013). “A visible band index for remote sensing leaf chlorophyll content at the canopy scale”. In: *International Journal of Applied Earth Observation and Geoinformation* 21, pp. 103–112. DOI: 10.1016/j.jag.2012.07.020.
- Ishihara, T., J. Vongkulbhisal, K. M. Kitani and C. Asakawa (2017). “Beacon-Guided Structure from Motion for Smartphone-Based Navigation”. In: *Proceedings of 2017 IEEE Winter Conference on Applications of Computer Vision (WACV). Santa Rosa, CA, US (24–31 March 2017)*. IEEE, pp. 769–777. DOI: 10.1109/wacv.2017.91.
- Kehl, C., S. J. Buckley, R. L. Gawthorpe, I. Viola and J. A. Howell (2016a). “Direct Image-to-Geometry Registration Using Mobile Sensor Data”. In: *ISPRS Annals of Photogrammetry, Remote Sensing and Spatial Information Sciences III-2*, pp. 121–128. DOI: 10.5194/isprs-annals-iii-2-121-2016.
- Kehl, C., J. R. Mullins, S. J. Buckley, R. L. Gawthorpe, J. A. Howell, I. Viola and S. Viseur (2016b). “Geological Registration and Interpretation Toolbox (GRIT): A Visual and Interactive Approach for Geological Interpretation in the Field”. In: *Proceedings of 2nd Virtual Geoscience Conference. Bergen, NO (21–23 Sep 2016)*, pp. 59–60.
- Kehl, C., J. R. Mullins, S. J. Buckley, J. A. Howell and R. L. Gawthorpe (2019). “Interpretation and mapping of geological features using mobile devices in outcrop geology – a case study of the Saltwick Formation, North Yorkshire, UK”. In: *AGU Books – Special Issue*. Wiley.
- Kehl, C., S. J. Buckley, S. Viseur, R. L. Gawthorpe and J. A. Howell (2017). “Automatic Illumination-Invariant Image-to-Geometry Registration in Outdoor Environments”. In: *The Photogrammetric Record* 32, 158, pp. 93–118. DOI: 10.1111/phor.12188.
- Kisters (2014). *Smarte Pegelüberwachung: Einfach und korrekt mit dem Mobile Water Tracker von KISTERS*. online. Accessed: 5th April 2019. URL: https://water.kisters.de/fileadmin/news_import/20141120_kisters_pm_mobile-water-tracker_final.docx.
- Kok, M., J. D. Hol and T. B. Schön (2017). “Using Inertial Sensors for Position and Orientation Estimation”. In: *Foundations and Trends in Signal Processing* 11, 1–2, pp. 1–89. DOI: 10.1561/20000000094.
- Kröhnert, M., C. Kehl, H. Litschke and S. J. Buckley (2017). “Image-to-Geometry Registration on Mobile Devices – Concepts, Challenges and Applications”. In: *Proceedings of 20th Workshop of 3D-NordOst, Berlin, DE (7–8 Dec 2017)*, pp. 99–108.
- Lin, Y.-T., Y.-C. Lin and J.-Y. Han (2018). “Automatic water-level detection using single-camera images with varied poses”. In: *Measurement* 127, pp. 167–174. DOI: 10.1016/j.measurement.2018.05.100.
- Liu, G., K. M. A. Hossain, M. Iwai, M. Ito, Y. Tobe, K. Sezaki and D. Matekenya (2014). “Beyond horizontal location context: measuring elevation using smartphone’s barometer”. In: *Proceedings of 2014 ACM International Joint Conference on Pervasive and Ubiquitous Computing: Adjunct Publication (UbiComp ’14 Adjunct). Seattle, WA, US (Sep 2014)*. ACM, pp. 459–468. DOI: 10.1145/2638728.2641670.

- Lowe, D. G. (2004). “Distinctive Image Features from Scale-Invariant Keypoints”. In: *International Journal of Computer Vision* 60, 2, pp. 91–110. DOI: 10.1023/B:VISI.0000029664.99615.94.
- Luhmann, T., S. Robson, S. Kyle and J. Boehm (2013a). In: *Close Range Photogrammetry and 3D Imaging*. 2nd ed. De Gruyter, Berlin, DE. Chap. 7.3 Strategies for camera calibration, 684: 567–578. ISBN: 9783110302783.
- Luhmann, T., S. Robson, S. Kyle and J. Boehm (2013c). In: *Close Range Photogrammetry and 3D Imaging*. 2nd ed. De Gruyter: Berlin, DE. Chap. 4.2.2 Collinearity equations, 684: 260–263. ISBN: 9783110302783.
- Masiero, A., F. Fissore, F. Pirotti, A. Guarnieri and A. Vettore (2016). “Toward the use of smartphones for mobile mapping”. In: *Geo-spatial Information Science* 19, 3, pp. 210–221. DOI: 10.1080/10095020.2016.1234684.
- Meek, S., G. Priestnall, M. Sharples and J. Goulding (2013). “Mobile capture of remote points of interest using line of sight modelling”. In: *Computers & Geosciences* 52, pp. 334–344. DOI: 10.1016/j.cageo.2012.09.028.
- Meierhold, N., M. Spehr, A. Schilling, S. Gumhold and H.-G. Maas (2010). “Automatic feature matching between digital images and 2D representations of a 3D laser scanner point cloud”. In: *International Archives of Photogrammetry, Remote Sensing and Spatial Information Sciences XXXVIII-5*, pp. 446–451. URL: <https://www.isprs.org/proceedings/XXXVIII/part5/papers/87.pdf>.
- Mikolajczyk, K. and C. Schmid (2004). “Scale & Affine Invariant Interest Point Detectors”. In: *International Journal of Computer Vision* 60, 1, pp. 63–86. DOI: 10.1023/B:VISI.0000027790.02288.f2.
- Moore, S. K. (2017). *IEEE Spectrum. Superaccurate GPS Coming to Smartphones in 2018*. online. Accessed: 5th April 2019. URL: <https://spectrum.ieee.org/semiconductors/design/superaccurate-gps-coming-to-smartphones-in-2018>.
- Morgenschweis, G. (2010). In: *Hydrometrie: Theorie und Praxis der Durchflussmessung in offenen Gerinnen*. 1st ed. Springer: Berlin/Heidelberg, DE. Chap. Messungen des Wasserstands, 582: 25–105. ISBN: 9783642053900. DOI: 10.1007/978-3-642-05390-0.
- Muja, M. and D. G. Lowe (2009). “Fast approximate nearest neighbors with automatic algorithm configuration”. In: *Proceedings of 4th International Conference on Computer Vision Theory and Applications - Volume 1: VISAPP (VISIGRAPP 2009). Lisboa, PT (5–8 Feb 2009)*. INSTICC Press, pp. 331–340. DOI: 10.5220/0001787803310340.
- Mulsow, C., R. Kenner, Y. Bühler, A. Stoffel and H.-G. Maas (2018). “Subaquatic digital elevation models from UAV-imagery”. In: *International Archives of the Photogrammetry, Remote Sensing and Spatial Information Sciences XLII-2*, pp. 739–744. DOI: 10.5194/isprs-archives-xlii-2-739-2018.
- Muratov, O., Y. Slynko, V. Chernov, M. Lyubimtseva, A. Shamsuarov and V. Bucha (2016). “3DCapture: 3D Reconstruction for a Smartphone”. In: *Proceedings of 2016 IEEE Conference on Computer Vision and Pattern Recognition Workshops (CVPRW). Las Vegas, NV, US (26. Jun–01. Jul 2016)*. IEEE, pp. 893–900. DOI: 10.1109/CVPRW.2016.116.
- Nuske, S., S. Choudhury, S. Jain, A. Chambers, L. Yoder, S. Scherer, L. Chamberlain, H. Cover and S. Singh (2015). “Autonomous Exploration and Motion Planning for an Unmanned

- Aerial Vehicle Navigating Rivers”. In: *Journal of Field Robotics* 32, 8, pp. 1141–1162. DOI: 10.1002/rob.21596.
- Pacha, A. (2015). *Sensor Fusion for Robust Outdoor Augmented Reality Tracking on Mobile Devices. Master’s Thesis, Augsburg University, DE*. GRIN Verlag: Munich, DE. ISBN: 9783656964025.
- Rodriguez, M. B., E. Gobbetti, F. Marton, R. Pintus, G. Pintore and A. Tinti (2012). “Interactive exploration of gigantic point clouds on mobile devices”. In: *Proceedings of 2012 International Symposium on Virtual Reality, Archaeology and Intelligent Cultural Heritage (VAST 2012). Brighton, UK (Nov 2012)*. The Eurographics Association, pp. 57–64. DOI: 10.2312/VAST/VAST12/057-064.
- Sardemann, H., A. Eltner and H.-G. Maas (2018). “Acquisition of geometrical data of small rivers with an unmanned water vehicle”. In: *International Archives of the Photogrammetry, Remote Sensing and Spatial Information Sciences XLII-2*, pp. 1023–1027. DOI: 10.5194/isprs-archives-xlii-2-1023-2018.
- Sattler, T., B. Leibe and L. Kobbelt (2011). “Fast image-based localization using direct 2D-to-3D matching”. In: *Proceedings of 2011 International Conference on Computer Vision. Barcelona, ES (6–13 Nov 2011)*. IEEE, pp. 667–674. DOI: 10.1109/iccv.2011.6126302.
- Scherer, S., J. Rehder, S. Achar, H. Cover, A. Chambers, S. Nuske and S. Singh (2012). “River mapping from a flying robot: state estimation, river detection, and obstacle mapping”. In: *Autonomous Robots* 33, 1–2, pp. 189–214. DOI: 10.1007/s10514-012-9293-0.
- Shahbudin, F. E. and F.-F. Chua (2013). “Design Patterns for Developing High Efficiency Mobile Application”. In: *Journal of Information Technology & Software Engineering* 3, 3, pp. 1–9. DOI: 10.4172/2165-7866.1000122.
- Sibbing, D., T. Sattler, B. Leibe and L. Kobbelt (2013). “SIFT-Realistic Rendering”. In: *Proceedings of 2013 International Conference on 3D Vision - 3DV 2013. Seattle, WA, US (29 Jun–1 Jul 2013)*. IEEE, pp. 56–63. DOI: 10.1109/3DV.2013.16.
- Sweeney, C., J. Flynn, B. Nuernberger, M. Turk and T. Hollerer (2015). “Efficient Computation of Absolute Pose for Gravity-Aware Augmented Reality”. In: *Proceedings of 2015 IEEE International Symposium on Mixed and Augmented Reality. Fukuoka, JP (29 Sep–3 Oct 2015)*. IEEE, pp. 19–24. DOI: 10.1109/ismar.2015.20.
- Torr, P. and A. Zisserman (2000). “MLESAC: A New Robust Estimator with Application to Estimating Image Geometry”. In: *Computer Vision and Image Understanding* 78, 1, pp. 138–156. DOI: 10.1006/cviu.1999.0832.
- Viseur, S., P. Roudaut, R. Bertozzi, M. Castelli and J.-L. Mari (2014). “3D interactive geological interpretations on digital outcrops using a touch pad”. In: *Proceedings of Vertical Geology Conference 2014 (VGC14). Lausanne, CH (6–7 Feb 2014)*, pp. 109–113.
- Wang, R., F. P. Ferrie and J. Macfarlane (2012). “Automatic registration of mobile LiDAR and spherical panoramas”. In: *2012 IEEE Computer Society Conference on Computer Vision and Pattern Recognition Workshops. Providence, RI, US (16–21 Jun 2012)*. IEEE, pp. 33–40. DOI: 10.1109/cvprw.2012.6238912.
- Wasserman, A. I. (2010). “Software engineering issues for mobile application development”. In: *Proceedings of the FSE/SDP workshop on Future of software engineering research (FoSER ’10). Santa Fe, NM, US (Nov 2010)*. ACM, pp. 397–400. DOI: 10.1145/1882362.1882443.

-
- Weiss, G. M. and J. W. Lockhart (2012). “A comparison of alternative client/server architectures for ubiquitous mobile sensor-based applications”. In: *Proceedings of 2012 ACM Conference on Ubiquitous Computing* September 2012. Pittsburgh, PA, US (Sep 2012). ACM, pp. 721–724. DOI: 10.1145/2370216.2370374.
- Wester-Ebbinghaus, W. (1985). In: *Kammerkalibrierung in der photogrammetrischen Praxis*. Vol. 275. Deutsche Geodätische Kommission, Reihe B: München, DE. Chap. Verfahren zur Feldkalibrierung von photogrammetrischen Aufnahmekammern im Nahbereich, pp. 106–114.
- Westhead, R., M. Smith, W. Shelley, R. Pedley, J. Ford and B. Napier (2013). “Mobile spatial mapping and augmented reality applications for environmental geoscience”. In: *Journal of Internet Technology and Secured Transactions* 2, 1–4, pp. 185–190. URL: <http://nora.nerc.ac.uk/id/eprint/504475/>.
- Wu, C. (2007). *SiftGPU: a GPU Implementation of Scale Invariant Feature Transform (SIFT)*. online. Accessed: 5th April 2019. URL: <https://github.com/pitzer/SiftGPU>.
- Zandbergen, P. A. and S. J. Barbeau (2011). “Positional Accuracy of Assisted GPS Data from High-Sensitivity GPS-enabled Mobile Phones”. In: *Journal of Navigation* 64, 03, pp. 381–399. DOI: 10.1017/s0373463311000051.
- Zhu, X., Q. Li and G. Chen (2013). “APT: Accurate outdoor pedestrian tracking with smartphones”. In: *Proceedings of 2013 IEEE INFOCOM. Turin, IT (14–19 Apr 2013)*. IEEE, pp. 2508–2516. DOI: 10.1109/INFOCOM.2013.6567057.

11 Related publications

11.1 Automatic waterline extraction from smartphone images

Paper 11.1 has been published in “The International Archives of the Photogrammetry, Remote Sensing and Spatial Information Sciences” (eISSN: 2194-90340).

Author: Melanie Kröhnert
Institute of Photogrammetry & Remote Sensing, TU Dresden, Germany

Publication history: submitted January 2016, accepted February 2016, published July 2016

Full reference: Kröhnert, M. (2016). “Automatic waterline extraction from smartphone images”. In: *International Archives of the Photogrammetry, Remote Sensing and Spatial Information Sciences XLI-B5*, pp. 857–863. DOI: 10.5194/isprs-archives-XLI-B5-857-2016

Abstract: Considering worldwide increasing and devastating flood events, the issue of flood defence and prediction becomes more and more important. Conventional methods for the observation of water levels, for instance gauging stations, provide reliable information. However, they are rather cost-expensive in purchase, installation and maintenance and hence mostly limited for monitoring large streams only. Thus, small rivers with noticeable increasing flood hazard risks are often neglected.

State-of-the-art smartphones with powerful camera systems may act as affordable, mobile measuring instruments. Reliable and effective image processing methods may allow the use of smartphone-taken images for mobile shoreline detection and thus for water level monitoring. The paper focuses on automatic methods for the determination of waterlines by spatio-temporal texture measures. Besides the considerable challenge of dealing with a wide range of smartphone cameras providing different hardware components, resolution, image quality and programming interfaces, there are several limits in mobile device processing power. For test purposes, an urban river in Dresden, Saxony was observed. The results show the potential of deriving the waterline with subpixel accuracy by a column-by-column four-parameter logistic regression and polynomial spline modelling. After a transformation into object space via suitable landmarks (which is not addressed in this paper), this corresponds to an accuracy in the order of a few centimetres when processing mobile device images taken from small rivers at typical distances.

Author’s contribution: The author contributed to the research design and implementation as well as writing the manuscript alone.

11.2 Versatile mobile and stationary low-cost approaches for hydrological measurements

Paper 11.2 has been published in “The International Archives of the Photogrammetry, Remote Sensing and Spatial Information Sciences” (eISSN: 2194-90340).

Authors: Melanie Kröhnert^a, Anette Eltner^a
^a Institute of Photogrammetry & Remote Sensing, TU Dresden,
01062 Dresden, Germany

Publication history: submitted May 2017, accepted July 2017, published September 2017

Full reference: Kröhnert, M. and A. Eltner (2018). “Versatile mobile and stationary low-cost approaches for hydrological measurements”. In: *International Archives of the Photogrammetry, Remote Sensing and Spatial Information Sciences XLII-2*, pp. 543–550. DOI: 10.5194/isprs-archives-xlii-2-543-2018

Abstract: In the last decades, an increase in the number of extreme precipitation events has been observed, which leads to increasing risks for flash floods and landslides. Thereby, conventional gauging stations are indispensable for monitoring and prediction. However, they are expensive in construction, management, and maintenance. Thus, density of observation networks is rather low, leading to insufficient spatio-temporal resolution to capture hydrological extreme events that occur with short response times especially in small-scale catchments. Smaller creeks and rivers require permanent observation, as well, to allow for a better understanding of the underlying processes and to enhance forecasting reliability. Today’s smartphones with inbuilt cameras, positioning sensors and powerful processing units may serve as wide-spread measurement devices for event-based water gauging during floods. With the aid of volunteered geographic information (VGI), the hydrological network of water gauges can be highly densified in its spatial and temporal domain even for currently unobserved catchments. Furthermore, stationary low-cost solutions based on Raspberry Pi imaging systems are versatile for permanent monitoring of hydrological parameters. Both complementary systems, i.e. smartphone and Raspberry Pi camera, share the same methodology to extract water levels automatically, which is explained in the paper in detail. The annotation of 3D reference data by 2D image measurements is addressed depending on camera setup and river section to be monitored. Accuracies for water stage measurements are in range of several millimetres up to few centimetres.

Author’s contribution: The author contributed to the research design and implementation of the smartphone-based water gauging system alone. Anette Eltner contributed to the development and implementation of a water gauging system based on fixed-installed Raspberry Pi cameras alone. The manuscript was largely written by the author. The paragraphs concerning the Raspberry Pi camera system were written by Anette Eltner who also revised the manuscript.

11.3 Automatic Image-Based Water Stage Measurement for Long-Term Observations in Ungauged Catchments

Paper 11.3 has been published in *Water Resources Research* (eISSN: 1944-7973).

Authors: Anette Eltner^a, Melanie Elias^a, Hannes Sardemann^a, Diana Spieler^b
^a Institute of Photogrammetry and Remote Sensing, Technische Universität Dresden, Dresden, Germany
^b Institute of Hydrology and Meteorology, Technische Universität Dresden, Dresden, Germany

Publication history: submitted August 2018, accepted October 2018, published October 2018

Full reference: Eltner, A., M. Elias, H. Sardemann and D. Spieler (2018). “Automatic Image-Based Water Stage Measurement for Long-Term Observations in Ungauged Catchments”. In: *Water Resources Research* 54, 12, pp. 10362–10371. DOI: 10.1029/2018wr023913

Abstract: Small-scale and headwater catchments are mostly ungauged, even though their observation could help to improve the understanding of hydrological processes. However, it is expensive to build and maintain conventional measurement networks. Thus, the heterogeneous characteristics and behavior of catchments are currently not fully observed. This study introduces a method to capture water stage with a flexible low-cost camera setup. By considering the temporal signature of the water surface, water lines are automatically retrieved via image processing. The image coordinates are projected into object space to estimate the actual water stage. This requires high-resolution 3D models of the river bed and bank area, which are calculated in a local coordinate system with structure from motion, employing terrestrial as well as unmanned aerial vehicle imagery. A medium- and a small-scale catchment are investigated to assess the accuracy and reliability of the introduced method. Results reveal that the average deviation between the water stages measured with the camera gauge and a reference gauge are below 6 mm in the medium-scale catchment. Trends of water stage changes are captured reliably in both catchments. The developed approach uses a low-cost camera design in combination with image-based water level measurements and high-resolution topography from structure from motion. In future, adding tracking algorithms can help to densify existing gauging networks.

Author’s contribution: The author largely contributed to the development of an approach to automatically detect water lines from time-lapse sequences. Furthermore, the author was involved in writing the manuscript to a minor part.

Part IV

Synthesis

12 Smartphones: The new photogrammetric measuring instruments?

The work was aimed at the development of a novel photogrammetric water level measurement method, which should be implemented in an app to use the smartphone as a measuring device. However, smartphones integrate low-cost mass market electronics rather than geodetic measurement technology, which is why the first part of the main section (Part II) dealt with the assessment of smartphone technology for the use in photogrammetric applications. Subsequently, the main findings of Part II are summarised.

12.1 Study on the impact of self-heating on the geometric integrity of smartphone cameras

It is already known from the literature that the physical integrity of smartphone cameras changes dramatically when the smartphone is exposed to external forces. Smartphones, however, combine several electro-mechanical components, which develop heat under load, but information on the geometric stability of low-cost cameras due to temperature changes was still missing and was investigated within the dissertation (Chapter 7).

Therefore, the geometries of two built-in smartphone cameras were examined for self-heating in addition to an external low-cost camera for ambient temperature impacts.

All examined cameras showed strong dependencies between the IOP and the temperature, which became already visible in the calibration images that appeared blurred and shifted with increasing temperature. The parameters of principal distance, principle point and lens decentration changed radically in relation to temperature so that the images got out of focus. During the cooling phases of the external camera, the parameters changed towards the original values. This was also reflected in the calibration images appearing more in focus again. Monte Carlo simulations were used to determine the significance of the identified changes in the imaging geometry on measurements in object space assuming a camera-to-object distance of 10 m. The results reveal that errors of 1–2 cm have to be expected solely through temperature-related changes in the IOP. Errors up to 10 cm are possible too, but occur less frequently.

To sum up, the physical integrity of smartphone cameras is highly susceptible to unavoidable device-internal temperature changes, which are difficult to predict and to model. It is possible that such changes could also result from movements of the camera module in the housing, which cannot be clearly determined due to the firm integration.

12.2 On the use of smartphone MEMS sensors for direct georeferencing in mobile imaging applications

A comprehensive investigation of built-in smartphone sensors based on MEMS technology and sensor fusion was carried out regarding the measurement of rotation parameters for

direct georeferencing. The majority of the studies known in the literature deal with the accuracy evaluation of relative rotation measurements with the smartphone in dynamic mode concentrating on navigation applications, but no studies were known that deal with absolute rotation measurements using the smartphone in different modes, indoors and outdoors, with or without exposure to magnetic perturbations and using different sensor fusion techniques.

Thus, Chapter 8 described a benchmark test on smartphone sensor fusion measuring the rotation parameters with different smartphones and a professional IMU, which served as reference, under different conditions to better estimate the accuracy potential.

It has been shown that the pitch and roll angle could be determined with accuracies of less than one degree, as long as the smartphone had been used in static mode. For devices operated in dynamic mode, errors of 3–4 degrees on average had been detected. Reasons could be residual linear accelerations or slight drifts, which could not be solved by sensor fusion.

The measurements of the azimuth angle in relation to true North were significantly worse with errors up to 90° especially when the device was used in dynamic mode or when it was exposed to magnetic perturbations. However, it was found that the IRS2 sensor fusion approach (Pacha, 2015) provided comparatively small errors in the measurement of the azimuth, which were less than 30° in 50% of all measurements.

12.3 On the use of smartphone-implemented GNSS for direct georeferencing in mobile imaging applications

In addition to the rotation parameters, the position parameters had to be examined for their accuracy potential, as they are also required for direct georeferencing in the water gauging app.

However, numerous studies on the positional accuracy of smartphone-implemented GNSS are already available in the literature, which is why no further studies have been conducted. According to the literature, the expected horizontal position accuracy when using the natively implemented PVT solution under good conditions, i.e. little shadowing and less multipath, is about 5 to 10 m, but becomes much worse as soon as the environmental conditions deviate from the ideal conditions. The vertical errors must be expected about 2–3 magnitudes higher. The investigations were carried out partly with Android and partly with iOS devices. Recent publications show that the accuracy can be greatly improved when processing the raw data instead of using the native PVT solution, so that the observations can be processed with geodetic processing strategies. Assuming that the ambiguities in phase processing can be resolved, accuracies in the range of a few centimetres are possible, requiring an observation time of a few minutes.

12.4 Summary

In a nutshell, smartphones can be used for photogrammetry but they are most likely not *the new* measuring instruments as their use as such is not straightforward.

One of the most challenging aspects is how to deal with the instabilities of the interior orientation, which make calibrating a smartphone camera before a measurement practically impossible. Therefore, it is recommended to determine the IOP within the measurement using on-the-job calibration.

Another important aspect is the direct georeferencing of camera images. Both the rotational and positional parameters can be determined with high accuracies under ideal conditions using smartphone sensors and built-in GNSS, i.e. no shading, no multipath, no magnetic interference, to name but a few. Under real conditions, however, these accuracies cannot be achieved by far, which is why the parameters determined with the smartphone are cannot be used for direct positioning in the field. Nevertheless, they provide valuable approximate values that can be used for determining both the EOP and IOP via extended space resection, see Chapter 10.

12.5 Future improvements

Smartphone technology is in an ongoing development, which could yield to improvements in the aforementioned topics such as the increasing implementation of dual-band GNSS receivers.

Dual-band GNSS receivers

With the presentation of the smartphone Xiaomi Mi 8 in May 2018, the first smartphone entered the market that integrates a dual-band GNSS module providing "up to decimetre-level accuracy for location-based services and vehicle navigation" (GSA, 2018) by analysing satellite signals broadcasted on two frequencies, i.e. L1/L5 (GPS), E1/E5 (Galileo). This, on the one hand, helps to increase the number of observations and, on the other hand, allows for the determination of ionosphere-induced signal delays (Wanninger and Heßelbarth, 2020). Chen et al. (2019a) applied PPP using the raw data of the Xiaomi Mi 8 and achieved horizontal accuracies of 80 cm in less than 30 seconds. The vertical error is with 1.65 m only two times higher than the error of the horizontal components. Aggrey et al. (2019) also achieved decimetre-level to metre-level accuracies applying static and kinematic PPP.

However, Wanninger and Heßelbarth (2020) found out that there are still significant differences in the observation quality of the first and second frequency of both the GPS and Galileo systems and that ambiguity fixing is currently only possible for L1 frequency due to poor quality carrier phase observations of the other GNSS frequencies. They emphasised that improvements in the receiver performance and thus in the processing of the signals of the second frequency will likely enable position accuracies of a few centimetres applying real-time PPP and RTK. Currently, only a few devices implement such receivers but it is likely that dual-band receivers become the new standard, which could significantly improve the position determination in several mobile imaging applications.

Research demand in rotational measurement

With regard to rotation determination, there are numerous studies dealing with the improvement of smartphone-measured rotation parameters, especially the azimuth, e.g. Chen et al. (2019b), Zeng et al. (2018) and Yuan et al. (2015), but all are focused on navigation applications and require the smartphone in dynamic mode. Consequently, there is still a need for research to optimise the rotation measurements when the smartphone is operated in static mode. On the one hand, alternative filter techniques could help to improve the azimuth angle, e.g. Poulouze et al. (2019b) and Deng et al. (2017). On the other hand, the combined use of vision-based methods and GNSS provides a possible solution. Georeferenced camera images could be compared with image data from databases, e.g. from Google Street View, in order to derive the viewing (azimuth) direction.

13 Open Water Levels: A new water gauging tool

The second part of the main section (Part III) introduced a novel photogrammetric water gauging tool, implemented on smartphones, called Open Water Levels (OWL). The logic behind OWL has been published in two papers, which have been provided in Chapter 9 and Chapter 10. The first publication dealt with the development of a novel method for water line detection in hand-held smartphone images. Once the water line has been detected, it needs to be translated into object space to derive information about the water level. This is done by registering the image measurement with 3D data, e.g. from a GIS database. The procedure is detailed in Chapter 10.

In the following, the developed methods are briefly summarised with regard to the implementation in OWL, unsolved difficulties are specified and ideas for future developments and improvements are provided. Finally, an overview is given about open issues that need to be resolved before OWL can be released for crowdsourcing water levels.

13.1 Water line detection

In Chapter 9, an algorithm was presented to detect arbitrary water lines in smartphone images without imposing specific requirements on the water surface, i.e. no need for calm waters, artificial banks or stage boards.

In short, the 2D water line is semi-automatically determined by means of spatio-temporal texture analysis (in case of rough waters) or edge detection by means of an average image (in case of calm waters) on the basis of a hand-held recorded time-lapse image sequence. The method has been implemented in the client application of OWL, i.e. the entire processing runs on the smartphone.

Generally, the OWL app provides a look and feel similar to an ordinary camera app as it is based on the framework *Open Camera* v1.38 (Harman, 2020), which was extended by a mode for water line detection. If the mode is activated, the image processing chains, which are computed asynchronously in the background, are extended by the water line detection logic in order to separate the UI from the business logic with respect to the *separation of concerns* paradigm.

Time-lapse image acquisition

Once the water gauging mode has been started, the user is asked to capture a short time-lapse image sequence of the shore area, in which the water line should be detected or rather where the water level should be measured.

Therefore, OWL implements a continuous shooting mode, which captures 15 images with a resolution of 2880×2160 Px (6.3 MP, aspect ratio 4:3). The reduced and fixed image resolution is justified, on the one hand, by the reduction of data heterogeneity regarding crowdsourcing,

where this image resolution can be achieved by most current smartphones, and, on the other hand, by the reduction of the computing time required for the following image processing.

It is worth mentioning that the image settings differ from those in the corresponding publication, which explains water line detection on the basis of a video sequence. The video solution was abandoned for reasons of time efforts for video decomposition as well as the high compression rates and the resulting low image qualities.

Meta data acquisition

Furthermore, meta data about the imaging situation are collected during the time-lapse image acquisition. The meta data are stored in the JavaScript Object Notation (JSON) data-interchange format and contain:

- an universally unique identifier (UUID)
- date/time of image acquisition
- approximate values for georeferencing:
 - 3D position from built-in GNSS processed by the native PVT solution
 - information about the spatial reference
 - estimation of the horizontal accuracy provided by Android's location API
 - 3D rotation from built-in MEMS applying IRS2 sensor fusion
- information about the camera, i.e. focal length, aperture, sensor size, pixel size

ROI selection and water line detection

Once the time-lapse sequence has been processed, the average image, which often allows for a good visual assessment of the water line, is displayed to the user, who is asked to roughly mark the water line to limit the search area. For better recognition, the image content can be enlarged with a zoom function to facilitate the marking of the water line. The principle of ROI selection is shown in Figure 13.1 on the left. After the user input, the calculation of the water line is performed as explained in Chapter 9.



Figure (13.1): Applying OWL for water line detection.
Left: ROI definition. Right: Detected water line.

The result is displayed to the user, see Figure 13.1 on the right. If the water line is detected, the user can accept the result and then proceed to the next processing steps. If the result is not satisfactory, the user can repeat the measurement or use the manually selected water line for further processing.

13.2 From water line to water level: Image-to-geometry registration

After the water line detection, the image measurement needs to be transferred into the object space by means of 3D reference data in order to derive the water level. Therefore, knowledge on the image geometry, i.e. the IOP and EOP, of the image-measured water line is required. As described in Section 12.4, smartphones offer opportunities to directly measure the EOP, but the expected accuracies are far from being sufficient to reconstruct the imaging configuration. Beside this, smartphone cameras suffer from geometric instabilities that impede the camera calibration. Consequently, a method was required that first reconstructs the image geometry to furthermore transfer the water line into the object space. The implementation of such a method in OWL is as follows:

Image synthesis

Once the user accepted the detected water line, a file package containing the master image, the image coordinates of the water line and the meta data is transferred to a cloud storage being connected to an application server. The meta data is analysed to select matching 3D data from a database. A synthetic image is rendered from the 3D data using the original image configuration and the meta data information, i.e. approximations of the IOP and EOP. This and the following steps are performed on the application server. During the processing time, the user can use the smartphone otherwise and is informed about the resulting water level via a push message.

Image-to-geometry registration

Master image and synthetic image are assigned by means of feature-based image matching applying SIFT+Fast Library for Approximate Nearest Neighbors (FLANN). The resulting correspondences between image coordinates and 3D object points are used to determine the IOP and EOP of the master image as a function of the 3D reference data via space resection.

Water level determination

Provided that sufficient, well-distributed matches can be found, the image-measured 2D water line is projected onto the object data to derive height information. The median height value is interpreted as the water level in the reference system of the 3D data.

13.3 Summary

In summary, a tool was developed within the thesis, which enables the flexible measurement of water levels on rivers in small-sized catchments using a smartphone. Its accuracy potential amounts to a few centimetres, determined by comparative measurements of conventional water level measuring stations. Thus, the attainable accuracies are within the range of the official requirements for water gauging.

Measuring the water level merely requires from the user the acquisition of a short hand-held time-lapse sequence using the app OWL. Thus, the method can be used by anyone without any prior knowledge of photogrammetry and hydrology for water level measurement and is consequently suited for the crowdsourcing-based densification of hydrometric monitoring networks as well as for setting up new measuring networks in previously unobserved areas using human sensors.

13.3.1 Pros and cons of water line detection by spatio-temporal texture analysis

Focussing on the results in Chapter 9, the water line could be successfully detected in study areas with different characteristics, i.e. small-scale catchments in rural and urban areas with the shore being natural and artificial.

In contrast to well-known edge detection methods, which are great for image segmentation having clearly visually distinguishable image areas, the calculation of the spatio-temporal texture for the classification of image content based on the time component is something new, and its advantage for water line detection becomes particularly evident on natural shores that are even hardly distinguishable from water by plain sight, see Figure 13.2.

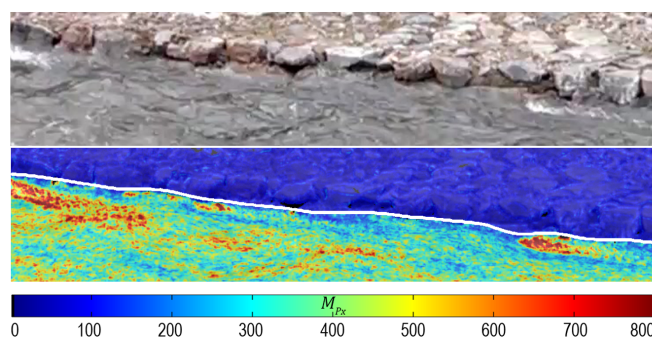


Figure (13.2): Water line detection by spatio-temporal texture analysis.

Top: Master image. Bottom: Spatio-temporal texture. M_{Px} : Magnitude of accumulated grey level differences per pixel. White line: water line. Figure adapted from Chapter 9.

Nevertheless, difficulties were observed when the time-lapse images suffer from casting shadows and underexposure, where neither the spatio-temporal texture can be analysed for variability due to low grey value differences in the water surface nor the average image has enough contrast for canny edge detection. A similar effect is also to be expected in the case of overexposure, but has not yet been investigated. Furthermore, calculating the spatio-temporal texture is very time-consuming due to the acquisition and processing of the time-lapse images.

With regard to the water line detection, the manual limitation of the search area can be a blessing and a curse. On the one hand, the user is actively involved in the measurement, which can have a positive effect on sustainable participation in crowdsourcing. Furthermore, if the water line has already been selected manually with great precision, it can undoubtedly be used to determine the water level, which can be advantageous in the aforementioned difficult lighting conditions. On the other hand, the error source "human" is not negligible; the app operator could impede the water line detection by incorrectly limiting the search area or forward incorrectly detected water lines for further processing.

13.3.2 Pros and cons of image-to-geometry registration

As mentioned at the beginning, the water gauging method is characterised by its flexibility, which does not require any pre-installed control points or stage boards. Furthermore, the implemented approach for image-to-geometry registration is able to perform the translation of an image measurement into the object space only with approximately determined camera parameters regarding the interior and exterior orientation. The computing effort on the client's side is low, since all computational processes are outsourced to an application server

where the actual data transfer is reduced to the master image, the image coordinates of the water line stored in a list and the meta data.

The flexibility of the water gauging tool is, however, limited by the need for coloured 3D reference data in the area of interest, which should have been collected at a similar time as the camera data in order to facilitate the correlation of image measurements from smartphones and object information. In addition, the better the smartphone-measured values for the images' position and rotation, the higher the probability that the image measurements can be registered with appropriate 3D object data.

13.4 Future work

In order to reduce the aforementioned limitations, approaches for future work are presented below that can contribute to water line detection in difficult image settings and increase the availability of 3D reference data to register the water line measurements. In this regard, an approach for image matching is presented, which can significantly improve image-to-geometry registration regarding geometric and radiometric challenges, see Section 10.6, as these are likely to complicate or prevent the assignment of camera and synthetic image resulting in false or no water level measurements. Current developments in smartphone technology are also taken up with a view to achieving possible improvements in OWL due to technical innovations. Knowledge of water levels is very important for hydrologists, but it is only one parameter among many, so an option is finally given to easily expand the functionality of OWL.

13.4.1 Water line detection applying machine learning

Targeting the mentioned difficulties for water line detection, recently published image segmentation algorithms using machine learning provide interesting approaches to this challenge.

On the one hand, Prabha et al. (2020) presented a novel convolutional neural network (CNN)-based image segmentation procedure that allows for the detection of water, snow and ice areas, which was furthermore optimised for heterogeneous image data from crowdsourcing. The results show that water surfaces could be detected even in case of reflections and shadows. Nevertheless, it became clear that the heterogeneity of the data is very challenging for training the network. This challenge is reflected in the object detection accuracy, indicated by the evaluation metric "intersection over union (IoU)" (also known as *Jaccard Index*). An example is given in Figure 13.3 on the left, where the water surface of a standing water could be segmented in crowdsourced images with an IoU of 64%.

On the other hand, Akiyama et al. (2020) trained a CNN exclusively for one study area in order to automatically detect the water surface of a river in images from a fixed-installed camera. Therefore, they manually labelled almost 3500 uniform images to train the CNN. The results, shown in Figure 13.3 on the right, reveal that the water surface could be detected with an IoU of about 98% independently of shadowed, reflective, underexposed or overexposed image areas. Both studies show, the better the training data, the better the CNN and the better the classification result.

Another interesting approach was presented by Chaudhary et al. (2019). They determined water levels during flood events from social media images. The images were classified by a CNN and the water level was determined in relation to objects being visible in the images, e.g. people or vehicles that are partly in the water. In some examples, the water level could be measured with accuracies of 8–9 cm. The statement of the authors again confirms that the

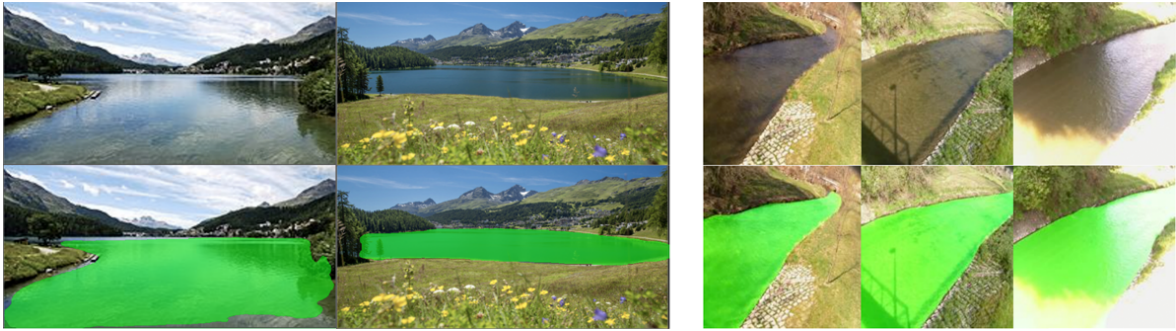


Figure (13.3): CNN-based water surface segmentation. Left: Lake detection on crowdsourced data. IoU: 64%. Adapted from Prabha et al. (2020). Right: River detection on uniform data; examples of different illumination conditions. IoU: \sim 98%. From Akiyama et al. (2020).

quality of the classification result depends strongly on the quality of the network and thus on the availability of versatile and appropriate training datasets, the generation of which is still subject of current research.

Nevertheless, CNN-based image classification already offers great potential for future optimisations of the water line detection approach, which might also yield considerable speed advantages as the time for capturing and processing the time-lapse sequence could be saved if the spatio-temporal texture is no longer needed. Furthermore, the approach could run fully automatic without requiring user interaction.

13.4.2 Image matching based on machine learning

It was shown that the success of the assignment of camera and synthetic image strongly depends on the accuracy of the smartphone-measured parameters of imaging position and rotation. When the perspectives of both images are too different due to false smartphone measurements, the image matching can fail and thus the reconstruction of the imaging geometry the water level detection. Furthermore, radiometric differences due to different vegetation levels between smartphone and reference data as well as slight snow cover or shadows due to varying sun light can impede the feature-based image matching.

Relief might be provided by replacing the currently implemented matching approach SIFT+FLANN by D2-Net+Brute-Force matching (BF) developed by Dusmanu et al. (2019). D2-Net uses a feature detection and description algorithm based on machine learning and shows stunning results matching images taken from completely different perspectives, under different lighting conditions and when matching different types of images, e.g. sketches and true photos, see Figure 13.4.



Figure (13.4): Examples of matches obtained by the D2-Net method, from Dusmanu et al. (2019).

Thus, D2-Net+BF has been implemented in an experimental version of OWL, showing already strong improvements in use cases that did not permit water level measurements so far.

Figure 13.5 shows the attempted water level measurement at upcoming high water in the study area known from Chapter 10. The measurement has been conducted in January 2019. The top row shows the result of camera-to-synthetic image matching applying SIFT+FLANN. Only 50 matches could be found, which, despite outlier elimination, still contain wrong matches. Consequently, the image situation could not be reconstructed correctly and led to large errors in the water level measurement. The problem becomes obvious when considering the back projection of the determined 3D water line into the image (pink line), which deviates strongly from the actual water line measured in the image (blue line). If the geometry of the image has been determined correctly, both lines would have to be displayed congruently.

The measurement was recently repeated using D2-Net+BF for image matching, visualised in the bottom row. It was possible to find 409 reliable matches that enabled the reconstruction of the imaging geometry. Again, the 3D water line was projected into the image where it completely overlaps the image-measured 2D water line, which indicates a correct determination of the IOP and EOP in relation to the 3D reference data.

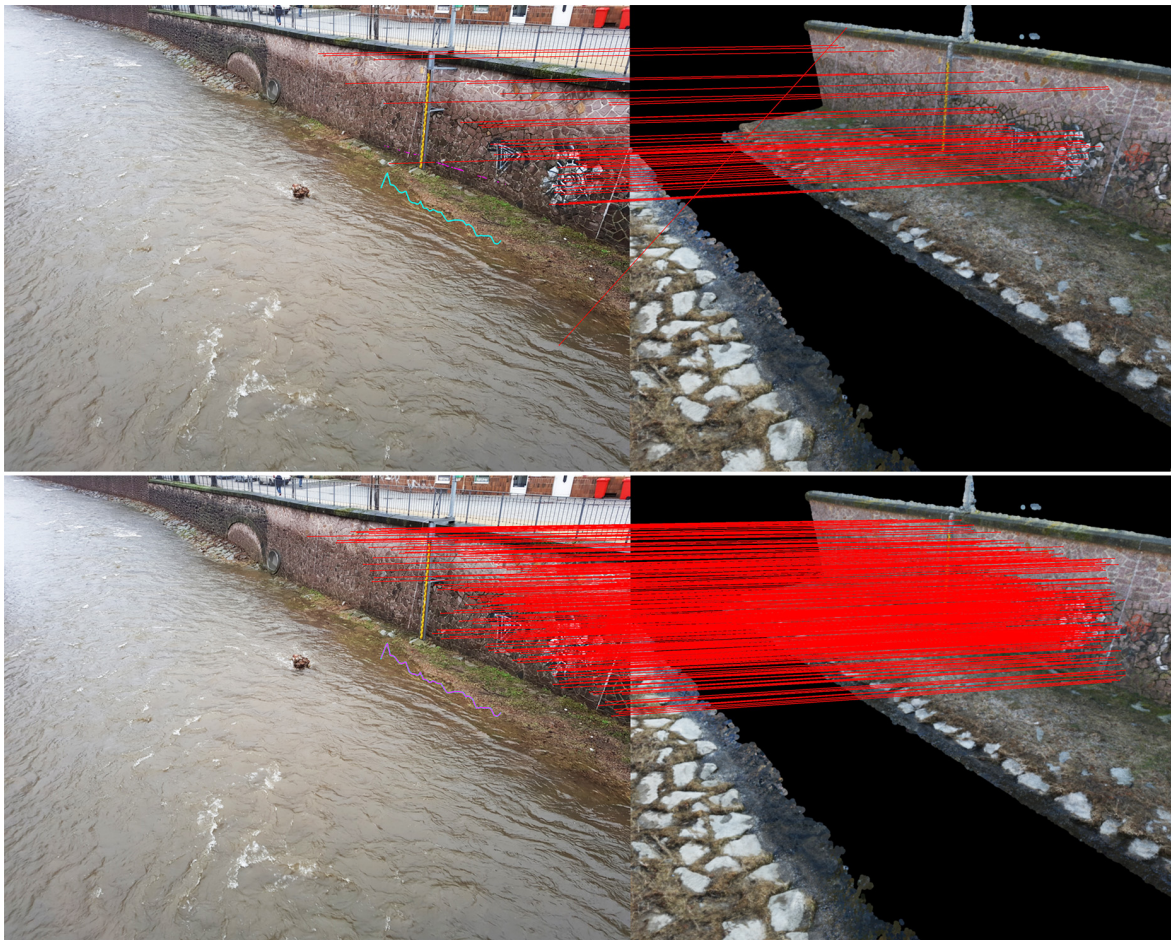


Figure (13.5): Comparison of real-to-synthetic image matching: SIFT+FLANN vs. D2-Net+BF. Top: SIFT+FLANN, 50 inlier matches still including false matches. Bottom: D2-Net+BF, 409 inlier matches. Blue line: image-measured 2D water line. Pink line: projected 3D water line.

It is obvious that the water line was difficult to detect at this time, as the water had already entered the meadow area on the bank, was very shallow and therefore did not show a distinct water line. In comparison with the level measurements of the local gauge installed on site, which was already used in Chapter 10 to assess the accuracy potential of OWL, the water level nevertheless deviates by only 3.6 cm from the conventionally measured level applying D2-Net+BF. This is slightly above the required accuracy for individual values (2.5 cm for 15-minutes mean) but still well below the requirements of instantaneous values (10 cm for single measurements). In contrast, the water level measured using SIFT+FLANN deviates by 20.1 cm from the reference value.

It became clear that at this point there is still a lot of potential left to improve OWL. Meanwhile other feature matching methods besides D2-Net have become known, e.g. R2D2 (Revaud et al., 2019), which would be equally interesting to test as their potential for matching real and synthetic image data is indisputable.

13.4.3 Increasing the availability of 3D data

A major limitation of the entire process is still the need for coloured and georeferenced 3D reference data to calculate the image geometry and then the water level. Nevertheless, there are several options to fastly and cost-efficiently generate 3D reference data. Some of them are outlined below.

3D point clouds from public street-/ river-view images

Thanks to the growing availability of street-level imagery, e.g. from Google Street View, and APIs to access this huge amount of panoramic images together with meta data, e.g. position information, the images can be used to process coloured, georeferenced 3D point clouds with accuracies of a few decimetres via SfM (Bruno and Roncella, 2019) to serve as reference data. Although the point clouds might not be highly accurate, relative water level measurements could still be possible with accuracies of a few centimetres, but this remains to be investigated. The same applies to absolute water level measurements if the water level has been calibrated with a staff gauge temporarily installed for this purpose.

No need to say that images taken from streets will only rarely cover catchment areas but as already was mentioned in Chapter 10, there are initiatives similar to Google River View that aim at the mapping and partly 3D modelling of shore areas from boats, e.g. Bowles (2017) and Babcock (2015).

Fast and accurate river mapping by UAVs and UWVs

Besides non-scientific and commercial surveys, there are also numerous scientific projects dealing with the acquisition of hydrologically relevant parameters, and so the mapping of the banks, by means of multi-sensor unmanned water vehicles (UWVs). These are equipped with, for example, precise GNSSs and IMUs as well as cameras and laser scanners, to generate 3D surface models of the shore areas, e.g. Alho et al. (2009) and Sardemann et al. (2018). Alho et al. (2009) emphasise that UWVs can be used to survey river sections of several kilometres within a few hours. Sardemann et al. (2018) state that especially the combined use of UWVs and UAVs allows for the generation of DTMs in large areas of the catchments. More examples are given in Eltner et al. (2020), Bertalan et al. (2020) and Hemmelder et al. (2018).

The demand for UAVs is growing steadily, both in the professional and private sectors, which is why the supply is increasing and consequently the costs of comparatively well-equipped UAVs are falling. Therefore the use of UAVs is a conceivable option to generate 3D data quickly and at relatively low cost in regions that have not yet been surveyed in three dimensions, e.g. remote and developing regions, in order to enable the use of OWL where it is most needed.

3D data from crowdsourcing

Basically, the generation of 3D surface information from camera images has been simplified by methods like SfM implemented in powerful and easy to use software like Agisoft Metashape/Photoscan (commercial) or Meshroom and Regard3D (both open source), which makes photogrammetry more and more interesting for the general public. In the future, it would be conceivable to supplement OWL with a crowdsourcing project for the generation of 3D data in order to obtain large amounts of reference data.

In summary, the limited availability of 3D data may be problematic at first sight, but there are many ways to generate reference data for different types of river catchments at relatively low cost and effort, which puts the problem into perspective.

13.4.4 Technical improvements

In Chapter 4, some technical innovations were pointed out that were published in the late development phases of OWL. Some of them might be considerable in future developments.

Geodetic GNSS signal processing

Regarding dual-frequency GNSS receivers, which are likely to become standard in smartphones in the near future, the native PVT solution currently implemented in OWL's app could be replaced by proprietary geodetic signal processing as presented by Wanninger and Heßelbarth (2020). This would, for example, permit the use of RTK for real-time positioning to within a few centimetres to improve image synthesis.

Multi- and periscope-zoom cameras

It has recently become possible to parallel control the cameras of multi-camera modules in smartphones. Assuming a smartphone that implements a periscope-zoom camera and an ultra-wide angle camera, this would enable the use of focal lengths of more than 70 mm (35 mm equivalent) to capture the water line with high level of detail and at the same time the environment with a large field of view making use of the ultra-wide angle camera. In doing so, the camera-to-synthetic image matching would be simplified, as it gives more margin to accept larger inaccuracies in the smartphone-measured EOP.

13.4.5 FlowVelo to go

Certainly, the water level is one of the most important parameters for hydrological modelling and understanding of water cycles. Equally important, however, is the flow velocity of a river. For this reason, Eltner et al. (2020) developed the *FlowVeloTool*, which uses co-registered image sequences captured from air by UAVs or from terrestrial close-range cameras for particle tracking on the water surface. If the image scale is known, flow velocity fields can be calculated.

Thus, the time-lapse images captured and co-registered for water line detection could also be examined for particles to be tracked. After reconstruction of the image geometry, the particles can be translated into the object space, as it is already been done for the water line, to measure flow velocity rates. Thus, OWL would become even more attractive for hydrologists, as not only one but two important parameters could be observed by volunteers without additional effort.

13.5 Outlook: Preparing OWL for crowdsourcing water levels

OWL is currently only available as a prototype. In order to use OWL for crowdsourcing, questions need to be addressed about technical issues, data quality assurance and user experience, which are summarised by non-functional requirements (Section 6.3.1). The following subsections describe which requirements (*highlighted in italics*) OWL already meets and which still have to be met before it can actually be used for crowdsourcing.

The functional requirements of OWL, i.e. the development of a *flexible, easy to use, low-cost water gauging tool implemented on smartphones for the crowdsourcing-based densification of hydrometric measurement networks targeting the accuracy requirements of conventional measurement methods*, can be considered as sufficiently solved. The handling of restrictions resulting from the availability of 3D data have to be dealt by non-functional requirements.

13.5.1 Technical issues

Technical issues comprise, on a large scale, questions on big data management, the parallel processing of multiple requests, system security and data privacy. On a small scale, they comprise questions on, for example, performance and robustness, system adaptability and comparability.

Large-scale technical issues

Currently, OWL's database and server application as well as the intermediate layer, which establishes the client-server communication, run on a single computer. The data exchange is conducted using the central data storage of TU Dresden and the secure file transfer protocol (SFTP) for data transfer. When considering OWL for crowdsourcing, professional cloud services could be used managing database, server application and communication layer in order to meet the requirements for *data management* and *scalability* when handling big data, for *efficiency*, *performance* and *robustness* when processing multiple requests as well as for *virtual system security* and *data privacy protection* when handling sensitive user data (Cartwright, 2016). Such services are, for example, Microsoft Azure or Google Cloud Platform.

Small-scale technical issues

Regarding the client app, the *data management* should be solved in a manner that only a small amount of data need to be stored on the device. Thus, OWL only stores the master image, the coordinates of the water line and the JSON meta data externally in a compressed zip-file. This allows for the transfer of the data for processing on the application server at a later time in case no internet is available at the site. Any other data are generated and deleted at runtime that is also important for *data security*.

Obviously, the requirements for *performance* and *robustness* also apply to the client app of OWL. Even if most processes with a high computing load are outsourced to the application server, tasks such as image signal processing are also computationally intensive and should operate in a crash-proof, high-performance manner in the app. Therefore, the app uses system design patterns such as the MVP pattern to separate the business logic from the view logic. This permits the user to perform other tasks on the smartphone during the processing, e.g. during water line detection or while waiting for the water level from the server, and is informed about the respective result when available to continue. At the same time, the app shall operate *efficiently* and in a *resource-saving* manner, which is why energy-intensive functions, such as GNSS and MEMS sensors, are only called on demand.

Furthermore, all components shall be independently *maintainable* and *updatable*, i.e. changing the app due to changes of the OS should not affect the server application and vice versa. Moreover, they shall be *modifiable*, *extensible* and *integrable*. This means modifying implemented methods, e.g. use machine learning instead of spatio-temporal texture analysis for water line detection, extending existing methods, e.g. use machine learning in addition to spatio-temporal texture analysis, and integrating entirely new functionalities without writing the software from scratch. Therefore, server application and client app have been loosely coupled in order to support both system components independently from each other. In this regard, changing the business logic of the app requires, thanks to the MVP pattern, relatively little effort since essentially only the model layer needs to be adapted.

Meeting the requirement for *compatibility* needs an extensive test phase of the entire system, but particularly of the app with various devices and/or simulation of different device types, separated into unit and integration tests (see Section 6.3). After testing, adjustments and workarounds will most likely be necessary to reliably use the app on as many devices as possible. The requirement for *portability* is currently not in the foreground, but will become interesting if the system should be available for iOS. In this case, all operations need to be checked to see whether they can be performed equally on Apple devices. Both ensuring compatibility and porting the tool to other platforms will require a lot of know-how, programming skills and man power. In this case it would be advisable to make the complete code of OWL, i.e. client app, server application and exchange layer, open source in order to get it tested, optimised and adapted by volunteers.

13.5.2 Data quality assurance

The necessity of quality measures to evaluate the user-generated data was already discussed in Chapter 5 in order to meet requirements on *data integrity* and *quality*. In view of OWL, the data should be verified for plausibility, imaging quality, and reliability of the water level. Such quality measures still need to be implemented whereas plausibility control could be realised by comparing, for example, the position information from the meta data with the geographical information of the reference data. So it can be checked whether there are any water bodies at the coordinates that can indicate a water level like the transmitted one. To find out whether the data on which the water line is based may have problems, e.g. image blur, over- and underexposure, the use of machine learning might be interesting to detect such difficulties by means of the master image, e.g. Afifi et al. (2020) and Brief (2019). Also, the standard deviation of the water level measurement can be checked, which refers to the variability of the 3D water line that should be almost planar.

Thanks to the defined data structure, e.g. image format and camera settings, as well as uniform meta data, common problems in crowdsourcing regarding data heterogeneity and unknown semantics are less relevant issues regarding the data quality assurance in relation to OWL.

13.5.3 User experience

User experience include everything to be considered to achieve a high degree of sustained participation. In Section 5.3, five factors according to Nielsen (2006) were carried out that should be taken into account. In short, technical, logistical and intellectual barriers have to be avoided, templates and instructions for the tasks to be done have to be provided, volunteer work and particularly good work has to be rewarded, and the task has to be designed in a way that the user experience is in the foreground and not the task itself.

Technical barriers are to be solved by addressing the aforementioned technical issues.

Logistical barriers could be solved in OWL by using a map. In this map all possible study areas should be marked where 3D reference data are available and which are of particular interest to the experts. Citizen scientists could check the map where in their vicinity water level measurements are possible and where data are urgently needed. In this way, the volunteers are not directly told where to measure, but are free to choose where they want to collect data. In order to meet the requirement for *physical safety*, the map should also inform about possible risk areas, e.g. river sections that are currently at risk of landslides due to heavy rainfall.

Intellectual barriers are solved by meeting the requirements for *intuitiveness/ autoplausibility* and *internationalisation*. OWL has the same look and feel as a regular camera application, which should be intuitive for any smartphone user who occasionally uses the native camera app. With regard to internationalisation, the Open Camera framework (Harman, 2020) already offers options for translating the UI into various languages. OWL uses very little textual communication, e.g. alerts when processing steps have been completed, which could be therefore easily adapted into various languages, but is still pending.

Instruction, guidance and autoplausibility

Volunteers can quickly become overwhelmed with a task if they are not guided through it or if they do not have sufficient explanations. Thus, OWL consists of sequential tasks, which have to be worked through step by step, i.e. once a subtask has been completed new functions are enabled for further work. For example, after processing the time-lapse sequence, options become available to select the water line. Therefore, autoplausible icons appear and disappear at runtime to reduce textual communication. In this way, the user is strictly guided through the task, leaving less room for errors, which furthermore benefits the requirements for data integrity and quality. Nevertheless before a final release for crowdsourcing, the app should be tested by a test group to check whether all steps are really autoplausible, the UI is *user-friendly*, e.g. check icon sizes, input masks and many more, or whether revisions are necessary.

Rewarding good and extensive work

Of course, particularly active users or particularly good contributions should be rewarded. On the one hand, this can be done through prestige, e.g. online rankings or through smaller (non-cash) prizes. Both concepts are used, for example, in the CrowdWater game (Strobl et al., 2019) where volunteers evaluate and improve their collected data. The game phases last several days and particularly good players, who find and correct a lot of mistakes, are published in a Top 10 list. At the end of each game phase there are smaller prizes to be won. The game serves the purpose of quality assurance of the user-generated content and allows for the evaluation of large amounts of data in a short time.

Regarding OWL, it is definitely recommended to use a reward system that rewards volunteers who record water levels particularly often, who may detect false measurements or who travel particularly far to study areas. However, no further consideration has yet been given to the implementation of such a system.

Make participation a side effect

The CrowdWater game is furthermore a prime example of how a scientific task can be playfully wrapped up in the sense of "making participation a side effect" and thus meeting the requirement for *emotional factors*, i.e. using the app should be fun. The actual CrowdWater project (Etter and Strobl, 2018) for data collection is also playfully structured and resembles geocaching in its concept; everyone can create a new virtual measuring station that can be visited by other volunteers to collect data. Even if gamification might be less suitable for OWL, it could be implemented with regard to a possible crowdsourcing project targeting the acquisition of 3D reference data.

Data transparency

One point which does not fit into the scheme of Nielsen (2006) but which could argue for or against the participation of a potential participant is *data transparency*. Consequently, it is essential that a data protection declaration is included in the app, which clearly informs the users about the data collection, protection and usage. The Open Camera framework already offers a data privacy statement, which still needs to be extended by all data security aspects regarding OWL.

13.5.4 Activation

It became clear that the development of a crowdsourcing app would have to take into account many aspects. Once OWL largely addressed the mentioned requirements, it could be released for crowdsourcing. Contact to potential participants could be established through the (social) media where the tool can be promoted in appropriate forums and groups or through cooperation with crowdsourcing projects with close interests that already have a community who is likely to be interested in participating OWL. In this context, a cooperation with CrowdWater, developed at the University of Zurich, might be interesting. Although CrowdWater already implements a method for estimating water levels using AR, i.e. a virtual gauge is placed at a water body to be displayed to estimate water level changes when the site is visited again, no actual measurement is made. OWL is designed for extensibility, so that once all remaining questions regarding technology, quality assurance and user experience have been clarified, cooperation should be sought here.

References

- Adhikari, S. (2019). *SamMobile. Infographic: The evolution of Samsung's smartphone cameras.* online. Accessed: 21th September 2020. URL: <https://www.sammobile.com/2019/05/24/infographic-evolution-samsung-smartphone-cameras/>.
- Affi, M., K. Derpanis, B. Ommer and M. Brown (2020). "Learning to Correct Overexposed and Underexposed Photos". In: *arXiv preprint* 2003.11596. URL: <https://arxiv.org/abs/2003.11596>.
- Aggrey, J., S. Bisnath, N. Naciri, G. Shinghal and S. Yang (2019). "Multi-GNSS precise point positioning with next-generation smartphone measurements". In: *Journal of Spatial Science* 65, 1, pp. 79–98. DOI: 10.1080/14498596.2019.1664944.
- Akiyama, T. S., J. M. Junior, W. N. Gonçalves, P. O. Bressan, A. Eltner, F. Binder and T. Singer (2020). "Deep learning applied to water segmentation". In: *ISPRS - International Archives of the Photogrammetry, Remote Sensing and Spatial Information Sciences XLIII-B2-2020*, pp. 1189–1193. DOI: 10.5194/isprs-archives-xliii-b2-2020-1189-2020.
- Alho, P., A. Kukko, H. Hyypä, H. Kaartinen, J. Hyypä and A. Jaakkola (2009). "Application of boat-based laser scanning for river survey". In: *Earth Surface Processes and Landforms* 34, 13, pp. 1831–1838. DOI: 10.1002/esp.1879.
- Alliance for Affordable Internet (2020). *Web Foundation. From luxury to lifeline: Reducing the cost of mobile devices to reach universal internet access.* Web Foundation. online. Accessed: 10th October 2020. URL: https://a4ai.org/wp-content/uploads/2020/08/Alliance-for-Affordable-Internet_Device-Pricing_PUBLIC.pdf.
- Alsdorf, D. E., J. M. Melack, T. Dunne, L. A. K. Mertes, L. L. Hess and L. C. Smith (2000). "Interferometric radar measurements of water level changes on the Amazon flood plain". In: *Nature* 404, 6774, pp. 174–177. DOI: 10.1038/35004560.
- Babcock, S. (2015). *Technical.ly. A small boat is mapping the entire Susquehanna River as we speak.* online. Accessed: 20th October 2020. URL: <https://technical.ly/baltimore/2015/07/27/summer-voyage-mapping-susquehanna-river/>.
- Balebako, R. and L. Cranor (2014). "Improving App Privacy: Nudging App Developers to Protect User Privacy". In: *IEEE Security & Privacy* 12, 4, pp. 55–58. DOI: 10.1109/msp.2014.70.
- Bandini, F., J. Jakobsen, D. Olesen, J. A. Reyna-Gutierrez and P. Bauer-Gottwein (2017). "Measuring water level in rivers and lakes from lightweight Unmanned Aerial Vehicles". In: *Journal of Hydrology* 548, pp. 237–250. DOI: 10.1016/j.jhydro1.2017.02.038.
- Bertalan, L., H. Sardemann, D. Mader, N. M. Szopos, B. Nagy and A. Eltner (2020). "Geomorphological and hydrological characterization of a meandering river by UAV and UUV applications". In: *Geophysical Research Abstracts of EGU General Assembly 2020. Online (4–8 May 2020)*. DOI: 10.5194/egusphere-egu2020-18069.

- Bianchi, S., C. Cahalan, S. Hale and J. M. Gibbons (2017). “Rapid assessment of forest canopy and light regime using smartphone hemispherical photography”. In: *Ecology and Evolution* 7, 24, pp. 10556–10566. DOI: 10.1002/ece3.3567.
- Borga, M., M. Stoffel, L. Marchi, F. Marra and M. Jakob (2014). “Hydrogeomorphic response to extreme rainfall in headwater systems: Flash floods and debris flows”. In: *Journal of Hydrology* 518, B, pp. 194–205. DOI: 10.1016/j.jhydro.2014.05.022.
- Bowles, N. (2017). *Vice. This startup wants to make a Google Street View for rivers, lakes, and bays.* online. Accessed: 15th October 2020. URL: <https://www.vice.com/en/article/9kd77v/fishviews-wants-to-make-a-google-street-view-for-rivers-streams-and-creeks>.
- Brief, B. (2019). *Medium. Mobile Image Blur Detection with Machine Learning.* online. Accessed: 15th October 2020. URL: <https://medium.com/snapaddy-tech-blog/mobile-image-blur-detection-with-machine-learning-c0b703eab7de>.
- Bruinink, M., A. Chandarr, M. Rudinac, P. J. van Overloop and P. Jonker (2015). “Portable, automatic water level estimation using mobile phone cameras”. In: *Proceedings of 2015 14th IAPR International Conference on Machine Vision Applications (MVA). Tokyo, JP (18–22 May 2015)*. IEEE, pp. 426–429. DOI: 10.1109/MVA.2015.7153102.
- Bruno, N. and R. Roncella (2019). “Accuracy assessment of 3D models generated from Google street view imagery”. In: *ISPRS - International Archives of the Photogrammetry, Remote Sensing and Spatial Information Sciences XLII-2/W9*, pp. 181–188. DOI: 10.5194/isprs-archives-xlii-2-w9-181-2019.
- Bund/Länder-Arbeitsgemeinschaft Wasser (2018). *Leitfaden zur Hydrometrie des Bundesund der Länder–Pegelhandbuch*. Stuttgart, Germany: Bund/Länderarbeitsgemeinschaft Wasser (LAWA), Ministerium für Umwelt, Klima und Energiewirtschaft Baden-Württemberg. URL: https://www.lawa.de/documents/02_anhang_2_lawa_pegelhandbuch_2_3_1552303807.pdf.
- Burghardt, D., W. Nejdil, J. Schiewe and M. Sester (2018). “Volunteered Geographic Information: Interpretation, Visualisation and Social Computing (VGIScience)”. In: *Proceedings of the ICA 1*, pp. 1–5. DOI: 10.5194/ica-proc-1-15-2018.
- Cardinal, D. (2019). *DXOMARK. Multi-camera smartphones: Benefits and challenges.* online. Accessed: 17th June 2020. URL: <https://www.dxomark.com/multi-camera-smartphones-benefits-and-challenges/>.
- Cartwright, J. (2016). “Technology: Smartphone science”. In: *Nature* 531, 7596, pp. 669–671. DOI: 10.1038/nj7596-669a.
- Cervantes, E. (2020). *Android Authority. Understanding aperture: What is it and how does it affect image quality?* online. Accessed: 05th October 2020. URL: <https://www.androidauthority.com/what-is-aperture-789927/>.
- Chandel, S. (2009). *Google Web Toolkit (GWT). Testing: GUI Design Patterns.* online. Accessed: 01th October 2020. URL: http://www.gwtproject.org/articles/testing_methodologies_using_gwt.html.
- Chaudhary, P., S. D’Aronco, M. M. de Vitry, J. P. Leitão and J. D. Wegner (2019). “Flood water level estimation from social media images”. In: *ISPRS Annals of Photogrammetry*,

-
- Remote Sensing and Spatial Information Sciences IV-2/W5*, pp. 5–12. DOI: 10.5194/isprs-annals-iv-2-w5-5-2019.
- Chebbi, A. (2019). *IBM Developer. Choosing the best programming language for mobile app development*. online. Accessed: 28th July 2020. URL: <https://developer.ibm.com/articles/choosing-the-best-programming-language-for-mobile-app-development/>.
- Chen, B., C. Gao, Y. Liu and P. Sun (2019a). “Real-time Precise Point Positioning with a Xiaomi MI 8 Android Smartphone”. In: *Sensors* 19, 12, p. 2835. DOI: 10.3390/s19122835.
- Chen, C., S. Rosa, Y. Miao, C. X. Lu, W. Wu, A. Markham and N. Trigoni (2019b). “Selective Sensor Fusion for Neural Visual-Inertial Odometry”. In: *Proceedings of 2019 IEEE/CVF Conference on Computer Vision and Pattern Recognition (CVPR). Long Beach, CA, US (15–20 Jun 2019)*. IEEE, pp. 10542–10551. DOI: 10.1109/cvpr.2019.01079.
- Chen, Y., R. Fan, X. Yang, J. Wang and A. Latif (2018). “Extraction of Urban Water Bodies from High-Resolution Remote-Sensing Imagery Using Deep Learning”. In: *Water* 10, 5, p. 585. DOI: 10.3390/w10050585.
- Chikatsu, H. and Y. Takahashi (2009). “Comparative evaluation of consumer grade cameras and mobile phone cameras for close range photogrammetry”. In: *Proceedings of SPIE 7447 Videometrics, Range Imaging, and Applications X. San Diego, CA, US (2–6 Aug 2009)*. Vol. 7447. International Society for Optics and Photonics. SPIE, pp. 130–141. DOI: 10.1117/12.825746.
- Chung, L., B. Nixon, E. Yu and J. Mylopoulos (2000). *Non-Functional Requirements in Software Engineering*. 5th ed. International Series in Software Engineering. Springer Science and Business Media: NYC, US. ISBN: 9781461552697.
- Dabove, P. and V. D. Pietra (2019). “Towards high accuracy GNSS real-time positioning with smartphones”. In: *Advances in Space Research* 63, 1, pp. 94–102. DOI: 10.1016/j.asr.2018.08.025.
- Dabove, P., V. D. Pietra and M. Piras (2020). “GNSS Positioning Using Mobile Devices with the Android Operating System”. In: *ISPRS International Journal of Geo-Information* 9, 4, p. 220. DOI: 10.3390/ijgi9040220.
- de Martino, M., F. Causa and S. B. Serpico (2003). “Classification of optical high resolution images in urban environment using spectral and textural information”. In: *Proceedings of IGARSS 2003. 2003 IEEE International Geoscience and Remote Sensing Symposium. Proceedings (IEEE Cat. No.03CH37477). Toulouse, FR (21–25 Jul 2003)*. Vol. 1, pp. 467–469. DOI: 10.1109/IGARSS.2003.1293811.
- Deng, Z., W. Si, Z. Qu, X. Liu and Z. Na (2017). “Heading estimation fusing inertial sensors and landmarks for indoor navigation using a smartphone in the pocket”. In: *EURASIP Journal on Wireless Communications and Networking* 2017, 1, p. 160. DOI: 10.1186/s13638-017-0941-0.
- Dinardo, S. (2020). “Techniques and Applications for Satellite SAR Altimetry over water, land and ice”. PhD thesis. Darmstadt: Technischen Universität Darmstadt. DOI: 10.25534/TUPRINTS-00011343.
- Dusmanu, M., I. Rocco, T. Pajdla, M. Pollefeys, J. Sivic, A. Torii and T. Sattler (2019). “D2-Net: A Trainable CNN for Joint Detection and Description of Local Features”. In: *CVPR 2019. arXiv preprint 1905.03561*. URL: <https://arxiv.org/abs/1905.03561>.

- DWD (2020). *Statista. Monatliche Durchschnittstemperatur in Deutschland von August 2019 bis August 2020*. online. Accessed: 04th September 2020. URL: <https://de.statista.com/statistik/daten/studie/5564/umfrage/monatliche-durchschnittstemperatur-in-deutschland/>.
- Eckerson, W. W. (1995). “Three Tier Client/Server Architecture: Achieving Scalability, Performance, and Efficiency in Client Server Applications”. In: *Open Information Systems* 3, pp. 46–50.
- Elliott, E. (2014). *Programming JavaScript Applications*. O’Reilly Media Inc: Sebastopol, CA, US. ISBN: 9781491950296. URL: https://www.ebook.de/de/product/21932734/eric_elliott_programming_javascript_applications.html.
- Eltner, A., H. Sardemann and J. Grundmann (2020). “Technical Note: Flow velocity and discharge measurement in rivers using terrestrial and unmanned-aerial-vehicle imagery”. In: *Hydrology and Earth System Sciences* 24, 3, pp. 1429–1445. DOI: 10.5194/hess-24-1429-2020.
- Etter, S. and B. Strobl (2018). *CrowdWater*. online. Accessed: 5th April 2019. URL: <http://www.crowdwater.ch/de/home/>.
- European GNSS Agency (GSA) (2017). *Using GNSS Raw Measurement on Android devices*. Luxembourg, LU: Publications Office of the European Union. DOI: 10.2878/449581.
- European GNSS Agency (GSA) (2018). *World’s first dual-frequency GNSS smartphone hits the market*. online. Accessed: 29th June 2020. URL: <https://www.gsa.europa.eu/newsroom/news/world-s-first-dual-frequency-gnss-smartphone-hits-market>.
- Fitzgerald, M. (2019). *BetterProgramming. Android vs. iOS App Development: Which Is the Better Choice for Your Business in 2019?* online. Accessed: 29th July 2020. URL: <https://medium.com/better-programming/android-vs-ios-app-development-which-is-the-better-choice-for-your-business-in-2019-933b20e4d9b8>.
- García, Á. M., R. Píriz, M. D. L. Samper and M. M. R. Merino (2010). “Multisystem real time precise-point-positioning, today with GPS+GLONASS in the near future also with QZSS, Galileo, Compass, IRNSS”. In: *Proceedings of International Symposium on GPS/GNSS. Taipei, TW (26–28 Oct 2010)*, pp. 1–6. URL: https://magicgnss.gmv.com/publications/2010/ASIAN_GNSS_2010_PPP.pdf.
- Gartner (2020). *Statista. Marktanteile der führenden Betriebssysteme am Absatz von Smartphones weltweit vom 1. Quartal 2009 bis zum 1. Quartal 2020*. online. Accessed 19th June 2020. URL: <https://de.statista.com/statistik/daten/studie/73662/umfrage/marktanteil-der-smartphone-betriebssysteme-nach-quartalen/>.
- George, C. (2019). *Digital Camera World. What is a time-of-flight camera?* online. Accessed 17th June 2020. URL: <https://www.digitalcameraworld.com/features/what-is-a-time-of-flight-camera>.
- Gikas, V. and H. Perakis (2016). “Rigorous Performance Evaluation of Smartphone GNSS/IMU Sensors for ITS Applications”. In: *Sensors* 16, 8, p. 1240. DOI: 10.3390/s16081240.
- Goodchild, M. F. (2007). “Citizens as sensors: the world of volunteered geography”. In: *GeoJournal* 69, 4, pp. 211–221. DOI: 10.1007/s10708-007-9111-y.

-
- Google (2020b). *Android Developers. Android API Guide. Sensors Overview*. online. Accessed: 21th January 2020. URL: <https://developer.android.com/guide/topics/sensors>.
- Google (2020c). *Android Developers. Android Documentation. Build location-aware apps*. online. Accessed: 21th June 2020. URL: <https://developer.android.com/training/location>.
- Google (2020d). *Google Developers. Guide to app architecture*. online. Accessed: 23rd June 2020. URL: <https://developer.android.com/jetpack/docs/guide>.
- Gunawan, D., Priyanka and O. S. Sitompul (2020). “The Development of Mobile and Server Application for Traffic Data Collection Based on Location-Based Services (LBS)”. In: *IOP Conference Series: Materials Science and Engineering* 851, p. 012068. DOI: 10.1088/1757-899x/851/1/012068.
- Haklay, M. (2013). In: *Crowdsourcing Geographic Knowledge: Volunteered Geographic Information (VGI) in Theory and Practice*. Springer: Dordrecht, NL. Chap. Citizen Science and Volunteered Geographic Information: Overview and Typology of Participation, pp. 105–122. ISBN: 9789400745872. DOI: 10.1007/978-94-007-4587-2_7.
- Hamad, M. (2020). “A Multilayer Secure Framework for Vehicular Systems”. PhD thesis. Braunschweig: Technische Universität Braunschweig.
- Harman, M. (2020). *Open Camera - Camera app for Android, Version 1.38*. online. Accessed: 20th January 2020. URL: <https://sourceforge.net/projects/opencamera/>.
- He, D.-C. and L. Wang (1992). “Unsupervised textural classification of images using the texture spectrum”. In: *Pattern Recognition* 25, 3, pp. 247–255. DOI: 10.1016/0031-3203(92)90108-U.
- Heipke, C. (2010). “Crowdsourcing geospatial data”. In: *ISPRS Journal of Photogrammetry and Remote Sensing* 65, 6, pp. 550–557. DOI: 10.1016/j.isprsjprs.2010.06.005.
- Hemmelder, S., W. Marra, H. Markies and S. M. D. Jong (2018). “Monitoring river morphology & bank erosion using UAV imagery – A case study of the river Buëch, Hautes-Alpes, France”. In: *International Journal of Applied Earth Observation and Geoinformation* 73, pp. 428–437. DOI: 10.1016/j.jag.2018.07.016.
- Hodel, H., T. Kersten and P. Hirner (1991). “Bestimmung der Abflussbeiwerte von Wildbächen mittels Hydrometrie und Photogrammetrie”. In: *Zeitschrift für Vermessung, Photogrammetrie, Kulturtechnik* 3/91, pp. 80–87.
- Huang, C., Y. Chen, S. Zhang and J. Wu (2018). “Detecting, Extracting, and Monitoring Surface Water From Space Using Optical Sensors: A Review”. In: *Reviews of Geophysics* 56, 2, pp. 333–360. DOI: 10.1029/2018rg000598.
- Huang, Q., X. Li, P. Han, D. Long, F. Zhao and A. Hou (2019). “Validation and application of water levels derived from Sentinel-3A for the Brahmaputra River”. In: *Science China Technological Sciences* 62, 10, pp. 1760–1772. DOI: 10.1007/s11431-019-9535-3.
- Jaakkola, H. and B. Thalheim (2010). “Architecture-Driven Modelling Methodologies”. In: *Proceedings of 20th European-Japanese Conference on Information Modelling and Knowledge Bases (EJC 2010). Jyväskylä, FI (31. May– 4. Jun 2010)*. Vol. 225. Frontiers in Artificial Intelligence and Applications. IOS Press, pp. 97–116. DOI: 10.3233/978-1-60750-690-4-97.

- Kampf, S., B. Strobl, J. Hammond, A. Anenberg, S. Etter, C. Martin, K. Puntenney-Desmond, J. Seibert and I. van Meerveld (2018). “Testing the Waters: Mobile Apps for Crowdsourced Streamflow Data”. In: *Eos* 99. DOI: 10.1029/2018eo096355.
- Kehl, C., J. R. Mullins, S. J. Buckley, J. A. Howell and R. L. Gawthorpe (2019). “Interpretation and mapping of geological features using mobile devices in outcrop geology – a case study of the Saltwick Formation, North Yorkshire, UK”. In: *AGU Books – Special Issue*. Wiley.
- Kenyeres, A. (1997). “A Strategy for GPS Heighting : The Hungarian Solution”. In: *Gravity, Geoid and Marine Geodesy. International Association of Geodesy Symposia*. Vol. 117. Springer: Berlin/Heidelberg, DE, pp. 651–658. DOI: 10.1007/978-3-662-03482-8_86.
- Kersten, T. P. (2020). *GIM International. The Smartphone as a Professional Mapping Tool*. online. Accessed: 05th September 2020. URL: <https://www.gim-international.com/content/article/the-smartphone-as-a-professional-mapping-tool>.
- Kirchner, J. W. (2006). “Getting the right answers for the right reasons: Linking measurements, analyses, and models to advance the science of hydrology”. In: *Water Resources Research* 42, 3. DOI: 10.1029/2005wr004362.
- Klubnikin, A. (2017). *Medium. Cross-platform vs Native Mobile App Development: Choosing the Right Development Tools for Your Project*. online. Accessed 10th July 2020. URL: <https://medium.com/all-technology-feeds/cross-platform-vs-native-mobile-app-development-choosing-the-right-dev-tools-for-your-app-project-47d0abafee81>.
- La, H. J. and S. D. Kim (2010). “Balanced MVC Architecture for Developing Service-Based Mobile Applications”. In: *Proceedings of 2010 IEEE 7th International Conference on E-Business Engineering. Shanghai, CN (10–12 Nov 2010)*. IEEE, pp. 292–299. DOI: 10.1109/icebe.2010.70.
- Laben, C. A. and B. V. Brower (2000). “Process For Enhancing The Spatial Resolution Of Multispectral Imagery Using Pan-sharpening”. Granted Patent US 6011875 A (United States). URL: <https://lens.org/135-660-046-023-136>.
- Leberl, F. (2010). “Time for neo-photogrammetry”. In: *GIS development* 14, 2, pp. 22–24.
- Lehmann, J., D. Coumou and K. Frieler (2015). “Increased record-breaking precipitation events under global warming”. In: *Climatic Change* 132, 4, pp. 501–515. DOI: 10.1007/s10584-015-1434-y.
- Lin, Y.-T., Y.-C. Lin and J.-Y. Han (2018). “Automatic water-level detection using single-camera images with varied poses”. In: *Measurement* 127, pp. 167–174. DOI: 10.1016/j.measurement.2018.05.100.
- Luhmann, T., S. Robson, S. Kyle and J. Boehm (2013a). In: *Close Range Photogrammetry and 3D Imaging*. 2nd ed. De Gruyter, Berlin, DE. Chap. 7.3 Strategies for camera calibration, 684: 567–578. ISBN: 9783110302783.
- Maenaka, K. (2008). “MEMS inertial sensors and their applications”. In: *Proceedings of 2008 5th International Conference on Networked Sensing Systems. Kanazawa, JP (7–19 Jun 2008)*. IEEE, pp. 71–73. DOI: 10.1109/inss.2008.4610859.
- Maggini, G. (2019). *IBM Developer. Deciding between native and cross-platform mobile frontend programming frameworks*. online. Accessed: 28th July 2020. URL: <https://>

-
- `developer.ibm.com/articles/choosing-the-best-programming-language-for-mobile-app-development/`.
- Majumder, S. and M. J. Deen (2019). “Smartphone Sensors for Health Monitoring and Diagnosis”. In: *Sensors* 19, 9, p. 2164. DOI: 10.3390/s19092164.
- Mandlbürger, G., N. Pfeifer and U. Soergel (2017). “Water surface reconstruction in airborne laser bathymetry from redundant bed observations”. In: *ISPRS Annals of Photogrammetry, Remote Sensing and Spatial Information Sciences IV-2/W4*, pp. 123–130. DOI: 10.5194/isprs-annals-iv-2-w4-123-2017.
- Mandlbürger, G., M. Pfennigbauer, U. Riegl, A. Haring, M. Wieser, P. Glira and L. Winiwarter (2015). “Complementing airborne laser bathymetry with UAV-based lidar for capturing alluvial landscapes”. In: *Proceedings of SPIE 9637 Remote Sensing for Agriculture, Ecosystems, and Hydrology XVII, Toulouse, FR (14 Oct 2015)*. Vol. 9637. International Society for Optics and Photonics. SPIE, pp. 60–73. DOI: 10.1117/12.2194779.
- McFeeters, S. K. (1996). “The use of the Normalized Difference Water Index (NDWI) in the delineation of open water features”. In: *International Journal of Remote Sensing* 17, 7, pp. 1425–1432. DOI: 10.1080/01431169608948714.
- Merry, K. and P. Bettinger (2019). “Smartphone GPS accuracy study in an urban environment”. In: *PLOS ONE* 14, 7, e0219890. DOI: 10.1371/journal.pone.0219890.
- Meyer, F. (2019). In: *SAR Handbook: Comprehensive Methodologies for Forest Monitoring and Biomass Estimation*. NASA: Washington, D.C., US. Chap. Spaceborne Synthetic Aperture Radar – Principles, Data Access, and Basic Processing Techniques, pp. 1–24. DOI: 10.25966/EZ4F-MG98.
- Miao, Z., K. Fu, H. Sun, X. Sun and M. Yan (2018). “Automatic Water-Body Segmentation From High-Resolution Satellite Images via Deep Networks”. In: *IEEE Geoscience and Remote Sensing Letters* 15, 4, pp. 602–606. DOI: 10.1109/lgrs.2018.2794545.
- Moreno, A. M., A. Seffah, R. Capilla and M.-I. Sanchez-Segura (2013). “HCI Practices for Building Usable Software”. In: *Computer* 46, 4, pp. 100–102. DOI: 10.1109/mc.2013.133.
- Morgenschweis, G. (2018). In: *Hydrometrie: Theorie und Praxis der Durchflussmessung in offenen Gerinnen*. 2nd ed. Springer: Berlin/Heidelberg, DE. Chap. Messung des Wasserstands, 637: 25–114. ISBN: 9783662553145. DOI: 10.1007/978-3-662-55314-5_3.
- Muller, C., L. Chapman, S. Johnston, C. Kidd, S. Illingworth, G. Foody, A. Overeem and R. Leigh (2015). “Crowdsourcing for climate and atmospheric sciences: current status and future potential”. In: *International Journal of Climatology* 35, 11, pp. 3185–3203. DOI: 10.1002/joc.4210.
- Mulsow, C., H.-G. Maas and B. Hentschel (2016). “Optical triangulation on instationary water surfaces”. In: *International Archives of the Photogrammetry, Remote Sensing and Spatial Information Sciences XLI-B5*, pp. 85–91.
- Muntenescu, F. (2016). *upday. Android Architecture Patterns Part 2: Model-View-Presenter*. online. Accessed: 23rd June 2020. URL: <https://upday.github.io/blog/model-view-presenter/>.
- Muratov, O., Y. Slynko, V. Chernov, M. Lyubimtseva, A. Shamsuarov and V. Bucha (2016). “3DCapture: 3D Reconstruction for a Smartphone”. In: *Proceedings of 2016 IEEE Conference*

- on *Computer Vision and Pattern Recognition Workshops (CVPRW)*. Las Vegas, NV, US (26. Jun–01. Jul 2016). IEEE, pp. 893–900. DOI: 10.1109/CVPRW.2016.116.
- Musa, Z. N., I. Popescu and A. Mynett (2015). “A review of applications of satellite SAR, optical, altimetry and DEM data for surface water modelling, mapping and parameter estimation”. In: *Hydrology and Earth System Sciences Discussions* 12, 5, pp. 4857–4878. DOI: 10.5194/hessd-12-4857-2015.
- National Oceanic and Atmospheric Administration (NOAA), Office of Education (2020). *Citizen science and crowdsourcing*. online. Accessed: 17th June 2020. URL: <https://www.noaa.gov/office-education/citizen-science-crowdsourcing>.
- Nedelkovski, D. (2015). *HowToMechatronics. MEMS Accelerometer Gyroscope Magnetometer and Arduino*. online. Accessed: 05th September 2020. URL: <https://howtomechatronics.com/how-it-works/electrical-engineering/mems-accelerometer-gyroscope-magneto-meter-arduino/>.
- Newzoo (2019). *Statista. Number of smartphone users worldwide from 2016 to 2021 (in billions)*. online. Accessed: 19th June 2020. URL: <https://www.statista.com/statistics/330695/number-of-smartphone-users-worldwide/>.
- Nielsen, J. (2006). *Nielsen Norman Group. The 90-9-1 Rule for Participation Inequality in Social Media and Online Communities*. online. Accessed: 16th June 2020. URL: <https://www.nngroup.com/articles/participation-inequality/>.
- Pacha, A. (2015). *Sensor Fusion for Robust Outdoor Augmented Reality Tracking on Mobile Devices. Master’s Thesis, Augsburg University, DE*. GRIN Verlag: Munich, DE. ISBN: 9783656964025.
- Pai, M. M., V. Mehrotra, S. Aiyar, U. Verma and R. M. Pai (2019). “Automatic Segmentation of River and Land in SAR Images: A Deep Learning Approach”. In: *Proceedings of 2019 IEEE Second International Conference on Artificial Intelligence and Knowledge Engineering (AIKE)*. Sardinia, IT (3–5 Jun 2019). IEEE. DOI: 10.1109/aike.2019.00011.
- Paolacci, G. and J. Chandler (2014). “Inside the Turk”. In: *Current Directions in Psychological Science* 23, 3, pp. 184–188. DOI: 10.1177/0963721414531598.
- Paul, J. D., W. Buytaert and N. Sah (2020). “A Technical Evaluation of Lidar-Based Measurement of River Water Levels”. In: *Water Resources Research* 56, 4. DOI: 10.1029/2019wr026810.
- Paziewski, J. D. (2020). “Recent advances and perspectives for positioning and applications with smartphone GNSS observations”. In: *Measurement Science and Technology* 31, 9, p. 091001. DOI: 10.1088/1361-6501/ab8a7d.
- Pei, L., R. Guinness, R. Chen, J. Liu, H. Kuusniemi, Y. Chen, L. Chen and J. Kaistinen (2013). “Human Behavior Cognition Using Smartphone Sensors”. In: *Sensors* 13, 2, pp. 1402–1424. DOI: 10.3390/s130201402.
- Pinto, C. M. and C. Coutinho (2018). “From Native to Cross-platform Hybrid Development”. In: *Proceedings of 018 International Conference on Intelligent Systems (IS)*. Funchal, PT (25–27 Sep 2018). IEEE, pp. 669–676. DOI: 10.1109/is.2018.8710545.

-
- Poulose, A., B. Senouci and D. S. Han (2019b). “Performance Analysis of Sensor Fusion Techniques for Heading Estimation Using Smartphone Sensors”. In: *IEEE Sensors Journal* 19, 24, pp. 12369–12380. DOI: 10.1109/jsen.2019.2940071.
- Prabha, R., M. Tom, M. Rothermel, E. Baltsavias, L. Leal-Taixe and K. Schindler (2020). “Lake ice monitoring with webcams and crowd-sourced images”. In: *ISPRS Annals of Photogrammetry, Remote Sensing and Spatial Information Sciences V-2-2020*, pp. 549–556. DOI: 10.5194/isprs-annals-v-2-2020-549-2020.
- Qiao, C., J. Luo, Y. Sheng, Z. Shen, Z. Zhu and D. Ming (2011). “An Adaptive Water Extraction Method from Remote Sensing Image Based on NDWI”. In: *Journal of the Indian Society of Remote Sensing* 40, 3, pp. 421–433. DOI: 10.1007/s12524-011-0162-7.
- Qin, T., P. Li and S. Shen (2018). “VINS-Mono: A Robust and Versatile Monocular Visual-Inertial State Estimator”. In: *IEEE Transactions on Robotics* 34, 4, pp. 1004–1020. DOI: 10.1109/tro.2018.2853729.
- Qiu, G., K. Cheng, L. Liu and S. Zeng (2018). “TMarkov: LBS Trajectory Prediction for Crowdsourcing Recommendation”. In: *Proceedings of 2018 International Conference on Networking and Network Applications (NaNA). Xi’an, CN (12–15 Oct 2018)*. IEEE, pp. 153–158. DOI: 10.1109/nana.2018.8648773.
- Rehm, L. (2020). *DPreview. OPPO announces dual-cam 5x optical zoom technology for smartphones*. online. Accessed: 21th September 2020. URL: <https://www.dpreview.com/news/6628566824/oppo-announces-5x-optical-zoom-technology-for-smartphone-cameras>.
- Revaud, J., P. Weinzaepfel, C. De Souza and M. Humenberger (2019). “R2D2: Repeatable and Reliable Detector and Descriptor”. In: *Proceedings of 33rd Conference on Neural Information Processing Systems (NeurIPS 2019). Vancouver, CA (8–11 Dec 2019)*, pp. 1–11. URL: <https://papers.nips.cc/paper/9407-r2d2-reliable-and-repeatable-detector-and-descriptor.pdf>.
- Ridolfi, E. and P. Manciola (2018). “Water Level Measurements from Drones: A Pilot Case Study at a Dam Site”. In: *Water* 10, 3, p. 297. DOI: 10.3390/w10030297.
- Rietdorf, A., C. Daub and P. Loeff (2006). “Precise positioning in real-time using navigation satellites and telecommunication”. In: *Proceedings of The 3rd Workshop on Positioning and Communication (WPNC’06). Hannover, DE (16 Mar 2006)*. Vol. 3. Hannoversche Beiträge zur Nachrichtentechnik. Shaker, pp. 123–128. URL: <http://citeseerx.ist.psu.edu/viewdoc/download?doi=10.1.1.581.2400&rep=rep1&type=pdf>.
- Royem, A. A., C. K. Mui, D. R. Fuka and M. T. Walter (2012). “Proposing a low-tech, affordable, accurate stream stage monitoring system”. In: *Transactions of the ASABE* 55, 6, pp. 2237–2242. DOI: 10.13031/2013.42512.
- Sardemann, H., A. Eltner and H.-G. Maas (2018). “Acquisition of geometrical data of small rivers with an unmanned water vehicle”. In: *International Archives of the Photogrammetry, Remote Sensing and Spatial Information Sciences XLII-2*, pp. 1023–1027. DOI: 10.5194/isprs-archives-xlii-2-1023-2018.
- Schiesser, T. (2014). *TechSpot. Know Your Smartphone: A Guide to Camera Hardware*. online. Accessed: 01th October 2020. URL: <https://www.techspot.com/guides/850-smartphone-camera-hardware/>.

- Shahbudin, F. E. and F.-F. Chua (2013). “Design Patterns for Developing High Efficiency Mobile Application”. In: *Journal of Information Technology & Software Engineering* 3, 3, pp. 1–9. DOI: 10.4172/2165-7866.1000122.
- Shu, S., H. Liu, R. A. Beck, F. Frappart, J. Korhonen, M. Xu, B. Yang, K. M. Hinkel, Y. Huang and B. Yu (2020). “Analysis of Sentinel-3 SAR altimetry waveform retracking algorithms for deriving temporally consistent water levels over ice-covered lakes”. In: *Remote Sensing of Environment* 239, p. 111643. DOI: 10.1016/j.rse.2020.111643.
- Siedschlag, S. (2015). “Wasserstände und Durchflüsse – messen, speichern und übertragen im digitalen Zeitalter”. In: *Dresdner Wasserbauliche Mitteilungen* 53, pp. 231–240. URL: <https://hdl.handle.net/20.500.11970/103383>.
- Snavely, N., S. M. Seitz and R. Szeliski (2007). “Modeling the World from Internet Photo Collections”. In: *International Journal of Computer Vision* 80, 2, pp. 189–210. DOI: 10.1007/s11263-007-0107-3.
- Solin, A., S. Cortes, E. Rahtu and J. Kannala (2018). “PIVO: Probabilistic Inertial-Visual Odometry for Occlusion-Robust Navigation”. In: *Proceedings of the 2018 IEEE Winter Conference on Applications of Computer Vision (WACV). Lake Tahoe, NV, US (12–15 Mar 2018)*. IEEE, pp. 616–625. DOI: 10.1109/WACV.2018.00073.
- Strobl, B., S. Etter, I. van Meerveld and J. Seibert (2019). “The CrowdWater game: A playful way to improve the accuracy of crowdsourced water level class data”. In: *PLOS ONE* 14, 9, e0222579. DOI: 10.1371/journal.pone.0222579.
- Subirana, J. S., J. M. J. Zornoza and M. Hernández-Pajares (2013). *GNSS Data Processing: Fundamentals and algorithms*. ESA Communications: Noordwijk, NL. ISBN: 9789292218867.
- Szot, T., C. Specht, M. Specht and P. S. Dabrowski (2019). “Comparative analysis of positioning accuracy of Samsung Galaxy smartphones in stationary measurements”. In: *PLOS ONE* 14, 4, e0215562. DOI: 10.1371/journal.pone.0215562.
- Tanaka, K., Y. Fujihara, K. Hoshikawa and H. Fujii (2019). “Development of a flood water level estimation method using satellite images and a digital elevation model for the Mekong floodplain”. In: *Hydrological Sciences Journal* 64, 2, pp. 241–253. DOI: 10.1080/02626667.2019.1578463.
- Tanskanen, P., K. Kolev, L. Meier, F. Camposeco, O. Saurer and M. Pollefeys (2013). “Live Metric 3D Reconstruction on Mobile Phones”. In: *Proceedings of 2013 IEEE International Conference on Computer Vision. Sydney, NSW, AU (01–08 Dec 2013)*. IEEE, pp. 65–72. DOI: 10.1109/iccv.2013.15.
- van Diggelen, F., C. Abraham, J. de Salas and R. Silva (2011). “GNSS Inside Mobile Phones”. In: *InsideGNSS* 03/04, pp. 50–60. URL: <https://insidegnss.com/wp-content/uploads/2018/01/marapr11-VanDiggelenREV.pdf>.
- Verma, A. (2011). “Identification of land and water regions in a satellite image: a texture based approach”. In: *International Journal of Computer Science Engineering and Technology* 1, pp. 361–365.
- Vickers, H., E. Malnes and K.-A. Høgda (2019). “Long-Term Water Surface Area Monitoring and Derived Water Level Using Synthetic Aperture Radar (SAR) at Altevatn, a Medium-Sized Arctic Lake”. In: *Remote Sensing* 11, 23, p. 2780. DOI: 10.3390/rs11232780.

-
- von Ahn, L. and L. Dabbish (2004). “Labeling Images with a Computer Game”. In: *Proceedings of SIGCHI Conference on Human Factors in Computing Systems (CHI '04)*. Vienna, AT (Apr 2004). ACM, pp. 319–326. DOI: 10.1145/985692.985733.
- VuMA (2019). *Statista. Anzahl der Smartphone-Nutzer in Deutschland in den Jahren 2009 bis 2019 (in Millionen)*. online. Accessed: 19th June 2020. URL: <https://de.statista.com/statistik/daten/studie/198959/umfrage/anzahl-der-smartphonennutzer-in-deutschland-seit-2010/>.
- Wanninger, L. and A. Heßelbarth (2020). “GNSS code and carrier phase observations of a Huawei P30 smartphone: quality assessment and centimeter-accurate positioning”. In: *GPS Solutions* 24, 64, pp. 1–9. DOI: 10.1007/s10291-020-00978-z.
- Wdowinski, S., S.-W. Kim, F. Amelung, T. H. Dixon, F. Miralles-Wilhelm and R. Sonenshein (2008). “Space-based detection of wetlands’ surface water level changes from L-band SAR interferometry”. In: *Remote Sensing of Environment* 112, 3, pp. 681–696. DOI: 10.1016/j.rse.2007.06.008.
- Wieggers, K. and J. Beatty (2013). *Software requirements*. 3rd ed. Microsoft Press: Redmond, WA, US. ISBN: 9780735679665.
- Wittlich, H. and R. Schönball (2017). *Der Tagesspiegel. Das erste Smartphone war ein Nokia*. online. Accessed: 23rd June 2020. URL: <https://www.tagesspiegel.de/wirtschaft/10-jahre-iphone-das-erste-smartphone-war-ein-nokia/19221898.html>.
- Wu, D., Y. Zhang, L. Bao and A. C. Regan (2013). “Location-Based Crowdsourcing for Vehicular Communication in Hybrid Networks”. In: *IEEE Transactions on Intelligent Transportation Systems* 14, 2, pp. 837–846. DOI: 10.1109/tits.2013.2243437.
- Yang, X., S. Zhao, X. Qin, N. Zhao and L. Liang (2017). “Mapping of Urban Surface Water Bodies from Sentinel-2 MSI Imagery at 10 m Resolution via NDWI-Based Image Sharpening”. In: *Remote Sensing* 9, 6, p. 596. DOI: 10.3390/rs9060596.
- Yuan, X., S. Yu, S. Zhang, G. Wang and S. Liu (2015). “Quaternion-Based Unscented Kalman Filter for Accurate Indoor Heading Estimation Using Wearable Multi-Sensor System”. In: *Sensors* 15, 5, pp. 10872–10890. DOI: 10.3390/s150510872.
- Zandbergen, P. A. (2009). “Accuracy of iPhone Locations: A Comparison of Assisted GPS, WiFi and Cellular Positioning”. In: *Transactions in GIS* 13, pp. 5–25. DOI: 10.1111/j.1467-9671.2009.01152.x.
- Zandbergen, P. A. and S. J. Barbeau (2011). “Positional Accuracy of Assisted GPS Data from High-Sensitivity GPS-enabled Mobile Phones”. In: *Journal of Navigation* 64, 03, pp. 381–399. DOI: 10.1017/s0373463311000051.
- Zeng, Q., S. Zeng, J. Liu, Q. Meng, R. Chen and H. Huang (2018). “Smartphone Heading Correction Based on Gravity Assisted and Middle Time Simulated-Zero Velocity Update Method”. In: *Sensors* 18, 10, p. 3349. DOI: 10.3390/s18103349.
- Zhang, Y., Y. Gu, L. Liu, M. Pan, Z. Dawy and Z. Han (2015). “Incentive mechanism in crowdsourcing with moral hazard”. In: *Proceedings of 015 IEEE Wireless Communications and Networking Conference (WCNC)*. New Orleans, LA, US (9–12 Mar 2015). IEEE, pp. 2085–2090. DOI: 10.1109/wcnc.2015.7127789.

List of Figures

4.1	Evolution of smartphones.	16
4.2	Structure of a smartphone camera module.	17
4.3	Periscope-zoom camera designed for the use in smartphones.	18
4.4	Three families of smartphone-based positioning solutions.	22
4.5	Pseudorange measurement impacts, from Subirana et al. (2013).	24
4.6	Generic block diagram of a smartphone-implemented GNSS receiver.	26
4.7	Basic structures of MEMSs accelerometer, gyroscope and magnetometer.	28
6.1	Simplified V-model describing six phases in software development.	37
6.2	MVC and MVP software design patterns, adapted from Chandel (2009).	40
7.1	Transformation of a 3D object point \vec{X} into a 2D image point \vec{x}'	49
7.2	Measurement setup.	51
7.3	IOP-to-temperature assessment using smartphones.	54
7.4	Visualisation of image point shifts/zooming effects (smartphone self-heating).	56
7.5	IOP-to-temperature assessment using RPi camera v2.1.	57
7.6	Visualisation of image point shifts/zooming effects (ambient temperature changes).	58
7.7	Visualisation of linear dependencies between IOP and temperature (c).	59
7.8	Correlation between IOP and temperature by Pearson correlation (ρ).	59
7.9	Median correlations $\tilde{\rho}$ between the individual IOP per camera.	60
7.10	Projection of image points $p'_i(x', y')$ onto a virtual object plane.	62
7.11	Directional error in object space by s_1^* and s_2^*	63
8.1	Smartphone sensor coordinate system in relation to a world coordinate system.	77
8.2	Experimental setup.	79
8.3	Accuracy investigation of smartphone-based rotation parameters.	81
8.4	Stability investigation of smartphone-based rotation parameters.	81
8.5	Histograms of the total deviations regarding azimuth.	82
9.1	Schematic use case of water level determination using hand-held smartphone.	90
9.2	Appearances of different running waters.	92
9.3	Process pipeline from data acquisition to result display.	94
9.4	Master image, average image, spatio-temporal texture.	95
9.5	Histogram analyses of spatio-temporal textures.	96
9.6	Histogram analyses of average images.	96
9.7	Overlaid spatio-temporal texture.	98
9.8	Average image with canny edge map overlay.	98
10.1	Four-step algorithmic concept for camera-based water gauging.	107
10.2	Radiometric variances in images of River Weißeritz, Dresden, DE.	108
10.3	View frustum and halo expansion.	111
10.4	Occlusion ambiguities.	112
10.5	Visualisation of the gap-filling algorithm.	112

10.6	Visual workflow summary.	113
10.7	Client–server architecture applied to "Open Water Levels".	115
10.8	Set-ups of camera-based and conventional systems.	117
10.9	Water-level deviation between camera-based water levels and reference values.	118
10.10	True-to-synthetic image registration with failed 3D water-level detection.	119
10.11	Image synthesis influencing water level determination.	121
10.12	Deviation of synthetic water stage regarding position and rotation errors.	121
10.13	Use cases to quantify the impact of radiometric variances on image–to–geometry registration.	123
10.14	See Figure 10.13, applying TGI vegetation masking.	124
10.15	See Figure 10.13, applying Wallis filter.	124
10.16	Deviation of synthetic water stage with radiometric variances.	125
13.1	Applying OWL for water line detection.	144
13.2	Water line detection by spatio-temporal texture analysis.	146
13.3	CNN-based water surface segmentation.	148
13.4	Examples of matches obtained by the D2-Net method.	148
13.5	Comparison of real-to-synthetic image matching: SIFT+FLANN vs. D2-Net+BF.	149

List of Tables

2.1	Overview of measuring systems used in conventional water gauging stations. . . .	7
7.1	Smartphone device information and camera specifications.	48
7.2	Changes in the IOP of the built-in smartphone cameras from LG Google Nexus 5 and Samsung Galaxy S8 between the last and first estimated variables.	55
7.3	Extracts from a subset of images of measurement series M1 with temperature overlay.	55
7.4	F-test parameters.	56
7.5	F-test success ratios $\zeta(k)$	57
7.6	Extracts from a subset of images of both measurement series M1 and M2 using the RPi camera v2.1.	58
7.7	Percentages of projected object points classified by their Euclidean distances to the expected object point coordinates.	62
8.1	Smartphone specifications.	78
8.2	Manufacturer's information to IMU <i>Spatial</i>	78
9.1	Study areas covering urban and rural running waters.	93
9.2	Summary of processing times.	99
9.3	Experimental investigations of water lines using the spatio-temporal texture and the average for image segmentation respectively.	100
10.1	Investigation of absolute smartphone positing using built-in sensors.	109
10.2	Accuracy investigation of smartphone-implemented water gauging.	118

List of Abbreviations

A-GNSS	Assisted GNSS	GPSS	Geodetic Postprocessing Positioning Service
ADC	Analogue-to-Digital Converter	GPS	Global Positioning System
AF	Autofocus	GPU	Graphics Processing Unit
ALB	Airborne Laser Bathymetry	GSD	Ground Sampling Distance
API	Application Programming Interface	GUI	Graphical User Interface
App	Smartphone Application	IMU	Inertial Measurement Unit
AR	Augmented Reality	InSAR	Interferometric SAR
ARV	Android Rotation Vector	IOP	Interior Orientation Parameters
ARW	Angular Random Walk	IoU	Intersection over Union
BBox	Bounding Box	IR	Infrared
BDS	BeiDou Navigation Satellite System	IRS1	Improved Rotation Sensor 1
BF	Brute-Force Matching	IRS2	Improved Rotation Sensor 2
CCD	Charge-Coupled Device	ISPRS	International Society of Photogrammetry, Remote Sensing and Spatial Information Sciences
CF	Complementary Filter	JDK	Java Development Kit
CMOS	Complementary Metal-Oxide-Semiconductor	JSON	JavaScript Object Notation
CNN	Convolutional Neural Network	LBS	Location-Based Services
CPU	Central Processing Unit	LGLN	Official German Surveying and Mapping Agency for Geoinformation and State Survey of Lower Saxony
DC	Direct Current	LIDAR	Light Detection and Ranging
DEM	Digital Elevation Model	LKF	Linear Kalman Filter
DLT	Direct Linear Transformation	MEMS	Micro-Electro-Mechanical System
DSLR	Digital Single-Lens Reflex	MI	Mutual Information
DSM	Digital Surface Model	MP	Megapixel
DTM	Digital Terrain Model	MSCR	Maximally Stable Colour Regions
EKF	Extended Kalman Filter	MVC	Model-View-Controller
EOP	Exterior Orientation Parameters	MVP	Model-View-Presenter
ESF	European Social Fund	NDWI	Normalized Difference Water Index
FLANN	Fast Library for Approximate Nearest Neighbors	NESW	North East South West
FTP	File Transfer Protocol	NIR	Near Infrared
GCP	Ground Control Point	ORB	Oriented FAST and Rotated BRIEF
GIS	Geographic Information System		
GLONASS	Global Navigation Satellite System		
GNSS	Global Navigation Satellite System		

OS	Operating System		
OWL	Open Water Levels	SNR	Signal-to-Noise Ratio
POI	Point of Interest	SoC	System on Chip
PPP	Precise Point Positioning	SONAR	Sound Navigation and Ranging
PRN	Pseudo Random Noise	SRTM	Shuttle Radar Topography Mission
PVT	Position Velocity and Time	SWIR	Short-Wave Infrared
Px	Pixel	TGI	Triangular Greenness Index
RADAR	Radio Detection and Ranging	TIR	Thermal Infrared
RANSAC	Random Sample Consensus	TLS	Terrestrial Laser Scanning
RF	Radio Frequency	ToF	Time of Flight
RFID	RF Identification	UAV	Unmanned Aerial Vehicle
RGB	Red/green/blue	UI	User Interface
RMSE	Root Mean Square Error	UKF	Unscented Kalman Filter
ROI	Regions of Interest	ULS	UAV-Based Laser Scanning
RPi	Raspberry Pi	UTM	Universal Transverse Mercator
RSSI	Received Signal Strength Indication	UUID	Universally Unique Identifier
RTK	Real-Time Kinematic	UWV	Unmanned Water Vehicle
SAPOS	Satellite Positioning Service	VGI	Volunteered Geographic Information
SAR	Synthetic Aperture Radar	WGS 84	World Geodetic System 1984
SDK	Software Development Kit	WWM-2015	World Magnetic Model 2015
SfM	Structure from Motion		
SFTP	Secure File Transfer Protocol		
SIFT	Scale-Invariant Feature Transform		